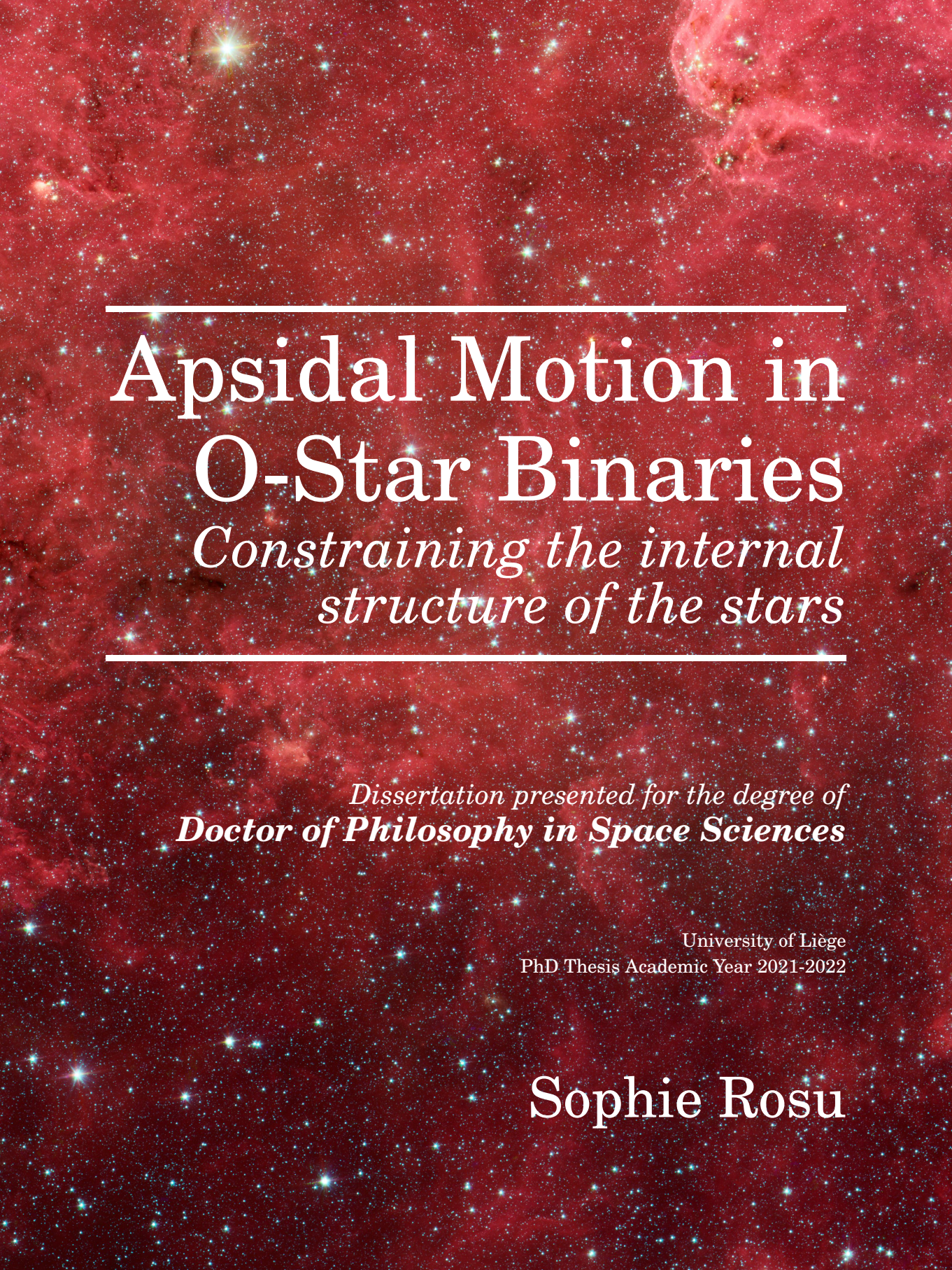

Apsidal Motion in O-Star Binaries

Constraining the internal structure of the stars

Dissertation presented for the degree of
Doctor of Philosophy in Space Sciences

University of Liège
PhD Thesis Academic Year 2021-2022

Sophie Rosu

Apsidal Motion in O-Star Binaries

Constraining the internal structure of the stars

Dissertation presented for the degree of
Doctor of Philosophy in Space Sciences

University of Liège
PhD Thesis Academic Year 2021-2022

Sophie Rosu

Apsidal Motion in O-Star Binaries

Constraining the internal structure of the stars

Dissertation presented for the degree of
Doctor of Philosophy in Space Sciences

University of Liège
PhD Thesis Academic Year 2021-2022

Sophie Rosu

Jury Members

Professor Gregor Rauw (Supervisor)
Professor Marc-Antoine Dupret (President)
Professor Alvaro Giménez
Professor Anne Lemaitre
Professor Georges Meynet
Doctor Yaël Nazé

LIÈGE université
Sciences
Astrophysique, Géophysique et Océanographie

fnrs
LA LIBERTÉ DE CHERCHER

This work is supported by the Fonds de la Recherche Scientifique (F.R.S. - FNRS), Belgium.

Cover image from NASA Image and Video Library, *The Case of the Disappearing Continent*, `https://www.nasa.gov/sites/default/files/images/529990main_PIA13843.jpg`, with permission.

To my Mum,
To her insatiable curiosity of Nature.

To my Dad,
To his astonishing perfectionism.

In memory of Rudy,
To our "Hurry up and wait! (Or eat a Trdelník...)."

Preface

How everything started

"If a cluttered desk is a sign of a cluttered mind, what is the significance of a clean desk?"

(Laurence J. Peter)

Once upon a time, several million years ago, somewhere in the Galaxy, around 16 54 08.51 -41 49 36.0 in ICRS coordinates, something intense happened. What exactly? Most probably a Supernova explosion. This death of a star transformed the surrounding region into a star-forming region, giving birth to NGC 6231. This young open cluster saw the birth of plenty of stars, the most spectacular being big O and B stars. At the Universe scale, or even at the Galaxy scale, such a Supernova explosion followed by a cluster formation is a common event.

At the human scale, each cluster formation event is a unique opportunity to accumulate observations, to develop theoretical models to explain these observations or to confront existing models to new observations. The objective? To increase the scientific knowledge. The immeasurable wish humans have to understand where we – at the human, Solar system, Galaxy, Universe scales – come from, how all planets, stars, clusters, and galaxies formed, how everything started and how everything will end, this immeasurable wish humans already had in the Antiquity, has been and will always be the driving force of our community and justifies the means deployed to find answers to these questions.

At the astronomer scale, such an event is nothing else than an additional reason to make our passion a work. Passionate to a point where we do not make any distinction between week and weekend. Passionate to a point where sunset does not indicate anymore that the workday comes to an end. Passionate to a point where debugging a code has become the highest priority of our life, completely forgetting about lunch or dinner. Passionate to a point where our wish is to always contribute more to the scientific knowledge.

NGC 6231, and especially four binary stars located in it, namely HD 152248, HD 152219, CPD-41° 7742, and HD 152218, have been the driving force of the research I carried out the last four years. The beginning of the story dates back to one day in the middle of April 2015, during my first year of Master in Space Science. I had a decisive meeting – even though I did not know it was decisive at that time – in the office of the person who became my supervisor afterwards, Gregor Rauw.

During this meeting, he proposed me a few Master Thesis subjects he could supervise. All subjects were mostly about coding and, to be honest, coding was not my cup of tea at that time. I was merely dreaming about having a pen, loads of sheet of papers, and making calculus by hand. Afterthought, I feel I was naive (not to say something else) but this naive answer was probably the starting point of this fantastic collaboration. Could I imagine it would end like this at that time? Absolutely not.

A bit surprised at first (but who would not be in such a situation?), he told me "let me cogitate, I think I have a very old subject on which I want to work for a long time, but I have not had the time for at least eight years". Saying that, he took the last mass of paper of one of the numerous huge piles of papers he has in his office. To be honest, I do not know how everything did not fall down on the ground... maybe due to the gravitational attraction exerted by the others huge piles of papers all around that prevented the paper-collapse (I do not have found a better explanation so far, but I am open to any suggestion!) neither how he remembered these papers were exactly in that mass of paper (to that, he told me that every single thing in his office has its right place... but we never agreed on this subject).

The subject we worked on was the apsidal motion in the massive binary HD 152218. Having developed all the mathematical background needed to study such a phenomenon in binary stars and having applied it successfully to the first candidate, we unhesitatingly wanted to extend our sample of binary stars to which applying our method. It is with enthusiasm and energy that, two years later, I started my PhD carrying on this project.

Taking the opportunity of having a huge set of observations for these stars, my colleagues and I could reassess the fundamental parameters of these stars and build stellar evolution models to confront theory with these observations to constrain the internal structure of the stars. This project set through, I hope it will influence the scientific research in this field in the coming years and will be the starting point of my continuous contribution in this field of research, towards a better understanding of the immensity of the Universe.

Sophie Rosu
Liège, Belgium, June 2022

Acknowledgements

The one who is more than grateful

"It would not be much of a Universe if it wasn't home to the people you love."

(Stephen Hawking)

This Thesis dissertation, much more than the achievement of a four-year PhD thesis, is above all the result of my passion in Stellar Astrophysics which has kept growing for years. This passion has been strongly reinforced throughout these last four years thanks to many people close to me. I would like, through these few lines, to express my most sincere thanks to those people who have contributed to this professional and personal achievement.

There is no word strong enough to express all my gratefulness to Gregor Rauw. I could write pages and pages of thanks that would still not be sufficient to recognise all his contribution to my daily life research. He took me by the hand from the first day to guide me, giving me more and more freedom as time went by. The most important thing he gave me was his time. Time to teach me specific techniques or scientific subjects, time to double-check my results, time to process data, time to read and correct, again and again, my papers, time to take stock of the situation. I remember very distinctly each and every discussion we had these last four years. These talks, part of a meeting or leafed through a corridor, were the most productive and enriching moments. His rigour and involvement have been the guardian of this research work.

My gratefulness also goes to Alain Detal. He did his utmost, with an extreme rapidity, to solve all kind of computer-related problems (as ridiculous as these were, sometimes) I had. I could give him my computer closed eyes, I knew he would find the solution in record time. It is with a lot of sense of humour and an uncommon patience that he explained me all technical details afterwards.

"Coding is about being lazy", just as my friend and colleague Martin Farnir likes to say. One could not appreciate this way of thinking wholeheartedly unless one experiences it. I thank him for teaching me how laziness could be important in scientific research by optimising codes and running scripts to make these automatic. Now, thanks to him, I even more appreciate drinking my cup of coffee watching my computer working for me!

Being an observer building theoretical models of stars would probably be unrealistic (or completely crazy!) without the assistance of two remarkable theorists, Arlette Noels and Marc-Antoine Dupret. I am thankful to them for their involvement in this part of the research project and for the completely unalike and complementary point of view they brought. When putting two observers and two theorists in the same room closed door to discuss about the same project, one never knows how things will end when one opens the door again. I thank them for the collaboration we built over months.

Special thanks go to Eric Gosset for the numerous discussions we had about the chi-square and Laurent Mahy for his help using the `PHOEBE` *code. In the same line, I would like to thank my colleagues Aurore Blazère and Jahanvi for their support and the happiness they brought in the team.*

I gratefully thank our Secretary Nicole Massin for her valuable assistance in the administrative tasks.

I could not continue without thanking Pierre Dauby who allowed me with complete confidence to teach analytics mechanics exercices sessions to third bachelor students in physics and mathematics during three years. This experience was very rewarding and I learned a lot being, for the first time, on the other side of the classroom! Following on from this, I also thank all the students who attended my lectures, for their participation and their interesting (and sometimes surprising) questions.

During these years, I discovered that one of the most beautiful way to express my passion for Astronomy is to popularise my knowledge to non-specialist people, especially to children. Seeing the wonderment in their eyes when telling them the Story of the Universe is one of the best accomplishment I could claim. The opportunities I had to communicate in front of children during "Printemps des Sciences" or other activities or even the opportunity I had to publish two popularised papers, were given to me thanks to Yaël Nazé. With her expertise in this domain, she could guide me and give me precious advices and I am more than grateful to her.

My deep gratitude goes to Professor Georges Meynet, who invited me for a talk during the weekly Stellar Group Meetings in the Geneva Observatory, and to Professor Raphael Hirschi and Dr Sylvia Ekström, who actively participated in the building of a post-doctoral project for me.

My most profound gratefulness goes to my parents Daniel and Dominique who lent me four attentive ears at home. From code bugs to final published papers, passing through all the small technical and scientific details about the methods implemented and the stars studied, they were updated on every single thing, almost everyday, like an activity report presented during dinner. They followed this achievement on a daily basis, asking me these kind of uncomfortable questions, setting the cat among pigeons, reminding me to come back to the basics. To be honest, I cannot remember how often the pennies dropped during dinners thanks to them!

I want to quote and express my deep gratitude to Florian Cleyet. I thank him for his numerous readings of my post-doctoral applications, for teaching me chess during evenings and evenings, for dragging me outside to take some fresh air and discover the wonders in my own country, and for making non-funny jokes (which, to be honest, make me laugh much more than I would admit) all days long.

I would be fooling myself if I did not mention the Covid-19 pandemic we went through and its impact on both my research activity and daily life. Fortunately, I have those kind of Friends who were there at any time and we sticked together during those hard times. I would like to give them my most heartfelt thanks for the happiness they brought to me in a way or another: Monique Marchand, my childhood friend, for our crazy discussions; Kristoffer Nielsen, who played online boardgames (and never let me win); Juan Manuel Calleja Vazquez, the most devoted friend; Elise Delhez and Guillaume Sicorello, for our countless board games evenings; Colin Dandumont, who always has the latest anecdote to tell.

I also thank very much Gregor Rauw for his active involvement in the manuscript correction, as well as my mum and Florian for their careful reading of the manuscript. I apologise for the unavoidable remaining mistakes, which are evidently my responsibility.

Special thanks go to Pavonet Company, and especially Marvin and Benoît, for their professionalism and perfectionism in the design and printing of this manuscript.

My last thanks go to you, the reader, for the time you will invest in reading this Thesis dissertation and your interest in the research I enthusiastically carried out. I sincerely hope you will read these pages with as much pleasure as I had writing these. I will be glad to hear your comments and I look forward to discussing with you about any topic covered in this manuscript.

Abstract

Stars more massive than about ten solar masses play a key role in many processes in the Universe, notably through their winds and powerful supernova explosions that contribute to the chemical enrichment of the Universe. More than 70% of them are bound by gravitational attraction to a companion star. These binary stars orbit around each other on an elliptic orbit. The tidal interactions occurring between the two stars give rise to the slow precession of the orbit, called the apsidal motion. The rate of this motion is directly related to the internal structure constant of each star, which is a measure of the mass distribution between the core and the external layers of the star. Measuring the apsidal motion rate hence provides a diagnostic of the otherwise difficult to constrain internal structure of stars and offers a test of our understanding of stellar structure and evolution.

We analyse four binary systems located in the young open cluster NGC 6231, namely HD 152248, HD 152219, CPD-41° 7742, and HD 152218. We make use of the extensive set of spectroscopic and photometric observations as well as radial velocity data of these systems to determine their fundamental stellar and orbital parameters, including the apsidal motion rate. We build stellar evolution models assuming different prescriptions for the internal mixing inside the stars. Whenever possible, we identify the models that best reproduce the observationally determined present-day properties of the stars, as well as their internal structure constants, and the apsidal motion rate of the system. We analyse the impact on the results of some poorly constrained input parameters in the models, including overshooting, turbulent diffusion, metallicity, rotation, and binarity. We discuss some effects that could bias our interpretation of the apsidal motion in terms of the internal structure constant.

We report the first measurement of apsidal motion in the binary system CPD-41° 7742 and we solve the discrepancy in the longitudes of periastron found in several past studies. The analysis of the stellar models reveals that, in the cases of HD 152248 and HD 152219, reproducing the internal stellar structure constant value and rate of apsidal motion simultaneously with the other stellar parameters requires a significant amount of internal mixing (either turbulent diffusion or overshooting) or enhanced mass-loss. We suggest that, qualitatively, the high turbulent diffusion required to reproduce the observations could be partly attributed to stellar rotation. For all binaries except HD 152219, we derive an age estimate compatible with the cluster age.

A better understanding of the stellar structure and evolution of these massive binary stars will allow us to predict their remnant masses after supernovae explosion and their fate as either single or binary systems. Understanding the earliest phases of these systems is of primary importance in the context of the recent detection of gravitational wave events with the LIGO and VIRGO experiments as the underlying coalescences of two stellar-mass black holes or neutron stars have massive binary systems as progenitors.

Résumé

Les étoiles d'environ dix masses solaires et plus jouent un rôle clé dans une multitude de processus au sein de l'Univers, notamment au travers de leurs vents stellaires et de leurs explosions en supernovae qui enrichissent le milieu interstellaire en éléments chimiques. Plus de 70% de ces étoiles sont liées à un compagnon par attraction gravitationnelle. Ces étoiles binaires orbitent l'une autour de l'autre sur une orbite elliptique. Les interactions de marées induites par l'attraction réciproque des deux étoiles génèrent une lente précession de l'orbite au cours du temps, connue sous le nom de mouvement des apsides. Le taux de cette précession est directement lié à la constante de structure interne de chaque étoile, une mesure de la distribution de masse entre le cœur et les couches externes de l'étoile. Mesurer ce taux de mouvement des apsides permet dès lors de sonder la structure interne des étoiles, autrement difficile à contraindre, et d'approfondir notre compréhension de l'évolution stellaire.

Quatre systèmes binaires appartenant à l'amas ouvert NGC 6231 sont considérés ici : HD 152248, HD 152219, CPD-41° 7742 et HD 152218. Les observations spectroscopiques et photométriques ainsi que les mesures des vitesses radiales de ces systèmes sont analysées et les paramètres stellaires et orbitaux sont déterminés, en ce inclus le taux de mouvement des apsides. Des modèles d'évolution stellaire sont construits en adoptant différentes prescriptions pour le mélange interne des étoiles. Les modèles qui reproduisent au mieux les propriétés observationelles des étoiles ainsi que leurs constantes de structure interne et le mouvement des apsides sont identifiés. L'impact d'une modification des paramètres d'entrée peu contraints (overshooting, diffusion turbulente, métallicité, rotation et binarité) sur les résultats est analysé. Les effets susceptibles de biaiser l'interprétation du mouvement des apsides en termes de constantes de structure interne sont discutés.

Le mouvement des apsides de CPD-41° 7742 est quantifié pour la première fois et l'incohérence dans les mesures de la longitude du périastre rapportée dans la littérature est ainsi levée. L'analyse des modèles stellaires révèle, dans les cas de HD 152248 et de HD 152219, qu'il n'est possible de reproduire les constantes de structure interne des étoiles, le taux de mouvement des apsides du système et les autres paramètres stellaires simultanément, qu'à moins d'introduire du mélange interne additionnel (diffusion turbulente ou overshooting) et/ou d'augmenter le taux de perte de masse. Qualitativement, la diffusion turbulente additionnelle nécessaire pour reproduire les observations devrait être partiellement attribuée à la rotation stellaire. Les âges estimés pour toutes les binaires excepté HD 152219 sont quant à eux compatibles avec l'âge de l'amas.

Une meilleure connaissance de la structure et de l'évolution des étoiles binaires massives permettra de mieux prédire les mécanismes de leur explosion en supernovae et par là même leur fin de vie en étoile isolée ou en système binaire. Mieux comprendre les premières phases d'évolution de ces systèmes est d'importance fondamentale dans le contexte de la détection récente d'évènements d'ondes gravitationnelles par les expériences LIGO et VIRGO étant donné que les coalescences de deux trous noirs de masses stellaires ou d'étoiles à neutrons ont comme progéniteurs les systèmes binaires massifs.

Contents

Chapter 1

Massive Binary Stars in a Nutshell

"The advance of scientific knowledge does not seem to make either our Universe or our inner life in it any less mysterious."

(John B. S. Haldane)

Massive stars, namely stars more massive than about ten solar masses, are called "Cosmic Engines" (Bresolin et al. 2008) because they drive many processes in the whole Universe. Their rarity compared to less massive stars does not make them less crucial. These hot and luminous objects are the main sources of UV radiation, and, through their radiation-driven stellar winds, they are important sources of chemical and mechanical feedback into the interstellar medium. After a short lifetime compared to Solar-like stars, on the order of ten millions years, the end of their life is up to their animated existence: a spectacular core collapse supernova during which the external layers of the star are expelled in the surrounding medium while the core keeps contracting until becoming a neutron star or a black hole.

Contents

1.1. The one which is not alone

Nowadays, it is thought that the majority of the massive stars (i.e. O and B-type stars having a mass larger than 8 $M_{\odot}$, see Hertzsprung-Russell diagram in Figure 1.1) are, or have been, part of a binary or higher multiplicity system (Duchêne & Kraus 2013). According to current estimates, more than 70% of the massive stars inhabiting our Galaxy have spent some part of their existence in a binary system (Sana et al. 2012). The simple fact of being bound to another star by gravitational attraction can deeply modify the evolutionary track of the considered star. Indeed, whilst the evolution of a single massive star is determined by its initial mass, its mass-loss rate, and its rotational rate (Ekström et al. 2012; Brott et al. 2011), the evolution of a massive binary is considerably more complex and depends not only on the properties of the stars, but also on the parameters of the binary orbit (Wellstein et al. 2001). Stars belonging to a binary system exchange angular momentum through tidal interactions and, for some of them, mass and angular momentum through Roche lobe overflow. The evolutionary sequences of both the mass gainer and the mass loser resulting from these interactions are as diverse as the number of existing binary systems (e.g. Vanbeveren et al. 1998; Raucq et al. 2017).

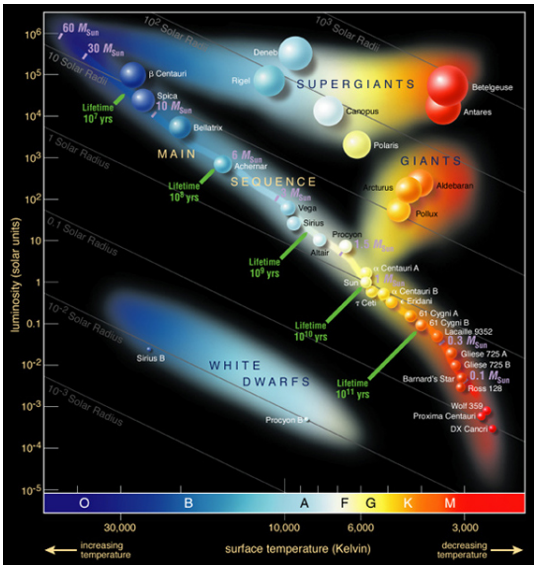

Figure 1.1. Hertzsprung-Russell diagram. ©`http://omsj.info`

1.1.1. Evolution of a massive binary system

The evolution of a massive binary is schematically illustrated in Figure 1.2 for a system made of stars having initial masses of 20 and 8 $M_{\odot}$ (panel (a)). In the following, we call the primary (respectively secondary) the initially more (respectively less) massive star. At stage (b), the primary star enters the supergiant phase and fills its Roche lobe, therefore transferring mass to its companion. Due to the loss of its external hydrogen envelope, the primary

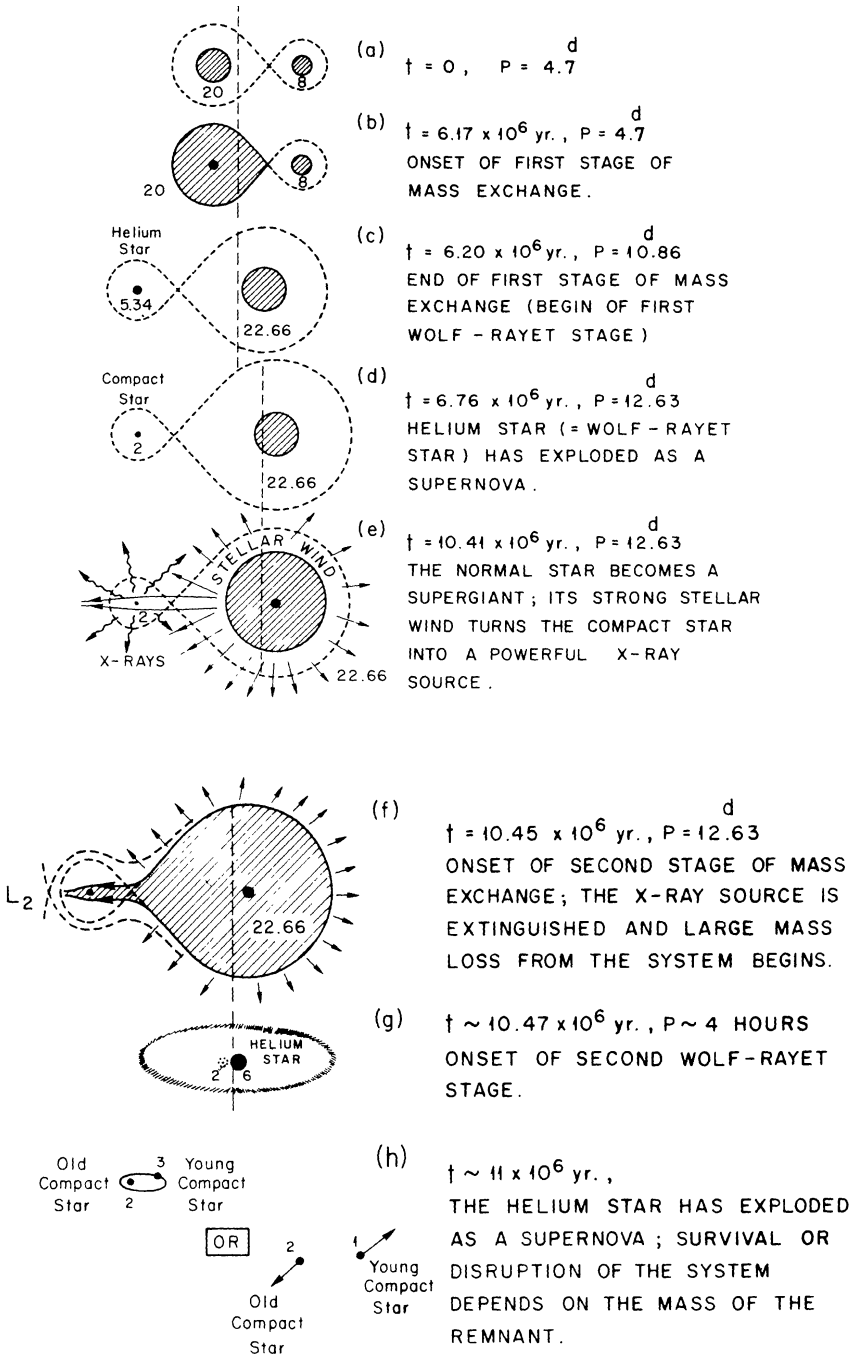

Figure 1.2. Schematic evolution of a close massive binary system. The time and orbital period are indicated for each evolutionary stage. Some alternatives to this scenario are discussed in the main text. ©van den Heuvel (1976).

star becomes a Wolf-Rayet (WR) star and the orbital period of the system progressively increases (panel (c)). The Wolf-Rayet primary star then explodes in a supernova event and produces a compact star, either a neutron star or a black hole. Depending on the masses of the stars and on the configuration of the system, the latter might either disrupt due to the supernova explosion (not shown) or survive to the explosion and remain bound (panel (d)). In the latter case, the secondary star evolves until reaching the supergiant phase. Its strong wind starts to accrete on the compact primary star, therefore producing a strong X-ray emission (panel (e)). The secondary star then fills its Roche lobe and a second mass-transfer episode is initiated from the secondary star to the compact primary companion (panel (f)). During this phase, a large amount of mass is expelled from the system and forms a surrounding nebula. The secondary star becomes a Wolf-Rayet star (panel (g)). At this stage, depending on the configuration of the system, the compact primary and the helium core secondary might merge and form a red supergiant with a neutron star or black hole core, called a Thorne-Zytkow object, which then finally fates as a single neutron star or black hole (not shown), or the secondary might explode in a supernova event (panel (h)). In this latter case, the system might either disrupt and form two single compact objects or stay bound in which case the two compact objects will finally merge and produce gravitational waves.

1.1.2. Constraining the internal structure of the stars through the apsidal motion

There is, however, no need to wait until the onset of mass and angular momentum transfer and/or exchange through Roche lobe overflow for binary interactions to take place. From the earliest phases of stellar evolution, tidal interactions occurring in close binary systems lead to dynamical deformations of the stellar surfaces as the stars orbit each other (Moreno et al. 2011). Tidal interactions are responsible for the non-spherical shape and gravitational field of the stars which in turn induce secular changes of the orbital parameters (Schmitt et al. 2016). The slow precession of the binary system major axis, known as *apsidal motion*, is certainly the most prominent manifestation of this effect: This is illustrated for the Earth-Moon system in Figure 1.3. The resulting apsidal motion rate is directly related to the internal structure constant of the stars that make up the binary system (Shakura 1985). This parameter is a sensitive indicator of the density stratification inside a star and its value strongly changes as the star evolves away from the main sequence. Measuring the rate of apsidal motion in a binary system hence not only provides a diagnostic of the – otherwise difficult to constrain – internal structure of the stars, but also offers a test of our understanding of stellar structure and evolution (Claret & Giménez 2010; Mazeh 2008).

The apsidal motion being a slow rate motion having a typical period of about two hundred years, both long-span observations and very accurate techniques are required to obtain meaningful results. This mostly explains why one had to wait until the late end of the 20^{th} century to see this field of research developing. Bulut & Demircan (2007) reported that till the time of their study, there were, however, only five systems hosting a massive star of at least twenty solar masses for which the apsidal motion rate had been measured. In most cases, the apsidal motion rates were determined from photometric observations of eclipsing

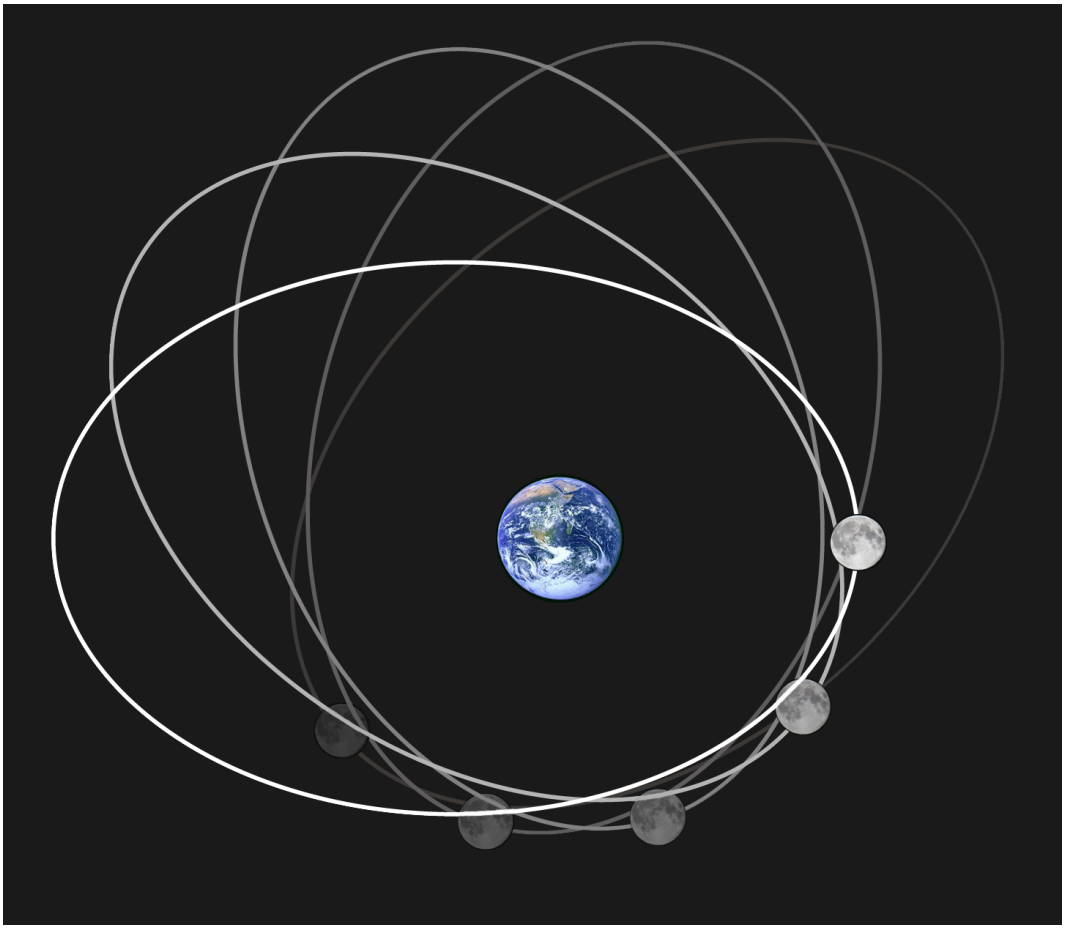

Figure 1.3. Apsidal motion in the Earth-Moon system.

binaries by recording the times of minima of the eclipses. Rauw et al. (2016) showed that long time series of spectroscopic data together with the associated radial velocity measurements also offer a powerful tool to constrain the apsidal motion rate. Hence, the very first goal of this PhD project has been to increase the number of systems with well-determined apsidal motion rates, using a series of modern analysis tools.

In the study of apsidal motion, the approches adopted at the time we started this project were suffering from one major limitation: The stellar evolution models used to compute the internal structure constants were designed for the study of single non-rotating massive stars. Yet, internal structure constants change with stellar evolution and depend upon the details of the internal mixing processes operating inside the stars (Claret & Giménez 2010; Rauw et al. 2016). One of the most prominent mixing processes occurring inside the stars comes from stellar rotation. A single star sees its rotational rate changing as it evolves and loses material and angular momentum through its stellar winds (Ekström et al. 2012; Brott et al.

2011). In a massive binary system, things appear to be more complex: In addition to the change due to the stellar winds, the stellar rotational rates change as a result of the coupling between the rotational and the orbital angular momentum which in turn impacts the mixing inside the stars (de Mink et al. 2009). This tidally-enhanced rotational mixing affects the evolution of the internal structure constants of the stars. Hence, our second objective has been to quantify the impact of tidally-enhanced rotational mixing on the theoretical models, and on the theoretically predicted apsidal motion rates.

Beyond a better understanding of massive binaries evolution, this field of research is of primary importance in the context of the detections of gravitational wave events with the Ligo and Virgo experiments over the past few years (Abbott et al. 2016). Indeed, the events that have been reported so far (at the time of writing) were associated either with the coalescence of two stellar-mass black holes or of two neutron stars. In either case, the progenitors of these events were end products of the evolution of two very massive stars in a binary system (Kruckow et al. 2016). The ultimate goal of this study has been to improve our overall understanding of the evolution of these "Cosmic Engines" that are the massive stars.

1.2. State of the art

At the crossroads between observational and theoretical stellar astrophysics, the study of apsidal motion takes advantage of the development, over recent years, of new powerful tools. To perform such a study, short-period eccentric eclipsing double-line spectroscopic binary systems for which photometric as well as high-quality spectroscopic observations are available are needed. An eclipsing binary is a binary system which shows eclipses of one component by the other during the orbital cycle, either because the inclination of the orbit is close to 90° or because of the proximity of the components of the system. The light curve of such a system thus presents reductions of the apparent brightness during the eclipses. Since the apsidal motion is a very slow motion, either radial velocity and/or photometric measurements of the system spanning several decades are needed to obtain an accurate measure of the apsidal motion rate. In this section, we recall the characteristics and main features of spectroscopic (Section 1.2.1) and eclipsing (Section 1.2.2) binaries, before diving into the heart of the subject and describing the methodology adopted throughout this study (Section 1.2.3).

1.2.1. Spectroscopic binary

A spectroscopic binary is a binary system which shows periodic variations in the wavelengths of its spectral lines. These variations are related to the Doppler effect: When the plane of the binary orbit is not perpendicular to the line of sight, each star of the system moves alternatively towards and away from the observer. Consequently, when the spectral lines of one component are blue-shifted, the spectral lines of the second component are simultaneously red-shifted, and conversely. This is illustrated in Figure 1.4 for the binary system HD 152248. Hence, the Doppler shift, defined as the difference between the observed wavelength λ of the spectral line and its rest wavelength λ_0, is a measure of the radial velocity

(RV) along the line of sight towards the observer:

$$RV = c\frac{\lambda - \lambda_0}{\lambda_0} = c\frac{\Delta\lambda}{\lambda_0}, \tag{1.1}$$

where c is the speed of light. To a negative (respectively positive) radial velocity corresponds a line that is blue-shifted (respectively red-shifted), meaning that the star moves towards (respectively away from) the observer.

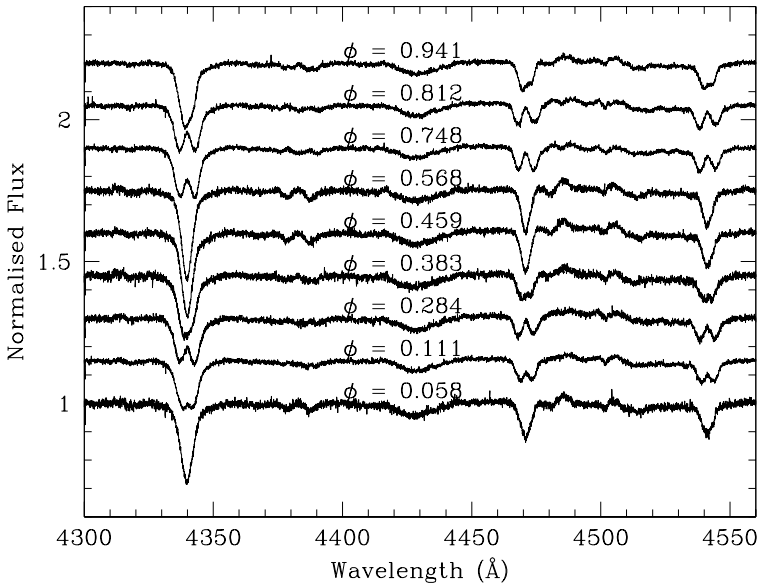

Figure 1.4. Variations, as observed in FEROS spectra of the massive binary system HD 152248, of the shapes of the lines in the spectral range [4300;4550]. Corresponding orbital phases are indicated on top of each spectrum. The lines of the primary and secondary stars – which have the same intensity – are alternatively blue- and red-shifted.

A spectroscopic binary can be either a single-lined (SB1) or a double-lined (SB2) spectroscopic binary.

In the spectra of an SB1 system, only the lines of one star, the most luminous and, usually, the most massive star of the system, are present. In this case, only the radial velocities of this star – which we call here the primary star – can be determined. If the radial velocity of the primary star is known for a number of well-sampled observations over the orbital cycle, the radial velocity curve of this star can be determined. This one is given by the expression

$$RV = \gamma_0 + \sqrt{\frac{\mu}{a(1-e^2)}}\sin i\,(\cos(\omega+\phi) + e\cos\omega)\,, \tag{1.2}$$

where γ_0 is the radial heliocentric velocity of the centre of mass of the binary system and

$\mu = \frac{G\,m_2^3}{(m_1+m_2)^2}$, with G the universal gravitational constant and m_1 and m_2 the masses of the primary and secondary stars, respectively. a, e, and i are the semi-major axis, the eccentricity, and the inclination (the angle between the orbital plane and the plane perpendicular to the line of sight of the observer, see Figure 1.5) of the orbit, respectively. ω and ϕ are the argument of periastron (the angle measured in the orbital plane between the line of nodes and the direction of periastron, see Figure 1.5) and the true anomaly (the angle measured in the orbital plane between the direction of periastron and the position of the primary star, see Figure 1.5), respectively. The semi-amplitude of the primary radial velocity curve K_1 is given by the constant term multiplying the periodic variation:

$$K_1 = \sqrt{\frac{\mu}{a(1-e^2)}}\sin i. \tag{1.3}$$

Starting from Kepler's law

$$a = \frac{\mu^{1/3} P_{\rm orb}^{2/3}}{(2\pi)^{2/3}}, \tag{1.4}$$

where $P_{\rm orb}$ is the orbital period of the system, and doing a bit of algebra, we can show that the semi-amplitude of the radial velocity curve is directly related to the individual masses of the stars through the following relation called the mass function:

$$f(m_1) = \frac{m_2^3 \sin^3 i}{(m_1+m_2)^2} = \frac{K_1^3}{2\pi G} P_{\rm orb}(1-e^2)^{3/2}. \tag{1.5}$$

However, nothing can be deduced from this relation about the mass ratio of the system or about the individual masses of the stars without making guesses relying, for instance, on empirical calibrations of absolute masses as a function of spectral type or on stellar evolution models.

In the spectra of an SB2 system, the lines of the two stars are present. This happens when the stars have comparable brightnesses. In this case, both the radial velocities of the primary and secondary stars can be determined. If the radial velocities of both stars are known for a number of well-sampled observations over the orbital cycle, the radial velocity curves of both stars can be determined. The mass function of the primary star is still given by the previously derived expression (Equation (1.5)) while the mass function of the secondary star is given by a similar expression:

$$f(m_2) = \frac{m_1^3 \sin^3 i}{(m_1+m_2)^2} = \frac{K_2^3}{2\pi G} P_{\rm orb}(1-e^2)^{3/2}, \tag{1.6}$$

where K_2 is the semi-amplitude of the radial velocity curve of the secondary star. Taking the ratio between Equations (1.5) and (1.6) directly gives the mass ratio of the binary system as a function of the ratio between the semi-amplitudes of the radial velocity curves:

$$\frac{m_1}{m_2} = \frac{K_2}{K_1}. \tag{1.7}$$

Inserting this relation into the mass functions (Equations (1.5) and (1.6)) gives us the min-

imum masses of the stars:

$$m_j \sin^3 i = K_j \frac{(K_1 + K_2)^2}{2\pi G} P_{\rm orb} (1 - e^2)^{3/2}, \tag{1.8}$$

where the index j stands for the primary ($j = 1$) or secondary ($j = 2$) star. In order to determine the absolute masses of the stars, the inclination has to be determined separately using, for instance, photometric data if the binary system displays eclipses.

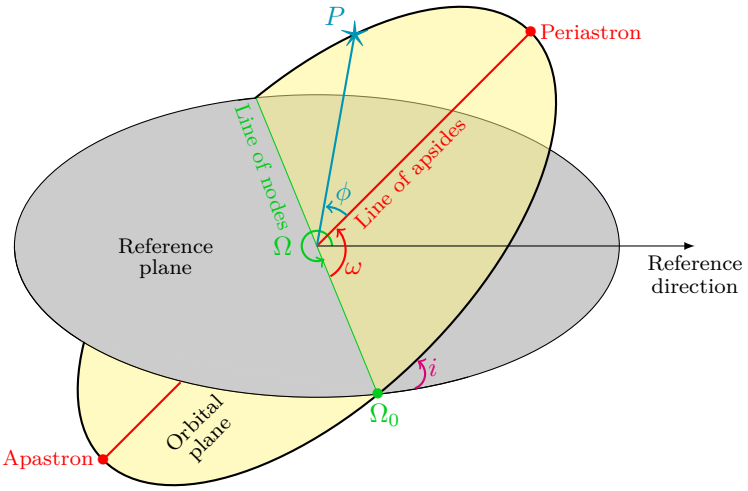

Figure 1.5. Definition of the orbital elements of a binary system. The plane of the sky (the reference plane) is depicted in gray. The orbital plane, inclined by an angle i with respect to the reference plane, is depicted in yellow. The intersection between these two planes is the line of nodes, depicted in green. The angle between the line of nodes and the reference direction is Ω. Located in the orbital plane, the primary star is schematised by the cyan star. The line joining the periastron and apastron, also known as the line of apsides, is depicted in red. The argument of periastron, ω, is the angle between the line of nodes and the line of apsides, while the true anomaly, ϕ, is the angle between the line of apsides and the position of the primary star, both measured in the orbital plane. Figure adapted from Rosu (2021).

1.2.2. Eclipsing binary

Eclipsing binaries are binary systems displaying periodic variations of their apparent brightness on a timescale of the orbital cycle. In these systems, either the inclination of the orbit is close to 90° or the stars eclipse each other because of their proximity. Depending on the case, only one eclipse can exist (the primary star eclipsing the secondary star or inversely) or two eclipses can be seen (both stars eclipse each other). In the forthcoming discussion, we will consider textbook cases were both eclipses are seen in the light curve. The exact shape of the light curve of an eclipsing binary depends upon five major parameters: the inclination of the orbit, the eccentricity of the orbit, the effective temperatures of the stars, the relative sizes and shapes of the stars, and the longitude of periastron at the time of the

observation. These parameters contribute all together in a complex way to the light curve. Numerical codes such as `Nightfall` and `PHOEBE` are therefore used to constrain the parameters of the stars and of the orbit by fitting the observations with synthetic light curves (see Sections 2.1.9 and 2.1.10 for the descriptions of these codes).

1.2.2.1. Orbital inclination

The inclination of the orbit impacts both the depth and the duration of the eclipses. An example is given in Figure 1.6(a) which shows three synthetic light curves (computed with `Nightfall`) of a binary system of zero eccentricity and composed of two identical stars (same mass, size, and effective temperature). Each light curve corresponds to a different inclination of the orbit (70°, 80°, and 90°, respectively), all other parameters being identical. The higher the inclination, the longer the duration of the eclipses and the larger their depth.

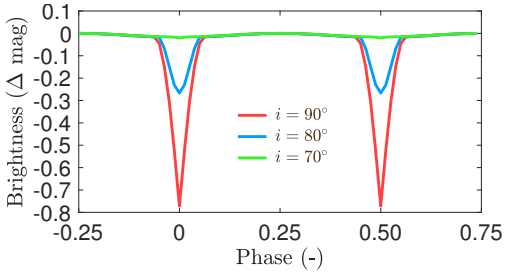

(a) Binary system with zero eccentricity and composed of two identical stars (same mass, size, and effective temperature).

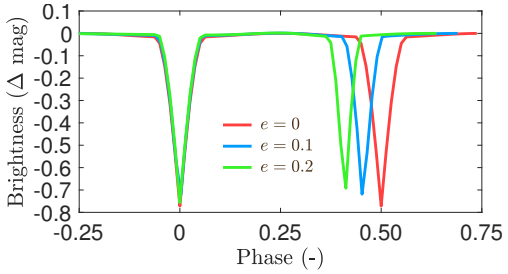

(b) Binary system with an inclination of 90° and composed of two identical stars (same mass, size, and effective temperature). The longitude of periastron $\omega = 45°$ when $e = 0.1$ and 0.2.

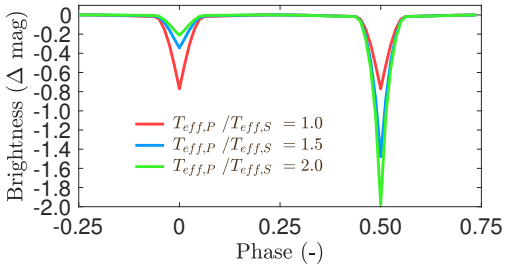

(c) Binary system with an inclination of 90° and zero eccentricity consisting of stars having different effective temperatures, all other parameters being identical for both stars.

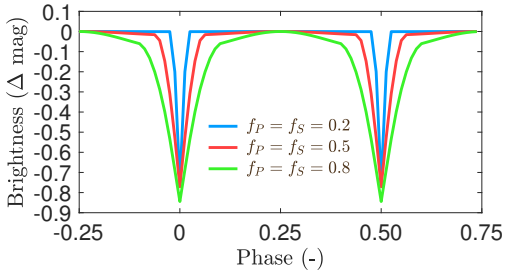

(d) Binary system with an inclination of 90°, zero eccentricity, and composed of two identical stars (same mass, size, and effective temperature).

Figure 1.6. Synthetic light curves (computed with `Nightfall`) of a binary system. (a) Influence of the inclination of the system. (b) Influence of the eccentricity of the system. (c) Influence of the effective temperature of the stars. (d) Influence of the Roche lobe filling factors of the stars.

1.2.2.2. Orbital eccentricity

As long as the orbit has a non-zero eccentricity, the velocities of the stars are not constant over time. The widths of both eclipses might therefore differ, as the times between the photometric minima might as well. This also affects the depths of the eclipses since an eclipse happening during periastron passage, when stars are the closest, would be deeper than an eclipse happening during apastron passage, when stars are further away from each other. This is illustrated in Figure 1.6(b) for a binary system having an inclination of 90° and composed of two identical stars (same mass, size, and effective temperature). Each light curve (computed with `Nightfall`) corresponds to a different eccentricity of the orbit (0, 0.1, and 0.2, respectively).

1.2.2.3. Effective temperatures

Regarding the effective temperatures of the stars, only the ratio between the temperatures affects the light curve, a scaling parameter applied on both temperatures having no impact on the light curve. If the orbit is circular, the depths of the two eclipses only differ if the stars have different effective temperatures. This is shown in Figure 1.6(c) which illustrates three synthetic light curves (computed with `Nightfall`) for a binary system having an inclination of 90° and zero eccentricity but a ratio of the effective temperatures between the primary and secondary stars of 1.0, 1.5, and 2.0, respectively. All other parameters are identical for both stars. The deepest eclipse corresponds to the hottest star being eclipsed.

1.2.2.4. Stellar sizes and shapes

The way the light curves are affected by a change of size and/or shape of the stars is rather trickier to visualise and requires to return to some concepts of Roche geometry beforehand. In a binary system, the stellar shapes are fixed by the equilibrium of the gravitational forces and the centrifugal force due to the orbital motion acting on the stars. An equilibrium situation thus implies that the stellar surface adopts the shape of an equipotential of the potential resulting from the combined effect of the gravitational field and the centrifugal field. This potentiel is called the *Roche potential*, after the French mathematician Edouard Albert Roche (1820-1883). Considering a binary system whose primary star of mass m_1 is bigger and more massive than its secondary companion of mass m_2, we can identify equipotential surfaces, that is to say, surfaces on which the potential is constant. These equipotentials, projected on the two-dimensional plane of the orbit, are illustrated in Figure 1.7. In this figure, the points denoted by L_i with $i = 1, ..., 5$ are the five equilibrium points present in such a system, called Lagrange points after the French mathematician and astronomer Joseph-Louis Lagrange (1736-1813). In the present context, the first Lagrangian point L_1, located on the line connecting the centres of mass of the two stars, is of particular interest. The equipotential of the two stars that connects at this point delimitates the largest size the stars can have in a binary system before starting to transfer material to their companion. This surface is also called the *Roche lobe*. Since the potential, and hence, the sum of the forces, acting on L_1 is identically zero, a star which fills its Roche lobe (and has this typical teardrop-like shape) can transfer matter to its companion through the Lagrange point L_1, provided its companion does not fill its Roche lobe itself. The more the star fills its Roche lobe, the more its shape is distorted and the more its Roche lobe filling factor – the ratio

of the (mean) stellar radius to the (mean) radius of the Roche lobe – is high. Whilst the relative size of the Roche lobe of the two stars depends on their mass ratio, the absolute size of the Roche lobe scales with the separation of the two stars. Hence, the same stars may fill their Roche lobe if belonging to a close binary system while they may only fill a tiny fraction of their Roche lobe in a wide binary system. A system in which none of the stars fills its Roche lobe is called a *detached* system, a system in which only one of the two stars fills its Roche lobe is called a *semi-detached* system, and a system in which both stars fill their Roche lobes is called a *contact/overcontact* system.

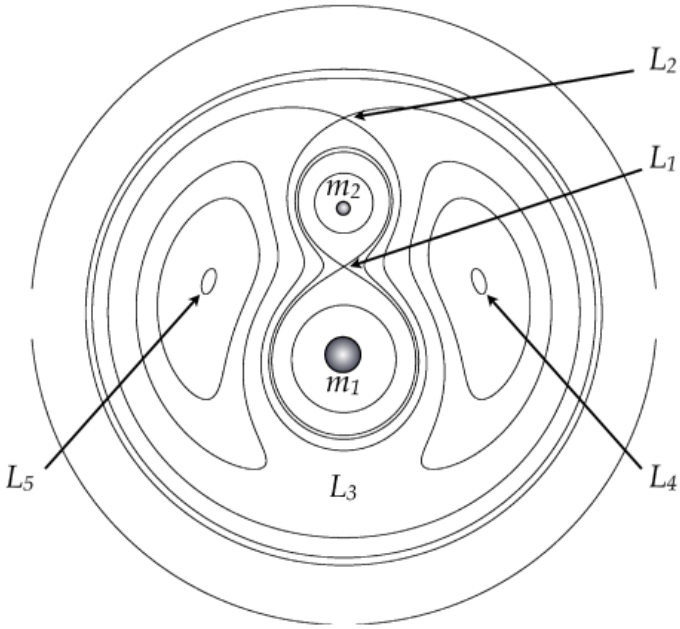

Figure 1.7. Equipotential surfaces of a binary system composed of two stars of masses m_1 and m_2, Roche lobes, and Lagrange points.

The impact of the relative size of the stars on the light curve of the system lies in the width of the eclipses. For instance, the bottom of an eclipse can become flat if a star – usually a very small star compared to its companion – is totally eclipsed for a certain time. The shapes of the stars, defined by the mass ratio and the Roche lobe filling factors, affect the shape of the light curve outside the eclipses. Indeed, in close binary systems, the visible surface area of the stars vary during the orbital cycle due to the aspherical shape of the stars which induces a non-flat shape of the light curve between two eclipses, as illustrated in Figure 1.6(d) where three synthetic light curves of a binary system having an inclination of 90° and zero eccentricity are plotted for different values of the Roche lobe filling factors of both stars (0.2, 0.5, and 0.8, respectively). In addition, important temperature and brightness variations exist all over the surface of the stars because of their non-spherical shapes. This effect, called *gravity brightening/darkening*, affects the light curve between eclipses too.

1.2.2.5. Longitude of periastron

The light curves of an eccentric binary system are affected by the longitude of periastron at the time of observation, a fact that has been used to determine the apsidal motion rate in eclipsing binaries (see e.g. Giménez & Bastero 1995). This is illustrated in Figure 1.8 where nine theoretical light curves are plotted for nine different values of ω ranging from 0° to 160° and for $e = 0.134$. We adopted the convention that the primary eclipse occurs at phase 0 whatever the value of ω and that the primary eclipse happens closer to periastron passage while the secondary eclipse happens closer to apastron passage.

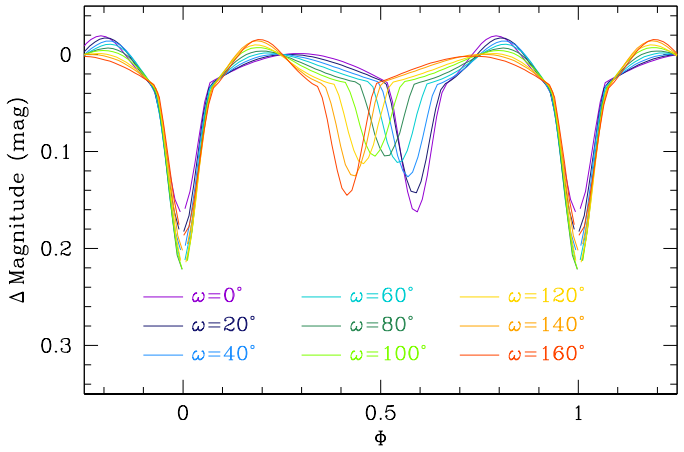

Figure 1.8. Synthetic light curves (computed with `Nightfall`) of a binary system made of two identical stars (same mass, size, and effective temperature) obtained for different values of the longitude of periastron ω. The eccentricity is equal to 0.134.

These light curves are computed assuming the two stars have exactly the same physical parameters. Hence, the change in depths of the eclipses, the change in phase of the secondary eclipse, and the photometric variations outside of the eclipses are entirely attributable to the longitude of periastron and do not reflect any temperature difference between the two stars. Indeed, the depths of the eclipses depend upon the orbital separation between the two stars at the time of the conjunctions: The depth is the largest when the conjunction occurs close to periastron passage; the orbital separation at conjunction phase depending itself on the orientation of the ellipse with respect to our line of sight, that is to say, the longitude of periastron. Likewise, the phase difference between the primary and secondary eclipses, defined as

$$\Delta\phi = \frac{t_2 - t_1}{P_{\rm orb}}, \tag{1.9}$$

where t_1 and t_2 are the primary and secondary times of photometric minima, respectively, depends upon the longitude of periastron. In the special case where the inclination is equal (or close) to 90°, then the relation writes

$$\Delta\phi = \frac{\Psi - \sin\Psi}{2\pi}, \tag{1.10}$$

where

$$\Psi = \pi + 2 \arctan\left(\frac{e\cos\omega}{\sqrt{1-e^2}}\right). \tag{1.11}$$

In the general case where $i \neq 90°$, the relation writes

$$\Delta\phi = \frac{1}{2} + A_1\frac{e}{\pi}\cos(\omega) - A_3\frac{e^3}{4\pi}\cos(3\omega) + A_5\frac{e^5}{16\pi}\cos(5\omega), \tag{1.12}$$

where A_1, A_3, and A_5 are functions of the inclination and the eccentricity given by Equations (16), (18), and (20) of Giménez & Bastero (1995).

Finally, the shape of the ellipsoidal variations occurring outside of the eclipses changes with ω due to the changing aspect angle of the stars with respect to our line of sight. The flattest bumps are observed when quadrature happens close to apastron passage.

1.2.3. Overview of the project

The state-of-the-art of the methodology adopted in this work to study the apsidal motion of binary systems is outlined in Figure 1.9.

On the observational side, the current generation of high-throughput high-resolution échelle spectrographs enables us to collect spectra, and thus radial velocities, of excellent quality for relatively bright stars within a very reasonable investment of observing time, even with moderate size telescopes. These observational data supplement the older measurements existing either in the literature or in the archives. Comparing the orbital solutions of short-period eccentric binary systems computed for different epochs frequently reveals a variation of the longitude of periastron ω, hinting at the presence of apsidal motion. By adjusting radial velocity curves explicitly taking into account the secular variation of the longitude of periastron, the apsidal motion rate can be accurately established (Rauw et al. 2016). In such an approach, six free parameters are relevant: the anomalistic orbital period $P_{\rm orb}$ (defined as the time interval between two consecutive periastron passages), the eccentricity e of the orbit, the time of periastron passage T_0, the longitude of periastron ω_0 at the epoch T_0, the apsidal motion rate $\dot{\omega}$, and the amplitude of the radial velocity curve K_1 (respectively K_2) of the primary (respectively secondary) star. Provided that observations over a sufficiently long time span are available, the apsidal motion rate can be determined within a 10% accuracy, which is significantly better than the $\sim 40\%$ accuracy obtained from the comparison of old and new orbital solutions (Rauw et al. 2016).

From a practical point of view, the iterative technique of spectral disentangling enables us to reconstruct the spectra of the primary and secondary stars of the binary system whilst simultaneously determining the radial velocities of the stars for the different observations (Mahy et al. 2010). This is a powerful tool as the reconstructed spectra can subsequently be analysed to reassess the spectral classification of the stars. The projected rotational velocities $v_{\rm eq}\sin i_{\rm rot}$, where $v_{\rm eq}$ is the equatorial rotational velocity and $i_{\rm rot}$ is the inclination of the rotational axis with respect to the line of sight, of the stars are then determined by fitting the Fourier transform of several well-chosen lines with theoretical Fourier transforms of the

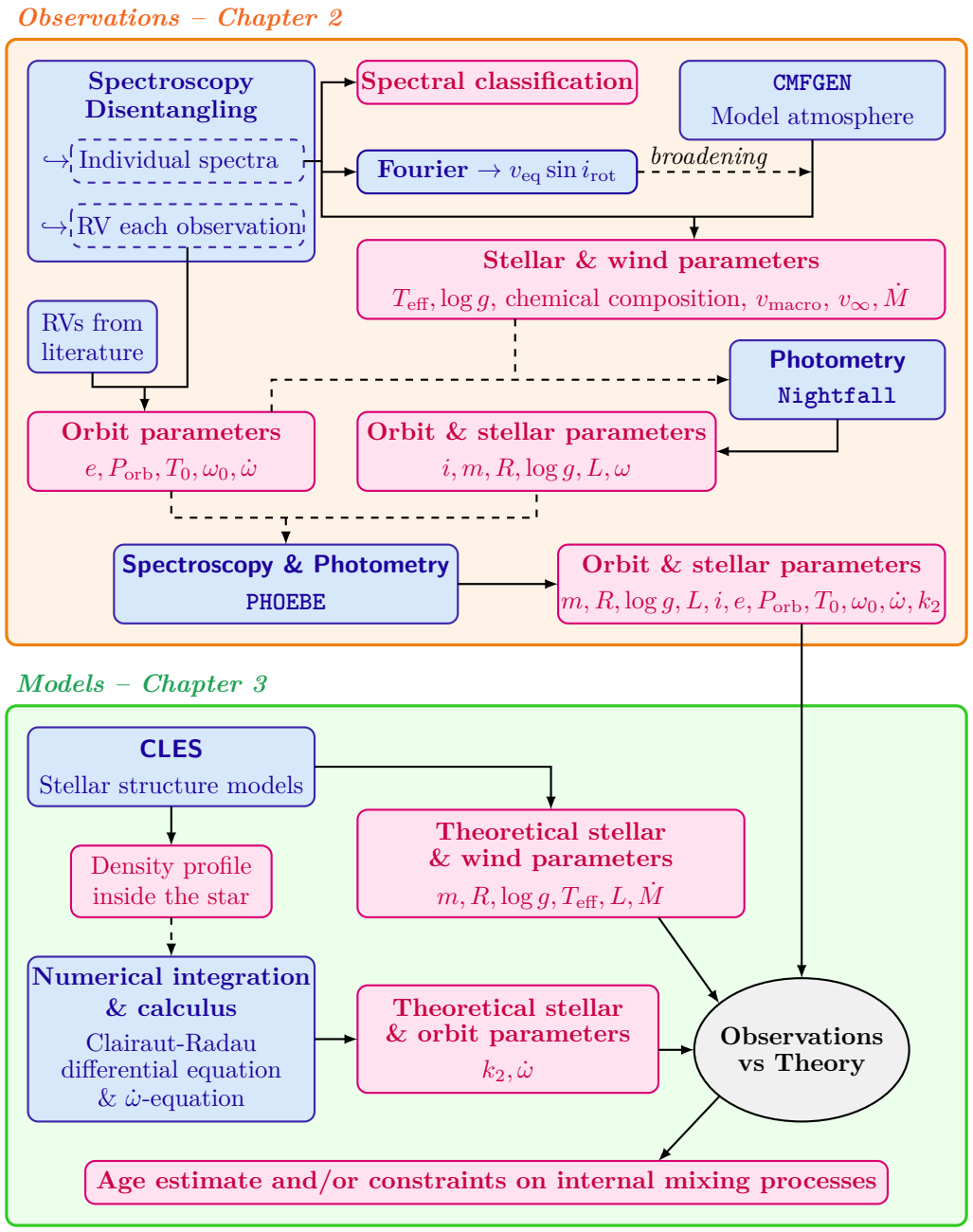

Figure 1.9. General outline of the methodology adopted to study the apsidal motion of a binary system. Alternatives to this outline are discussed in the main text.

rotational profile. The reconstructed spectra can subsequently be analysed with modern non-local thermodynamical equilibrium (non-LTE) model atmosphere codes such as `CMFGEN` (Hillier & Miller 1998). The stellar parameters (e.g. the effective temperature, the surface gravity, and the surface chemical composition) as well as the wind parameters (e.g. the macroturbulence velocity, the wind terminal velocity, and the mass-loss rate) are obtained. The results of the analysis of the spectra and of the radial velocities are then used to analyse the photometric data of the system. The light curves of the system are fitted by means of the `Nightfall` code to constrain the orbital inclination of the system. This approach yields the absolute masses and radii of the stars.

As advocated by several authors, the photometric data can be used to determine the apsidal motion rate of binary systems (Giménez & Garcia-Pelayo 1983; Zasche & Wolf 2019). For the binary systems under consideration in this project, the time span covered by photometric observations is much shorter than the time span covered by radial velocity measurements. Hence, results obtained with photometric observations only are expected to be less accurate than those obtained with spectroscopic observations. For CPD-41° 7742, these photometric data allowed us, nonetheless, to lift the degeneracy in $\dot{\omega}$ found in the radial velocity analysis (see Section 2.4.3.3). For the other systems, these data were useful to make a consistency check of the results obtained from the radial velocity analysis.

Aside from the radial velocity and photometric analyses, for the binary system HD 152248 only, a `PHOEBE` model was constructed based on the results previously obtained. `PHOEBE` deals with both photometric and spectroscopic data simultaneously, and hence, derives values for the stellar masses and radii, the inclination, the eccentricity, the orbital period, the time of periastron passage, the longitude of periastron at the time of periastron passage, and the apsidal motion rate which are coherent for both types of observations.

On the theoretical side, theoretical stellar structure models are traditionally computed with modern stellar evolution codes for single stars such as `Clés` (Code Liégeois d'Evolution Stellaire, Scuflaire et al. 2008), `GENEC` (GENeva stellar Evolution Code, Eggenberger et al. 2008), `MESA` (Modules for Experiments in Stellar Astrophysics, Paxton et al. 2011, 2013, 2015) or the one developed by the Bonn group (Brott et al. 2011). These codes include various prescriptions for the internal mixing (convective core overshooting, rotational mixing, turbulent diffusion) and account for mass-loss through stellar winds. For the purpose of this work, we used models computed with the `Clés` code complemented by models computed with the `GENEC` code as this last one offers the possibility to build binary-like models. As an input, the observational parameters of the stars such as the mass, the radius, and the effective temperature have been used to constrain the models. The internal structure constants can be obtained by numerically solving the Clairaut-Radau differential equation for the density distribution of the stellar models (Schmitt et al. 2016; Shakura 1985; Rauw et al. 2016). This can be achieved with conventional fourth-order Runge-Kutta methods. The resulting evolution of the theoretically predicted rate of apsidal motion can then be compared to the observed rate, yielding an estimate of the age of the system and constraints on the mixing processes occurring inside the stars.

1.3. NGC 6231 at the focus

The very young and rich open cluster NGC 6231 (Sung et al. 1998; Reipurth 2008; Kuhn et al. 2017b, and references therein) is located at the core of the Sco OB1 association (see illustration in Figure 1.10). NGC 6231 hosts a substantial population of massive O- and B-type stars with a high incidence of short-period binaries (Sana et al. 2008a, and references therein). Based on the properties of the low-mass stars population, the age of the cluster was estimated to range between one and seven million years, with a slight peak near three million years (Sana et al. 2007; Sung et al. 2013). Variations of the mean age across the cluster are, however, small and no obvious global trend (e.g. a radial age gradient) was found

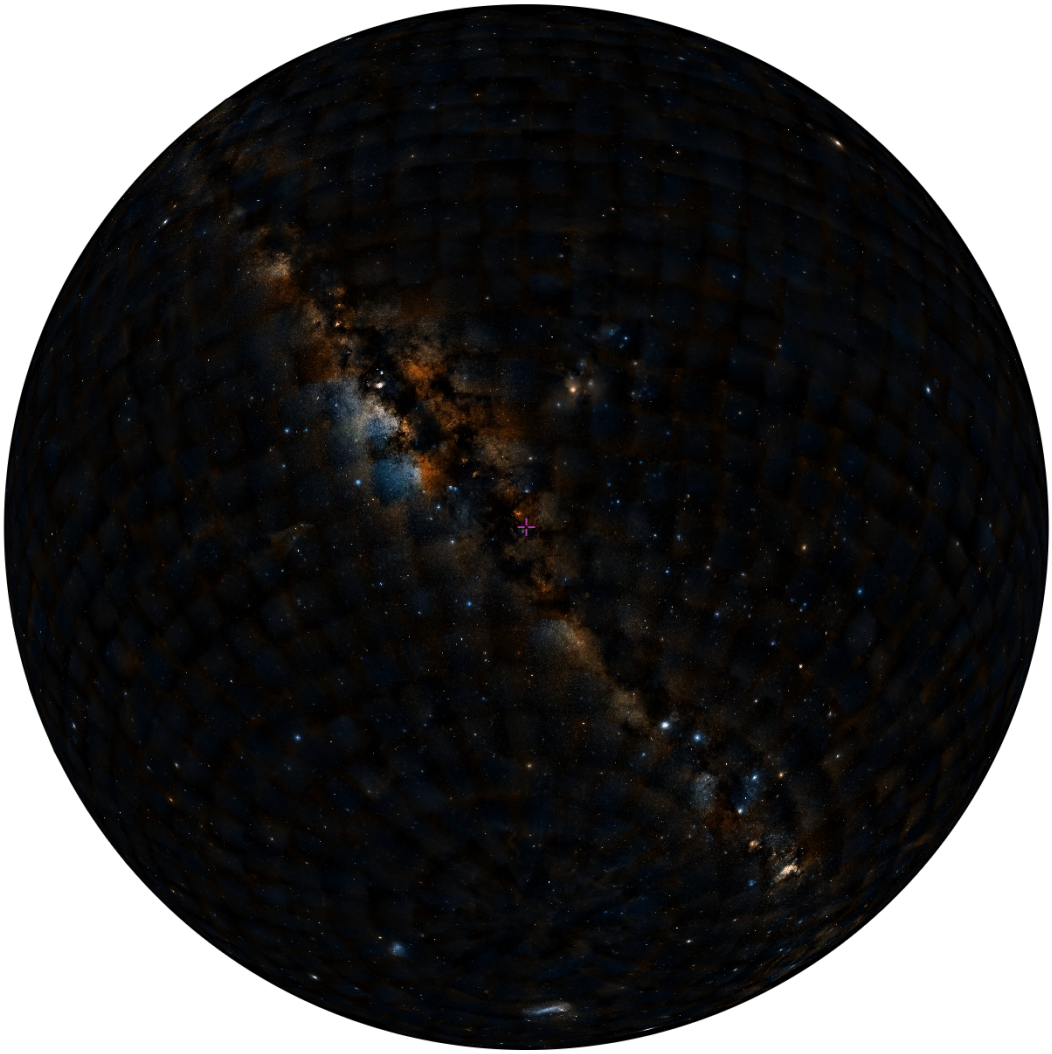

Figure 1.10. Digitized Sky Survey – © 1995 by the Association of Universities for Research in Astronomy, Inc. The purple cross indicates the location of the NGC 6231 cluster.

(Kuhn et al. 2017a). The cluster has probably undergone considerable expansion from its initial size (Kuhn et al. 2017a). The cluster core itself has a radius of 1.2 ± 0.1 pc. Stars more massive than eight solar masses appear more concentrated in the cluster core, whereas low- and intermediate-mass stars display no mass segregation (Raboud & Mermilliod 1998; Kuhn et al. 2017a). There is a priori no observational evidence that the massive stars in NGC 6231 would have a metallicity that significantly deviates from solar although Baume et al. (1999) drew attention to the work of Kilian et al. (1994) who found that the CNO mass fraction of a sample of ten B-type stars in NGC 6231 was sub-solar (between 0.7 and 1.3% compared to the then-accepted value of 1.8% for the Sun). Our set of selected targets is composed of four massive binary systems belonging to this cluster: HD 152248, HD 152219, CPD-41° 7742, and HD 152218 (see illustration in Figure 1.11).

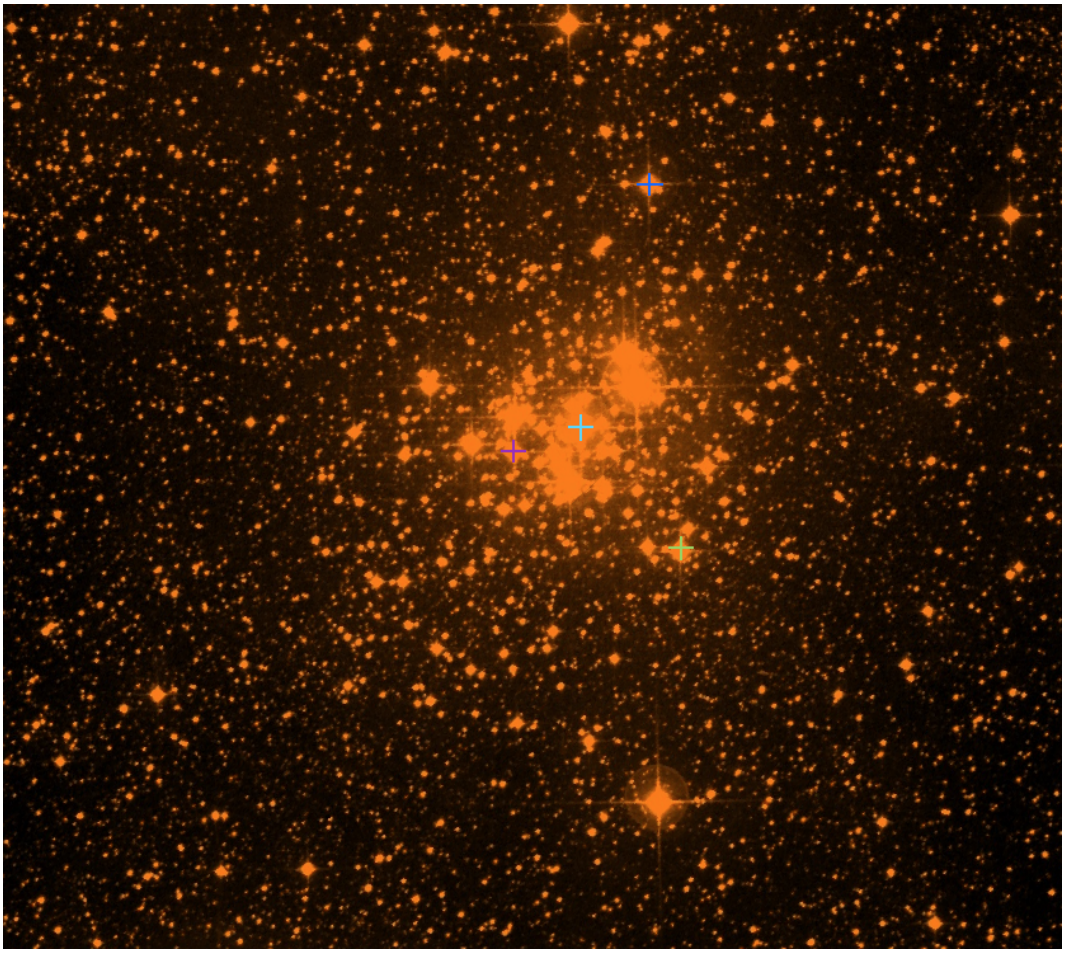

Figure 1.11. Digitized Sky Survey – © 1995 by the Association of Universities for Research in Astronomy, Inc. The cyan, green, purple, and blue crosses indicate the locations of HD 152248, HD 152219, CPD-41° 7742, and HD 152218, respectively.

1.3.1. The twin binary: HD 152248

The most emblematic O-star binary in NGC 6231 is probably the eccentric massive binary HD 152248 – also known as V 1007 Sco –, which hosts two O7.5 III-II(f) stars (Sana et al. 2001; Mayer et al. 2008; Rosu et al. 2020b). In accordance with previous studies (Stickland et al. 1996; Penny et al. 1999; Sana et al. 2001; Mayer et al. 2008), we call the primary star the one that is eclipsed during primary minimum. Almost eighty years ago the binarity of this star was discovered by Struve (1944). About thirty years after this discovery, Hill et al. (1974) were the first to establish the orbital period of this system near six days. The value of the orbital period was subsequently refined to close to 5.816 days while the orbital eccentricity was estimated to range between 0.10 and 0.15 (Mayer et al. 1992, 2008; Stickland et al. 1996; Sana et al. 2001; Nesslinger et al. 2006). Brownless & Cox (1953) were the first to suspect the existence of photometric eclipses in the light curve of HD 152248. This discovery was confirmed later on by Mayer et al. (1992). Stellar wind interactions have been found both in optical spectroscopy (Sana et al. 2001) and through phase-locked variations of the X-ray emission (Sana et al. 2004). A secular variation of the argument of periastron ω was highlighted by several authors (Sana et al. 2001; Nesslinger et al. 2006; Mayer et al. 2008). With a short orbital period and a mass ratio very close to one (Sana et al. 2001; Mayer et al. 2008; Rosu et al. 2020b), HD 152248 is a remarkable example of a twin system. In the context of star formation, such a system is a real textbook case (Tokovinin 2000) since it could be formed through orbital decay of a wider binary system as a result of gas accretion or dynamical interactions with a circumbinary disk (Bate et al. 2002). Altogether, the properties of HD 152248 render the system an interesting target for studying tidally-induced apsidal motion (Schmitt et al. 2016; Rauw et al. 2016; Zasche & Wolf 2019). In addition, its twin property offers a unique opportunity to obtain direct insight into the internal structure of the stars.

1.3.2. The slow motion binary: HD 152219

The second target of our study is the massive binary HD 152219 – also known as V 1292 Sco –, which hosts an O9.5 III primary star and a B1-2 V-III secondary star, located further away from the centre of the NGC 6231 cluster. The spectroscopic binarity of HD 152219 was first reported almost fifty years ago by Hill et al. (1974) who published an SB1 orbital solution with an orbital period of 4.16 days and an eccentricity of about 0.1. Subsequent SB1 solutions were published by Levato & Morrell (1983) and García & Mermilliod (2001). One had to wait until the beginning of the 21st century for the first full SB2 orbital solution to be derived by Sana et al. (2006) thanks to the systematic detection of the spectral signature of the secondary star. An O9.5 III + B1-2 V-III spectral classification was proposed (Sana et al. 2006). Combining their own data with radial velocities coming from the literature, for a total of seventy-nine observations spanning 13 186 days, Sana et al. (2006) derived an orbital period of 4.24028 days for the system. At the same time, Otero & Wils (2005) discovered the eclipsing nature of HD 152219 through the photometric eclipses seen in the ASAS-3 data and reported a photometric period of 4.24038 days. Apparent line profile variations on top of the orbital motion of the primary star were reported by Sana et al. (2006). At that time, they tentatively attributed these variations to non-radial pulsations. However, using an intensive spectroscopic monitoring of the star in a subsequent study, Sana (2009) showed that these

line profile variations were restricted to a short phase interval around primary eclipse. Sana (2009) deduced that these variations arise from the Rossiter-McLaughlin effect and that any additional line profile variability due to non-radial pulsations would have an amplitude below 0.5% of the continuum level. With the NACO instrument, six companions of the binary system were detected (Sana et al. 2014). The closest component was found at an angular separation of 83.6 mas, with a ΔK_s of 2.8 magnitudes. Five additional companions were found at angular separations between 2.2 and 7.2 arcsec and with ΔK_s (compared to the main binary) between 4.2 and 6.9 magnitudes. The closest companion was, however, not detected during a speckle interferometric survey by Mason et al. (2009).

1.3.3. The high rate apsidal motion binary: CPD-41° 7742

The third target of our study is the massive binary CPD-41° 7742 – also known as V 1034 Sco –, which hosts an O9.5 V primary star and a B1-2 V secondary star. CPD-41° 7742 is the second known SB2 eclipsing early-type binary system of NGC 6231 after HD 152248. Struve (1944) was the first to suspect the binarity of CPD-41° 7742. With more data, Hill et al. (1974) derived the first orbital solution for the system (see Table 1.1) and reported a photometric variability of $\Delta V = 0.45$ mag. The primary star was assigned a spectral type O9 IV by Levato & Malaroda (1980). Levato & Morrell (1983) derived a new orbital solution (see Table 1.1). Whilst Perry et al. (1990) published additional radial velocity data points, they did not present a new orbital solution for the system. García & Mermilliod (2001) reported the first evidence of the presence of the secondary star in three out of their eight new medium-resolution spectra. They derived the first SB2 solution of the system (see Table 1.1). However, Sana et al. (2003) reported errors in the Julian dates of some

Table 1.1. Physical and orbital parameters of CPD-41° 7742 from the literature.

Parameter	Value					
Reference	H74	LM83	GM01	S03 & S05	B05	T10
$P_{\rm orb}$ (d)	2.446(5)	2.430255(10)	2.453087(12)	2.44070(43)	2.440656	...
e	0.07(4)	0.08(3)	0.205(53)	0.027(6)	0	...
K_1 (km s^{-1})	162.5(8.2)	160(5)	171(11)	167.1(9)	167.1(2.1)	...
K_2 (km s^{-1})	...	...	364(59)	301.3(1.8)	299.9(3.8)	...
i (°)	...	...	...	77.35(80)	81.4(1)	...
m_1 ($M_\odot$)	...	...	...	17.97(45)	16.83(48)	17.21(46)
m_2 ($M_\odot$)	...	...	...	9.96(22)	9.38(27)	9.59(27)
R_1 ($R_\odot$)	...	...	...	7.45(45)	7.45(7)	7.507(81)
R_2 ($R_\odot$)	...	...	...	5.39(43)	4.18(4)	4.217(89)
$T_{\rm eff,1}$ (K)	...	...	...	34 000	33 200	33 200(900)
$T_{\rm eff,2}$ (K)	...	...	...	26 260(420)	26 330(30)	26 330(900)
$\log g_1$ (cgs)	...	...	...	3.93(48)	3.90	3.923(8)
$\log g_2$ (cgs)	...	...	...	3.96(64)	4.16	4.170(13)
$\log(L_{\rm bol,1}/L_\odot)$	...	...	...	4.82(7)	4.785(8)	4.789(48)
$\log(L_{\rm bol,2}/L_\odot)$	...	...	...	4.09(10)	3.899(9)	3.885(62)

Notes. The references are the following: H74 (Hill et al. 1974), LM83 (Levato & Morrell 1983), GM01 (García & Mermilliod 2001), S03 (Sana et al. 2003), S05 (Sana et al. 2005), B05 (Bouzid et al. 2005), and T10 (Torres et al. 2010). The parameters are the following: $P_{\rm orb}$, the orbital period of the system; e, the eccentricity of the orbit; K_1 (respectively K_2) the amplitude of the radial velocity curve of the primary (respectively secondary) star; i the orbital inclination; m_1 (respectively m_2) the mass; R_1 (respectively R_2) the radius; $T_{\rm eff,1}$ (respectively $T_{\rm eff,2}$) the effective temperature; $\log g_1$ (respectively $\log g_2$) the surface gravity; and $\log(L_{\rm bol,1}/L_\odot)$ (respectively $\log(L_{\rm bol,2}/L_\odot)$) the luminosity of the primary (respectively secondary) star. Errors are indicated in parentheses in terms of the last digits and represent 1σ.

of the observations of García & Mermilliod (2001), and redetermined the orbital period and the eccentricity of the system based on thirty-four new data points complementing the previous literature data available at that time (see Table 1.1). They determined an O9 III + B1 III spectral classification for the system, even though they claimed that the stars would be main-sequence stars rather than giant stars considering the physical configuration of the system. Sana et al. (2005) reassessed the spectral classification considering optical photometric observations of the system and inferred O9 V + B1-1.5 V spectral types. They also derived the inclination of the system, as well as the masses and radii of the stars (see Table 1.1). Based on multi-band photometry, Bouzid et al. (2005) derived orbital and physical parameters for the system (see Table 1.1). They assumed a circular orbit and interpreted the small eccentricity found in spectroscopy as a possible result of circumstellar matter or other radiating material not connected to the orbital motion of the binary system. Torres et al. (2010) determined an O9 V + B1.5 V spectral classification for the system, and inferred absolute parameters for the stars (see Table 1.1). CPD-41° 7742 is a well-detached system and it is unlikely that this system could have undergone any mass-exchange episode in its past (Sana et al. 2005). Independent studies of CPD-41° 7742 in the past (Sana et al. 2003, 2005; Bouzid et al. 2005) showed large discrepancies in the longitude of periastron of the orbit, hinting at the presence of apsidal motion.

1.3.4. The revisited binary: HD 152218

The fourth and last target of our study is the massive binary HD 152218 – also known as V 1294 Sco –, which hosts an O9 IV primary star and an O9.7 V secondary star, located further away from the centre of the NGC 6231 cluster. Otero & Wils (2005) reported HD 152218 to display shallow eclipses and classified the system as an Algol-type eclipsing binary. They did not perform any detailed analysis of its light curve. Comparing their radial velocity curve obtained from data collected between 1997 and 2004 with previously published solutions from the literature (Struve 1944; Hill et al. 1974; Stickland et al. 1997), Sana et al. (2008b) noted the probable presence of a significant apsidal motion at a rate ranging between 1.4 and 3.3° yr^{-1} depending on the datasets that were considered. A modulation in the X-ray flux of the binary system was revealed by the XMM-Newton data with orbital phase that was interpreted as a result of a wind-wind interaction (Sana et al. 2008b; Rauw & Nazé 2016). More recently, Rauw et al. (2016) performed a detailed analysis of the binary system. They inferred masses of 19.8 ± 1.5 and $15.0 \pm 1.1\,M_{\odot}$ for the primary and secondary stars, respectively, radii of $8.4^{+1.1}_{-1.0}$ and $7.8^{+1.0}_{-1.6}\,R_{\odot}$ for the primary and secondary stars, respectively, and effective temperatures of $33\,400 \pm 1000$ and $29\,900 \pm 1000$ K for the primary and secondary stars, respectively. The system has a rather high eccentricity ($e = 0.280^{+0.010}_{-0.008}$) given its orbital period of 5.60445 ± 0.00005 days (Rauw et al. 2016). Finally, Rauw et al. (2016) inferred an orbital inclination of $(66.3^{+3.0}_{-3.3})°$ and a rate of apsidal motion of $(2.04^{+0.23}_{-0.24})°\,\mathrm{yr}^{-1}$ for the system.

Chapter 2

The Eyes Turned Skywards

"I have no special talent,
I am only passionately curious."

(Albert Einstein)

Spectroscopy and photometry make up the two complementary sets of observations needed to study tidally-induced apsidal motion in close eccentric massive binaries such as those studied in this work. The amount of information that can be extracted from raw data is impressive when appropriate dedicated tools are used. This chapter aims to show, in a straightforward way, how the techniques implemented throughout this study, explained in a general framework in Section 2.1, can turn out to be useful when applied to appropriate binary systems. Each of the binaries considered here has its own characteristics and specificities and deserves a whole complete analysis, justifying why each binary system has its own dedicated section, respectively Section 2.2, 2.3, 2.4, and 2.5. Always looking at the same region of the sky and accumulating similar data for the same objects, observing the same binary stars again and again, is the best way to discover, hopefully one day, the stars' most profound secrets and mysteries.

Contents

2.1. Tools and methodologies to analyse observational data

To determine the apsidal motion rate of a close eccentric binary system, as explained in Chapter 1, Section 1.2, a series of dedicated tools is necessary. All these tools and associated methodologies are described in this section[1]. The pre-processing of spectroscopic observations is briefly described in Section 2.1.1 and the disentangling method used to obtain the individual spectra of the stars from the combined spectra of the binary system is detailed in Section 2.1.2. The criteria used to assess the spectral classification of stars based on their respective spectra are summarised in Section 2.1.3. The general equations used to determine the absolute magnitudes of the stars are recalled in Section 2.1.4 whilst the method used to determine the brightness ratio of a binary system is presented in Section 2.1.5. The Fourier method applied to determine the projected rotational velocities of the stars based on their individual spectra is explained in Section 2.1.6. The `CMFGEN` model atmosphere code is presented in Section 2.1.7 together with the methodology adopted to fit spectra in order to determine stellar and wind properties of stars. Section 2.1.8 is devoted to the radial velocity analysis and the ensuing determination of the apsidal motion rate. The `Nightfall` code used to analyse the photometric data of a binary system and fit its light curve is presented in Section 2.1.9. Eventually, the `PHOEBE` code, an eclipsing modelling code reproducing and fitting light curves, radial velocity curves, and spectral line profiles simultaneously, is described in Section 2.1.10 together with the Markov Chain Monte Carlo (MCMC) method.

2.1.1. Pre-processing of spectroscopic observations

The pre-processing of all spectroscopic observations consisted in cleaning the spectra from the residual cosmic rays and from the telluric absorption lines. The former were removed manually in `MIDAS` while the latter were removed within `IRAF` using the *telluric* tool along with the atlas of telluric lines of Hinkle et al. (2000). The spectra were then normalised within `MIDAS` by fitting low-order polynomials to the continuum[2]. The continuum was defined based on the spectrum for which the lines were the most deblended. However, if two well deblended lines are very weak, their contrast against the continuum might not be sufficient to distinguish them. Therefore, the continuum was checked with the spectrum for which the lines were the most blended. In each continuum region, a linear interpolation was performed. Between two continuum regions, that is to say, in the lines, a linear interpolation was performed between the continua present on each side of the considered line.

2.1.2. Spectral disentangling

The spectral disentangling is a method used to reconstruct the spectra of the individual components of a binary system and to simultaneously establish their radial velocities as a function of time. An illustration of the result we get is depicted in Figure 2.1 for a small

[1] We note that these methods are explained in a very general framework. Depending on the specific case, we might deviate from it if necessary.

[2] The same normalisation process was applied to all spectra otherwise the disentangling code would assign to the orbital motion the variation of the continuum from one spectrum to the other.

wavelength interval in the case of HD 152248. In the context of this project, we used our spectral disentangling code based on the method described by González & Levato (2006) and continuously improved according to our needs. This method is an iterative method which we describe hereafter.

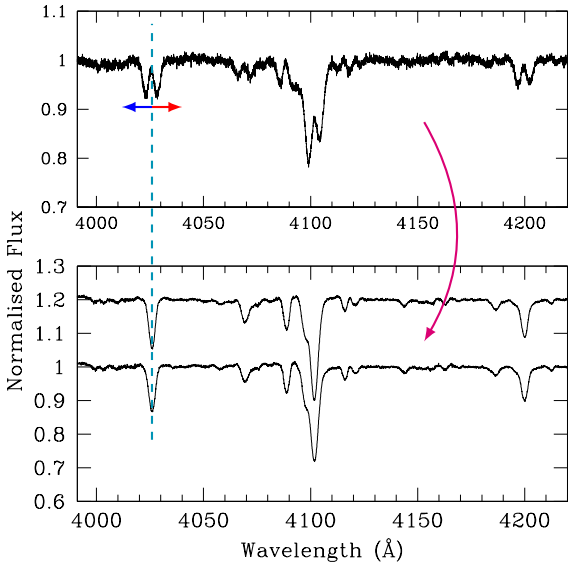

Figure 2.1. *Upper panel:* One normalised spectrum of HD 152248 at an orbital phase where the lines of the primary and secondary stars are well-deblended. *Bottom panel:* Normalised spectra of the primary and secondary stars (the spectrum of the secondary star has been shifted vertically by +0.2 for convenience) obtained after disentangling.

2.1.2.1. Method

We denote by $S_{\rm A}(x)$ and $S_{\rm B}(x)$ the spectra of stars A and B, respectively, where $x = \ln\lambda$, λ being the wavelength. Since $\lambda = \lambda_0\left(1 - \frac{v}{c}\right)$, with λ_0 the wavelength at rest, we get

$$\begin{aligned} \ln\lambda &= \ln\lambda_0 + \ln\left(1 - \frac{v}{c}\right) \\ &\approx \ln\lambda_0 - \frac{v}{c} \qquad (2.1) \\ &= x_0 - \frac{v}{c}, \qquad (2.2) \end{aligned}$$

where the second line has been obtained assuming small Doppler shifts.

We denote by $RV_{\rm A}(t)$ and $RV_{\rm B}(t)$ the radial velocities at time t of stars A and B, respectively. The spectrum of the binary system at time t is expressed as the sum of the spectra of star A and star B at the same time t:

$$S(x) = S_{\rm A}\left(x - \frac{RV_{\rm A}(t)}{c}\right) + S_{\rm B}\left(x - \frac{RV_{\rm B}(t)}{c}\right). \qquad (2.3)$$

Let us consider we are working on the spectrum of star A. The first iteration is computed assuming a featureless spectrum for star B with a flux level equal to half the normalised flux of the combined spectrum. At each step of the iterative procedure, the current best approximation of the reconstructed spectrum of star B shifted to the current estimate of $RV_{\rm B}(t)$ is first subtracted from the observed spectrum at time t. The resulting residual spectra are shifted by the current estimate of $RV_{\rm A}(t)$. The mean of these spectra is computed to obtain an estimated solution for $S_{\rm A}$. The latter is then shifted again in the observer reference frame by the current estimate of $RV_{\rm A}(t)$ and subtracted from the observed spectra. In this way, residual spectra are built, which correspond to the new estimate of the spectrum of star B. These spectra are then shifted into the reference frame of star B and a mean of these spectra is computed. This estimate of the spectrum of star B is shifted in the observer reference frame and subtracted from the observed spectra. The residuals obtained in this way correspond to the new estimate of the spectrum of star A. The estimates of $RV_{\rm A}(t)$ and $RV_{\rm B}(t)$ are updated through the cross-correlation of the residual spectra with synthetic `TLUSTY` spectra (Lanz & Hubeny 2003) and through the fit of a parabola to the peak of the correlation function to determine its centre (Verschueren & David 1999). The resulting spectrum of star A (respectively B) is an average, over the total number of spectra n, of the observed spectra shifted to the reference frame of star A (respectively B) to which the spectrum of star B (respectively A) shifted to the reference frame of star A (respectively B) has been subtracted:

$$\begin{cases} S_{\rm A} = \dfrac{1}{n}\displaystyle\sum_{i=1}^{n}\left[S_i\left(x+\frac{RV_{\rm A}(t_i)}{c}\right) - S_{\rm B}\left(x+\frac{RV_{\rm A}(t_i)}{c}-\frac{RV_{\rm B}(t_i)}{c}\right)\right], \\ S_{\rm B} = \dfrac{1}{n}\displaystyle\sum_{i=1}^{n}\left[S_i\left(x+\frac{RV_{\rm B}(t_i)}{c}\right) - S_{\rm A}\left(x+\frac{RV_{\rm B}(t_i)}{c}-\frac{RV_{\rm A}(t_i)}{c}\right)\right]. \end{cases} \tag{2.4}$$

The quality of the resulting spectra depends on the number of observed spectra: the larger n, the higher the signal-to-noise ratio of the reconstructed spectra.

The initial approximation adopted for star B could introduce a bias in the resulting reconstructed spectra. In order to get an estimate of this bias on the results of the disentangling and/or to get rid of this bias, the disentangling procedure is repeated from the beginning interchanging the roles of stars A and B. As an illustration, we show in Figure 2.2 the spectra obtained for the primary star of HD 152248 after disentangling when star A is assumed to be the primary star of the system (in magenta) and when star A is assumed to be the secondary star of the system (in blue), respectively. Artefacts clearly appear in these spectra through bumps and dips. The final reconstructed spectra of the two stars are then taken to be the mean of the two approches, therefore ensuring to get rid (at least partially) of these artefacts.

Another version of the disentangling code exists which is designed to deal with a third spectral component (Mahy et al. 2012). The third component can be a third star, for instance, or can alternatively correspond to the interstellar medium (ISM). In this latter case, the spectrum of the system at time t is thus expressed as the sum of the spectra of stars A and B, and the interstellar medium whose spectrum is $S_{\rm C}$ and whose radial velocity

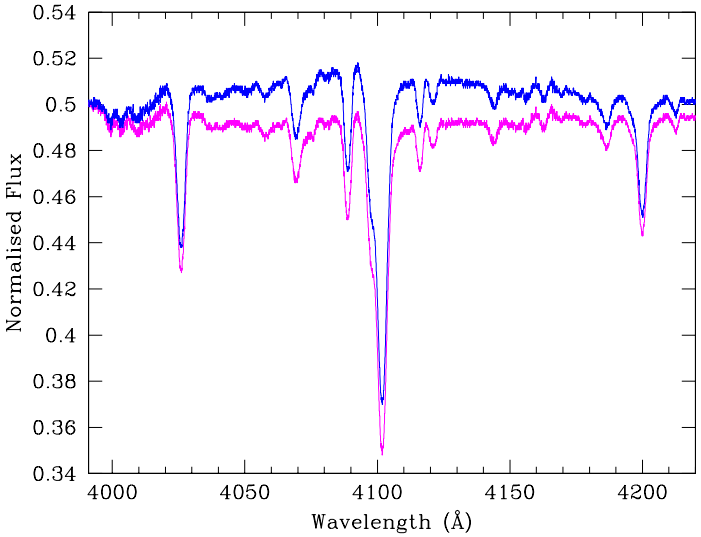

Figure 2.2. Spectra of the primary star of HD 152248 obtained after disentangling when star A is assumed to be the primary star of the system (in magenta) and when star A is assumed to be the secondary star of the system (in blue).

is equal to zero (i.e. $RV_{\rm C} = 0$) at each time of observation t:

$$S(x) = S_{\rm A}\left(x - \frac{RV_{\rm A}(t)}{c}\right) + S_{\rm B}\left(x - \frac{RV_{\rm B}(t)}{c}\right) + S_{\rm C}(x). \tag{2.5}$$

The resulting spectra are given by

$$\begin{cases} S_{\rm A} = \dfrac{1}{n}\displaystyle\sum_{i=1}^{n}\left[S_i\left(x + \frac{RV_{\rm A}(t_i)}{c}\right) - S_{\rm B}\left(x + \frac{RV_{\rm A}(t_i)}{c} - \frac{RV_{\rm B}(t_i)}{c}\right) - S_{\rm C}\left(x + \frac{RV_{\rm A}(t_i)}{c}\right)\right], \\ S_{\rm B} = \dfrac{1}{n}\displaystyle\sum_{i=1}^{n}\left[S_i\left(x + \frac{RV_{\rm B}(t_i)}{c}\right) - S_{\rm A}\left(x + \frac{RV_{\rm B}(t_i)}{c} - \frac{RV_{\rm A}(t_i)}{c}\right) - S_{\rm C}\left(x + \frac{RV_{\rm B}(t_i)}{c}\right)\right], \\ S_{\rm C} = \dfrac{1}{n}\displaystyle\sum_{i=1}^{n}\left[S_i\left(x\right) - S_{\rm A}\left(x - \frac{RV_{\rm A}(t_i)}{c}\right) - S_{\rm B}\left(x - \frac{RV_{\rm B}(t_i)}{c}\right)\right]. \end{cases} \tag{2.6}$$

The most severe limitation of this version of the code is that it works with fixed radial velocities, meaning that it does not simultaneously adjust the radial velocities of the components and is therefore less precise than the original version of the code. This version is usually used when lines of the interstellar medium are present in the part of the spectrum under consideration and close to stellar lines. Indeed, the presence of interstellar lines or diffuse interstellar bands close to spectral lines affects the quality of the resulting reconstructed spectra as well as the determination of the stellar radial velocities.

2.1.2.2. In practice

As input, the disentangling code needs the normalised spectra of the binary with their time of observation at mid-exposure as well as a first estimate of $RV_{\rm A}(t)$ and $RV_{\rm B}(t)$ for each observation. It happens, especially when the two stars are very similar, that the disentangling code gets confused and accidentally assigns the primary radial velocities to the secondary star and vice versa. As a consequence, the reconstructed spectra are incoherent. Usually, this happens near conjunction phases, when the spectral lines are blended. To avoid this problem and increase the robustness of the code, the first iterations were performed with the radial velocities fixed to the initial input values. We showed that thirty iterations performed in this way were sufficient to obtain well reconstructed spectra. The remaining iterations were performed as previously explained with radial velocities free to change. We showed that thirty additional iterations performed in this way were also sufficient to reach convergence of both well-reconstructed spectra and coherent radial velocities for both stars. An example of the convergence of spectra with the number of iterations is presented for the primary and secondary stars of HD 152248 in Figure 2.3.

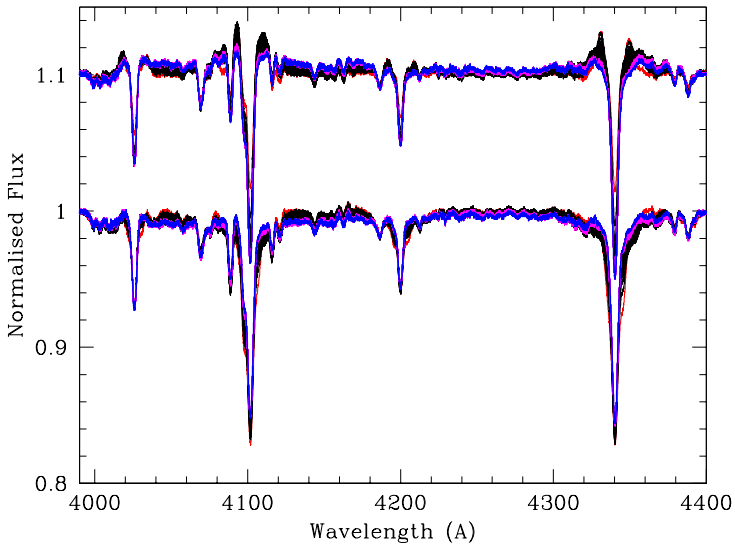

Figure 2.3. Convergence of spectra with the number of iterations using the disentangling method for the primary and secondary stars of HD 152248. For convenience, the spectra of the primary and secondary stars have been vertically shifted by respectively +0.5 and +0.6. The red spectra represent the approximate spectra after the first iteration, the sets of black spectra represent the approximations of the spectra for iterations 2 to 30 included, the sets of magenta spectra represent the spectra for iterations 31 to 59 included, and the blue spectra represent the final spectra of the stars at iteration 60.

The disentangling method requiring a lot of computational resources, we performed the spectral disentangling separately over a number of wavelength domains, restricting ourselves to the sole domains of interest for the subsequent analysis.

Once the stellar spectra were reconstructed, a value of 0.5 was added to recover a mean

continuum flux of 1. There might be some small residual oscillations close to the lines introduced by the disentangling method in the reconstructed spectra due to remaining normalisation errors in the input spectra. Hence, these spectra were renormalised afterwards.

In order to obtain the spectra of the stars as if they were single, these spectra were scaled by the brightness ratio of the system in the visible domain through the following relations:

$$\textit{Primary star:} \quad (\text{Spectrum}_{\text{primary, normalised}} - 1)\left(\frac{l_2}{l_1} + 1\right) + 1, \tag{2.7}$$

$$\textit{Secondary star:} \quad (\text{Spectrum}_{\text{secondary, normalised}} - 1)\left(\frac{l_1}{l_2} + 1\right) + 1, \tag{2.8}$$

where l_1 and l_2 are the brightness in the visible domain of the primary and secondary stars, respectively.

2.1.2.3. Limitations of the method

The disentangling method is a very powerful tool that nonetheless suffers from some limitations that might affect the subsequent analysis.

Firstly, only features that are well sampled by the Doppler excursions during the orbital cycle are reconstructed by the spectral disentangling. This often leads to artefacts in the wings of broad lines if these lines only partially deblend over the orbital cycle (e.g. Raucq et al. 2016). In the cases of HD 152248, HD 152219, and CPD-41° 7742, the radial velocity amplitudes are sufficient to ensure a reliable reconstruction of the wings of such absorption lines.

Secondly, in a close binary system, the stars are no longer spherically symmetric but are described by the shape of the equipotentials of the Roche potential Ω. Thence, the surface gravity is not homogeneous all over the surface of the star but has a complex distribution given by the gradient of the Roche potential $|\nabla\Omega|$. Gravity-darkening hence leads to a non-uniform temperature distribution (Palate & Rauw 2012; Palate et al. 2013), which in turn induces a phase-dependence of the spectral line strengths seen by an external observer as the stars revolve around each other. In addition, due to the eccentricity of the binary system, the stellar shape varies as a function of the orbital phase, leading to dynamical deformations that can induce line profile variations (Palate et al. 2013). This effect is clearly highlighted in Figures 2-4 of Sana et al. (2001). As a result, the spectra obtained by disentangling provide an average over time and over the parts of the stellar surface seen by the observer.

Finally, there might exist emission lines in the spectra of the stars which could be at least partially formed in the wind interaction zone of the system. This is effectively the case of the He II λ 4686 and Hα emissions lines of HD 152248 (Sana et al. 2001). Yet, the spectral disentangling method implicitly assumes that each spectral feature belongs to one of the stars. Hence, these emissions lines are shared between the two stars and appear in the separated spectra with shapes and fluxes which do not reflect those of the stellar spectra themselves. However, these lines are usually the only diagnostics lines to constrain the wind properties of the stars such as the mass-loss rate, the clumping, and the wind terminal velocity, to cite only a few (Martins 2011, and references therein). Therefore, these lines can only be used as an indication. For instance, if the level of emission predicted by the model exceeds the strength of the lines in the reconstructed spectrum, then the mass-loss rate of the model is likely too high.

2.1.3. Spectral classification

Different criteria exist to assess the spectral classification of massive stars.

To determine the spectral type of an O-type star, the most commonly used criterion is Conti's criterion (Conti & Alschuler 1971) complemented by Mathys (1988) based on the ratio W' between the equivalent widths (EWs) of the He I $\lambda\,4471$ and He II $\lambda\,4542$ lines, as summarised in Table 2.1, where

$$\log_{10} W' = \log_{10}[\mathrm{EW}(\mathrm{He\,I}\,\lambda\,4471)] - \log_{10}[\mathrm{EW}(\mathrm{He\,II}\,\lambda\,4542)]. \tag{2.9}$$

Table 2.1. Spectral types based on the ratio W' between the equivalent widths of the He I $\lambda\,4471$ and He II $\lambda\,4542$ lines (Conti & Alschuler 1971; Mathys 1988).

$\log_{10} W'$ upper limit	Spectral type	$\log_{10} W'$ lower limit
	O9.7	$\geq +0.65$
$+0.65 >$	O9.5	$\geq +0.45$
$+0.45 >$	O9	$\geq +0.30$
$+0.30 >$	O8.5	$\geq +0.20$
$+0.20 >$	O8	$\geq +0.10$
$+0.10 >$	O7.5	≥ 0
$0 >$	O7	≥ -0.10
$-0.10 >$	O6.5	≥ -0.20
$-0.20 >$	O6	≥ -0.30
$-0.30 >$	O5.5	≥ -0.50
$-0.50 >$	O5	≥ -0.70
$-0.70 >$	O4	≥ -0.90

For stars of spectral types equal to or later than O8, this criterion can be complemented by Sota's criterion (Sota et al. 2014) which is based on the ratio between peak intensities of three absorption-line pairs – namely He II $\lambda\,4542$ and He I $\lambda\,4388$, He II $\lambda\,4200$ and He I $\lambda\,4144$, and Si III $\lambda\,4552$ and He II $\lambda\,4542$ – as summarised in Table 2.2. The criteria of Martins (2018) based on the ratio of EWs for the same three absorption-line pairs as those used in Sota's criterion are also used for late O-type stars (see Table 2.3).

Table 2.2. Spectral classification criteria for O8 to B0 types based on the ratio between peak intensities of absorption-line pairs (Sota et al. 2014).

Spectral type	$\frac{\mathrm{He\,II}\,\lambda\,4542}{\mathrm{He\,I}\,\lambda\,4388}$	$\frac{\mathrm{He\,II}\,\lambda\,4200}{\mathrm{He\,I}\,\lambda\,4144}$	$\frac{\mathrm{Si\,III}\,\lambda\,4552}{\mathrm{He\,II}\,\lambda\,4542}$
O8	> 1	> 1	N/A
O8.5	≥ 1	≥ 1	N/A
O9	$= 1$	$= 1$	$\lll 1$
O9.2	≤ 1	≤ 1	$\ll 1$
O9.5	< 1	< 1	< 1
O9.7	$\ll 1$	$\ll 1$	≤ 1 to ≥ 1
B0	$\lll 1$	$\lll 1$	> 1

Table 2.3. Spectral classification criteria for O8 to O9.7 types based on the ratio between equivalent widths of absorption-line pairs (Martins 2018).

Spectral type	$\frac{\mathrm{EW(He\,I\,\lambda\,4388)}}{\mathrm{EW(He\,II\,\lambda\,4542)}}$	$\frac{\mathrm{EW(He\,I\,\lambda\,4144)}}{\mathrm{EW(He\,II\,\lambda\,4200)}}$	$\frac{\mathrm{EW(Si\,III\,\lambda\,4552)}}{\mathrm{EW(He\,II\,\lambda\,4542)}}$
O8	0.55 ± 0.25	0.38 ± 0.14	0.07 ± 0.04
O8.5	0.96 ± 0.17	0.67 ± 0.15	0.13 ± 0.04
O9	1.08 ± 0.20	0.85 ± 0.28	0.28 ± 0.09
O9.2	1.14 ± 0.13	1.11 ± 0.27	0.31 ± 0.09
O9.5	1.53 ± 0.40	1.37 ± 0.32	0.39 ± 0.17
O9.7	2.45 ± 0.99	1.98 ± 1.00	0.96 ± 0.57

To determine the luminosity class of an O-type star, one can use different criteria. For stellar types later than O7, there is Conti's criterion (Conti & Alschuler 1971) based on the ratio W'' between the equivalent widths of the Si IV $\lambda\,4089$ and He II $\lambda\,4144$ lines, as summarised in Table 2.4, where

$$\log_{10} W'' = \log_{10}[\mathrm{EW(Si\,IV\,\lambda\,4089)}] - \log_{10}[\mathrm{EW(He\,I\,\lambda\,4144)}]. \tag{2.10}$$

Table 2.4. Luminosity class of O-type stars with spectral types later than O7 based on the ratio W'' between the equivalent widths of the Si IV $\lambda\,4089$ and He I $\lambda\,4144$ lines (Conti & Alschuler 1971; Mathys 1988).

$\log_{10} W''$ upper limit	Luminosity class	$\log_{10} W''$ lower limit
$+0.10 >$	V	≥ -0.20
$+0.30 >$	III	$\geq +0.11$
	I	$\geq +0.31$

For stellar types O8 or earlier, Mathys's (Mathys 1988) and Walborn's criteria (Walborn & Fitzpatrick 1990) are used complemented by Sota's criterion (Sota et al. 2011, 2014). These criteria are based on the intensity of the absorption or emission in the He II $\lambda\,4686$ line and N III $\lambda\lambda\,4634$-40-42 triplet, as summarised in Table 2.5. Eventually, Walborn & Fitzpatrick (1990) infer that a luminosity class III is characterised by the He I $\lambda\,4471$ line of lower intensity than the Hγ line while a luminosity class I is characterised by the He I $\lambda\,4471$ line of same intensity as the Hγ line.

Table 2.5. Luminosity class for spectral types O8 or earlier based on the intensities of the absorption or emission in the He II $\lambda\,4686$ line and N III $\lambda\lambda\,4634$-40-42 triplet (Mathys 1988; Walborn & Fitzpatrick 1990).

Luminosity class	He II $\lambda\,4686$	N III $\lambda\lambda\,4634$-40-42
V((f))	Strong absorption	Weak emission
III(f)	Weak[a] absorption or weak[a] emission	Medium emission
If	Strong emission	Strong emission

[a] He II $\lambda\,4686$ is considered to be weak if $\log_{10}[\mathrm{EW(He\,II\,\lambda\,4686)}] < 2.70 - 2.75$, with the EW given in mÅ.

For spectral types O9 to O9.7 included, Sota's criterion (Sota et al. 2011) based on the ratio between peak intensities of two absorption-line pairs – namely He II λ 4686 and He I λ 4713, and Si IV λ 4089 and He I λ 4026 (see Table 2.6) – is used. The criteria of Martins (2018) based on the ratio of EWs for the same two absorption-line pairs as those used in Sota's criterion are also used for O9- to O9.7-type stars included (see Table 2.7).

Table 2.6. Luminosity class for spectral types O9 to O9.7 included based on the ratio between peak intensities of absorption-line pairs (Sota et al. 2011).

Luminosity Class	$\frac{\text{He II } \lambda 4686}{\text{He I } \lambda 4713}$	$\frac{\text{Si IV } \lambda 4089}{\text{He I } \lambda 4026}$
V	$\gg 1$	$\ll 1$
III	> 1	$<$ to $\ll 1$
II	$= 1$	< 1
Ib	≤ 1	≤ 1
Iab	$\ll$ to < 1	$\geq$ to ≤ 1
Ia	~ 0	> 1

Table 2.7. Luminosity class for spectral types O9 to O9.7 included based on the ratio between equivalent widths of absorption-line pairs (Martins 2018).

Luminosity Class	$\frac{\text{EW(He II } \lambda 4686)}{\text{EW(He I } \lambda 4713)}$	$\frac{\text{EW(Si IV } \lambda 4089)}{\text{EW(He I } \lambda 4026)}$
V	3.17 ± 0.49	0.35 ± 0.07
IV	2.44 ± 0.62	0.40 ± 0.08
III	1.94 ± 0.33	0.52 ± 0.15
II	1.04 ± 0.11	0.75 ± 0.26
Ib	1.04 ± 0.12	0.74 ± 0.07
I/Iab	0.90 ± 0.30	0.85 ± 0.11
Ia	0.31 ± 0.10	1.07 ± 0.20

The determination of the spectral type and luminosity class of B-type stars relies on the digital spectral classification atlases of Gray (2009) and Walborn & Fitzpatrick (1990) and on the classification criteria of Liu et al. (2019, their Table 2).

2.1.4. Absolute magnitudes

In order to compute the absolute magnitudes of the stars that are part of a binary system, a series of calculations are performed starting from the estimated distance of the system. These steps are recalled hereafter.

Nowadays, the second *Gaia* data release and third *Gaia* early data release (DR2 and EDR3, Gaia Collaboration 2018, 2021) quote parallaxes ϖ for a huge number of stars, including the binary stars of interest in the present context[3]. We can compute the distance d by inverting the parallax. However, Bailer-Jones et al. (2018, 2021) stressed that reliable distances cannot be obtained by simply inverting the parallax of *Gaia* DR2 or EDR3 but that a correct inference procedure has to be used instead in order to account for the nonlinearity of

[3] The EDR3 was unfortunately not available at the time of the study of HD 152248 and HD 152219.

the transformation and the asymmetry of the resulting probability distribution. Accordingly, the distances used hereafter for the binary systems under consideration are those inferred by Bailer-Jones et al. (2018, 2021). From this distance, expressed in parsec, the distance modulus is determined through the relation

$$DM = 5 \log d - 5. \tag{2.11}$$

The colour excess is computed through the relation

$$E(B-V) = (B-V) - (B-V)_0, \tag{2.12}$$

where B and V are the apparent magnitude in the blue and visible Johnson photometric system, respectively, and $(B-V)_0$ is the intrinsic colour index of the system. The visual extinction is then computed as

$$A_V = E(B-V)\, R_V, \tag{2.13}$$

where the reddening factor in the V-band R_V is assumed to be equal to 3.3 ± 0.1 (Sung et al. 1998). The absolute magnitude of the binary system is

$$M_V = V - A_V - DM. \tag{2.14}$$

Knowing the brightness ratio in the visible domain l_1/l_2, we can infer the absolute magnitudes of the stars in the V-filter:

$$M_{V,i} = M_V - 2.5 \log \left(\frac{l_i}{l_1 + l_2} \right), \tag{2.15}$$

where the index i refers to the primary ($i = 1$) or secondary ($i = 2$) star.

The bolometric magnitude of star i is computed through the relation

$$M_{\mathrm{bol},i} = M_{V,i} + BC_i, \tag{2.16}$$

where BC_i is the bolometric correction computed with the formula of Martins & Plez (2006):

$$BC_i = -6.89 \log(T_{\mathrm{eff},i}) + 28.07; \tag{2.17}$$

from which the bolometric luminosity $L_{\mathrm{bol},i}$ is deduced

$$\frac{L_{\mathrm{bol},i}}{L_\odot} = 10^{\frac{4.76 - M_{\mathrm{bol},i}}{2.5}}, \tag{2.18}$$

where $L_\odot$ is the bolometric luminosity of the Sun.

The spectroscopic radius is then inferred from the relation

$$\frac{R_i}{R_\odot} = \sqrt{\frac{L_{\mathrm{bol},i}}{L_\odot}} \left(\frac{T_{\mathrm{eff},i}}{T_\odot} \right)^{-2}, \tag{2.19}$$

where $R_\odot = 6.957 \times 10^8\,\mathrm{m}$ is the radius of the Sun and $T_\odot = 5772\,\mathrm{K}$ is the effective

temperature of the Sun (IAU Resolution B3, Mamajek et al. 2015; Prša et al. 2016b). Knowing the surface gravity of the star g_i, we can infer the mass of the star through the expression

$$\frac{m_i}{M_\odot} = g_i \left(\frac{R_i}{R_\odot}\right)^2 \frac{R_\odot^2}{GM_\odot}, \tag{2.20}$$

where G is the universal gravitational constant and $M_\odot$ is the solar mass, with $GM_\odot = 1.3271244 \times 10^{20}\,\mathrm{m^3\,s^{-2}}$ (IAU Resolution B3, Mamajek et al. 2015; Prša et al. 2016b).

2.1.5. Brightness ratio

The brightness ratio in the visible domain can be estimated based on the ratio between the EWs of the spectral lines of the primary and secondary stars and synthetic spectra of respective similar effective temperatures. The equivalent width EW_i of a spectral line of star i can be expressed as the ratio between the area A_i of the line and the total luminosity of the binary $l_i + l_j$, where $j = 2$ if $i = 1$ and inversely:

$$\begin{aligned} \mathrm{EW}_i &= \frac{A_i}{l_i + l_j} \\ &= \frac{A_i}{l_i}\frac{l_i}{l_i + l_j} \\ &= \mathrm{EW}_{\mathrm{synthetic},i}\frac{l_i}{l_i + l_j}, \end{aligned} \tag{2.21}$$

where $\mathrm{EW}_{\mathrm{synthetic},i}$ is the EW of the line in the synthetic spectrum corresponding to star i. Hence, we get

$$\frac{\mathrm{EW}_{\mathrm{synthetic},i}}{\mathrm{EW}_i} = \frac{l_i + l_j}{l_i}. \tag{2.22}$$

2.1.6. Projected rotational velocities

The projected rotational velocities of the stars were derived using the Fourier transform method (Simón-Díaz & Herrero 2007, 2014; Gray 2008). This method is able to separate the effect of rotation from other broadening mechanisms such as macroturbulence. It consists in fitting the Fourier transform of a given line with the Fourier transform of a synthetic line having a projected rotational velocity $v_{\mathrm{eq}} \sin i_{\mathrm{rot}}$. In the ideal case where there is no noise affecting the data, the observed line profile D is the convolution in the wavelength domain of the intrinsic H, rotational G, and instrumental L line profiles:

$$D(\Delta\lambda) = \frac{\mathcal{F}_\nu}{\mathcal{F}_c} = H(\Delta\lambda) * G(\Delta\lambda) * L(\Delta\lambda), \tag{2.23}$$

where $\mathcal{F}_\nu$ and $\mathcal{F}_c$ are the emergent flux per unit frequency leaving the stellar surface of a spectral line and the continuum flux, respectively. $\Delta\lambda = \lambda_0 \frac{v_z}{c}$, with c the speed of light, λ_0 the rest wavelength of the line, and v_z the line of sight component of the rotational velocity.

Taking the Fourier transform of this line profile, the convolution product in the wavelength

space transforms into a simple product in the Fourier space:

$$d(\sigma) = h(\sigma)g(\sigma)l(\sigma), \tag{2.24}$$

where σ is expressed in cycles per Å.

The intrinsic line profile H being close to a Dirac impulse function, its Fourier transform h is a simple constant. Assuming the instrumental profile L is a Gaussian function, its Fourier transform l is also a Gaussian function. Hence, the Fourier transform d of the observed profile D is mostly dominated by the Fourier transform g of the rotational profile G. The first zero σ_1 of $g(\sigma)$ is directly related to the projected rotation velocity through the relation

$$v_{\rm eq} \sin i_{\rm rot} = \frac{0.66\, c}{\lambda\, \sigma_1}. \tag{2.25}$$

Hence, only the first peak of the Fourier transform has to be fitted.

As suggested by Simón-Díaz & Herrero (2007), it is preferable to estimate the projected rotational velocity on metallic lines. Indeed, the H I, He I and II line profiles are more affected by non-rotational broadening mechanisms such as Stark broadening than the metallic lines, which in turn alters the positions of the first zeros in the Fourier transform (Simón-Díaz & Herrero 2007). Nonetheless, the effect of Stark broadening on the He I lines decreases as the projected rotational velocity of the star increases to such an extent that beyond approximately $100\,{\rm km\,s^{-1}}$, this effect is so small that the He I lines can be used as a complement to metallic lines.

2.1.7. `CMFGEN` model atmosphere fitting

The reconstructed spectra of the binary components were analysed by means of the Co-Moving Frame GENeral (`CMFGEN`) model atmosphere code (Hillier & Miller 1998) to constrain the fundamental properties of the stars. Amongst all the existing atmosphere codes for massive stars, `CMFGEN` is surely the most sophisticated one at the time of writing. This code solves the radiative transfer, that is to say, statistical and radiative equilibrium equations in the co-moving frame for a single star assuming the star and its wind are spherically symmetric. `CMFGEN` is a non-local thermodynamical equilibrium (non-LTE) code, which is required for massive stars as the radiative processes such as photo-excitation and photo-ionisation dominate over the collisional processes and give rise to severe deviations from local thermodynamical equilibrium. The code includes line-blanketing by taking into account the impact of overlapping lines, especially the lines of heavy elements, on the atmosphere. Indeed, heavy metallic elements block the radiation coming from the inner part of the atmosphere and the corresponding photons are backscattered towards the star. This screen effect acts towards increasing the temperature, and hence, the degree of ionisation in that region, effect that is called backwarming. Consequently, the higher the metallicity of the star, the cooler the effective temperature needed to reach the same ionisation state. For O-type stars and more evolved stars, the radiative transfer equations have to be solved accounting for the stellar wind. Indeed, due to stellar winds, the stellar atmospheres are in expansion and particularly extended compared to the radius of the stellar photosphere.

`CMFGEN` solves the equations in an iterative manner. The temperature and the level populations are determined iteratively through the linearisation of the equations. Including line-blanketing into the model increases by a huge amount the total number of statistical equilibrium equations. To reduce the number of equations and improve the accuracy of the results at the same time, a super-level approach is adopted in `CMFGEN`: The levels having similar properties and energies are gathered together and treated as a unique level. In a super-level, the population of each level is computed assuming local thermodynamical equilibrium. This enables us to reliably include the following elements in the models: hydrogen, helium, carbon, nitrogen, oxygen, neon, magnesium, silicon, sulphur, argon, iron, and nickel. The temperature structure is determined assuming radiative equilibrium from the energy conservation throughout the atmosphere.

In stellar atmospheres, microturbulence due to small-scale motions shorter than the mean free path of the photons broadens the line profiles. The broadening induced is similar to thermal broadening, and hence, is represented by a Gaussian velocity distribution of width ξ. Microturbulence also affects the strength of the lines, especially strong lines as their equivalent widths are more sensitive to microturbulence than the equivalent widths of weak lines are. The microturbulence velocity increases with decreasing surface gravity, and hence, depends upon the luminosity of the star (Gray 2005). `CMFGEN` assumes that the microturbulence velocity $v_{\rm micro}$ depends on the radial position inside the wind r as

$$v_{\rm micro}(r) = v_{\rm micro}^{\rm min} + \left(v_{\rm micro}^{\rm max} - v_{\rm micro}^{\rm min}\right) \frac{v(r)}{v_\infty}, \tag{2.26}$$

where v_∞ is the wind terminal velocity and $v_{\rm micro}^{\rm min}$ and $v_{\rm micro}^{\rm max}$ are the minimum and maximum $v_{\rm micro}$, respectively. These latter two parameters being difficult to constrain by means of the optical spectra, their values are usually fixed (unless otherwise specified) to $15\,{\rm km\,s^{-1}}$ and $0.1\,v_\infty$, respectively, values which are typical of O-type stars.

The hydrodynamical structure cannot directly be computed in `CMFGEN`. A `TLUSTY` hydrostatic structure in the photosphere, constructed from the OSTAR2002 grid of models generated by Lanz & Hubeny (2003) or linearly interpolated from this grid of effective temperature and surface gravity if necessary, is rather used together with a standard β-velocity law for the wind implemented through the relation

$$v(r) = v_\infty \left(1 - \frac{R_*}{r}\right)^\beta, \tag{2.27}$$

where R_* is the radius of the star. For O-type stars having a thin wind, Repolust et al. (2004) showed that a typical value for β is 0.8. We note that for binary stars, it does not really make sense to speak about wind terminal velocity. For instance, let us consider the wind of the primary star. When the primary star eclipses the secondary star, the part of the primary star wind we observe can reach the value of v_∞. However, if the secondary star eclipses the primary star, then the part of the primary wind we see cannot reach the value of v_∞ because it is blocked by the presence of the secondary star in our line of sight. More generally, the wind over the hemisphere facing the companion star cannot reach the wind terminal velocity.

It has become evident in the last decades that the winds of massive stars are not homogeneous (Hillier 1991; Eversberg et al. 1998; Bouret et al. 2005). Wind clumping is introduced in the models using the two-parameter exponential law for the volume filling factor

$$f(r) = f_1 + (1 - f_1) \exp\left(-\frac{v(r)}{f_2}\right), \tag{2.28}$$

where the parameters f_1 and f_2 are the filling factor value when $r \to \infty$ and the onset velocity of clumping, respectively. Including clumping increases the line strength by $1/f_1$. As the line intensity is the same for similar $\dot{M}/\sqrt{f_1}$ ratio, including clumping in the models leads to a reduced estimate of the mass-loss rate compared to an unclumped model. Hence, in order to compare it with mass-loss rates obtained with unclumped models, the mass-loss rate derived in this paper has to be multiplied by a factor $1/\sqrt{f_1}$ (Martins 2011). The parameters f_1 and f_2 being difficult to estimate accurately based on the optical spectra only, they are usually fixed to currently adopted values (see Sections 2.2.1.5, 2.3.1.6, and 2.4.1.5).

Once the atmospheric structure is obtained, `CMFGEN` computes the solution in the observer's frame through the code `CMF_FLUX` in order to get a synthetic spectrum to be confronted to the observations. The `CMFGEN` spectra should first be broadened by the projected rotational velocity of the star. The macroturbulence velocity is then adjusted on the wings of metallic lines. The origin of macroturbulence in stellar atmospheres, linked to large-scale variations, is highly uncertain. It can either come from large individual granulation cells in cool stars, larger than the mean free path of the photons, or from convection in a subsurface convective layer due to Fe opacity (Cantiello et al. 2021), or from the pulsations in massive stars (Simón-Díaz et al. 2017). In the former case, the complete spectrum is shifted due to the cells motion and slightly asymmetric profiles result. In the latter case, the line profiles show low-level variability. The `CMFGEN` synthetic spectra are broadened by the macroturbulence velocity using the `macturb` program of the `SPECTRUM` suite of routines[4] by convolution of the synthetic spectra with radial-tangential macroturbulence profiles (Gray 2005). In the context of this project, we showed that the macroturbulence velocity does not affect the atmospheric parameters nor the chemical composition.

The stellar and wind parameters are adjusted following the procedure outlined by Martins (2011).

The effective temperature is the first parameter to be adjusted using the ionisation balance method. It consists in computing synthetic spectra at different effective temperatures and comparing the strength of given lines such as the helium or silicon lines to those of the observed spectra. Silicon lines can be used if helium lines are not sufficient, because this element is not influenced by CNO processes, and hence, is not affected by the chemical composition of the star. Indeed, the higher the effective temperature, the more ionised the wind. The lines of the same element but of different ionisation states are sensitive to the effective temperature; hence, measuring their relative strength is a good indicator of the effective temperature of the star (Martins 2011).

The second parameter to be adjusted is the surface gravity, usually estimated based

[4] These routines can be retrieved on the following webpage: `http://www.appstate.edu/~grayro/spectrum/spectrum276/node38.html`

on the wings of Balmer lines such as Hβ, Hγ, and Hδ if these are not contaminated by wind emission. Indeed, the wings of these lines are broadened by collisional processes such as the linear Stark effect which increases in importance if the atmosphere is denser and, consequently, the surface gravity is higher (Martins 2011).

Regarding the mass-loss rate, the main diagnostic line is Hα. If the wind is sufficiently dense, an emission in Hα due to hydrogen recombination is superimposed to the photospheric absorption (Martins 2011). In case of a strong wind, the emission completely dominates the photospheric absorption. If the line is a pure photospheric absorption line, no mass-loss rate determination based on this line is possible. The second diagnostic line is He II λ 4686. However, because we are dealing with binary systems, where the interaction of the winds can also lead to an additional emission of Hα and He II λ 4686, these lines are only indicators and give an upper limit on the mass-loss rate. Hence, if the strength of this line in the `CMFGEN` spectra is higher than the strength of the observed line, then the mass-loss rate is likely too high.

The wind terminal velocity v_∞, that is to say, the maximum velocity reached by the wind, is determined based on the blueward extent of UV absorption lines having a P-Cygni profile. Indeed, the blue-shifted part of the P-Cygni profile sees its origin in the Doppler shift associated with the wind outflow in front of the photospheric disk. In our case, this is done independently of the `CMFGEN` models.

These steps are made manually, meaning by visual comparison, which enables us to highlight all the special features present in the spectra and to grant a higher importance to some lines compared to others depending on what seems more reliable to us. Naturally, all these parameters are interconnected. This means that the procedure is a manual-iterative procedure where one parameter has to be changed at a time until it seems reasonably well reproduced before another parameter is changed which could affect the previous changes, this procedure being applied until all parameters seem reasonably well adjusted.

The surface chemical abundances (in number compared to H) of C, N, and O are adjusted on corresponding lines, but in the context of this work, we decided to set the abundances of the other elements, including He, to solar abundances as taken from Asplund et al. (2009). For the CNO elements, a χ^2 analysis is performed to obtain an estimate of their abundances and associated uncertainties. We use the method proposed by Martins et al. (2015): For each of the three elements, we run four models in addition to the one taken as a reference. For each `CMFGEN` model m and each diagnostic line l, we compute the χ^2 as follows:

$$\chi^2_{l,m} = \sum_{\lambda=\lambda_{\min,l}}^{\lambda_{\max,l}} \left(F_{\rm obs}(\lambda) - F_{\texttt{CMFGEN},m}(\lambda)\right)^2 , \tag{2.29}$$

where $F_{\rm obs}$ is the normalised observed flux of the star and $F_{\texttt{CMFGEN}}$ is the normalised flux of the `CMFGEN` model. For each line, we determine the minimum of the χ^2_l function by fitting a cubic spline to the values of the five `CMFGEN` models. We renormalise this function by its minimum so that $\chi^2_{l,\min}$ is now equal to 1. Following Martins et al. (2015), the 1σ uncertainty on the abundances is then obtained from the abundance values corresponding to $\chi^2 = 2$ (but see the caveats of Andrae (2010)).

It is important to recall that `CMFGEN` assumes that the stars are spherical, static, and isolated. However, because of the binarity, these three assumptions are not verified. The

effective temperature is thus not homogeneous all over the stellar surface and the computed temperature has to be considered as a mean value over the stellar surface. In addition, because of the companion, the norm of the local surface gravity is given by $|\nabla(\Omega)|$ instead of $\frac{GM}{R^2}$. This parameter is not homogeneous over the stellar surface and the local surface gravity is lower than that of an isolated star of same mass and mean radius. As a consequence, the values of $\log g$ computed with `CMFGEN` lead to spectroscopic masses that underestimate the actual masses.

2.1.8. Radial velocity analysis

For a spectroscopic binary, a morphology change in the radial velocity curves of its components is an indicator of the presence of apsidal motion in the system. In the present case, we restrict to the case of an SB2 binary system. The primary and secondary radial velocities of such a binary are given by

$$RV_1(t) = K_1 \left(\cos\left(\phi(t) + \omega(t)\right) + e\, \cos\omega(t)\right) + \gamma_1, \tag{2.30}$$

and

$$RV_2(t) = -K_2 \left(\cos\left(\phi(t) + \omega(t)\right) + e\, \cos\omega(t)\right) + \gamma_2, \tag{2.31}$$

where K_1 and K_2 are the amplitudes of the radial velocity curves of the primary and secondary stars, respectively, and γ_1 and γ_2 are the apparent systemic velocities of the primary and secondary stars, respectively. $\phi(t)$ is the true anomaly computed with Kepler's equation with a specific value of the anomalistic orbital period (time interval between two consecutive periastron passages) $P_{\rm orb}$, the eccentricity e, and the time of periastron passage T_0. Likewise, $\omega(t)$ is the longitude of periastron of the primary star at time t. Multiplying Equation (2.31) by $\frac{K_1}{K_2}$ and adding the result to Equation (2.30), we get

$$RV_1(t) + \frac{K_1}{K_2}\, RV_2(t) = \gamma_1 + \frac{K_1}{K_2}\, \gamma_2, \tag{2.32}$$

or, written in an equivalent form

$$RV_1(t) = -q\, RV_2(t) + B, \tag{2.33}$$

where $q = \frac{K_1}{K_2} = \frac{m_2}{m_1}$ is the mass ratio of the binary system and B is defined according to $B = \gamma_1 + q\, \gamma_2$.

The mass ratio of an SB2 binary system can be estimated by fitting the linear relation (2.33) to the datasets of the system. This relation is further used to convert the radial velocities of both stars into equivalent radial velocities of the primary star with

$$RV_{\rm eq}(t) = \frac{RV_1(t) - q\, RV_2(t) + B}{2}. \tag{2.34}$$

For each time of observation t, we adjust the primary, secondary, and equivalent radial velocity data with the following general relation

$$RV(t) = \gamma + K \left[\cos\left(\phi(t) + \omega(t)\right) + e\, \cos\omega(t)\right], \tag{2.35}$$

where

$$\omega(t) = \omega_0 + \dot{\omega}\,(t - T_0), \tag{2.36}$$

with ω_0 the value of ω at time T_0 and $\dot{\omega}$ the rate of secular apsidal motion.

The problem then consists in finding the six free parameters ($P_{\rm orb}$, e, T_0, ω_0, $\dot{\omega}$, and K_1 or K_2 or, for the equivalent radial velocities, $K_{\rm eq}$) that provide the best fit to the whole set of radial velocity data. We have designed a `Fortran` routine that simultaneously adjusts these six parameters.

2.1.9. `Nightfall`

`Nightfall` is a freely available code, developed by R. Wichmann, M. Kuster, and P. Risse[5] (Wichmann 2011), for modelling eclipsing binary stars. It is an interactive application capable of producing best-fit binary star parameters for a given set of observational data, light curves, and radial velocity curves as well as animated views of eclipsing binary stars (Wichmann 2002).

Eclipsing binaries are of fundamental importance as fitting the light curve of such systems is the only model-independent way to determine the masses of the stars. Eclipsing binaries are usually close systems in which tidal interactions play a key role in the deformation of the shape of the stars, rendering these stars highly non-spherical. The physical model on which `Nightfall` is based takes into account this non-spherical shape of the stars (Wichmann 2002).

`Nightfall` can handle overcontact systems, eccentric orbits, surface spots, asynchronous irradiation as well as the presence of a source of third light. It can also take into account the mutual irradiance of both stars (Wichmann 2002), which might be important if the stars are close or if the ratio between the effective temperatures of the stars is significant. `Nightfall` uses the Roche potential scaled by the instantaneous separation between the stars to describe the shapes of the stars. `Nightfall` uses a dimensionless potential, meaning that the distance between the two stars is set to one. Hence, while keeping the absolute masses fixed, decreasing the Roche lobe filling factors is equivalent to increasing the distance between the stars (Wichmann 2002). For an eccentric binary without surface spots, the model is described by eight parameters: the mass ratio q, the orbital inclination i, the primary and secondary Roche lobe filling factors ($f_{\rm P}$ and $f_{\rm S}$, defined as the ratio between the stellar polar radius and the polar radius of the associated instantaneous Roche lobe at periastron), the primary and secondary effective temperatures ($T_{\rm eff,1}$ and $T_{\rm eff,2}$), the eccentricity e, and the argument of periastron ω.

2.1.10. `PHOEBE`

`PHOEBE 2` is an eclipsing binary modelling code that reproduces and fits light curves, radial velocity curves, and spectral line profiles of eclipsing systems (Prša et al. 2016a; Jones et

[5] The code is available at the URL: `http://www.hs.uni-hamburg.de/DE/Ins/Per/Wichmann/Nightfall.html`

al. 2020)[6]. It includes advanced physics such as mutual irradiation, limb-darkening, light travel time effects, Doppler boosting, spin-orbit misalignment, and interstellar extinction. Particularly relevant to the present analysis, `PHOEBE 2` handles apsidal motion by allowing the argument of periastron to vary linearly with time. In contrast to `Nightfall`, `PHOEBE 2` parameterises each component according to its equivalent (volumetric) radius instead of filling factor or equipotential. For eccentric orbits or misaligned systems, `PHOEBE 2` then makes the assumption that the surface of the star instantaneously reacts to a change in the gravitational potential in such a way that the volume of each star is conserved.

`PHOEBE 2` works in flux units, therefore we converted the observed differential magnitudes into relative fluxes and allowed the synthetic light curve model to automatically scale to these fluxes at each instance of the model. This removed the need for fitting over the luminosities, but sacrificed the ability to extract absolute luminosities directly from the results.

`PHOEBE 2` defines all time-dependent parameters at a provided time t_0. `PHOEBE 2` then accounts for apsidal motion by adjusting $\omega(t)$ and precessing the Keplerian orbit in time through the relation

$$\omega(t) = \omega_0 + \dot{\omega}(t - t_0). \tag{2.37}$$

While we allow ω_0 and $\dot{\omega}$ to be explored during the Markov Chain Monte Carlo run (using the `emcee` package, see Foreman-Mackey et al. 2013), we keep t_0 fixed to avoid meaningless degenerate solutions between t_0 and ω_0. $t_{0,\mathrm{supconj}}$, which enforces the positions of the stars in the orbit to be at superior conjunction at a particular time-stamp, is allowed to vary during the MCMC solution to allow freedom in the model to shift to fit the exact timings of the eclipses.

The MCMC samples the local parameter space with a number of walkers, that is to say, particules undergoing a random walk through the posterior distribution where the probability of moving to any given point is determined by the transition probability of the Markov chain. Each walker is initially drawn from a provided distribution for each of the marginalised parameters. For each iteration, the parameter values are adopted, the forward model is computed, and the χ^2 between the model and the observations is determined. Each chain (i.e. stochastic process of walkers) then decides how to move with respect to the other chains for the following iteration. After a burn-in period during which the chains converge to the local minimum, necessary to ensure that the walkers have settled into a steady state before beginning to accumulate samples from the posterior distribution, the chains then sample the local optimum solution in a way that allows us to determine posteriors and uncertainties that account for the correlations and degeneracies between the marginalised parameters.

[6] `PHOEBE 2` is an open-source project available at the URL `http://phoebe-project.org`

2.2. The twin binary: HD 152248

The methodology presented in Chapter 1, Section 1.2.3, highlighted in orange in Figure 1.9, is applied to the binary system HD 152248. The spectroscopic analysis is performed in Section 2.2.1, where the reconstruction of the individual component spectra together with the establishment of their radial velocities are performed by means of our disentangling code. Subsequent analysis of these spectra are carried out to reassess the spectral classification of the stars and to determine their properties as well as their wind characteristics. The rate of apsidal motion is established in Section 2.2.2 based on radial velocity measurements spanning seven decades. The possibility that HD 152248 might actually belong to a triple system is discussed in Section 2.2.3. The optical photometry is analysed in Section 2.2.4 by means of the `Nightfall` binary star code. In Section 2.2.5, a complete photometric and radial velocity model is constructed in `PHOEBE 2` to determine robust uncertainties. The main conclusions are drawn in Section 2.2.6. The most important results of this section are presented in Rosu et al. (2020b).

2.2.1. Spectroscopic analysis

This section is devoted to the spectral analysis of the binary system HD 152248. The extensive set of observational spectroscopic data we used is introduced. The spectral disentangling is performed to reconstruct the individual spectra as well as to determine the radial velocities of the stars over the orbital cycle. The spectral classification is reassessed and the projected rotational velocities are derived for both stars. The fundamental properties of the stars and their winds are constrained through the fit of the individual spectra with synthetic `CMFGEN` spectra.

2.2.1.1. Observational data

The set of spectroscopic data of HD 152248 in the optical domain consists of forty-eight high-resolution échelle spectra collected between May 1999 and April 2014. Twenty-seven of these were obtained with the Fiber-fed Extended Range Optical Spectrograph (FEROS) mounted on the European Southern Observatory (ESO) 1.5 m or 2.2 m telescopes in La Silla, Chile (Kaufer et al. 1999) while the remaining twenty-one spectra were obtained with the ESPaDOnS spectrograph attached to the Canada-France-Hawaï (CFH) 3.6 m telescope in Hawaï (Donati 2003).

The FEROS instrument has a spectral resolving power of 48 000 and its EEV CCD detector has 2048×4096 pixels of $15 \times 15\,\mu$m. The wavelength domain, covered by thirty-seven orders, ranges from 3650 to 9200 Å. Typical exposure times of the observations range from 150 to 700 seconds. The FEROS pipeline of the `MIDAS` software was used to reduce the FEROS data. The ESPaDOnS instrument has a spectral resolving power of 68 000 and its CCD detector has 2000×4500 pixels of $13.5 \times 13.5\,\mu$m. The wavelength domain, covered by forty orders, ranges from 3700 to 10 500 Å (with three small gaps, namely between 9224 and 9234 Å, between 9608 and 9636 Å, and between 10 026 and 10 074 Å). The ESPaDOnS observations all have an exposure time of 540 seconds. The reduced ESPaDOns data were retrieved from the CFHT archive.

The pre-processing of all these observations was performed following the methodology outlined in Section 2.1.1.

2.2.1.2. Spectral disentangling

The spectral disentangling of the spectra was performed following the methodology outlined in Section 2.1.2. For the cross-correlation, we used `TLUSTY` spectra having an effective temperature of 35 000 K, a surface gravity $\log g$ of 3.5 and a projected rotational velocity $v_{\rm eq} \sin i_{\rm rot}$ of 150 km s^{-1} for both stars. The initial input values for the radial velocities were estimated using a Gaussian fitting of the He I $\lambda\lambda$ 4026, 4471, He II $\lambda\lambda$ 4200, 4542, 5412, and O III λ 5592 lines of spectra taken far from conjunction phases.

Performing the disentangling on the whole set of spectroscopic data appeared to be problematic for two major reasons: (1) The two stars have nearly the same luminosity and (2) eight spectra were taken during eclipses. For the former reason, the disentangling code struggles because at the first iteration the companion's spectrum is assumed to be featureless. However, because the two stars have lines of same strength, more important adjustments are necessary, requiring more iterations. This problem has been solved by setting the total number of iterations to sixty. For the latter reason, during eclipse phases, the relative strength of the lines changes because less light is coming from the star when eclipsed compared to out-of-eclipses phases. Hence, to avoid any biases of the reconstruction process due to the eclipses, we discarded the eight spectra taken during eclipses and restricted ourselves to the remaining forty out of the forty-eight for which the raw data indicate a significant separation of the components, well away from conjunction phases.

The spectral disentangling was performed separately over the following nine domains: A0 [3800:3920] Å, A1 [3990:4400] Å, A2 [4300:4570] Å, A3 [4570:5040] Å, A4 [5380:5760] Å, A5 [5380:5860] Å, A6 [5830:6000] Å, A7 [6400:6750] Å, and A8 [7000:7100] Å. In four domains out of the nine, namely A0, A5, A6, and A7, interstellar lines or diffuse interstellar bands close to spectral lines of interest are present. Therefore, we proceeded as follows: We first processed the wavelength domains (A1, A2, A3, A4, and A8) for which the code was able to reproduce the individual spectra and simultaneously estimate the radial velocities of the stars. We present the convergence of the radial velocities as a function of the number of iterations in the A1-domain for the primary and secondary stars in Figure 2.4. The convergence is effectively ensured after sixty iterations. We observe the same trend for the four other domains. We performed the disentangling again interchanging the roles of the primary star and the secondary star (we call it *version 2*, in opposition to *version 1* where the primary star of the code was also the primary star of the binary system). The radial velocities computed interchanging the roles of the primary and secondary stars agreed within less than 2 km s^{-1} in absolute value over every wavelength domain. The relative error δRV computed as

$$\delta RV = \frac{RV_{A=1,B=2} - RV_{A=2,B=1}}{RV_{A=1,B=2}} \tag{2.38}$$

where $RV_{A=1,B=2}$ (respectively $RV_{A=2,B=1}$) refers to the case where the primary (respectively secondary) star is star A (respectively B) of the code and the secondary (respectively primary) star is star B (respectively A) of the code, is presented for each spectrum, each

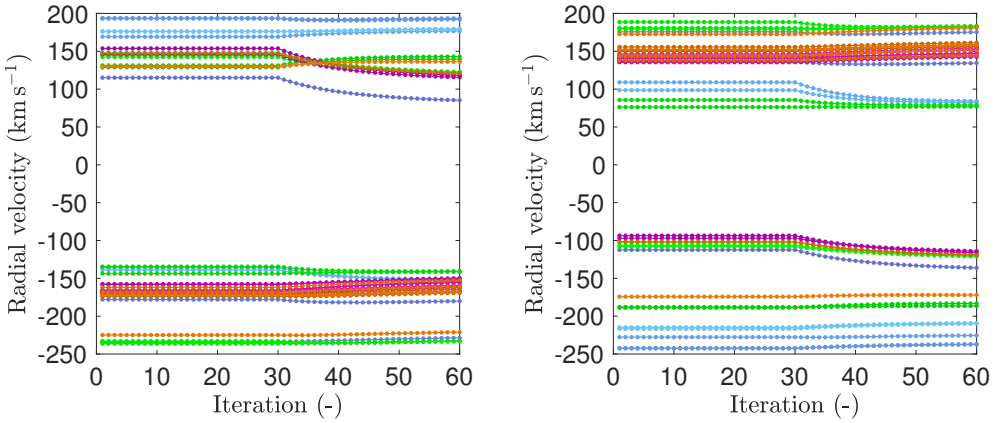

(a) Primary star.

(b) Secondary star.

Figure 2.4. Convergence of the radial velocities as a function of the number of iterations in the disentangling method applied in the A1-domain for (a) the primary star and (b) the secondary star of HD 152248. Each line corresponds to one particular spectrum. The first 30 iterations are performed with fixed radial velocities.

of the five wavelength domains and for both stars in Figure 2.5. Its maximum value is of 8×10^{-3}, meaning that the robustness of the code is ensured. We then computed a weighted-average mean of the stellar radial velocities. The radial velocities from the individual wavelength domains were weighted according to the number of strong lines present in these domains (five lines for A1, three for A2, one for A3, three for A4, and one for A8). The radial velocities obtained for each wavelength domain are presented as a function of the phase in Figure 2.6 together with the mean value over the five domains, for the case where star A of the code is the primary star of the system. The differences in radial velocities mainly come from the fact that these are estimated on different lines which form in different layers of the stellar atmosphere, therefore having a different velocity. In addition, for the case of Hβ for instance, this line is actually polluted by a weak He II line which introduces a shift in the Hβ line itself. This shift depends upon the proportion of H and He. The resulting mean radial velocities of both stars are reported in Table 2.8 together with their 1σ errors. We finally performed the disentangling on the remaining four domains (A0, A5, A6, and A7) with radial velocities fixed to these weighted averages and using the version of the code designed to deal with a third spectral component. For these domains, we also performed the disentangling interchanging the roles of the primary and secondary stars.

We verified afterwards that discarding the eight spectra near conjunction phase was justified. To this aim, we added one of the eight spectra at a time to the forty spectra and ran the disentangling code. We observed a 10 to 50 km s^{-1} difference in the radial velocity of the added spectrum when the roles of the primary and secondary stars were interchanged. In addition, the radial velocities of the other forty spectra were different by about 2 km s^{-1} compared to the case were the eight spectra near conjunction were discarded. Hence, we

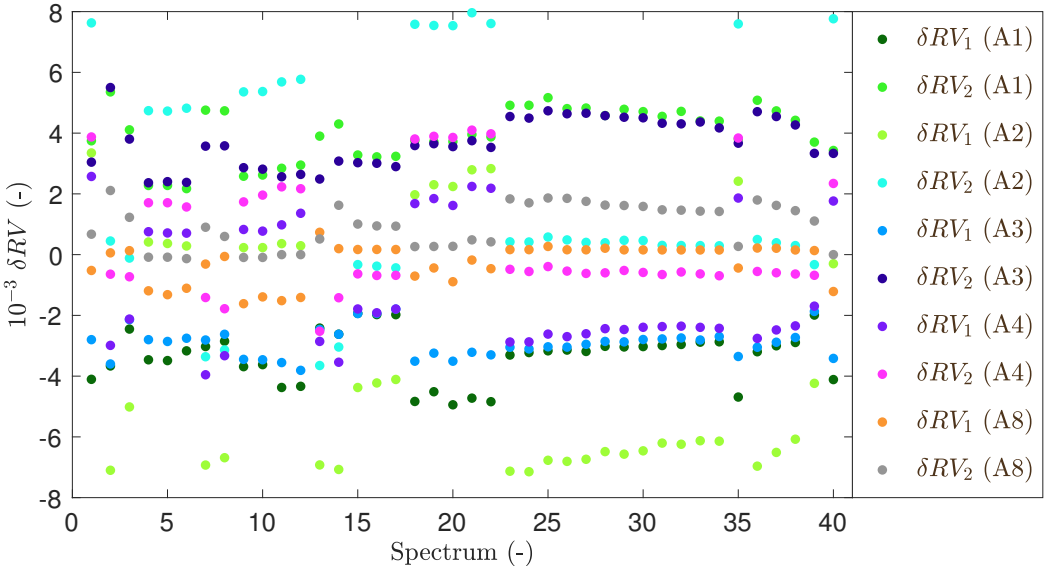

Figure 2.5. Relative error δRV computed with Equation (2.38) for each spectrum, each wavelength domain, and for both stars of HD 152248.

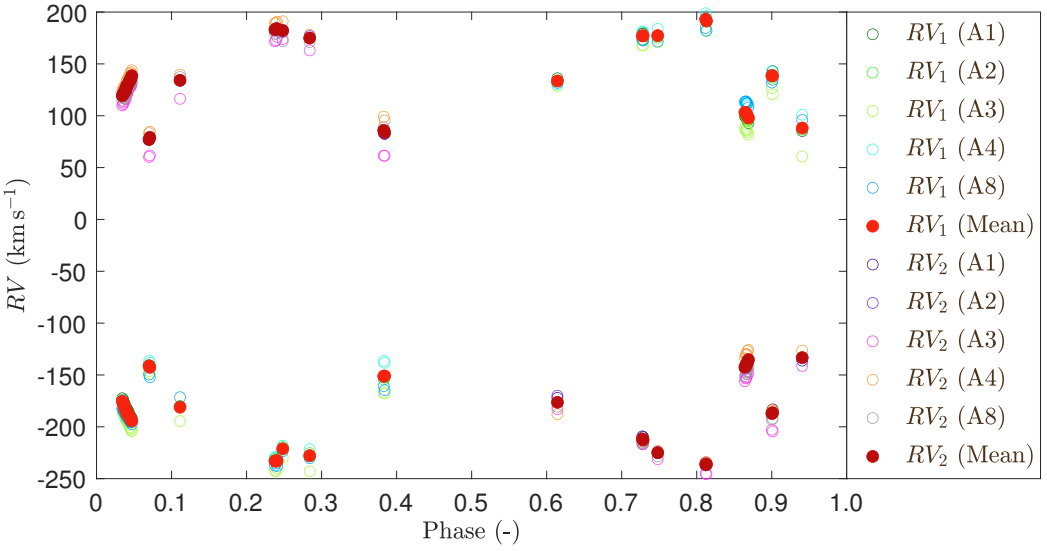

Figure 2.6. Radial velocities of both stars of HD 152248 as a function of the phase obtained for each of the five wavelength domains A1, A2, A3, A4, and A8 for *version 1*, and mean value of the radial velocities over these five domains and over *versions 1* and *2*. The observational phase is computed with the orbital period determined in Section 2.2.2 (last column of Table 2.14).

Table 2.8. Journal of the spectroscopic observations of HD 152248. Column 1 gives the heliocentric Julian date (HJD) of the observations at mid-exposure. Column 2 gives the observational phase ϕ computed with the orbital period determined in Section 2.2.2 (last column of Table 2.14). Columns 3 and 4 give the radial velocities RV_1 and RV_2 of the primary and secondary stars, respectively. The errors represent $\pm 1\sigma$. Column 5 provides information about the instrumentation.

HJD $-2\,450\,000$	ϕ	RV_1 (km s^{-1})	RV_2 (km s^{-1})	Instrumentation
1299.817	0.941	88.2 ± 2.7	-133.2 ± 1.4	ESO 1.5 m + FEROS
1300.809	0.111	-181.1 ± 0.9	134.2 ± 1.4	ESO 1.5 m + FEROS
1301.815	0.284	-227.7 ± 1.4	174.9 ± 1.0	ESO 1.5 m + FEROS
1304.886	0.812	193.1 ± 1.2	-236.1 ± 0.8	ESO 1.5 m + FEROS
1304.891	0.813	191.3 ± 1.1	-236.2 ± 0.7	ESO 1.5 m + FEROS
1327.780	0.748	177.3 ± 1.2	-225.0 ± 0.6	ESO 1.5 m + FEROS
1668.828	0.383	-151.1 ± 2.7	86.0 ± 2.6	ESO 1.5 m + FEROS
1668.836	0.384	-151.0 ± 2.4	83.9 ± 2.3	ESO 1.5 m + FEROS
1670.832	0.728	177.1 ± 1.2	-211.7 ± 0.8	ESO 1.5 m + FEROS
1670.838	0.729	177.0 ± 1.3	-212.6 ± 0.9	ESO 1.5 m + FEROS
1671.836	0.900	138.5 ± 1.1	-187.3 ± 1.2	ESO 1.5 m + FEROS
1671.842	0.901	138.5 ± 1.7	-186.4 ± 1.4	ESO 1.5 m + FEROS
1672.825	0.070	-141.2 ± 0.9	77.1 ± 1.4	ESO 1.5 m + FEROS
1672.831	0.071	-142.6 ± 1.0	79.0 ± 1.3	ESO 1.5 m + FEROS
1673.801	0.238	-232.8 ± 0.8	183.0 ± 1.2	ESO 1.5 m + FEROS
1673.809	0.239	-233.2 ± 0.8	183.8 ± 1.2	ESO 1.5 m + FEROS
1673.817	0.241	-232.7 ± 0.8	183.9 ± 1.3	ESO 1.5 m + FEROS
3546.769	0.248	-221.2 ± 0.7	182.2 ± 1.7	ESO 2.2 m + FEROS
5642.820	0.614	133.5 ± 1.0	-176.4 ± 2.5	ESO 2.2 m + FEROS
6761.037	0.864	103.3 ± 2.1	-142.5 ± 1.7	CFHT 3.6 m+ ESPaDOns
6761.044	0.865	103.1 ± 2.3	-140.7 ± 1.9	CFHT 3.6 m+ ESPaDOns
6761.047	0.866	102.1 ± 2.3	-140.0 ± 1.9	CFHT 3.6 m+ ESPaDOns
6761.050	0.867	100.9 ± 2.2	-139.8 ± 2.0	CFHT 3.6 m+ ESPaDOns
6761.057	0.868	99.8 ± 2.5	-136.9 ± 1.9	CFHT 3.6 m+ ESPaDOns
6761.064	0.869	97.8 ± 2.6	-135.2 ± 1.8	CFHT 3.6 m+ ESPaDOns
6762.026	0.034	-175.3 ± 1.0	119.3 ± 1.0	CFHT 3.6 m+ ESPaDOns
6762.033	0.035	-177.3 ± 1.1	121.2 ± 1.0	CFHT 3.6 m+ ESPaDOns
6762.036	0.036	-178.3 ± 1.0	121.4 ± 1.0	CFHT 3.6 m+ ESPaDOns
6762.040	0.037	-180.1 ± 1.0	121.9 ± 1.0	CFHT 3.6 m+ ESPaDOns
6762.046	0.038	-181.5 ± 1.0	124.3 ± 1.0	CFHT 3.6 m+ ESPaDOns
6762.053	0.039	-184.7 ± 0.9	124.3 ± 1.0	CFHT 3.6 m+ ESPaDOns
6762.060	0.040	-185.1 ± 0.9	128.4 ± 1.0	CFHT 3.6 m+ ESPaDOns
6762.062	0.041	-187.1 ± 0.9	128.9 ± 1.0	CFHT 3.6 m+ ESPaDOns
6762.063	0.041	-186.1 ± 0.9	128.6 ± 1.0	CFHT 3.6 m+ ESPaDOns
6762.073	0.042	-188.0 ± 0.9	131.3 ± 1.0	CFHT 3.6 m+ ESPaDOns
6762.080	0.044	-190.2 ± 0.9	133.2 ± 0.9	CFHT 3.6 m+ ESPaDOns
6762.087	0.045	-191.6 ± 0.8	134.2 ± 1.1	CFHT 3.6 m+ ESPaDOns
6762.093	0.046	-193.5 ± 0.9	136.2 ± 1.1	CFHT 3.6 m+ ESPaDOns
6762.090	0.045	-192.7 ± 0.8	135.6 ± 1.0	CFHT 3.6 m+ ESPaDOns
6762.100	0.047	-194.3 ± 0.9	138.5 ± 1.0	CFHT 3.6 m+ ESPaDOns

conclude that discarding those spectra is justified. It is even more justified by the fact that during eclipses, the strengths of the lines which form in the hidden zone of the eclipsed star are reduced compared to the strengths of the same lines when the stars are far from conjunction phases. As a consequence, this could introduce a bias in the determination of the luminosity ratio between the two stars as well as in the spectral classification since these characteristics are estimated based on the ratio between the equivalent widths of several lines.

2.2.1.3. Spectral classification and absolute magnitudes

We reassessed the spectral classification of the stars based on their reconstructed spectra. The spectral types of the stars were determined based on Conti's criterion (Conti & Alschuler 1971) complemented by Mathys (1988, see Table 2.1 in Section 2.1.3). We found that $\log_{10} W'$ amounts to 0.07 ± 0.01 for the primary star and to 0.09 ± 0.01 for the secondary star, values corresponding to spectral type O7.5 for both stars. The luminosity class of the stars was determined based on Mathys and Walborn criteria (Mathys 1988; Walborn & Fitzpatrick 1990, see Table 2.5 in Section 2.1.3). The He II λ 4686 line is neither in strong absorption nor in strong emission and the N III $\lambda\lambda$ 4634-40-42 triplet is in weak emission, suggesting a luminosity class between III(f) and II(f) for the two stars. Following Walborn & Fitzpatrick (1990) argument, the intensity of the He I λ 4471 line is lower than the intensity of the Hγ line, therefore excluding the luminosity class I. We conclude that both stars are of O7.5 III-II(f) type, in agreement with Sana et al. (2001) and Mayer et al. (2008).

The brightness ratio of the two stars in the visible domain was estimated based on the ratio between the equivalent widths of several spectral lines of the primary and secondary stars. Indeed, since the two stars have the same spectral type, the EWs of their lines can be compared directly and there is no need to use synthetic spectra for the comparison. For this purpose, five lines were used: He I $\lambda\lambda$ 4026, 4471, He II $\lambda\lambda$ 4200, 4542, and Hγ. The results are presented in Table 2.9. We observe that depending on the line considered, the equivalent width of the line of the primary star is either larger or smaller than the one of the secondary star. We obtained a mean value for the brightness ratio of $l_1/l_2 = 1.000 \pm 0.025$. This brightness ratio is applied to the reconstructed spectra of the stars through the relations (2.7) and (2.8) recalled in Section 2.1.2.2.

Table 2.9. Equivalent width of the lines used to determine the brightness ratio in the visible domain of the binary system HD 152248.

Line	$EW_{primary}$	$EW_{secondary}$	$EW_{primary}/EW_{secondary}$
He I λ 4026	0.230	0.238	0.967
He I λ 4471	0.245	0.249	0.984
He II λ 4200	0.150	0.152	0.988
He II λ 4542	0.209	0.201	1.041
Hγ	0.745	0.737	1.010

The second *Gaia* data release (DR2, Gaia Collaboration 2018) quotes a parallax of $\varpi = 0.59 \pm 0.06$ mas for the binary system, corresponding to a distance of 1631^{+178}_{-147} pc (Bailer-Jones et al. 2018). Thence, we inferred a distance modulus of $11.06^{+0.24}_{-0.20}$. The V and B apparent magnitudes of the system are respectively 6.05 ± 0.01 and 6.15 ± 0.01 (Hog et al. 2000). The intrinsic colour index $(B-V)_0$ is taken equal to -0.27 ± 0.01, as inferred for an O7.5 III star by Martins & Plez (2006). These values yield an absolute magnitude in the V-band of the binary system $M_V = -6.23^{+0.25}_{-0.21}$. From the brightness ratio determined previously, we get individual absolute magnitudes $M_{V,1} = M_{V,2} = -5.48^{+0.25}_{-0.21}$ for both stars. Compared to those reported by Martins et al. (2005) and Martins & Plez (2006), these magnitudes show that the supergiant luminosity class I is clearly to be excluded for these stars. The absolute magnitudes inferred are closer to those of an O8 III type star than an O7.5 III type star, although this latter lies within the error bars.

In Section 2.1.2.3, we pointed out the fact that the acceleration of gravity at the surface of the components of a close binary system is not given by the usual $\frac{Gm}{R^2}$ but instead by $|\nabla\Omega|$. As a consequence, the spectrum of a star belonging to a close binary system might mimic that of an object of higher luminosity (Palate & Rauw 2012). This probably explains the difference between the luminosity class III-II obtained through spectral classification criteria and the giant classification obtained from photometric analyses.

2.2.1.4. Projected rotational velocities

The projected rotational velocities of both stars were derived using the Fourier transform method as explained in Section 2.1.6. We applied this method to seven well-isolated spectral lines which are expected to be free of blends, three metallic lines and four He I lines. The results are presented in Table 2.10, and the Fourier transforms are illustrated for the seven lines in Figure 2.7. The mean $v_{\rm eq} \sin i_{\rm rot}$ computed on metallic lines alone or on all the lines agree very well. We adopted a mean $v_{\rm eq} \sin i_{\rm rot}$ of $138 \pm 4\,{\rm km\,s^{-1}}$ for the primary star and of $137 \pm 6\,{\rm km\,s^{-1}}$ for the secondary star. These value agree within the error bars with the values inferred by Mayer et al. (2008) which were obtained through comparison of the He I λ 4922 line with rotationally broadened synthetic spectral lines, but are lower than those quoted by Stickland et al. (1996), Howarth et al. (1997), and Penny et al. (1999). This result was expected because the projected rotational velocities quoted by these authors were obtained by a cross-correlation technique applied to combined spectra taken with the short-wavelength primary (SWP) camera of the International Ultraviolet Explorer (*IUE*) satellite, technique which does not separate the rotational broadening from other broadening mechanisms.

2.2.1.5. Model atmosphere fitting

The `CMFGEN` spectra were first broadened by the projected rotational velocities determined previously. The macroturbulence velocity was adjusted on the wings of the O III λ 5592 line. In this way, macroturbulence velocities of $130 \pm 10\,{\rm km\,s^{-1}}$ and $120 \pm 10\,{\rm km\,s^{-1}}$ were obtained for the primary and secondary stars, respectively.

The effective temperature was determined by searching for the best fit of the He I $\lambda\lambda$ 4026, 4471, 4713, 4922, 5016, 5876, 7065 and He II $\lambda\lambda$ 4200, 4542, 5412 lines. The resulting effective

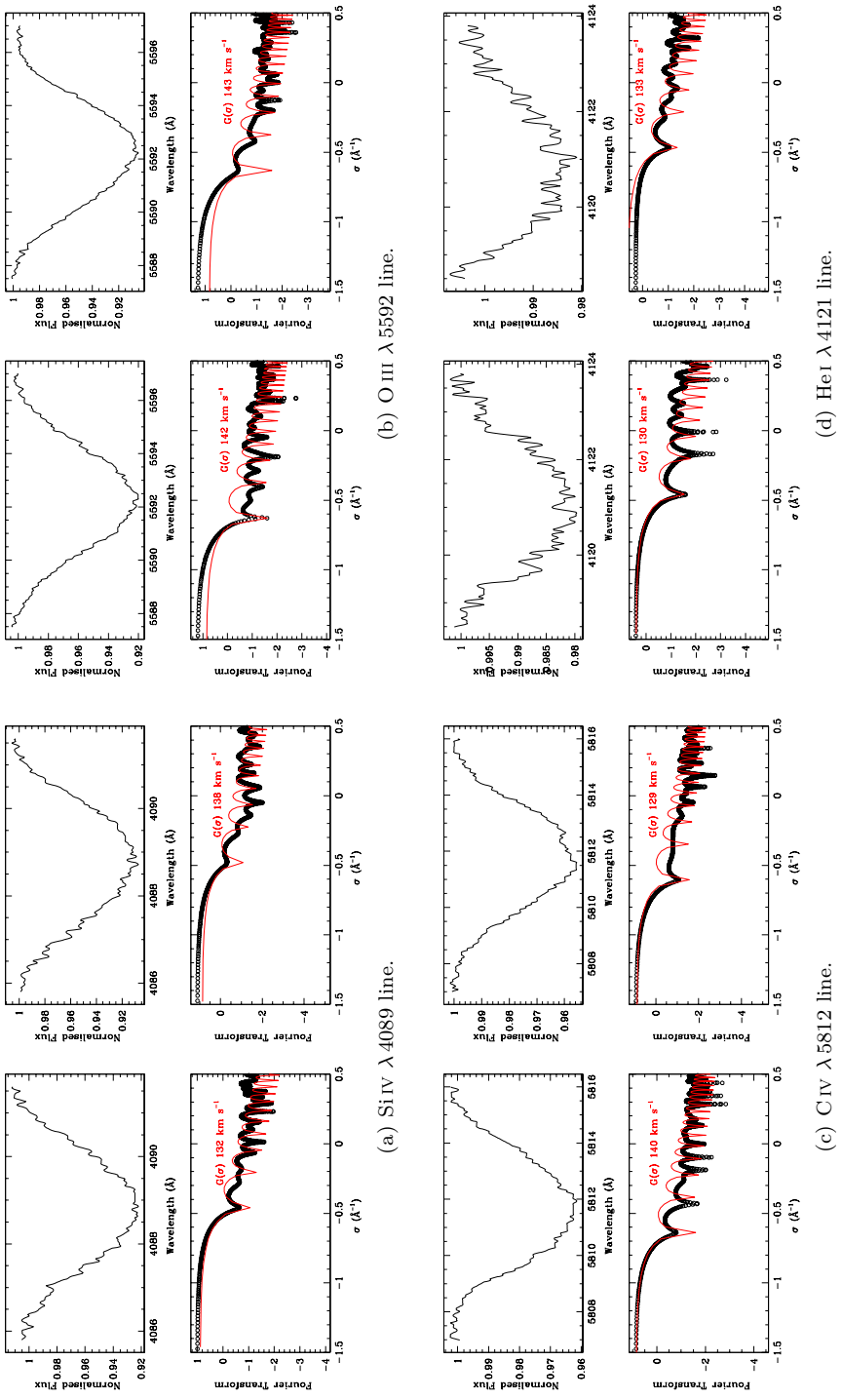

(a) Si IV λ 4089 line. (b) O III λ 5592 line. (c) C IV λ 5812 line. (d) He I λ 4121 line.

Figure 2.7. Fourier transforms of line profiles of HD 152248. *Top row:* Line profiles ((a) Si IV λ 4089, (b) O III λ 5592, (c) C IV λ 5812, (d) He I λ 4121, (e) He I λ 4713, (f) He I λ 4922, and (g) He I λ 5016) of the separated spectra obtained after application of the brightness ratio for the primary (*left panel*) and secondary (*right panel*) stars. *Bottom row:* Fourier transform of these lines (in black) and best-match rotational profile (in red) for the primary (*left panel*) and secondary (*right panel*) stars. Figure taken from Rosu et al. (2020b).

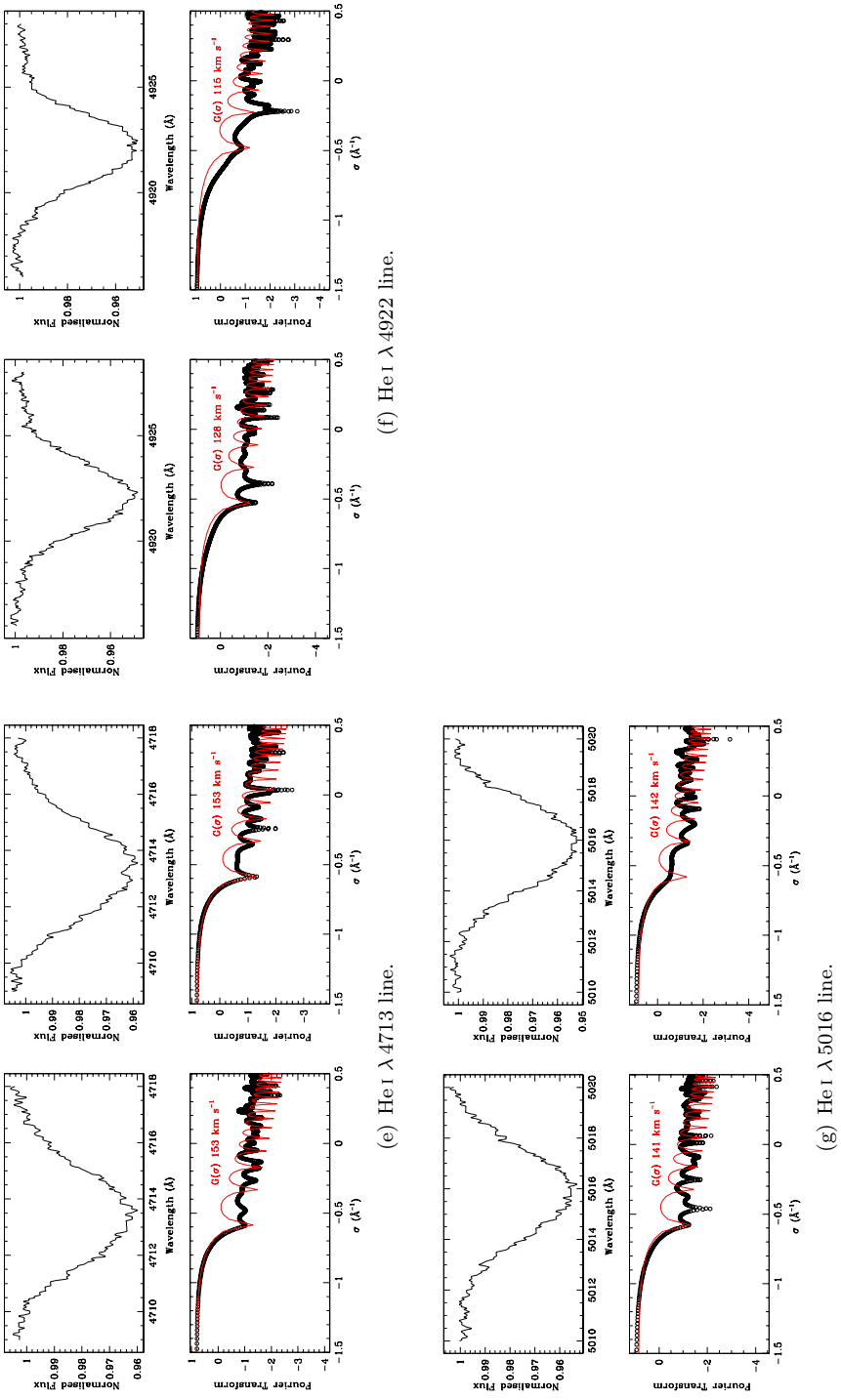

(f) He I λ 4922 line.

(e) He I λ 4713 line.

(g) He I λ 5016 line.

Figure 2.7. Continued.

Table 2.10. Best-fit projected rotational velocities as derived from the disentangled spectra of HD 152248 and comparison with results coming from the literature.

Line	$v_{\rm eq} \sin i_{\rm rot}$ (km s^{-1})	
	Primary	Secondary
Si IV 4089	132	138
O III 5592	142	143
C IV 5812	140	129
He I 4121	130	133
He I 4713	153	153
He I 4922	128	115
He I 5016	141	142
Mean (metallic lines)	138 ± 4	137 ± 6
Mean (all lines)	138 ± 8	136 ± 11
Stickland et al. (1996)	190 ± 20	190 ± 20
Howarth et al. (1997)	159 ± 14	165 ± 14
Penny et al. (1999)	163	173
Mayer et al. (2008)	135 ± 5	135 ± 5

temperatures are 34 000 $\pm$ 1000 K for both stars.

The surface gravity was obtained by adjusting the wings of the Balmer lines Hβ, Hγ, Hδ, and H I $\lambda\lambda$ 3835, 3890. We excluded the Balmer line Hε which is not correctly reproduced by the disentangling code because of the blend with the interstellar Ca II line. We obtained $\log g_{\rm spectro} = 3.48 \pm 0.10$ for both stars.

The oxygen abundance was determined by adjusting the O III λ 5592 line. We verified that the O III λ 5508 line was well-adjusted with this oxygen abundance. The best fit is obtained for an abundance in number O/H of $4.29^{+1.07}_{-0.70} \times 10^{-4}$ and $6.01^{+1.81}_{-1.21} \times 10^{-4}$ for the primary and secondary stars, respectively. Within the error bars, both stars have a solar oxygen abundance. The synthetic `CMFGEN` spectra display a series of O III absorption lines ($\lambda\lambda$ 4368, 4396, 4448, 4454, 4458) that are not present in the observed spectra (neither before nor after disentangling). These lines are not correctly reproduced by the model, as several authors pointed it out for other binary systems (e.g. Raucq et al. 2016, and references therein) and were not considered for the determination of the oxygen abundance.

The nitrogen abundance was determined by adjusting the N III $\lambda\lambda$ 4510-4530 lines. Special attention was paid to the fact that the N III $\lambda\lambda$ 4510-4530 complex is polluted by the C III λ 4516 line. We did not use the N III $\lambda\lambda$ 4634-4640 lines because they are blended with Si IV, O II, and C III lines. We determined a nitrogen abundance in number N/H of $1.32^{+0.90}_{-0.72} \times 10^{-4}$ and $1.15^{+0.69}_{-0.55} \times 10^{-4}$ for the primary and secondary stars, respectively. Both stars display a nitrogen enrichment compared to the solar abundance. This situation is quite common for somewhat evolved O stars and likely stems from the various internal mixing processes that exist in these stars (Song et al. 2013, and references therein).

Finally, the carbon abundance was adjusted on the C III λ 4070 line. We obtained a depleted carbon abundance in number C/H of $1.17^{+0.30}_{-0.27} \times 10^{-4}$ for the primary star and of $2.12^{+0.31}_{-0.28} \times 10^{-4}$ for the secondary star. We note that the C III $\lambda\lambda$ 4647-51 blend and the C III λ 5696 emission are not well reproduced by our model. These lines are known to be

problematic because their formation processes are complex and are controlled by a number of other far-UV lines (Martins & Hillier 2012). As a result, the strength and nature of C III $\lambda\lambda$4647-51 and C III λ5696 critically depend on subtle details of the stellar atmosphere model. We therefore decided not to consider these lines in our fitting procedure. We further note that the C IV λ5801 and λ5812 lines are not well reproduced either by our model. These two lines are usually problematic and rarely correctly reproduced (F. Martins 2019, private communication, see also Raucq et al. 2017). Therefore, we did not use them to adjust the carbon abundance.

These chemical compositions suggest that the primary star is the slightly more evolved component of the system.

Regarding the wind parameters, the clumping parameters were fixed: The volume filling factor f_1 was set to 0.1 and the f_2 parameter that determines the wind velocity and thus the position where clumping starts was set to 100 km s^{-1}. For the sake of completeness, we varied f_1 from 0.09 to 0.11 and f_2 from 70 to 130 km s^{-1}. We observed that decreasing (respectively increasing) f_1 led to a small increase (respectively decrease) of the Hα emission while decreasing (respectively increasing) f_2 led to a small increase (respectively decrease) of both Hα and He II λ4686 emission lines. The exact values of these two parameters do not affect the results of our study because Hα and He II λ4686 are not used to constrain the stellar parameters (except for the mass-loss rate, see below). Likewise, the β parameter of the velocity law was fixed to the value of 1.07. This value is between values of O7.5 giant and supergiant stars as inferred by Muijres et al. (2012). Again for the sake of completeness, we varied this parameter from 1.00 to 1.15. We observed that decreasing (respectively increasing) β led to a small increase (respectively decrease) in Hβ and a small decrease (respectively increase) in Hα and He II λ4686 emission lines. When all other parameters were fixed, the best adjustment of Hβ was achieved for $\beta = 1.07$, suggesting that the adopted β value is representative of the system or is at least not too far from the exact value.

In principle, the wind terminal velocity could be derived from the Hα line. However, in the spectra of HD 152248, this line is at least partially formed in the wind collision zone. Therefore, we decided to fix the value of v_∞ for each star to 2420 km s^{-1} as determined by Howarth et al. (1997) on *IUE* spectra. Regarding the mass-loss rate, the main diagnostic lines in the optical domain are the Hα and He II λ4686 lines. However, as for Hα, the weak He II λ4686 emission line in the spectra of HD 152248 is at least partially formed in the wind collision zone, leading to an enhanced emission strength. To obtain a first-order estimate, we thus decided to adjust the mass-loss rate on the depths of the Hβ, Hγ, and Hδ lines. As a second step, we lowered the mass-loss rate in order to avoid stronger Hα and He II λ4686 emissions in the synthetic spectrum than in the disentangled spectra. The normalised disentangled spectrum of the primary star is presented in Figure 2.8 for Hβ, Hγ, Hα, and He II λ4686 together with five `CMFGEN` models having different values of the mass-loss rate: $10^{-6}\,M_\odot\,\mathrm{yr}^{-1}$, $9\times10^{-7}\,M_\odot\,\mathrm{yr}^{-1}$, $8\times10^{-7}\,M_\odot\,\mathrm{yr}^{-1}$, $7\times10^{-7}\,M_\odot\,\mathrm{yr}^{-1}$, and $6\times10^{-7}\,M_\odot\,\mathrm{yr}^{-1}$. We observe that the He II λ4686 line is in absorption when the mass-loss rate is lower than or equal to $7 \times 10^{-7}\,M_\odot\,\mathrm{yr}^{-1}$ while the Hα line is in absorption when the mass-loss rate is lower than or equal to $8 \times 10^{-7}\,M_\odot\,\mathrm{yr}^{-1}$. The adjustment of the Hβ line is nearly perfect when the mass-loss rate equals $10^{-6}\,M_\odot\,\mathrm{yr}^{-1}$, while the strength of the line increases when the mass-loss rate decreases. The same effect is observed for Hγ and Hδ (not shown) but it is less visible than for Hβ. In this way, we found that $\dot{M} \leq 8\times10^{-7}\,M_\odot\,\mathrm{yr}^{-1}$ for both stars.

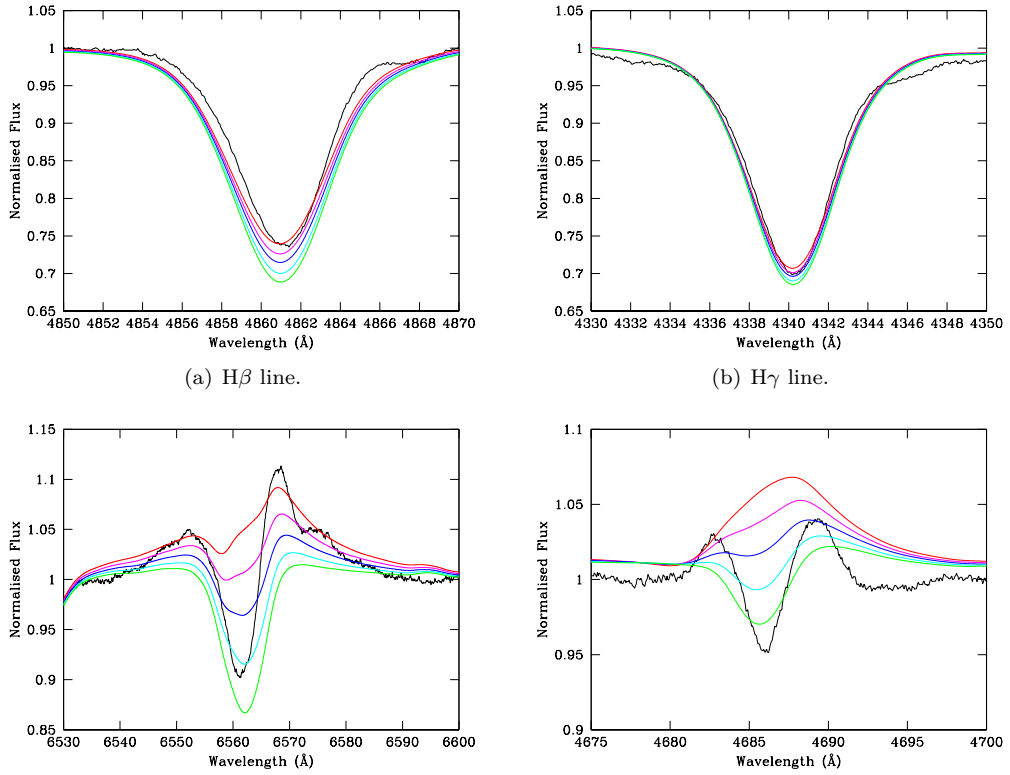

(a) Hβ line.

(b) Hγ line.

(c) Hα line.

(d) He II λ 4686 line.

Figure 2.8. Normalised disentangled spectrum of the primary star of HD 152248 (in black) together with `CMFGEN` synthetic spectra having different values of the mass-loss rate: $10^{-6}\,M_\odot\,\mathrm{yr}^{-1}$ (in red), $9\times10^{-7}\,M_\odot\,\mathrm{yr}^{-1}$ (in magenta), $8\times10^{-7}\,M_\odot\,\mathrm{yr}^{-1}$ (in blue), $7\times10^{-7}\,M_\odot\,\mathrm{yr}^{-1}$ (in cyan), and $6\times10^{-7}\,M_\odot\,\mathrm{yr}^{-1}$ (in green).

The stellar and wind parameters of the best-fit `CMFGEN` model atmosphere are summarised in Table 2.11 and the chemical abundances are given in Table 2.12. The normalised disentangled spectra of the binary components of HD 152248 are illustrated in Figure 2.9 along with the best-fit `CMFGEN` adjustments.

The bolometric magnitudes of the stars $M_{\mathrm{bol},1} = M_{\mathrm{bol},2} = -8.63^{+0.26}_{-0.23}$ were computed through the relations recalled in Section 2.1.4. We further obtained bolometric luminosities L_{bol} of $2.27^{+0.55}_{-0.47}\times10^5 L_\odot$ for both stars. From the relation between bolometric luminosity, radius, and effective temperature, we inferred a spectroscopic radius $R_{\mathrm{spectro}} = 13.7^{+1.9}_{-1.6}\,R_\odot$ for both stars. Using the surface gravity determined with `CMFGEN`, we obtained a spectroscopic mass $M_{\mathrm{spectro}} = 20.8^{+7.4}_{-6.9}\,M_\odot$ for both stars.

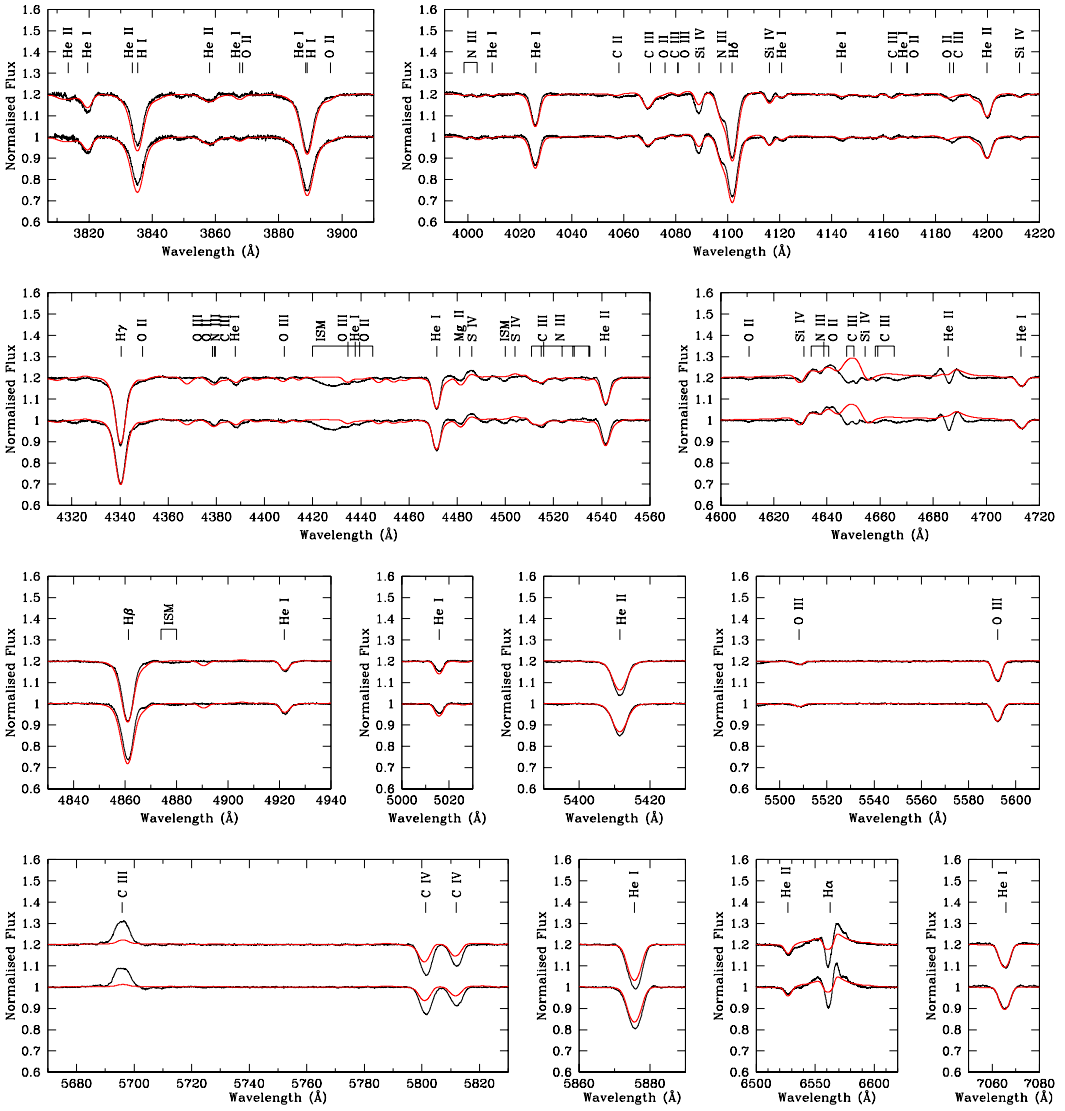

Figure 2.9. Normalised disentangled spectra (in black) of the primary and secondary stars of HD 152248 (the spectrum of the secondary star is shifted by +0.2 in the y-axis for convenience) together with the respective best-fit `CMFGEN` model atmosphere (in red). Figure taken from Rosu et al. (2020b).

Table 2.11. Stellar and wind parameters of the best-fit `CMFGEN` model atmosphere derived from the separated spectra of HD 152248.

Parameter	Value	
	Primary	Secondary
$T_{\rm eff}$ (K)	$34\,000 \pm 1000$	$34\,000 \pm 1000$
$\log g_{\rm spectro}$ (cgs)	3.48 ± 0.10	3.48 ± 0.10
$v_{\rm macro}$ ($\rm km\,s^{-1}$)	130 ± 10	120 ± 10
$\dot{M}$ ($M_\odot\,\rm yr^{-1}$)	$\leq 8 \times 10^{-7}$	$\leq 8 \times 10^{-7}$
$\dot{M}_{\rm unclumped}$ ($M_\odot\,\rm yr^{-1}$)[a]	$\leq 2.5 \times 10^{-6}$	$\leq 2.5 \times 10^{-6}$
v_∞ ($\rm km\,s^{-1}$)	2420[b]	2420[b]
f_1	0.1 (fixed)	0.1 (fixed)
f_2 ($\rm km\,s^{-1}$)	100 (fixed)	100 (fixed)
β	1.07 (fixed)	1.07 (fixed)
$R_{\rm spectro}$ ($R_\odot$)	$13.7^{+1.9}_{-1.6}$	$13.7^{+1.9}_{-1.6}$
$M_{\rm spectro}$ ($M_\odot$)	$20.8^{+7.4}_{-6.9}$	$20.8^{+7.4}_{-6.9}$

Notes. [a] $\dot{M}_{\rm unclumped} = \dot{M}/\sqrt{f_1}$. [b] Value fixed to the value determined by Howarth et al. (1997).

Table 2.12. Surface chemical abundances of the best-fit `CMFGEN` model atmosphere derived from the separated spectra of HD 152248 (Columns 2 and 3). The solar chemical abundances are given in Column 4 for comparison and are taken from Asplund et al. (2009).

Element	Primary	Secondary	Sun
He/H (nb)	0.0851[a]	0.0851[a]	0.0851 ± 0.0020
C/H (nb)	$1.17^{+0.30}_{-0.27} \times 10^{-4}$	$2.12^{+0.31}_{-0.28} \times 10^{-4}$	$2.69 \pm 0.31 \times 10^{-4}$
N/H (nb)	$1.32^{+0.90}_{-0.72} \times 10^{-4}$	$1.15^{+0.69}_{-0.55} \times 10^{-4}$	$6.76 \pm 0.78 \times 10^{-5}$
O/H (nb)	$4.29^{+1.07}_{-0.70} \times 10^{-4}$	$6.01^{+1.81}_{-1.21} \times 10^{-4}$	$4.90 \pm 0.56 \times 10^{-4}$

Notes. [a] Value fixed to the solar value (Asplund et al. 2009).

2.2.2. Radial velocity analysis

Combining our new radial velocities determined through spectral disentangling (see Table 2.8) with the literature data (see Table 2.13) from Struve (1944), Hill et al. (1974), Stickland et al. (1996, reviewed by Penny et al. (1999)), the ESO 1.5 m + B&C, CAT/CES/LC and CTIO 1.5 m + BME data from Sana et al. (2001), and the data from Mayer et al. (2008), we obtained hundred forty-three radial velocity measurements spread over sixty-seven years. For all these datasets, we only took into account the observations dates for which the separation in radial velocities between the primary and secondary stars was of at least $100\,\rm km\,s^{-1}$. Regarding Struve (1944) data, a maximum uncertainty of 1.7×10^{-3} days exists on the dates as it is not specified if the observations are given at mid-exposure or at the beginning of the exposure, and as the exposure times are of about five minutes. For the radial velocity data from Struve (1944) and Hill et al. (1974), we estimated errors on individual data points of $15\,\rm km\,s^{-1}$. The only difference in the *IUE* datasets of Stickland et al. (1996) and Penny et al. (1999) lies in the star used to compute

Table 2.13. Journal of the literature radial velocity measurements of HD 152248. Column 1 gives the heliocentric Julian date (HJD) of the observations. Columns 2 and 3 give the radial velocities RV_1 and RV_2 of the primary and secondary stars, respectively. Column 4 gives the estimated error Δ. Column 5 provides the reference of the measurements.

Date (HJD)	RV_1	RV_2	Δ	Ref.	Date (HJD)	RV_1	RV_2	Δ	Ref.
-2 400 000	(km s^{-1})	(km s^{-1})	(km s^{-1})		-2 400 000	(km s^{-1})	(km s^{-1})	(km s^{-1})	
31 210.910	76.4	-193.6	15.0	[1]	44 121.833	191.3	-211.2	10.0	[4]
31 212.814	-231.6	101.0	15.0	[1]	44 449.183	-111.4	61.0	10.0	[4]
31 212.818	-235.7	139.3	15.0	[1]	44 450.140	-184.9	163.1	10.0	[4]
31 212.954	-238.0	106.1	15.0	[1]	44 452.324	42.7	-115.9	10.0	[4]
31 212.960	-278.7	147.8	15.0	[1]	44 454.242	96.0	-125.6	10.0	[4]
31 213.825	-166.9	116.4	15.0	[1]	44 460.054	95.5	-141.7	10.0	[4]
31 215.899	225.1	-257.2	15.0	[1]	48 863.966	-178.5	122.9	10.0	[4]
31 216.833	24.3	-135.7	15.0	[1]	48 867.575	188.4	-227.2	10.0	[4]
31 218.835	-182.0	96.3	15.0	[1]	48 870.571	-216.9	156.1	10.0	[4]
31 218.853	-225.5	183.5	15.0	[1]	49 778.550	-158.9	86.2	10.0	[4]
31 218.911	-252.0	178.8	15.0	[1]	49 817.640	-154.5	96.6	10.0	[4]
31 218.921	-222.0	165.8	15.0	[1]	49 818.062	-209.5	150.8	10.0	[4]
31 219.815	-124.4	89.2	15.0	[1]	49 819.042	-195.4	126.5	10.0	[4]
31 219.819	-136.8	66.0	15.0	[1]	49 819.730	-91.9	36.9	10.0	[4]
31 221.838	222.3	-292.2	15.0	[1]	49 820.749	94.5	-146.5	10.0	[4]
31 221.844	258.6	-265.9	15.0	[1]	49 821.530	190.4	-220.8	10.0	[4]
31 221.926	199.0	-235.9	15.0	[1]	49 840.180	26.6	-81.4	10.0	[4]
31 221.937	189.3	-202.2	15.0	[1]	49 910.341	-79.7	30.5	10.0	[4]
31 223.902	-97.5	61.5	15.0	[1]	49 911.317	-227.7	170.2	10.0	[4]
31 224.840	-230.8	189.6	15.0	[1]	49 912.329	-177.1	84.5	10.0	[4]
31 224.844	-218.1	173.7	15.0	[1]	49 915.321	150.8	-182.5	10.0	[4]
31 224.911	-184.7	197.5	15.0	[1]	49 964.852	-144.2	59.7	10.0	[4]
31 224.916	-211.1	160.8	15.0	[1]	49 966.016	51.4	-127.6	10.0	[4]
40 808.570	-123.0	37.0	15.0	[2]	50 205.859	207.4	-208.0	10.0	[5]
40 808.709	-133.0	44.0	15.0	[2]	50 207.816	-207.2	203.6	10.0	[5]
40 809.553	-222.0	116.0	15.0	[2]	50 208.795	-156.1	155.8	10.0	[5]
40 812.464	194.0	-254.0	15.0	[2]	50 208.879	-150.4	136.7	10.0	[5]
40 812.590	195.0	-242.0	15.0	[2]	50 210.782	167.3	-173.9	10.0	[5]
40 812.684	203.0	-257.0	15.0	[2]	50 210.910	187.2	-196.4	10.0	[5]
40 814.514	-156.0	62.0	15.0	[2]	50 211.777	186.7	-187.8	10.0	[5]
40 814.684	-127.0	135.0	15.0	[2]	50 211.912	175.0	-177.9	10.0	[5]
40 815.556	-221.0	129.0	15.0	[2]	50 534.902	-75.7	129.5	10.0	[5]
43 647.872	-179.3	202.0	8.0	[3]	50 535.904	70.7	-110.5	10.0	[5]
43 648.908	-57.5	80.2	8.0	[3]	50 536.888	213.2	-208.9	10.0	[5]
43 650.933	192.4	-250.0	8.0	[3]	50 537.897	98.7	-73.8	10.0	[5]
48 675.845	225.3	-219.9	5.0	[3]	50 538.889	-165.6	135.6	10.0	[5]
48 677.852	-181.5	165.5	5.0	[3]	50 539.907	-201.4	191.8	10.0	[5]
48 678.841	-188.5	183.1	5.0	[3]	50 531.908	160.2	-155.2	5.0	[5]
49 023.836	122.3	-151.2	5.0	[3]	50 532.881	-97.9	122.7	5.0	[5]
49 027.881	-178.6	173.7	5.0	[3]	50 533.859	-206.7	219.7	5.0	[5]
49 029.877	154.0	-146.6	5.0	[3]	50 534.844	-99.7	108.2	5.0	[5]
49 146.707	221.3	-200.6	5.0	[3]	50 535.859	48.7	-85.6	5.0	[5]
49 148.720	-142.7	140.6	5.0	[3]	50 536.856	219.0	-201.2	5.0	[5]
49 149.690	-200.0	218.8	5.0	[3]	50 623.628	154.2	-170.8	5.0	[5]
49 448.729	169.8	-184.1	5.0	[3]	50 624.554	215.8	-211.1	5.0	[5]
49 448.832	169.8	-165.9	5.0	[3]	50 626.571	-202.0	214.9	5.0	[5]
49 451.693	-198.7	206.3	5.0	[3]	51 328.734	151.8	-150.2	5.0	[5]
49 451.715	-198.7	206.3	5.0	[3]	51 329.738	-130.2	117.9	5.0	[5]
49 451.766	-206.1	198.4	5.0	[3]	51 330.739	-215.9	194.0	5.0	[5]
49 454.677	171.6	-170.4	5.0	[3]	51 331.771	-81.4	36.7	5.0	[5]
49 454.748	164.7	-168.0	5.0	[3]	51 332.798	84.8	-108.4	5.0	[5]
49 454.771	177.5	-165.4	5.0	[3]					

References. [1] Struve (1944), [2] Hill et al. (1974), [3] Mayer et al. (2008), [4] Stickland et al. (1996); Penny et al. (1999), [5] Sana et al. (2001).

the cross-correlation function: Whilst Stickland et al. (1996) used τ Sco for the ISM lines and an O-star for the remaining lines, Penny et al. (1999) only used an O-star. None of the O-stars used by the two authors is of the same spectral type as the stars of HD 152248. The amplitudes of the radial velocities of Stickland et al. (1996) are in better agreement with the amplitudes of Sana et al. (2001) while the amplitudes of Penny et al. (1999) are in better agreement with the amplitudes of Hill et al. (1974). We then decided to adopt the values quoted by Penny et al. (1999) and adopted an error estimate of $10\,\mathrm{km\,s^{-1}}$ for these data. For the datasets of Sana et al. (2001), we took the values given for the He I λ 4471 line as it is more homogeneous and appropriate for the CAT/CES data. The radial velocities of these data are corrected from the systemic velocity γ, which value is -30.5 and $-28.5\,\mathrm{km\,s^{-1}}$ for the primary and secondary stars, respectively. We adopted an error estimate of $10\,\mathrm{km\,s^{-1}}$ for the B&C radial velocities and of $5\,\mathrm{km\,s^{-1}}$ for the CAT/CES and BME radial velocities. The radial velocity amplitudes of the B&C data are smaller than those of the CAT/CES data as the resolution of the CAT/CES is higher. For the Cerro-Tololo, Echelec, and CAT/CES data of Mayer et al. (2008), we estimated errors of $8\,\mathrm{km\,s^{-1}}$, $5\,\mathrm{km\,s^{-1}}$, and $5\,\mathrm{km\,s^{-1}}$, respectively. Finally, for the radial velocities derived from our spectral disentangling, we adopted a global error estimate of $3\,\mathrm{km\,s^{-1}}$ to avoid bias due to the small error estimates obtained as part of the disentangling (see Table 2.8). We did not take into account the data given by García & Mermilliod (2001) on purpose as these data suffer from high uncertainties.

Applying a linear regression to the various datasets mentioned above, we obtained the parameters q and B of Equation (2.33). Notably, the mass ratio $q = \frac{m_2}{m_1} = 1.04 \pm 0.03$ for the binary system. Because each literature source of radial velocity data has its own convention for the apparent systemic velocities, we found different values for the B parameter for each dataset. The apparent systemic velocity was adjusted for each radial velocity dataset so as to minimise the sum of the residuals of the data about the curve given by Equation (2.35). We tested different values of K_1 ranging from 213 to $219\,\mathrm{km\,s^{-1}}$. The best quality of the fit, as judged from its global χ^2, was obtained for $216^{+2}_{-1}\,\mathrm{km\,s^{-1}}$. We accordingly adopted this value for the amplitude of variations of the primary and equivalent radial velocities. Likewise, we tested different values of K_2 between 209 and $216\,\mathrm{km\,s^{-1}}$, and the best results were obtained for $K_2 = 212^{+2}_{-2}\,\mathrm{km\,s^{-1}}$. For the equivalent radial velocities, we finally determined the value of $q = 1.01^{+0.02}_{-0.01}$, which yields the best global fit to the data through Equation (2.35). We therefore conclude that the mass ratio is consistent with 1.0.

To determine the five free parameters ($P_{\rm orb}$, e, T_0, ω_0, and $\dot{\omega}$) that provide the best fit to the whole set of radial velocity data, we scanned the parameter space in a systematic way. The most important projections of the five-dimensional parameter space onto two-dimensional planes are shown in Figure 2.10. We obtained slightly different values of ω_0 and T_0 for the different radial velocity sets (primary, secondary, or equivalent) that were considered. Nonetheless, the rate of apsidal motion $\dot{\omega}$, the orbital period $P_{\rm orb}$, and to a lesser extent, the eccentricity e are consistent for all datasets.

The best-fit parameters and their 1σ errors are given in Table 2.14. $a_j \sin i$ and $m_j \sin^3 i$ stand respectively for the minimum semi-major axis and the minimum mass of star j, where i is the inclination of the orbit with respect to the reference plane. The best fit of the radial velocity data at six different epochs is illustrated in Figure 2.11. The change in morphology

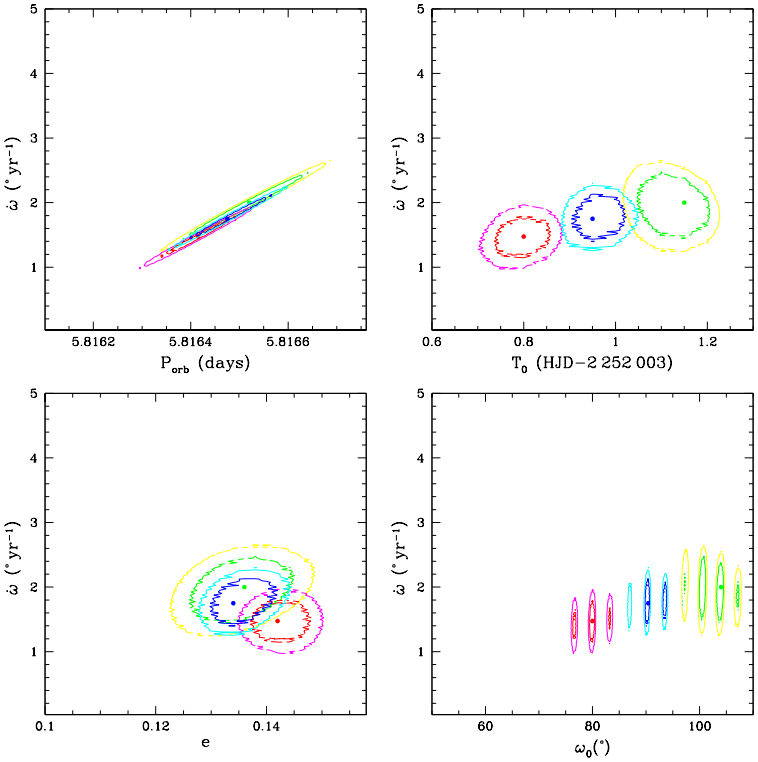

Figure 2.10. Confidence contours for the best-fit parameters obtained from the adjustment of the full set of hundred forty-three radial velocity data of HD 152248 with Equations (2.35) and (2.36). The best-fit solutions for the primary, secondary, and equivalent radial velocities are shown by the red, green, and blue filled dots, respectively. The corresponding $1\,\sigma$ and 90% confidence levels are shown by the red and magenta, green and yellow, and blue and cyan contours for the primary, secondary, and equivalent radial velocities, respectively. Figure taken from Rosu et al. (2020b).

of the radial velocity curve over more than six decades between the Struve (1944) data and the most recent observations is clearly visible.

Within the error bars, our value for the apsidal motion rate and the value of $(2.13 \pm 0.23)^\circ\,\mathrm{yr}^{-1}$ derived by Mayer et al. (2008) from the full set of radial velocities available to them, overlap. By discarding the Struve (1944) measurements, Mayer et al. (2008) favoured a higher value of $(3.07 \pm 0.47)^\circ\,\mathrm{yr}^{-1}$ for the apsidal motion rate. We therefore determined the apsidal motion rate again, discarding in a first step the Struve (1944) data, and, in a second step, also the Hill et al. (1974) data. Our best-fit results lead to a reduction by nearly 30% of $\dot{\omega}$ compared to our best-fit value, instead of an increase as advocated by Mayer et al. (2008). At the same time, the uncertainties increased due to the significantly reduced time span of the dataset. Thence, we decided to keep all the radial velocity data in our analysis.

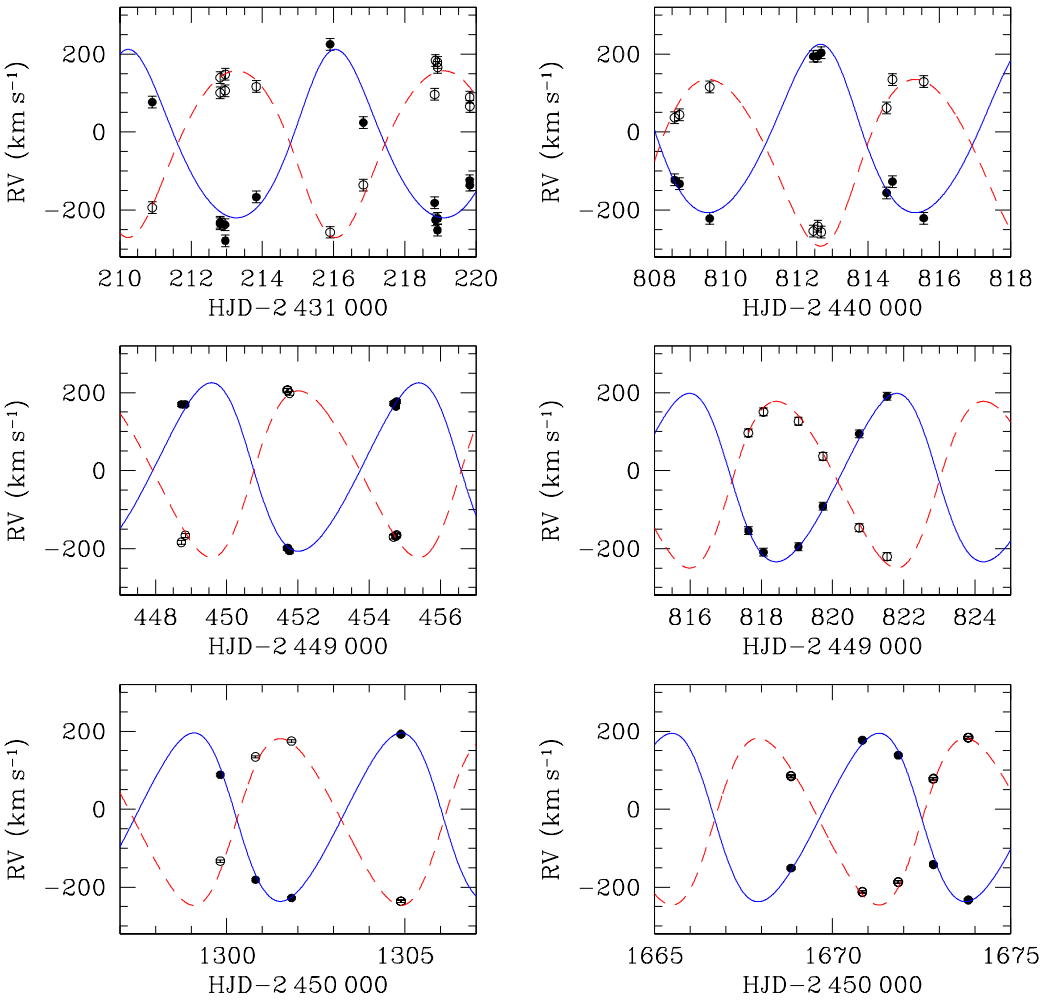

Figure 2.11. Comparison between the measured radial velocities of the primary (filled dots) and secondary (open dots) stars of HD 152248 and the radial velocities expected from Equations (2.35) and (2.36) with the best-fit parameters given in Table 2.14. The top panels correspond to data from Struve (1944, *left*) and Hill et al. (1974, *right*). The middle panels show one epoch from Mayer et al. (2008, *left*), as well as one epoch of *IUE* data from Penny et al. (1999, *right*). The bottom panels correspond to radial velocities that we re-derived here. Figure taken from Rosu et al. (2020b).

We made a consistency check of our determination of $\dot{\omega}$ by determining the values of ω at all epochs for which at least five radial velocity data points were available. The eccentricity, the anomalistic orbital period, the semi-amplitude of the primary radial velocity curve, and the mass ratio were fixed to the values obtained from the analysis of the equivalent radial velocities ($e = 0.134$, $P_{\rm orb} = 5.816475\,{\rm d}$, $K_1 = 216\,{\rm km\,s^{-1}}$, $q = 1.01$, see Table 2.14). For each subset of radial velocity data, the systemic velocity and the ω value were then adjusted

Table 2.14. Best-fit orbital parameters of HD 152248 obtained with Equations (2.35) and (2.36).

Parameter	Primary RVs	Secondary RVs	Equivalent RVs
$P_{\rm orb}$ (d)	$5.816415^{+0.000085}_{-0.000075}$	$5.816520^{+0.000130}_{-0.000120}$	$5.816475^{+0.000085}_{-0.000075}$
e	$0.142^{+0.005}_{-0.004}$	$0.136^{+0.009}_{-0.010}$	$0.134^{+0.007}_{-0.004}$
$\dot{\omega}$ ($^\circ\,{\rm yr}^{-1}$)	$1.48^{+0.36}_{-0.31}$	$2.00^{+0.48}_{-0.53}$	$1.75^{+0.35}_{-0.32}$
ω_0 ($^\circ$)	$80.0^{+3.6}_{-3.6}$	$104.0^{+3.6}_{-6.7}$	$90.4^{+3.6}_{-3.3}$
T_0 (HJD$-$2 450 000)	$2\,003.80^{+0.05}_{-0.06}$	$2\,004.15^{+0.05}_{-0.10}$	$2\,003.95^{+0.07}_{-0.04}$
$q = m_2/m_1$	...	...	$1.01^{+0.02}_{-0.01}$
K_1 (km s^{-1})	216^{+2}_{-1}	...	216 (adopted)
K_2 (km s^{-1})	...	212^{+2}_{-2}	...
$a_1 \sin i$ ($R_\odot$)	$24.6^{+0.2}_{-0.1}$	...	$24.6^{+0.2}_{-0.1}$
$a_2 \sin i$ ($R_\odot$)	...	$24.1^{+0.2}_{-0.2}$	$24.4^{+0.2}_{-0.2}$
$m_1 \sin^3 i$ ($M_\odot$)	...	...	$23.2^{+0.7}_{-0.6}$
$m_2 \sin^3 i$ ($M_\odot$)	...	...	$23.4^{+0.7}_{-0.4}$
χ^2_ν	2.831	3.967	2.082

in order to achieve the smallest χ^2 between the observed and computed radial velocities. The results agree very well with the ω values obtained from the global fit of the equivalent radial velocities. Some scatter exists around the linear $\omega(t) = \omega_0 + \dot{\omega}\,(t - T_0)$ relation, but we found no compelling evidence for a more complex dependence of ω on time. The scatter is fully consistent with the errors on the individual ω determinations and with the uncertainties of the global fit to the equivalent radial velocities (see Section 2.2.4.3, especially Figure 2.16). Further aspects of the radial velocities of HD 152248, notably regarding the possibility of a triple system, are discussed in Section 2.2.3.

2.2.3. Evidence for a triple system?

The triple nature of HD 152248 has been discussed for years. Based on speckle interferometry, Mason et al. (1998) reported the presence of a nearby object at an angular separation of 0.05" on two observations out of four, whilst a two-magnitudes difference compared to the HD 152248 binary was listed by Mason et al. (2009). These authors also indicated that the detections were uncertain. The mere existence of this object and its physical association with HD 152248 are thus unclear and require confirmation. Guessing a distance of 100 UA between this object and the binary system HD 152248, and assuming these two ones are physically connected, an orbital period of 150 yr was derived by Mason et al. (1998). Scaling this estimate to the *Gaia*-DR2 distance yields a putative period of 115 yr for a circular orbit observed at quadrature.

We hence reassessed the possible presence of a third component in the system by searching for reflex motion of the binary's centre of mass in the radial velocities of the binary system. We used Equation (2.33) and assumed that both stars have the same systemic velocity,

meaning that $\gamma_1 = \gamma_2 \equiv \gamma$, and we obtained the expression

$$RV_1(t) + \frac{m_2}{m_1} RV_2(t) = \left(1 + \frac{m_2}{m_1}\right) \gamma. \tag{2.39}$$

Taking the mass ratio $m_2/m_1 = 1.01$ as derived in Section 2.2.2, we computed the left-hand side of Equation (2.39) for all data. The result is presented in Figure 2.12 as a function of time. The oldest data are plotted in blue, the FEROS data in cyan, and the ESPaDOns data in red. The oldest data display a huge dispersion, even within short observing campaigns of a few days. These short-term variations are difficult to reconcile with a tertiary component as we would rather expect much slower variations for a wide tertiary orbit. The most recent radial velocity values determined through spectral disentangling of the FEROS and ESPaDOns data display a significantly lower dispersion. Considering the FEROS and ESPaDOns data only, we may have the impression of a slow variation that could be characteristic of a highly eccentric tertiary orbit along with more rapid variations at certain epochs that may correspond to periastron passages. This suggests that the orbital period would be of about a decade rather than a century which, in turn, would imply a higher multiplicity system with at least four components (including the astrometric companion of Mason et al. 1998). However, this scenario is highly unlikely. Indeed, large variations between the two

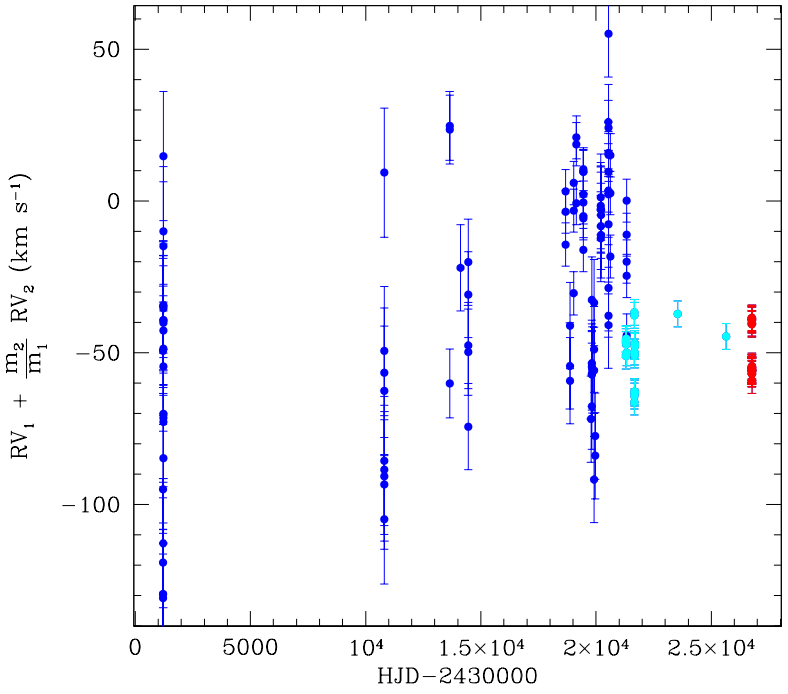

Figure 2.12. Sum of the radial velocity of the primary star and the radial velocity of the secondary star times the mass ratio for all spectroscopic observations of HD 152248 as computed from Equation (2.39). The FEROS data are plotted in cyan, the ESPaDOns data in red, and all other data in blue. Figure taken from Rosu et al. (2020b).

sets of ESPaDOns data taken during two consecutive nights are observed. These fast variations seem inconsistent with a stable hierarchical triple system where the orbital period of the third star should be much longer than that of the inner binary. Therefore, either our estimates of the systemic velocities are biased or the ESPaDOns campaign occurred exactly on the periastron passage of the third component, which seems highly improbable. In addition, the second FEROS campaign reveals another problem with the tertiary orbit interpretation: Large variations occurred on the timescale of the orbital period of the binary. Though, these variations should have been removed in the present analysis. We found that the value of the mass ratio m_2/m_1, that we varied from 0.99 to 1.05, has an effect on the dispersion. However, none of the values in this range allowed us to remove the 5.816-day periodic variations. These variations probably reflect the small shape differences between the radial velocity curves of the primary and secondary stars, which can be seen in Table 2.14 as the differences in e and ω_0. These differences in shape of the radial velocity curve might be due to the various interactions occurring between the stars, such as mutual heating and dynamical tides (see, e.g. Moreno et al. 2005; Palate et al. 2013), as well as due to wind-wind interactions. The presence of a third component in the binary system is therefore impossible to (dis-)confirm from the radial velocity analysis only.

2.2.4. Photometric analysis

This section is devoted to the photometric analysis of the binary system HD 152248. The extensive set of observational photometric data we used is introduced. Light curve analysis by means of the `Nightfall` code is performed to constrain the inclination of the orbit and the Roche lobe filling factors of the stars. The apsidal motion is reviewed in light of this photometric analysis.

2.2.4.1. Observational data

The binary system was observed with the 0.6 m Bochum telescope at La Silla observatory, Chile, between 22 March and 19 April 1997. The Cassegrain focus of the telescope was equipped with an imaging camera featuring a CCD detector with a field of view of 3.2 arcmin $\times$ 4.8 arcmin. Two narrow-band filters designed for the study of Wolf-Rayet stars (Royer et al. 1998) were used. The central wavelength of the He II λ 4686 filter is 4684 Å and its full width at half-maximum (FWHM) is of 30 Å. The c_2 continuum filter has a central wavelength of 6051 Å and a full width at half-maximum of 28 Å. Dome flats were collected each day, and bias exposures were taken at various times over the night. The description of the data reduction can be found in Sana et al. (2005). The root mean square of the differences between the comparison stars ranged between 0.008 and 0.010 mag, and we therefore adopted 0.010 mag as an estimate of the measurement error. Our total dataset consists of hundred and three data measurements in the He II λ 4686 filter and hundred twenty-five data measurements in the c_2 filter (see Tables 2.15 and 2.16, respectively).

We extracted V-band photometry of HD 152248 taken from the All Sky Automated Survey (ASAS-3, Pojmański & Maciejewski 2004) carried out at the Las Campanas Observatory in Chile. The ASAS-3 system consisted of two wide-field ($8.8^\circ \times 8.8^\circ$) telescopes, each equipped with a 200/2.8 Minolta telephoto lens and a 2048 $\times$ 2048 pixels AP-10 CCD camera. These

Table 2.15. Journal of the photometric observations of HD 152248 through the He II λ 4686 filter. Column 1 gives the heliocentric Julian date (HJD) at mid-exposure of the observations. Column 2 provides the differential magnitude Δ mag. Column 3 provides the error in magnitude.

HJD -2 450 000	Δ mag. (mag)	Error (mag)	HJD -2 450 000	Δ mag. (mag)	Error (mag)	HJD -2 450 000	Δ mag. (mag)	Error (mag)
534.8722	0.0008	0.010	544.8465	−0.0285	0.010	551.9173	−0.0102	0.010
535.7976	0.0145	0.010	544.8928	−0.0225	0.010	552.7569	0.0533	0.010
535.8262	0.0208	0.010	544.9202	−0.0215	0.010	552.7614	0.0563	0.010
535.9103	0.0078	0.010	544.9272	−0.0210	0.010	552.8551	0.0755	0.010
537.7754	−0.0087	0.010	545.7744	−0.0227	0.010	552.8782	0.0758	0.010
537.8168	−0.0030	0.010	545.8333	−0.0295	0.010	552.9174	0.0773	0.010
537.8576	0.0098	0.010	545.8758	−0.0145	0.010	553.7500	0.0000	0.010
537.8590	0.0053	0.010	545.9226	−0.0050	0.010	553.7941	0.0065	0.010
538.7595	−0.0095	0.010	546.7415	0.0245	0.010	553.8321	−0.0062	0.010
538.9045	0.0040	0.010	546.7979	0.0355	0.010	553.8729	−0.0082	0.010
539.7730	−0.0155	0.010	546.8556	0.0483	0.010	553.9188	−0.0067	0.010
539.8246	−0.0190	0.010	546.9197	0.0703	0.010	554.7062	−0.0337	0.010
539.8655	0.0133	0.010	547.7870	0.0025	0.010	554.7533	−0.0420	0.010
539.8983	−0.0225	0.010	547.8468	−0.0030	0.010	554.7928	−0.0387	0.010
540.7890	0.0068	0.010	547.8905	−0.0140	0.010	554.8312	−0.0162	0.010
540.8306	0.0083	0.010	548.7645	−0.0247	0.010	554.8680	−0.0285	0.010
540.8815	0.0235	0.010	548.8095	−0.0305	0.010	554.9149	−0.0327	0.010
540.9135	0.0232	0.010	548.8509	−0.0275	0.010	555.7662	0.1950	0.010
540.9217	0.0303	0.010	548.8781	−0.0385	0.010	555.8110	0.1840	0.010
540.9280	0.0283	0.010	548.9168	−0.0335	0.010	555.8573	0.1703	0.010
541.7689	0.0028	0.010	548.9212	−0.0270	0.010	555.9148	0.1195	0.010
541.7931	0.0130	0.010	549.7466	0.1448	0.010	555.9303	0.1160	0.010
541.8423	0.0085	0.010	549.8067	0.1648	0.010	556.7881	−0.0280	0.010
541.8681	0.0070	0.010	549.8637	0.1830	0.010	556.8690	−0.0330	0.010
542.7503	−0.0150	0.010	549.9214	0.1860	0.010	557.7451	0.0043	0.010
542.7888	−0.0180	0.010	550.7748	−0.0362	0.010	557.7899	−0.0035	0.010
542.8183	−0.0090	0.010	550.8190	−0.0230	0.010	557.8334	0.0078	0.010
542.8474	−0.0237	0.010	550.8586	−0.0495	0.010	557.8599	0.0030	0.010
542.8898	−0.0205	0.010	550.8864	−0.0362	0.010	557.9249	0.0015	0.010
543.7516	0.0220	0.010	550.9155	−0.0270	0.010	558.6961	0.0780	0.010
543.8076	0.0430	0.010	550.9208	−0.0072	0.010	558.7425	0.0998	0.010
543.8693	0.0888	0.010	551.7489	−0.0095	0.010	558.7897	0.0903	0.010
543.8947	0.1085	0.010	551.7930	−0.0102	0.010	558.8082	0.0890	0.010
543.9218	0.1173	0.010	551.8052	−0.0102	0.010			
544.7840	−0.0182	0.010	551.8623	−0.0030	0.010			

Table 2.16. Journal of the photometric observations of HD 152248 through the c_2 filter. Column 1 gives the heliocentric Julian date (HJD) at mid-exposure of the observations. Column 2 provides the differential magnitude Δ mag. Column 3 provides the error in magnitude.

HJD -2 450 000	Δ mag. (mag)	Error (mag)	HJD -2 450 000	Δ mag. (mag)	Error (mag)	HJD -2 450 000	Δ mag. (mag)	Error (mag)
530.8192	−0.0063	0.010	540.8314	0.0245	0.010	549.8075	0.1660	0.010
531.8341	−0.0145	0.010	540.8836	0.0052	0.010	549.8645	0.1782	0.010
531.8354	−0.0192	0.010	540.9142	0.0195	0.010	549.9225	0.2165	0.010
533.8033	−0.0152	0.010	540.9223	0.0320	0.010	550.7756	−0.0300	0.010
533.8041	−0.0155	0.010	541.7697	0.0055	0.010	550.8198	−0.0045	0.010
533.8291	−0.0173	0.010	541.7939	0.0050	0.010	550.8872	−0.0195	0.010
533.8299	−0.0085	0.010	541.8431	0.0072	0.010	551.7497	0.0040	0.010
533.8307	−0.0135	0.010	541.8689	−0.0023	0.010	551.7937	0.0000	0.010
533.8571	−0.0120	0.010	541.8974	0.0072	0.010	551.8631	0.0010	0.010
533.8579	−0.0135	0.010	542.7511	−0.0155	0.010	552.7605	0.0590	0.010
533.8587	−0.0168	0.010	542.7896	−0.0162	0.010	552.8081	0.0673	0.010
533.8823	−0.0122	0.010	542.8482	−0.0140	0.010	552.8566	0.0750	0.010
533.8831	−0.0090	0.010	542.8906	−0.0125	0.010	552.8789	0.0772	0.010
533.8839	−0.0128	0.010	543.7525	0.0145	0.010	552.8798	0.0755	0.010
533.9053	−0.0140	0.010	543.8084	0.0412	0.010	552.9189	0.0800	0.010
533.9063	−0.0128	0.010	543.8701	0.0862	0.010	553.7507	0.0005	0.010
533.9270	−0.0023	0.010	543.8955	0.1075	0.010	553.7947	0.0050	0.010
533.9278	−0.0017	0.010	543.9226	0.1202	0.010	553.8328	0.0008	0.010
533.9286	−0.0115	0.010	544.7848	−0.0128	0.010	553.8736	−0.0135	0.010
533.9294	−0.0088	0.010	544.8936	−0.0210	0.010	554.7069	−0.0340	0.010
533.9302	−0.0072	0.010	544.9210	−0.0238	0.010	554.7540	−0.0402	0.010
534.7974	−0.0068	0.010	544.9281	0.0015	0.010	554.7937	−0.0417	0.010
534.8227	−0.0060	0.010	545.7752	−0.0230	0.010	554.8319	−0.0115	0.010
534.8456	−0.0042	0.010	545.8341	−0.0137	0.010	554.8686	−0.0278	0.010
534.8730	−0.0042	0.010	545.8766	−0.0057	0.010	554.9156	−0.0312	0.010
534.8976	0.0012	0.010	545.9234	−0.0112	0.010	555.7669	0.1935	0.010
535.7984	0.0245	0.010	546.7423	0.0255	0.010	555.8117	0.1845	0.010
535.8270	0.0242	0.010	546.7987	0.0440	0.010	555.8581	0.1635	0.010
535.8678	0.0217	0.010	546.8564	0.0537	0.010	555.9156	0.1178	0.010
535.9111	0.0185	0.010	546.9205	0.0745	0.010	555.9311	0.1230	0.010
537.7762	0.0020	0.010	547.7881	0.0042	0.010	556.7887	0.0032	0.010
537.8176	0.0045	0.010	547.8476	0.0010	0.010	556.8698	−0.0250	0.010
537.9021	0.0250	0.010	547.8913	−0.0045	0.010	557.7458	0.0175	0.010
538.7603	−0.0065	0.010	547.9250	0.0023	0.010	557.7907	0.0110	0.010
538.8030	−0.0032	0.010	548.7674	−0.0213	0.010	557.8342	0.0135	0.010
538.8623	−0.0115	0.010	548.8105	−0.0322	0.010	557.8607	0.0055	0.010
538.9053	0.0027	0.010	548.8519	−0.0300	0.010	557.9094	0.0060	0.010
539.7738	−0.0090	0.010	548.8789	−0.0345	0.010	557.9257	0.0122	0.010
539.8254	−0.0020	0.010	548.9179	−0.0268	0.010	558.6969	0.0873	0.010
539.8663	0.0328	0.010	548.9200	−0.0280	0.010	558.7433	0.0902	0.010
539.8991	−0.0125	0.010	548.9223	−0.0245	0.010	558.7910	0.0990	0.010
540.7898	0.0128	0.010	549.7474	0.1405	0.010			

instruments were complemented by a narrow-field ($2.2° \times 2.2°$) 25 cm Cassegrain telescope equipped with the same type of CCD camera. The ASAS-3 photometric catalogue provides magnitude measurements performed with five different apertures varying in diameter from 2 to 6 pixels. Substantial differences between large- and small-aperture magnitudes indicate either contamination by close neighbours, in which case large apertures should be avoided, or saturation. The ASAS-3 data are not uniform in terms of exposure time and thus in terms of saturation limit, as the exposure time was changed in the course of the project from 180 seconds (saturation near $V \sim 7.5$) to 60 seconds (saturation around $V \sim 6$). The saturation limit also depends on the quality of the focus and the zenith distance. The ASAS-3 catalogue lists a grade for each epoch at which the star was observed. However, this grade is calculated for the frame as a whole, not for a specific object inside the field of view. Hence, a frame can have grade A, but still contain stars that are saturated. The whole ASAS-3 photometry is presented in the top panel of Figure 2.13. The bottom panel of Figure 2.13 shows one light curve for the data between HJD 2 453 391 and HJD 2 453 662 put in phase using the orbital period given in the last column of Table 2.14. Saturation problems are clearly apparent before HJD 2 453 000, dates which correspond to the exposure time of 180 seconds. After this date, when the exposure time drops to 60 seconds, the situation improves but the dispersion of the data points remains quite important with some deviant points (see for instance the data points around phases 0.25-0.32 and 0.90-0.95 in the bottom panel of Figure 2.13).

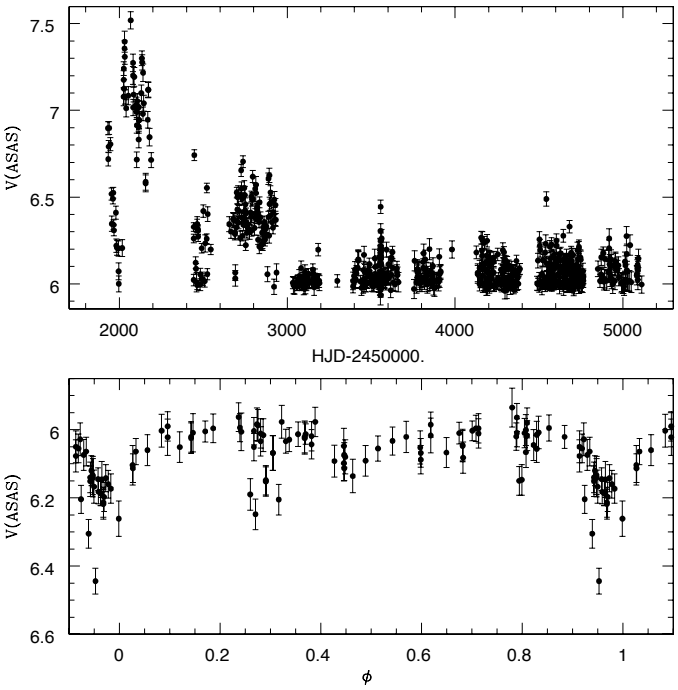

Figure 2.13. *Upper panel:* Whole ASAS-3 photometry of HD 152248. *Bottom panel:* ASAS-3 light curve of HD 152248 for the data between HJD 2 453 391 and HJD 2 453 662 put in phase using the orbital period given in the last column of Table 2.14.

More recently, NASA's Transiting Exoplanet Survey Satellite (TESS, Ricker et al. 2015) observed the binary HD 152248. The instrument onboard TESS has a bandpass ranging from 6000 Å to 1 μm and is centred on the Cousins I-band with central wavelength 786.5 nm (Ricker et al. 2015). The CCD detectors have 15×15 μm pixels sizes. This corresponds to 21" on the sky, thereby undersampling the instrument point spread function (PSF). HD 152248 saturates the central pixel, but the excess charges created are spread into adjacent pixels through the blooming effect, which allows us to recover the photometry. The TESS pipeline (Jenkins et al. 2016) is based on the *Kepler* pipeline (Jenkins et al. 2010). We extracted simple background-corrected aperture photometry (SAP). We removed signatures in the light curve that correlate with systematic spacecraft or instrument effects, and obtained so-called PDC photometry. We extracted the TESS light curve of HD 152248 corrected in this way and kept data points having a quality flag equal to 0 only. We ended up with a time series of 12 372 measurements with a nominal time step of 2 minutes. These data range from HJD 2 458 629.86 to 2 458 639.00 (6372 data points) and from HJD 2 458 644.44 to 2 458 652.90 (6000 data points). The pipeline-processed TESS light curve displays a number of artefacts that have amplitudes well beyond the theoretical photometric accuracy (which should be about 0.0002 mag). It is most probably due to the severe crowding in the NGC 6231 cluster and to the complicated pattern produced by saturated targets.

2.2.4.2. Light curve analysis

We analysed the light curves of HD 152248 by means of the `Nightfall` code version 1.86 (see Section 2.1.9 for detailed explanations about the code). We set the mass ratio q to 1.0 and the eccentricity e to 0.134 as derived from the radial velocity analysis (see Section 2.2.2). The stellar effective temperatures of both stars were fixed to 34 000 K as derived from the `CMFGEN` analysis (see Section 2.2.1.5). We adopted a quadratic limb-darkening law. Reflection effects were accounted for by considering the mutual irradiation of all pairs of surface elements of the two stars (Hendry 1992). Leaving the Roche lobe filling factors of the primary and secondary stars, $f_{\rm P}$ and $f_{\rm S}$, unconstrained yielded solutions that were often at odds with the spectroscopic brightness ratio of 1.0. Therefore, we enforced that $f_{\rm P} = f_{\rm S}$. We searched for the values of ω, i, and $f_{\rm P} = f_{\rm S}$ that yielded the best fit to the observed light curves. We stress that the light curves of HD 152248 display minima of unequal depths. This difference in depth does not arise from a difference in surface brightness of the two stars, but rather arises from the fact that the orbit is eccentric and that ω was close to 90° at the time of the photometric campaigns (see Section 1.2.2.5 for a discussion of this effect).

Since, as indicated by Sana et al. (2001), the He II λ 4686 line filter could be affected by phase-dependent emission from the interaction zone of the stellar winds, we decided to first focus on the c_2 light curve. Among all existing light curves of HD 152248 at the time of writing, the c_2 light curve provides the best coverage of the orbital cycle at a specific epoch. The best-fit parameters of the c_2-band light curve are listed in Table 2.17 while the best fit is illustrated in Figure 2.14. $T_{\rm prim.\ ecl.}$ stands for the time of primary eclipse. It is worth noting that the He II λ 4686 light curve is in excellent agreement with the best-fit c_2-band light curve, and does not reveal any strange behaviour due to the phase-dependent He II λ 4686 emission. The dispersion of the data points about the theoretical

Table 2.17. Parameters of the best-fit `Nightfall` model for the c_2 light curve of HD 152248.

Parameter	Value
$T_{\rm eff,1} = T_{\rm eff,2}$ (K)	34 000 (fixed)
e	0.134 (fixed)
$f_{\rm P} = f_{\rm S}$	$0.86^{+0.03}_{-0.02}$
i (°)	$68.6^{+0.2}_{-0.3}$
ω (°)	$84.7^{+2.4}_{-2.7}$
$T_{\rm prim.\ ecl.}$ (HJD - 2 450 000)	549.92
χ^2_ν	1.395

light curve exceeds the formal photometric errors. Mayer et al. (2008) made the same observation for their photometric data, indicating that the additional variability might not be of instrumental origin but is most probably intrinsic to the stars that make up the binary system. This is a relatively common situation for light curves of massive stars, which frequently display low-level intrinsic photometric variations (see, e.g. the red noise variability of the O-star binary HD 149404, Rauw et al. 2019).

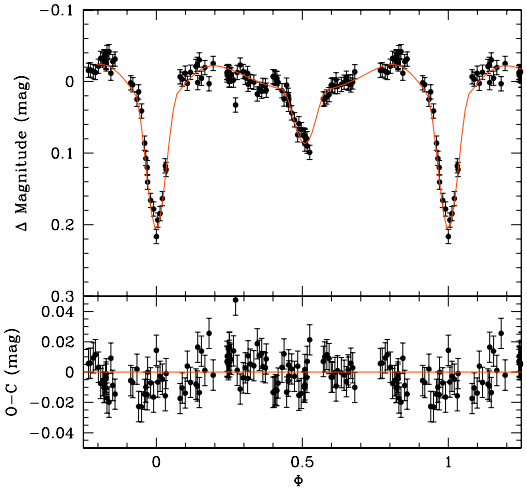

Figure 2.14. Best-fit `Nightfall` solution of the c_2 light curve of HD 152248. The lower panel shows the residuals over the best-fit solution. Figure taken from Rosu et al. (2020b).

Regarding the TESS photometry, we noted several problems with both the SAP and the PDC corrected light curve. By comparing the SAP light curve to our model of the c_2 light curve, we observed discontinuities (shifts in the zero point) in the SAP data and different observations of the secondary minimum disagree about their depth and exact phase. Compared to SAP data, the discontinuities disappear in the PDC corrected data but the problems with the secondary minimum remain and, to some extent, get even worse. Another surprising feature appears in the PDC light curve compared to the SAP light curve: Whilst

the flux in the SAP light curve increases slowly from phase 0.50 to phase 0.75 – which is what we would expect from our model –, the PDC light curve displays a bump near phase 0.60, followed by a dip around phase 0.70. All these differences are much larger than the nominal error bars on the data points. Altogether, it prevents us from deriving any independent photometric solution from this dataset.

2.2.4.3. Apsidal motion

As already mentioned in Section 1.2.3, since the total time span over which the photometric data were collected ($\sim$ 27 years) is much shorter than the time span covered by the radial velocities data (67 years), an accurate determination of the apsidal motion rate based on photometric observations only is trickier to achieve. Nonetheless, the photometric data are used to perform a consistency check of the apsidal motion determined in Section 2.2.2. To do so, we followed two different avenues.

As a first step, from the UBV photometry of Mayer et al. (2008), we built three well-sampled light curves collected over a duration shorter than a month, obtained in March 1992, June 1993, and April-May 2004. The remaining data of their sample form subsamples that are too scarce to derive meaningful constraints on ω for a given individual epoch. We fitted the light curves from the three epochs with `Nightfall` setting the Roche-lobe filling factors, the inclination, and the eccentricity to the best-fit values of the c_2 light curve (see Table 2.17), and keeping ω as the only free parameter. The values of ω obtained this way are listed in Table 2.18, together with the value inferred for the c_2 light curve.

We proceeded similarly for the TESS data: We adjusted ω either on the two time intervals of the TESS data separately or combining them into a single dataset, and derived a best-fit value of 128.7 ± 0.9 (see Table 2.18).

Table 2.18. Best-fit values of ω from the photometry of HD 152248. The first three lines correspond to the fits of the UBV photometry from Mayer et al. (2008), the fourth line corresponds to the fit of the c_2 light curve, lines 5 to 7 correspond to the ASAS-3 photometry, and the last line corresponds to the TESS photometry. N is the number of photometric data points and Δt is the duration of the observing campaign.

Epoch HJD-2 440 000	N	Δt (d)	Filter	ω (°)
8686.5	234	9.05	UBV	70.4 ± 1.2
9157.0	246	9.92	UBV	83.6 ± 1.2
13123.5	220	11.20	UBV	102.3 ± 2.1
10 545.0	125	27.97	c_2	$84.7^{+2.4}_{-2.7}$
13 112.0	39	158	ASAS-3	91.8 ± 7.8
13 526.5	109	271	ASAS-3	98.4 ± 7.4
13 868.0	52	226	ASAS-3	107.5 ± 9.5
18 641.4	12 372	23.04	TESS	128.7 ± 0.9

Finally, we proceeded in the same manner for the ASAS-3 photometry. We fitted the data of the first three observation epochs after HJD 2 453 000. The first epoch – thirty-nine points between HJD 2 453 033 and HJD 2 453 191 – yields $\omega = (91.8 \pm 7.8)°$. However, the primary is not well-constrained as only one point is situated close to the primary minimum. The second epoch – hundred and nine points between HJD 2 453 391 and HJD 2 453 662 – yields $\omega = (98.4 \pm 7.4)°$. The third epoch – fifty-two points between HJD 2 453 755 and HJD 2 453 981 – yields $\omega = (107.5 \pm 9.5)°$. These results are reported in Table 2.18. The large error bars mostly reflect the impact of deviant points. The most probable explanation is that ASAS-3 is affected by saturation and/or blends with stars close to HD 152248, which is highly plausible since NGC 6231 is a dense cluster. In addition, the secondary eclipse is drown in a bunch of points, and hence, when the period is changed, is the bunch of points as well, and we go from one local minimum to another one (see Figure 2.13).

The variation of ω with time is illustrated in Figure 2.15. The overall trend of the photometric data agrees with the result inferred from the global fit of the radial velocity data. However, the photometric values show some dispersion compared to the relation derived from the radial velocity data. This dispersion could partially result from the intrinsic photometric variability of the stars, but the position of the UBV photometry at epoch 2 449 157.0 HJD seems difficult to reconcile with a linear relation for the apsidal motion, even when we

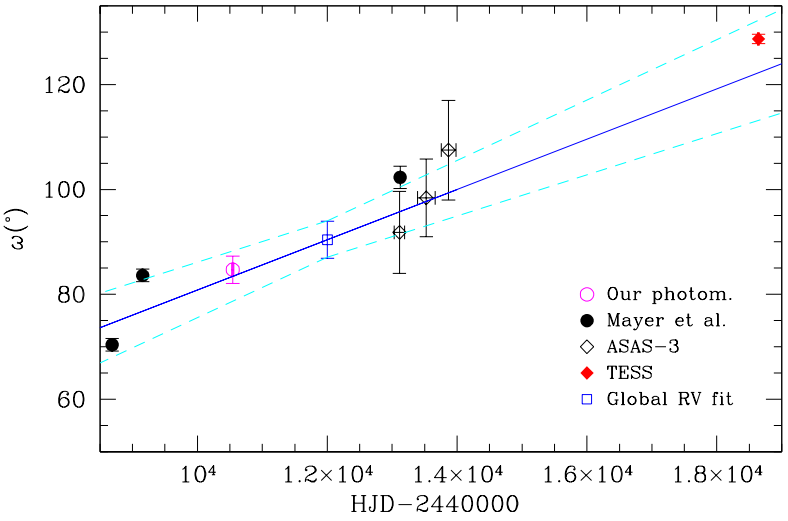

Figure 2.15. Values of ω as a function of time inferred from the photometric light curves and the radial velocities of HD 152248. The black filled dots correspond to the data of the fits of the UBV photometry from Mayer et al. (2008, the first three lines in Table 2.18), the pink open dot corresponds to the fit of the c_2 light curve (the fourth line in Table 2.18), the black open squares correspond to ASAS-3 data (lines 5 to 7 in Table 2.18), the red filled square corresponds to the data of the fit of the TESS photometry (last line in Table 2.18), and the blue open square indicates the ω_0 value obtained from the global fit of all radial velocities data (see Table 2.14). The solid blue line corresponds to our best-fit value of $\dot{\omega}$ from the equivalent radial velocities and the dashed cyan lines correspond to the range of values according to the $1\,\sigma$ uncertainties on ω_0 and $\dot{\omega}$ (see Table 2.14).

account for intrinsic photometric variations. Despite, the ω value inferred from the TESS photometry is consistent with the rate of apsidal motion determined from the radial velocity data, which lends further support to our result.

The observed variations might also be attributed to intrinsic periodic variations of the binary system. This is supported by the fact that many parameters of the orbit vary periodically. However, the apsidal motion is a secular motion and, if such a periodic variation of ω exists, this would be of small amplitude. To verify this assertion, we derived the value of ω for each spectroscopic set of radial velocities (see Section 2.2.2). As Figure 2.16 indicates, there is no evident oscillations of ω with time; only variations compatible with the error bars are seen (at least for the spectroscopic data points).

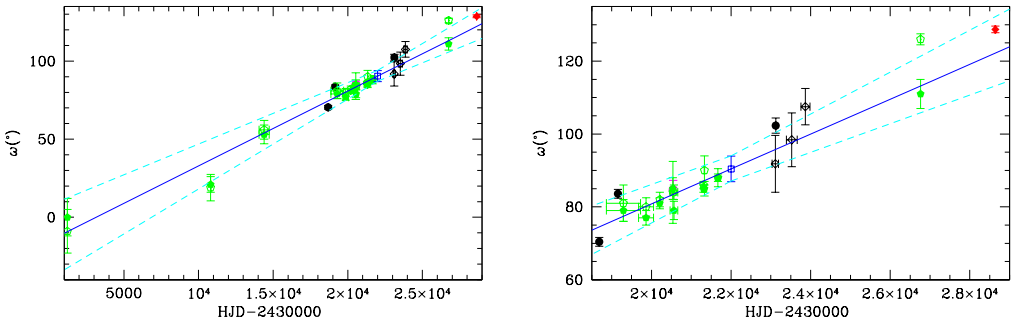

Figure 2.16. Values of ω as a function of time inferred from the photometric light curves and the radial velocities of HD 152248. The green filled and open pentagons represent the spectroscopic values inferred from the primary and secondary stars, respectively. The other symbols have the same meaning as in Figure 2.15.

As a second step, we used a maximum of the photometric data available at the time of writing, spanning as long a total duration as possible. We selected the V-band and Strömgren y data from Mayer et al. (2008). This choice is motivated by the fact that these filters are the closest in wavelength to the c_2 filter and thus have similar morphologies. Combining these two sets with the c_2-band data, we ended up with 517 measurements that are (highly) unequally spread over 14.26 years. We did not take the TESS data into account in this analysis due to the above-mentioned artefacts and to their large number, because they would clearly dominate all other datasets.

We set the Roche-lobe filling factors and the orbital inclination to the values found from the c_2 light curve (see Table 2.17) and the eccentricity to the value found from the equivalent radial velocities (see Table 2.14). We computed a grid of synthetic light curves for different values of ω, covering the full range of possible values given the domain of ω_0 and $\dot{\omega}$ to explore. We computed the χ^2 between observed and expected magnitudes for all times of observation and for a set of four parameters ($P_{\rm orb}$, T_0, ω_0, and $\dot{\omega}$). As pointed out by Schmitt et al. (2016), due to the presence of the apsidal motion, the instantaneous period $P_{\rm ecl}$, that is to say, the time interval between two primary eclipses, is not equal to the anomalistic period $P_{\rm orb}$, but amounts to

$$P_{\rm ecl} = \left[1 - \frac{(1-e^2)^{3/2}}{(1+e\,\sin\omega)^2}\,\frac{\dot{\omega}\,P_{\rm orb}}{2\,\pi}\right] P_{\rm orb}. \tag{2.40}$$

We applied this correction to the calculation of the orbital phases from the times of the individual photometric data points.

The best-fit value of $\dot{\omega}$ amounts to only $0.85° \, \mathrm{yr}^{-1}$. The results are illustrated in Figure 2.17. As expected from the dispersion of photometrically-inferred ω values (see Figure 2.15), the results are much less clear than those inferred from the radial velocity analysis. Indeed, applying this method to the restricted set of 392 data points from Mayer et al. (2008) yields very different results: the best-fit $\dot{\omega}$ amounts to $2.23° \, \mathrm{yr}^{-1}$. Although the analysis of the individual photometric datasets reveals that ω changes from epoch to epoch, the currently available photometric data of HD 152248 do not allow us to independently establish a reliable rate of apsidal motion.

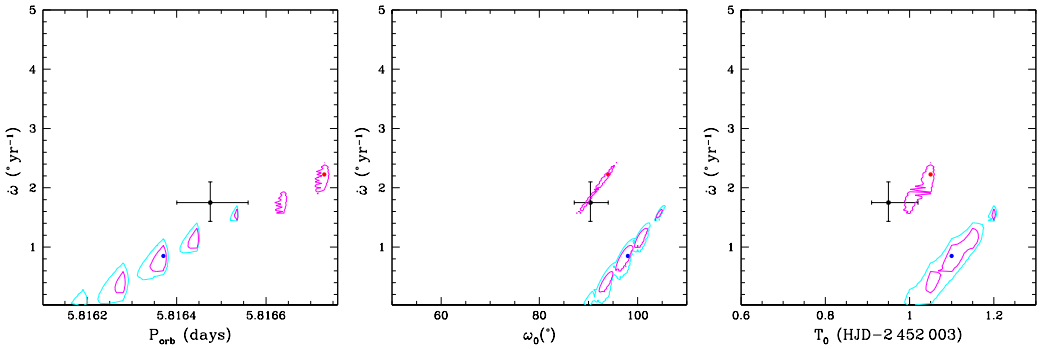

Figure 2.17. Contours of χ^2 of the overall fits of the photometric data of HD 152248. The blue and red dots correspond to the best fits for the entire set of V, y, and c_2-band data, and to the V and y data alone, respectively. The cyan and magenta contours provide the corresponding confidence levels for the full dataset and for the sole V and y data, respectively. The open square with error bars corresponds to our best-fit result of the equivalent radial velocity data. Figure taken from Rosu et al. (2020b).

2.2.5. Complete PHOEBE binary model

The radial velocity analysis (see Section 2.2.2) and the light curve analysis (see Section 2.2.4) were made independently, with each dataset being analysed with its own value of ω (see Figures 2.15, 2.16, and 2.17). This did not enforce any consistent linear rate of change in ω between the different datasets. In order to overcome this limitation and to enforce a consistent linear rate of apsidal motion between the different datasets, we constructed a comprehensive model from these independent analyses in PHOEBE 2 (version 2.2.0, see detailed explanations of the code in Section 2.1.10, Prša et al. 2016a; Jones et al. 2020). Robust posteriors using the Markov Chain Monte Carlo package, emcee (Foreman-Mackey et al. 2013), were determined on both the photometry and radial velocity data simultaneously.

We used blackbody atmospheres along with the Johnson passband set (V for the c_2 light curve, B for He II λ 4686, and respective bands for all Mayer et al. (2008) archival datasets) instead of the supported Castelli-Kurucz (Castelli & Kurucz 2004) grids within PHOEBE 2 because both stars lie well outside these grids. Regarding the limb-darkening model, we

adopted the power model with coefficients from Claret (2000) for both the passband and bolometric limb-darkening. We assumed that all incident bolometric light is reprocessed through irradiation.

For the `PHOEBE 2` model, the two Bochum light curves, six Mayer et al. (2008) archival light curves, the TESS light curve, and all radial velocities presented in Section 2.2.2 were used. Any systematics from the TESS light curve were removed using `DIPS` (Prša et al. 2019). `DIPS` separates any periodic signal at a given period from all other signals. The orbital period derived in Section 2.2.2 was used to extract the phased periodic signal from TESS. The light curve was then unphased and placed at the mid-time of the TESS observations. In this process, we explicitly assumed that the effects of apsidal motion are negligible during the relatively short few orbital cycles covered by the TESS light curve. We accounted for the apsidal motion between the older light curves and the much more recent TESS light curve, henceforth placing a stronger constraint on $\dot{\omega}$. In order to consistently handle photometric uncertainties during the MCMC analysis, we adopted per-dataset sigmas from the residuals between each individual light curve and the initial model.

The stellar effective temperatures of both stars were fixed to 34 000 K as derived from the `CMFGEN` analysis (Section 2.2.1.5), the mass ratio q was fixed to 1.0, and $a \sin i$ was fixed to the value of $49\,R_\odot$ derived from the radial velocity analysis (see the last column of Table 2.14). Synchronisation between stellar rotation and orbital motion was assumed. For each radial velocity dataset, we used the apparent systemic velocities per-component as determined in Section 2.2.2. We adopted as preliminary values for the time-independent parameters the following values: $P_{\rm orb} = 5.816475\,{\rm d}$ and $e = 0.134$ as derived from the radial velocity analysis (see Table 2.14), equivalent radii $R_{\rm equiv}$ of $14.2\,R_\odot$, $i = 68.6°$, and the time of primary eclipse $t_{0,{\rm supconj}} = 2\,450\,549.92$ as derived from the `Nightfall` analysis (see Section 2.2.4.2). We set $t_0 = 2\,450\,545$, value corresponding to the mid-time of the c_2 light curve. The preliminary value of ω_0 was set to the one determined from the `Nightfall` analysis (see Table 2.17), and the preliminary value of $\dot{\omega}$ was set to the one estimated from the radial velocity analysis (see Section 2.2.2).

We explored the parameter space using seventy-two walkers, with the following seven free parameters: $P_{\rm orb}$, e, i, $R_{\rm equiv}$, $t_{0,{\rm supconj}}$, ω_0, and $\dot{\omega}$. The walkers were initially drawn from a small window around the preliminary values, and wider uninformative priors (i.e. priors constructed when the priors cannot be derived from the available information) were used to discourage any walkers from wandering too far from the solution. We removed a burn-in of 150 iterations, after which the walkers randomly explored the local parameter space of the final solution. The resulting posteriors taken from the $\sim 25\,000$ remaining evaluations of the model are depicted in the corner plot in Figure 2.18. In this manner, all the uncertainties in correlated parameters are taken into account, while any uncertainties in fixed or assumed parameters are ignored. The final model and spreads caused by these uncertainties are shown in Figure 2.19 for the c_2 light curve. This shows that there are no significant systematics in the residuals and that the model agrees well with the observations, given the observation and model uncertainties. The linear apsidal motion from these posteriors compared to the independently measured estimates of ω for each independent dataset (see Section 2.2.4.3) is shown in Figure 2.20. The maximum likelihood and 1σ uncertainties adopted from the 68%

confidence intervals were determined from the 1D posteriors using `chainconsumer` (Hinton 2016). The results are given in Table 2.19.

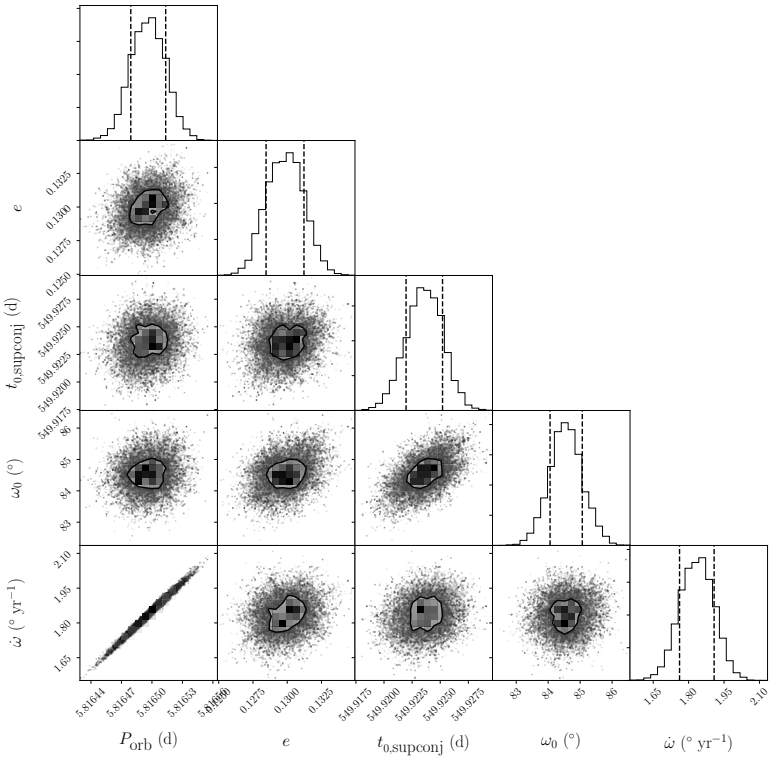

Figure 2.18. Corner plot depicting the posteriors and correlations between parameters in the `PHOEBE 2` analysis of HD 152248 using the MCMC package `emcee` (Foreman-Mackey et al. 2013) and `corner` (Foreman-Mackey 2016). Only parameters related to apsidal motion are shown here. 1σ contours are drawn. See the text for details on all marginalised parameters. Figure taken from Rosu et al. (2020b).

From the inferred best-fit orbital inclination and the minimum semi-major axis and minimum stellar masses inferred from the radial velocity curves (see Section 2.2.2), a semi-major axis a of $53.0^{+0.3}_{-0.2}\,R_\odot$ and individual absolute masses of $29.5^{+0.5}_{-0.4}\,M_\odot$ for both stars are derived. Photometric values of the surface gravities for the primary and secondary stars are derived: $\log g_1 = \log g_2 = 3.55 \pm 0.01$. These values are higher than those derived from spectroscopy (see discussion in Section 2.2.1.5). The photometric radius of $15.07^{+0.08}_{-0.12}\,R_\odot$ agrees with the spectroscopic radius determined with `CMFGEN` (see Section 2.2.1.5). Using the `PHOEBE` radii and the temperatures determined in Section 2.2.1.5, we inferred bolometric luminosities of $(2.73 \pm 0.32) \times 10^5\,L_\odot$ for both stars. These values are slightly higher than those determined from the distance in Section 2.2.1.5, but they still agree within the error bars. Table 2.20 lists the physical parameters expressed in so-called nominal solar units as adopted by the International Astronomical Union (Prša et al. 2016b). We note that the

conventional solar units used throughout this analysis agree with these nominal values. We found slightly bigger stars than Sana et al. (2001), but slightly less massive and smaller stars than Nesslinger et al. (2006) and Mayer et al. (2008), though the values of the parameters overlap within their error bars.

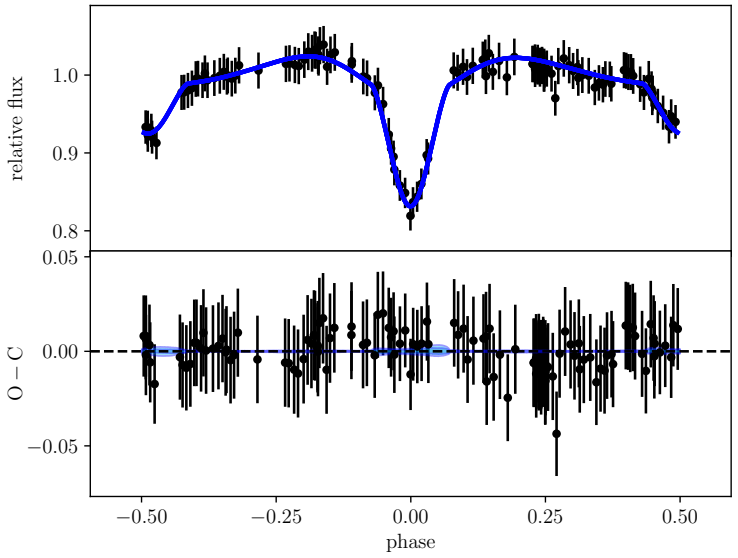

Figure 2.19. Average of 72 samples (the last iteration for each of the walkers) of the synthetic `PHOEBE 2` model for the c_2 light curve of HD 152248. The upper panel shows the light curve computed in time space to account for apsidal motion, but then phase folded on the orbital period (the shift caused by apsidal motion during the few orbital cycles is smaller than the width of the blue line). The lower panel shows the residuals between the observations and the mean of these models. The shaded regions represent the $1\,\sigma$ and $2\,\sigma$ representation of the posteriors in Figure 2.18 as propagated through the model.

Table 2.19. Posteriors for all marginalised parameters from the `PHOEBE 2` analysis of HD 152248 using `emcee`.

Parameter	Posterior
$P_{\rm orb}$ (d)	$5.816498^{+0.000016}_{-0.000018}$
e	$0.130^{+0.002}_{-0.002}$
i (°)	$67.6^{+0.2}_{-0.1}$
$R_{\rm equiv}$ ($R_\odot$)	$15.07^{+0.08}_{-0.12}$
$t_{0,\rm supconj}$ (HJD)	$2\,450\,549.923^{+0.002}_{-0.001}$
ω_0 (°)	$84.5^{+0.5}_{-0.5}$
$\dot{\omega}$ (° yr^{-1})	$1.843^{+0.064}_{-0.083}$

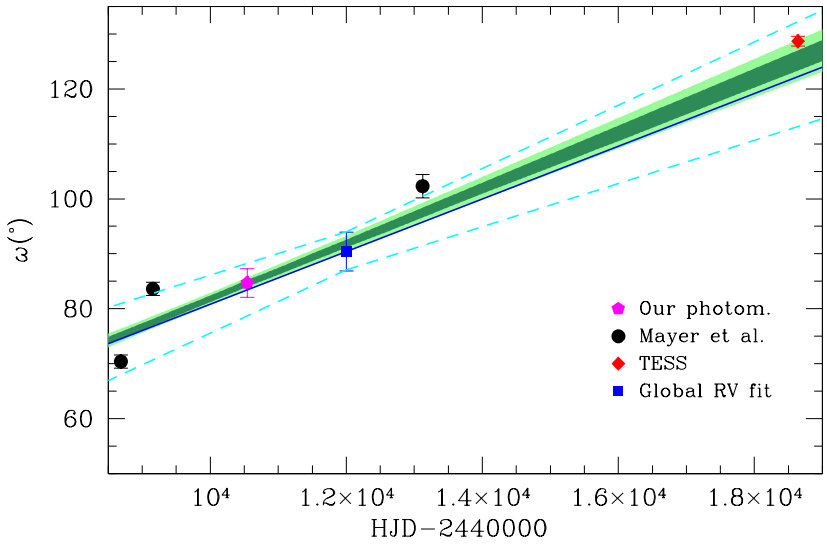

Figure 2.20. Values of ω as a function of time inferred from the photometric light curves and the radial velocities of HD 152248. The black filled dots correspond to the data of the fits of the UBV photometry from Mayer et al. (2008, the first three lines in Table 2.18), the pink filled dot corresponds to the fit of the c_2 light curve (the fourth line in Table 2.18), the red filled square corresponds to the data of the fits of the TESS photometry (last line in Table 2.18), and the blue filled square indicates the ω_0 value obtained from the global fit of all radial velocity data (see Table 2.14). The solid blue line corresponds to our best value of $\dot{\omega}$ from the equivalent radial velocities, and the dashed cyan lines correspond to the range of values according to the $1\,\sigma$ uncertainties on ω_0 and $\dot{\omega}$ (see Table 2.14). In dark green and light green we represent the 1σ and 2σ uncertainties on $\omega(t)$ from the posteriors for ω and $\dot{\omega}$ as shown in Figure 2.18. The `PHOEBE` model is fitted directly to the observations, not to the estimates shown in this figure. Figure taken from Rosu et al. (2020b).

Table 2.20. Physical parameters of the components of HD 152248 as derived from the `PHOEBE` analysis.

Parameter	Value		
	Primary		Secondary
$m_{\rm photo}$ $(\mathcal{M}^{\rm N}_\odot)$	$29.5^{+0.5}_{-0.4}$		$29.5^{+0.5}_{-0.4}$
$R_{\rm equiv}$ $(\mathcal{R}^{\rm N}_\odot)$	$15.07^{+0.08}_{-0.12}$		$15.07^{+0.08}_{-0.12}$
a $(\mathcal{R}^{\rm N}_\odot)$		$53.0^{+0.3}_{-0.2}$	
$\log g_{\rm photo}$ (cgs)	3.55 ± 0.01		3.55 ± 0.01
$L_{\rm bol,photo}$ $(\mathcal{L}^{\rm N}_\odot)$	$(2.73 \pm 0.32) \times 10^5$		$(2.73 \pm 0.32) \times 10^5$

If we further assume that the rotational axes of the stars are orthogonal to the orbital plane, we can combine the best-fit values of the inclination and stellar radii with the projected rotational velocities of the stars determined in Section 2.2.1.4 to derive rotational periods of 5.11 ± 0.15 and 5.14 ± 0.23 days for the primary and secondary stars, respectively. The stars

have their rotation synchronised with each other within the error bars. The ratio between rotational angular velocity and instantaneous orbital angular velocity at periastron amounts to 0.87 ± 0.03 for the primary star and to 0.86 ± 0.04 for the secondary star. We conclude that pseudo-synchronisation is about to be achieved in the system for both stars.

2.2.6. HD 152248 in a nutshell

The most emblematic eclipsing O-star binary in the young open cluster NGC 6231, namely HD 152248, has been completely reanalysed. The individual spectra of the components were reconstructed using our disentangling code. We reassessed the spectral classification of the stars: both stars are of spectral type O7.5 III-II(f). Projected rotational velocities of 138 ± 4 and 137 ± 6 km s^{-1} were derived for the primary and secondary stars, respectively. We analysed these spectra by means of the `CMFGEN` model atmosphere code to determine the stellar and wind properties of the system. Effective temperature of 34 000 ± 1000 K and surface gravity $\log g_{\rm spectro} = 3.48 \pm 0.10$ were derived for both stars. Within the error bars, both stars have a solar oxygen abundance, an enhanced nitrogen abundance compared to solar, and a depleted carbon abundance compared to solar, which is common for evolved O-type stars. These chemical compositions suggest the primary star is the most evolved component of the binary system. A maximum value for the clumped mass-loss rate of $8 \times 10^{-7}\,M_\odot\,{\rm yr}^{-1}$, corresponding to an unclumped mass-loss rate of $2.5 \times 10^{-6}\,M_\odot\,{\rm yr}^{-1}$, was determined for both stars.

The orbital inclination and Roche-lobe filling factors were constrained through the analysis of the light curve by means of the `Nightfall` code. From the `PHOEBE` analysis which simultaneously takes into account radial velocity and photometric data, the inclination of the orbit was refined to a value of $(67.6^{+0.2}_{-0.1})^\circ$. Mean stellar radii of $15.07^{+0.08}_{-0.12}\ \mathcal{R}^{\rm N}_\odot$ and masses of $29.5^{+0.5}_{-0.4}\ \mathcal{M}^{\rm N}_\odot$ were obtained for both stars. We established a rate of apsidal motion of $(1.843^{+0.064}_{-0.083})^\circ\,{\rm yr}^{-1}$, an eccentricity of 0.130 ± 0.002, and an orbital period of $5.816498^{+0.000016}_{-0.000018}$ days.

In contrast to what has been envisaged by some authors (Penny et al. 1999; Sana et al. 2001), there is no reason to consider that the evolutionary states of the components of HD 152248 were influenced by an ongoing or past Roche-lobe overflow episode. The stars are currently far from filling their Roche lobes, even around periastron passage. Moreover, our spectroscopic analysis revealed no indication of a past episode of mass and angular momentum transfer. In contrast to systems that have gone through such a mass exchange episode (e.g. HD 47129, HD 149404, and LSS 3074; Linder et al. 2008; Raucq et al. 2016, 2017), the CNO surface abundances only slightly deviate from solar and are essentially identical in both stars, and there is no strong asynchronism in the rotational velocities of both components.

The twin property of HD 152248 renders the system an interesting target to study tidally-induced apsidal motion from a theoretical point of view. In Chapter 3, we use stellar evolution models to determine theoretical rates of apsidal motion and compare them to the observed rate.

2.3. The slow motion binary: HD 152219

The methodology presented in Chapter 1, Section 1.2.3, highlighted in orange in Figure 1.9, is applied to the binary system HD 152219. The spectroscopic analysis is performed in Section 2.3.1, where the reconstruction of the individual components spectra together with the establishment of their radial velocities are performed by means of a disentangling code. Subsequent analyses of these spectra are carried out to reassess the spectral classification of the stars and to determine their properties as well as their wind characteristics. The rate of apsidal motion is established in Section 2.3.2 based on radial velocity measurements spanning thirty-eight years. The optical photometry is analysed in Section 2.3.3 by means of the `Nightfall` binary star code. The Rossiter-McLaughlin effect is investigated in Section 2.3.4. The main conclusions are drawn in Section 2.3.5. The most important results of this section are presented in Rosu et al. (2022a).

2.3.1. Spectroscopic analysis

This section is devoted to the spectral analysis of the binary system HD 152219. The extensive set of observational spectroscopic data we used is introduced. The spectral disentangling is performed to reconstruct the individual spectra as well as to determine the radial velocities of the stars over the orbital cycle. The spectral classification is reassessed and the projected rotational velocities are derived for both stars. The wind terminal velocity of the primary star is determined. The fundamental properties of the stars and their winds are constrained through the fit of the individual spectra with synthetic `CMFGEN` spectra.

2.3.1.1. Observational data

The set of spectroscopic data of HD 152219 in the optical domain consists of hundred ninety-five high-resolution échelle spectra collected between May 1999 and April 2014. Hundred eighty-five of these were obtained with the FEROS spectrograph while the remaining ten spectra were obtained with the ESPaDOnS spectrograph. We refer to Section 2.2.1.1 for more information about the instrumentations. Exposure times of the FEROS observations range from 228 to 1500 seconds. The FEROS pipeline of the `MIDAS` software was used to reduce the FEROS data. The ESPaDOnS observations all have an exposure time of 840 seconds. The reduced ESPaDOns data were retrieved from the CFHT archive.

The pre-processing of all these observations was performed following the methodology outlined in Section 2.1.1.

2.3.1.2. Spectral disentangling

The spectral disentangling was performed following the methodology outlined in Section 2.1.2. For the cross-correlation, we used `TLUSTY` synthetic spectra having $T_{\rm eff} = 30\,000\,{\rm K}$, $\log g = 3.75$, and $v_{\rm eq} \sin i_{\rm rot} = 160\,{\rm km\,s^{-1}}$ for the primary star and $T_{\rm eff} = 21\,000\,{\rm K}$, $\log g = 4.00$, and $v_{\rm eq} \sin i_{\rm rot} = 160\,{\rm km\,s^{-1}}$ for the secondary star. The initial input values for the radial velocities were estimated using a Gaussian fitting of the He I $\lambda\,4026$ line on spectra taken far from conjunction phases.

In order to avoid biasing the reconstruction of the spectra of the binary components (see discussion in the case of HD 152248 in Section 2.2.1.2), we only considered those ninety-three spectra taken well outside of the photometric eclipses. This is even more critical in the case of HD 152219 since the contribution of the secondary star to the total luminosity of the binary system is low, meaning that during secondary eclipse phases, there is no chance for the disentangling code to associate any line to the secondary star. In the present case, Hα and He II λ 4686 do not appear in emission, and hence, there is no problem of reconstruction of these lines.

The spectral disentangling was performed separately over the following eight wavelength domains: A0 [3800:3920] Å, A1 [3990:4400] Å, A2 [4300:4570] Å, A3 [4570:5040] Å, A4 [5380:5860] Å, A5 [5830:6000] Å, A6 [6400:6750] Å, and A7 [7000:7100] Å. As in the case of HD 152248, the presence of interstellar lines or diffuse interstellar bands close to spectral lines in the spectral domains A0 and A4 affects the quality of the resulting reconstructed spectra. In these cases, the disentangling code erroneously associated some of the line flux of the non-moving interstellar medium to the stars. In addition, not enough spectral lines – especially lines of the secondary star – are present in the A5 and A7 domains. These two situations can affect the determination of the stellar radial velocities. Therefore, we proceeded as follows: We first processed the wavelength domains (A1, A2, A3, and A6) for which the code was able to reproduce the individual spectra and simultaneously estimate the radial velocities of the stars. We present the convergence of the radial velocities as a function of the number of iterations in the A6-domain for the primary and secondary stars in Figure 2.21. The convergence is effectively ensured after sixty iterations. We observed the same trend for the three other wavelength domains.

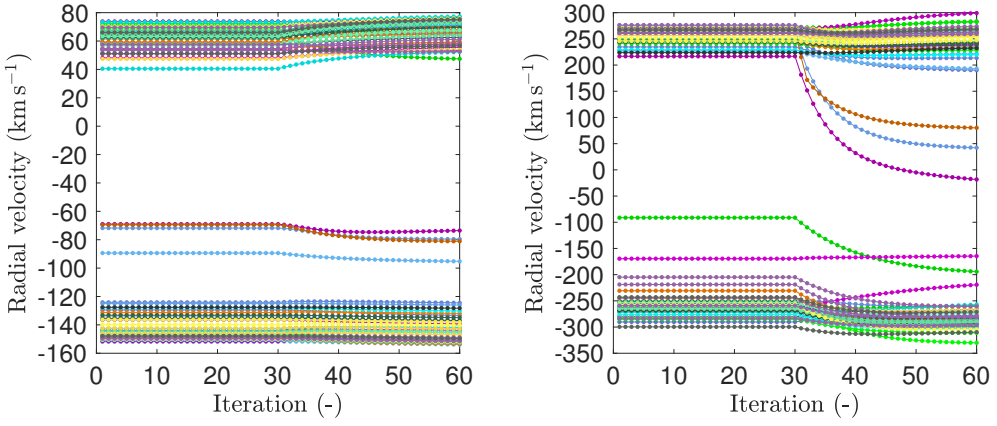

(a) Primary star.

(b) Secondary star.

Figure 2.21. Convergence of the radial velocities as a function of the number of iterations in the disentangling method applied in the A6-domain for (a) the primary star and (b) the secondary star of HD 152219. Each line corresponds to one particular spectrum.

We performed the disentangling again interchanging the roles of the primary and secondary stars (we call it *version 2*, as opposed to *version 1* corresponding to the case where the primary star of the code is also the primary star of the system). The relative error δRV computed with Equation (2.38) is presented for each spectrum, each of the four wavelength domains, and for both stars in Figure 2.22. The maximum relative error is of 0.1 except for seven deviant points for the secondary star, meaning that the robustness of the code is ensured at least for the primary star.

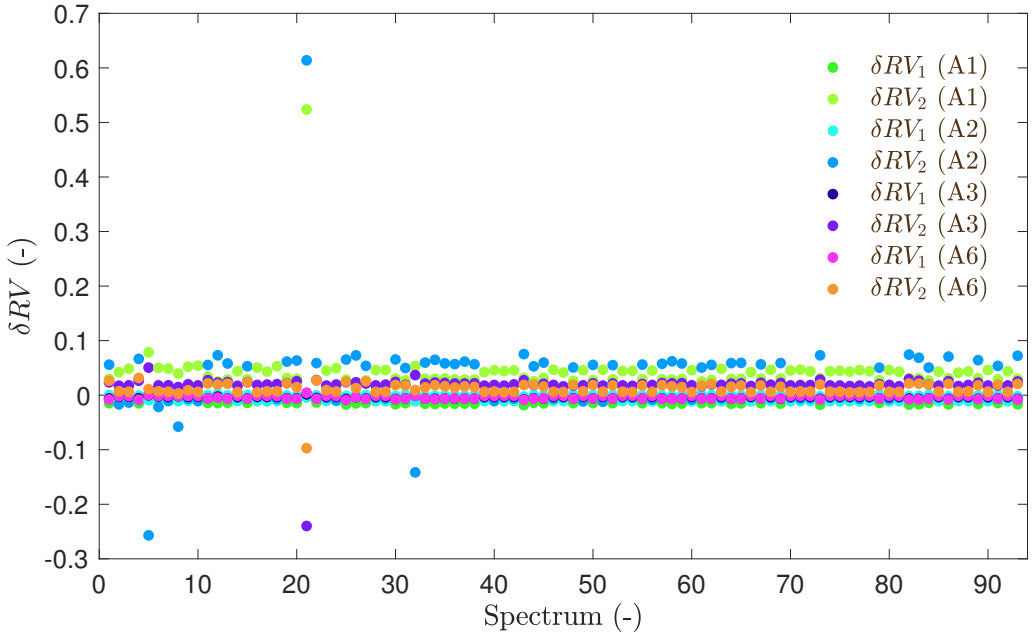

Figure 2.22. Relative error δRV computed with Equation (2.38) for each spectrum, each wavelength domain, and for both stars of HD 152219.

We then computed a weighted-average mean of the stellar radial velocities. The radial velocities from the individual wavelength domains were weighted according to the number of strong primary lines present in these domains (five lines for A1, three for A2, four for A3, and two for A6). The radial velocities obtained for each of these four wavelength domains are presented as a function of the phase in Figure 2.23 together with the mean value over these four domains, for the case where star A of the code is the primary star of the system. The differences in radial velocities mainly come from the fact that the radial velocities are estimated on different lines which form in different layers of the stellar atmosphere, therefore having different velocities. When interchanging the roles of the primary and secondary stars, the values of the wavelength-averaged radial velocities for the primary star differed by about 0 to 1.5 $\mathrm{km\,s^{-1}}$, resulting in a relative error of less than 1%. The difference in wavelength-averaged radial velocities obtained for the secondary star can amount to 20 $\mathrm{km\,s^{-1}}$ at the utmost, giving a relative error of at most 10%. This is acceptable (at least for the primary star) and confirms, again, the robustness of the code. The resulting radial velocities of

both stars are reported in Table 2.21 together with their 1σ errors. We finally performed the disentangling on the remaining four domains (A0, A4, A5, and A7) with the radial velocities fixed to these weighted averages, and, for the A0 and A4 domains only, using the version of the code designed to deal with a third spectral component. For all these domains, we performed the disentangling again interchanging the roles of the primary and secondary stars.

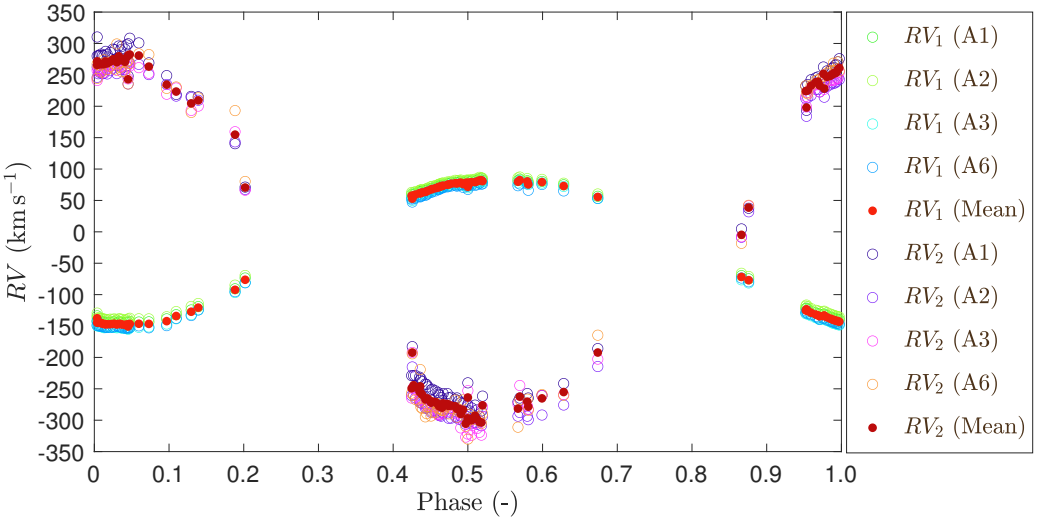

Figure 2.23. Radial velocities of both stars of HD 152219 as a function of the phase obtained for each of the four wavelength domains A1, A2, A3, and A6 and mean value of the radial velocities over these four domains, for *version 1*. The observational phase is computed with the orbital period determined in Section 2.3.2 (see Table 2.27).

2.3.1.3. Spectral classification and absolute magnitudes

The reconstructed spectra of the binary components allowed us to reassess the spectral classification of the stars.

The spectral type of the primary star was determined based on Conti's criterion (Conti & Alschuler 1971) complemented by Mathys (1988, see Table 2.1 in Section 2.1.3). We found that $\log_{10} W'$ amounts to 0.61 ± 0.01, which corresponds to spectral type O9.5. We complemented this criterion with Sota's criteria (Sota et al. 2011, 2014, see Table 2.2 in Section 2.1.3) based of the ratio of the strengths of several lines: The ratio He II λ 4542/He I λ 4388 amounts to 0.67 ± 0.01, the ratio He II λ 4200/He I λ 4144 amounts to 0.88 ± 0.01, and the ratio Si III λ 4552/He II λ 4542 amounts to 0.48 ± 0.01. All three ratios being lower than one, the spectral type O9.7 is clearly excluded and the spectral type O9.5 is confirmed. The criteria of Martins (2018, see Table 2.3 in Section 2.1.3) were further applied: Whilst the ratio of the equivalent widths of He I λ 4144 and He II λ 4200, of 1.03 ± 0.01, suggests an O9.2 spectral type with spectral types O9, O9.5, and O9.7 within the error bars, the ratios of the equivalent widths of He I λ 4388 and He II λ 4542, of 1.81 ± 0.01, and of Si III λ 4552

Table 2.21. Journal of the spectroscopic observations of HD 152219. Column 1 gives the heliocentric Julian date (HJD) of the observations at mid-exposure. Column 2 gives the observational phase ϕ computed with the orbital period determined in Section 2.3.2 (see Table 2.27). Columns 3 and 4 give the radial velocities RV_1 and RV_2 of the primary and secondary stars, respectively, with their 1σ uncertainties. Column 5 provides information about the instrumentation.

HJD $-2\,450\,000$	ϕ	RV_1 (km s^{-1})	RV_2 (km s^{-1})	Instrumentation
1300.802	0.060	-146.7 ± 1.7	277.1 ± 6.4	ESO 1.5 m + FEROS
1304.806	0.004	-137.9 ± 2.0	268.2 ± 12.0	ESO 1.5 m + FEROS
1323.872	0.500	72.1 ± 0.8	-259.7 ± 10.1	ESO 1.5 m + FEROS
1669.881	0.097	-142.5 ± 1.7	231.2 ± 4.7	ESO 1.5 m + FEROS
1671.875	0.567	80.2 ± 1.2	-277.0 ± 5.0	ESO 1.5 m + FEROS
2037.824	0.866	-71.7 ± 1.3	-5.3 ± 3.0	ESO 1.5 m + FEROS
2040.806	0.569	82.8 ± 1.0	-258.2 ± 4.7	ESO 1.5 m + FEROS
2335.774	0.130	-127.5 ± 1.7	202.5 ± 4.1	ESO 1.5 m + FEROS
2335.814	0.139	-121.0 ± 1.2	206.9 ± 2.6	ESO 1.5 m + FEROS
2337.765	0.599	79.6 ± 0.8	-260.8 ± 3.4	ESO 1.5 m + FEROS
2339.774	0.073	-146.9 ± 1.7	260.2 ± 3.8	ESO 1.5 m + FEROS
2381.671	0.953	-123.6 ± 1.3	195.7 ± 3.8	ESO 1.5 m + FEROS
2381.772	0.977	-133.4 ± 1.4	225.3 ± 2.4	ESO 1.5 m + FEROS
2382.668	0.188	-92.5 ± 1.3	154.0 ± 6.3	ESO 1.5 m + FEROS
2383.674	0.426	53.0 ± 1.2	-189.4 ± 3.3	ESO 1.5 m + FEROS
3130.655	0.581	75.9 ± 1.3	-274.0 ± 4.6	ESO 2.2 m + FEROS
3130.856	0.628	73.3 ± 1.2	-250.6 ± 4.4	ESO 2.2 m + FEROS
3131.906	0.876	-77.0 ± 1.3	38.3 ± 1.1	ESO 2.2 m + FEROS
3132.624	0.045	-151.1 ± 1.3	239.7 ± 2.1	ESO 2.2 m + FEROS
3132.897	0.109	-134.4 ± 1.4	220.5 ± 3.2	ESO 2.2 m + FEROS
3134.636	0.520	81.2 ± 0.8	-272.0 ± 4.8	ESO 2.2 m + FEROS
3134.890	0.579	80.7 ± 0.8	-266.3 ± 4.6	ESO 2.2 m + FEROS
3861.670	0.971	-134.8 ± 1.7	230.0 ± 3.4	ESO 2.2 m + FEROS
3861.921	0.030	-147.9 ± 1.5	266.9 ± 4.9	ESO 2.2 m + FEROS
3863.643	0.436	61.9 ± 1.2	-242.0 ± 5.5	ESO 2.2 m + FEROS
3863.886	0.493	76.4 ± 1.0	-279.1 ± 4.6	ESO 2.2 m + FEROS
3864.651	0.674	55.8 ± 0.9	-189.3 ± 4.5	ESO 2.2 m + FEROS
3912.477	0.952	-125.3 ± 1.5	221.6 ± 3.0	ESO 2.2 m + FEROS
3912.488	0.955	-126.5 ± 1.6	222.6 ± 2.6	ESO 2.2 m + FEROS
3912.507	0.959	-129.2 ± 1.4	230.2 ± 2.8	ESO 2.2 m + FEROS
3912.533	0.966	-131.9 ± 1.5	235.5 ± 2.3	ESO 2.2 m + FEROS
3912.546	0.969	-133.3 ± 1.5	236.4 ± 2.5	ESO 2.2 m + FEROS
3912.577	0.976	-134.5 ± 1.5	248.7 ± 3.0	ESO 2.2 m + FEROS
3912.597	0.981	-136.4 ± 1.6	243.9 ± 3.2	ESO 2.2 m + FEROS
3912.615	0.985	-138.5 ± 1.6	245.4 ± 3.0	ESO 2.2 m + FEROS
3912.625	0.987	-139.4 ± 1.6	247.2 ± 3.5	ESO 2.2 m + FEROS
3912.634	0.989	-140.7 ± 1.7	249.4 ± 4.1	ESO 2.2 m + FEROS
3912.643	0.991	-141.3 ± 1.6	249.3 ± 4.0	ESO 2.2 m + FEROS
3912.651	0.993	-142.0 ± 1.6	251.0 ± 3.9	ESO 2.2 m + FEROS
3912.659	0.995	-142.6 ± 1.6	255.6 ± 4.6	ESO 2.2 m + FEROS
3912.667	0.997	-143.3 ± 1.7	257.9 ± 4.2	ESO 2.2 m + FEROS
3912.695	0.004	-145.0 ± 1.6	262.6 ± 4.3	ESO 2.2 m + FEROS

Table 2.21. Continued.

HJD $-2\,450\,000$	ϕ	RV_1 ($\mathrm{km\,s^{-1}}$)	RV_2 ($\mathrm{km\,s^{-1}}$)	Instrumentation
3912.702	0.005	-145.1 ± 1.7	264.3 ± 4.0	ESO 2.2 m + FEROS
3912.710	0.007	-145.3 ± 1.6	264.0 ± 4.0	ESO 2.2 m + FEROS
3912.717	0.009	-145.7 ± 1.6	264.0 ± 4.4	ESO 2.2 m + FEROS
3912.725	0.011	-146.3 ± 1.8	264.0 ± 4.2	ESO 2.2 m + FEROS
3912.734	0.013	-147.3 ± 1.8	263.9 ± 4.5	ESO 2.2 m + FEROS
3912.743	0.015	-147.4 ± 1.7	268.2 ± 4.8	ESO 2.2 m + FEROS
3912.752	0.017	-147.6 ± 1.7	265.1 ± 4.1	ESO 2.2 m + FEROS
3912.769	0.021	-147.4 ± 1.7	267.8 ± 4.1	ESO 2.2 m + FEROS
3912.785	0.025	-146.9 ± 1.7	271.8 ± 4.5	ESO 2.2 m + FEROS
3912.794	0.027	-146.8 ± 1.7	271.2 ± 4.3	ESO 2.2 m + FEROS
3912.818	0.033	-146.8 ± 1.8	276.5 ± 4.5	ESO 2.2 m + FEROS
3912.827	0.035	-147.1 ± 1.7	270.1 ± 4.6	ESO 2.2 m + FEROS
3912.836	0.037	-147.8 ± 1.9	271.2 ± 6.0	ESO 2.2 m + FEROS
3912.853	0.041	-148.5 ± 1.8	267.7 ± 5.8	ESO 2.2 m + FEROS
3912.862	0.043	-148.1 ± 1.9	274.3 ± 5.9	ESO 2.2 m + FEROS
3912.871	0.045	-147.6 ± 1.8	278.1 ± 5.3	ESO 2.2 m + FEROS
3912.880	0.047	-146.9 ± 2.1	279.2 ± 7.7	ESO 2.2 m + FEROS
3913.535	0.202	-76.4 ± 1.5	70.1 ± 1.7	ESO 2.2 m + FEROS
3914.480	0.425	57.9 ± 1.2	-244.8 ± 6.7	ESO 2.2 m + FEROS
3914.491	0.427	58.4 ± 1.0	-239.9 ± 4.9	ESO 2.2 m + FEROS
3914.502	0.430	59.7 ± 1.1	-243.1 ± 5.9	ESO 2.2 m + FEROS
3914.525	0.435	61.8 ± 1.1	-250.3 ± 7.3	ESO 2.2 m + FEROS
3914.533	0.437	62.2 ± 1.0	-252.4 ± 7.2	ESO 2.2 m + FEROS
3914.541	0.439	63.1 ± 1.0	-255.1 ± 6.6	ESO 2.2 m + FEROS
3914.558	0.443	63.8 ± 1.0	-262.6 ± 7.8	ESO 2.2 m + FEROS
3914.565	0.445	65.0 ± 1.0	-261.1 ± 7.1	ESO 2.2 m + FEROS
3914.573	0.447	65.9 ± 0.9	-261.6 ± 6.2	ESO 2.2 m + FEROS
3914.590	0.451	67.8 ± 0.9	-268.0 ± 6.5	ESO 2.2 m + FEROS
3914.597	0.452	68.6 ± 0.9	-266.1 ± 6.3	ESO 2.2 m + FEROS
3914.615	0.457	69.8 ± 0.9	-267.1 ± 5.7	ESO 2.2 m + FEROS
3914.629	0.460	71.1 ± 0.8	-270.0 ± 6.5	ESO 2.2 m + FEROS
3914.633	0.461	71.3 ± 0.8	-272.3 ± 5.9	ESO 2.2 m + FEROS
3914.637	0.462	72.0 ± 0.9	-274.0 ± 6.1	ESO 2.2 m + FEROS
3914.647	0.464	73.1 ± 0.9	-273.2 ± 4.5	ESO 2.2 m + FEROS
3914.653	0.465	73.3 ± 0.8	-275.9 ± 4.2	ESO 2.2 m + FEROS
3914.659	0.467	73.9 ± 0.8	-269.0 ± 5.1	ESO 2.2 m + FEROS
3914.683	0.473	75.3 ± 0.9	-270.0 ± 5.7	ESO 2.2 m + FEROS
3914.690	0.474	75.9 ± 0.7	-273.1 ± 4.5	ESO 2.2 m + FEROS
3914.705	0.478	77.1 ± 0.8	-272.6 ± 4.4	ESO 2.2 m + FEROS
3914.727	0.483	77.8 ± 0.9	-273.5 ± 4.5	ESO 2.2 m + FEROS
3914.737	0.485	77.4 ± 0.9	-277.8 ± 5.6	ESO 2.2 m + FEROS
3914.748	0.488	78.2 ± 0.9	-277.5 ± 4.1	ESO 2.2 m + FEROS
3914.759	0.490	78.7 ± 1.1	-285.9 ± 7.2	ESO 2.2 m + FEROS
3914.787	0.497	78.4 ± 0.9	-301.4 ± 7.3	ESO 2.2 m + FEROS
3914.798	0.500	78.7 ± 1.3	-293.2 ± 8.3	ESO 2.2 m + FEROS

Table 2.21. Continued.

HJD $-2\,450\,000$	ϕ	RV_1 (km s^{-1})	RV_2 (km s^{-1})	Instrumentation
3914.809	0.502	78.6 ± 0.9	-293.7 ± 5.5	ESO 2.2 m + FEROS
3914.820	0.505	79.2 ± 1.1	-296.3 ± 7.7	ESO 2.2 m + FEROS
3914.840	0.510	79.6 ± 1.0	-288.9 ± 5.7	ESO 2.2 m + FEROS
3914.851	0.512	80.7 ± 1.0	-294.1 ± 5.5	ESO 2.2 m + FEROS
3914.865	0.515	82.3 ± 1.2	-298.8 ± 4.9	ESO 2.2 m + FEROS
3914.876	0.518	82.6 ± 1.4	-299.6 ± 6.9	ESO 2.2 m + FEROS

and He II λ 4542, of 0.46 $\pm$ 0.01, both suggest an O9.5 spectral type, with the O9.7 spectral type within the error bars. The luminosity class of the primary star was determined based on Conti's criterion (Conti & Alschuler 1971, see Table 2.4 in Section 2.1.3). We found that $\log_{10} W''$ amounts to 0.21 ± 0.01, which corresponds to the giant luminosity class III. Furthermore, following Gray's digital atlas (Gray 2009), for stars of spectral type O9, if the spectral lines Si IV λ 4116 and He I λ 4121 are weak but of the same order of magnitude, then the luminosity class is III, as it is indeed the case here. The criteria and atlases of Sota et al. (2011, see Table 2.6 in Section 2.1.3), based on the relative strengths of the He I λ 4026 and Si IV λ 4089 lines, and He II λ 4686 and He I λ 4713 lines, suggest a luminosity class between V and III. According to the criteria of Martins (2018, see Table 2.7 in Section 2.1.3) based on the ratios between the equivalent widths of Si IV λ 4089 and He I λ 4026, of 0.50 $\pm$ 0.01, and He II λ 4686 and He I λ 4713, of 1.77 $\pm$ 0.01, the luminosity class is III, excluding both the IV and II luminosity classes.

The spectral classification of the secondary star is more difficult to establish with certainty. The digital atlases of Gray (2009), Walborn & Fitzpatrick (1990), and Liu et al. (2019) were used for this purpose. Inasmuch as He II lines are absent from the spectrum of the secondary star, spectral type O is excluded. We used the ratio between the strengths of the He I λ 4471 and Mg II λ 4481 lines, which qualitatively suggests that the spectral type cannot be later than B2.5. The fact that the Si II $\lambda\lambda$ 4128-32 lines are consistent with noise whilst they should be clearly visible for spectral types later than B2.5 enforces this statement. In addition, the Si IV λ 4089 line is clearly visible but weaker than the Si III λ 4552 line, suggesting a spectral type B1, with an uncertainty of one spectral type. The C III λ 4650, N III λ 4097, and Si IV λ 4116 are present in the spectrum, and hence, spectral types later than B2 are indeed excluded. Regarding the luminosity class, we also used the digital atlas of Gray (2009). The ratio of the strengths of the Si III λ 4552 and He I λ 4387 lines suggests a main-sequence star. As the O II λ 4348 line is not visible, O II λ 4416 is weak, and the Balmer lines are broad, the secondary star should be of luminosity class V. However, using the Walborn atlas (Walborn & Fitzpatrick 1990), the facts that the strengths of the He I λ 4387 and 4471 lines are nearly identical, that the strength of the O II λ 4416 line is much weaker than the strength of the He I λ 4387 line, and that the He I λ 4713 line is stronger than the O II $\lambda\lambda$ 4639-42 doublet and the N II λ 4630 and C III λ 4647 lines, imply that the secondary star should be a B2 III rather than a B1 III. In conclusion, it is quite difficult to distinguish the B1 and B2 spectral types as well as the V and III luminosity classes. Hence, we classify the secondary star as a B1-2 V-III star. We note that this spectral classification agrees with that proposed by Sana et al. (2006).

Notwithstanding, it seems rather unlikely that the primary star is a giant star given the small radius determined in Sana et al. (2006). Indeed, the primary star would most probably appear to be a main-sequence star. Furthermore, the secondary star is of later spectral type than the primary and so, evolves slower. Hence, it is even more unlikely that the secondary star is a giant star if the primary star turns out to be a main-sequence star. Indeed, the surface gravity we measure in spectroscopy is underestimated since the surface gravity determined for a star belonging to a binary system is lower than that of a single star of same mass and radius. Therefore, the stars are more likely main-sequence stars even though the characteristics of their spectra indicate a giant luminosity class.

We estimated the brightness ratio in the visible domain on the basis of the ratio between the EWs of the spectral lines of the primary and secondary stars and TLUSTY synthetic spectra of respective similar effective temperatures. For this purpose, we used the Hβ, He I $\lambda\lambda$ 4026, 4144, 4471, 4922, 5016, 5876, and He II λ 4542 lines for the primary star and the same lines except the He II λ 4542 line for the secondary star. We used TLUSTY spectra of effective temperatures of 30 000 and 32 500 K for the primary star and of 20 000, 21 000, and 22 000 K for the secondary star. These choices of TLUSTY spectra were guided by the effective temperatures reported by Martins et al. (2005) for an O9.5 III star and by Humphreys & McElroy (1984) for B-type stars. Indeed, Martins et al. (2005) indicated an effective temperature of 30 800 K for an O9.5 III star. Humphreys & McElroy (1984) reported the following effective temperatures for spectral types ranging from B1 to B2: $T_{\rm eff,B1V} = 24\,150$ K, $T_{\rm eff,B1.5V} = 21\,800$ K, $T_{\rm eff,B2V} = 19\,700$ K, $T_{\rm eff,B1IV\text{-}III\text{-}II} = 21\,100$ K, $T_{\rm eff,B1.5IV\text{-}III\text{-}II} = 20\,000$ K, and $T_{\rm eff,B2IV\text{-}III\text{-}II} = 18\,000$ K. The ratio of the equivalent widths of the lines between TLUSTY spectra and the stellar spectra are reported in Tables 2.22 and 2.23 for the primary and secondary stars, respectively.

Table 2.22. Equivalent widths of the lines used to determine the brightness ratio in the visible domain of the binary system HD 152219 based on the primary star. Column 1 provides the line used, Column 2 indicates the EWs of the primary spectral lines, and Columns 3 and 4 indicate the ratio between the EWs of TLUSTY spectral lines and the primary spectral lines for TLUSTY spectra of 30 000 and 32 500 K, respectively.

Line	$EW_{primary}$	$\frac{EW_{TLUSTY,\ 30\,000\ K}}{EW_{primary}}$	$\frac{EW_{TLUSTY,\ 32\,500\ K}}{EW_{primary}}$
Hβ	1.93	1.17	1.16
He I λ 4026	0.68	1.12	1.00
He I λ 4144	0.25	1.08	0.66
He I λ 4471	0.85	0.94	0.73
He I λ 4922	0.52	1.15	0.76
He I λ 5016	0.29	0.98	0.87
He I λ 5876	0.99	0.75	0.77
He II λ 4542	0.21	0.88	0.37
Mean	...	1.01 ± 0.15	0.79 ± 0.23

The results obtained for the primary star are not coherent. Indeed, a mean ratio of 0.79 implies that an effective temperature of 32 500 K is likely too high since the He I lines are too weak. However, the TLUSTY spectrum of 30 000 K gives a mean value of 1.01, meaning that in this case, the secondary star would contribute 3% to the total brightness of the

Table 2.23. Equivalent widths of the lines used to determine the brightness ratio in the visible domain of the binary system HD 152219 based on the secondary star. Column 1 provides the line used, Column 2 indicates the EWs of the secondary spectral lines, and Columns 3, 4, and 5 indicate the ratio between the EWs of TLUSTY spectral lines and the secondary spectral lines for TLUSTY spectra of 20 000, 21 000, and 22 000 K, respectively.

Line	$EW_{secondary}$	$\frac{EW_{TLUSTY,\ 20\,000\ K}}{EW_{secondary}}$	$\frac{EW_{TLUSTY,\ 21\,000\ K}}{EW_{secondary}}$	$\frac{EW_{TLUSTY,\ 22\,000\ K}}{EW_{secondary}}$
Hβ	0.32	13.49	13.03	12.43
He I λ 4026	0.11	11.49	11.37	11.06
He I λ 4144	0.07	8.11	7.99	7.71
He I λ 4471	0.10	11.99	11.92	11.63
He I λ 4922	0.11	8.38	8.15	8.04
He I λ 5016	0.02	12.69	12.51	12.01
He I λ 5876	0.06	10.49	10.42	10.27
Mean	...	10.95 ± 2.07	10.77 ± 2.02	10.45 ± 1.89

binary system. Given the strength of the detected signature of the secondary, this is likely too small a contribution. This incoherence might be due to the fact that the primary spectrum is only slightly diluted by the presence of the secondary star, all the more so as the errors coming from the disentangling are of the same order of magnitude as the secondary contribution. In addition, the uncertainties on the brightness ratio determined in this manner are of the order of the contribution of the secondary star. Hence, it is preferable to use the results obtained for the secondary star, especially since the three corresponding TLUSTY models give similar results. As the secondary star is more likely a B1-2 V-III star, we decided to take the TLUSTY spectrum of 21,000 K. Using Equation (2.22), we get a brightness ratio $l_2/l_1 = 0.101 \pm 0.021$. This brightness ratio is applied to the reconstructed spectra of the stars through the relations (2.7) and (2.8) recalled in Section 2.1.2.2.

A parallax of $\varpi = 0.644 \pm 0.084$ mas is quoted by the second *Gaia* data release (DR2, Gaia Collaboration 2018), which corresponds to a distance of 1507^{+231}_{-178} pc (Bailer-Jones et al. 2018). A distance modulus of $10.89^{+0.33}_{-0.26}$ is derived. Mean V and B apparent magnitudes of 7.552 ± 0.013 and 7.705 ± 0.035, respectively, are reported by Sung et al. (1998). Adopting a value of -0.26 ± 0.01 for the intrinsic colour index $(B-V)_0$ of an O9.5 V-III star (Martins & Plez 2006) and assuming the reddening factor in the V-band R_V equal to 3.3 ± 0.1 (Sung et al. 1998), we inferred an absolute magnitude in the V-band $M_V = -4.70^{+0.29}_{-0.36}$ for the binary system. Adopting the brightness ratio in the visible domain inferred previously yields individual absolute magnitudes $M_{V,1} = -4.60^{+0.29}_{-0.36}$ and $M_{V,2} = -2.12^{+0.35}_{-0.41}$ for the primary and secondary stars, respectively. Comparing the magnitude obtained for the primary star to those reported by Martins & Plez (2006) shows that the value inferred for $M_{V,1}$ is between the values of an O9.5 V and an O9.5 III star. As already mentioned in the discussion of the spectral type, this seems to confirm that contrarily to what the spectroscopy suggests, the primary star should be a main-sequence star or a class IV star rather than a giant star. The results hence seem coherent with those of Martins & Plez (2006). When compared to the magnitudes reported by Humphreys & McElroy (1984), the magnitude obtained for the secondary star seems to indicate that the luminosity classes IV and III can clearly be

excluded. The secondary star absolute magnitude is coherent within the error bars with the magnitude obtained for a B2 V star as given by Humphreys & McElroy (1984).

2.3.1.4. Projected rotational velocities

The projected rotational velocities of both stars were derived using the Fourier transform method as explained in Section 2.1.6. We applied this method to twenty well-isolated spectral lines of the primary star which are expected to be free of blends, nine metallic lines and eleven He I lines, and to six well-isolated lines of the secondary star, two metallic lines and four He I lines. The results are presented in Table 2.24, and the Fourier transforms are illustrated in Figure 2.24. The mean $v_{\rm eq} \sin i_{\rm rot}$ computed on metallic lines alone or on all the lines agree very well. We adopted a mean $v_{\rm eq} \sin i_{\rm rot}$ of $166 \pm 10\,{\rm km\,s^{-1}}$ for the primary star and of $95 \pm 9\,{\rm km\,s^{-1}}$ for the secondary star. The value for the primary star agrees within the error bars with the values inferred by Levato & Morrell (1983) and Sana et al. (2006) but is lower than the one quoted by Conti & Ebbets (1977). The value quoted by Conti & Ebbets (1977) was obtained by visual comparison with their standards and the value quoted by Levato & Morrell (1983) was obtained by visual comparison with the standards given by Slettebak et al. (1975). The values of Sana et al. (2006) were estimated through a comparison of the FWHMs measured on the various lines with those measured, for a range of $v_{\rm eq} \sin i_{\rm rot}$, on model spectra of equivalent effective temperature and gravity computed using the codes `TLUSTY` and `SYNSPEC`.

2.3.1.5. Wind terminal velocity

The wind terminal velocity v_∞ of the primary star of HD 152219 was estimated based on the seven high-resolution spectra taken with the SWP camera of the *IUE* satellite that we extracted. The saturated C IV $\lambda\lambda$1548,1551 P-Cygni profile is certainly the most prominent wind feature observed in these spectra. The velocity of the violet edge of zero residual intensity in the absorption trough $v_{\rm black}$ was measured and we derived a value of $1930 \pm 120\,{\rm km\,s^{-1}}$. Indeed, $v_{\rm black}$ is a good indicator of v_∞ for OB stars, as shown by Prinja et al. (1990). The binarity of HD 152219 should be responsible, at least partially, for the dispersion. Indeed, the interaction of the primary wind with either the secondary star or the secondary stellar wind leads to a reduction of the primary wind velocity in some directions and thus at some orbital phases.

2.3.1.6. Model atmosphere fitting

We used the projected rotational velocities determined previously to broaden the `CMFGEN` spectra. The stellar and wind parameters were then adjusted following the procedure outlined by Martins (2011). We proceeded slightly differently for the two stars as they have different spectral types.

Primary star First of all, we adjusted the macroturbulence velocity on the wings of the O III λ5592 and Balmer lines and we derived a value of $v_{\rm macro} = 120 \pm 10\,{\rm km\,s^{-1}}$. We inferred a value of $15 \pm 3\,{\rm km\,s^{-1}}$ for the microturbulence velocity based on the adjustment of the metallic lines.

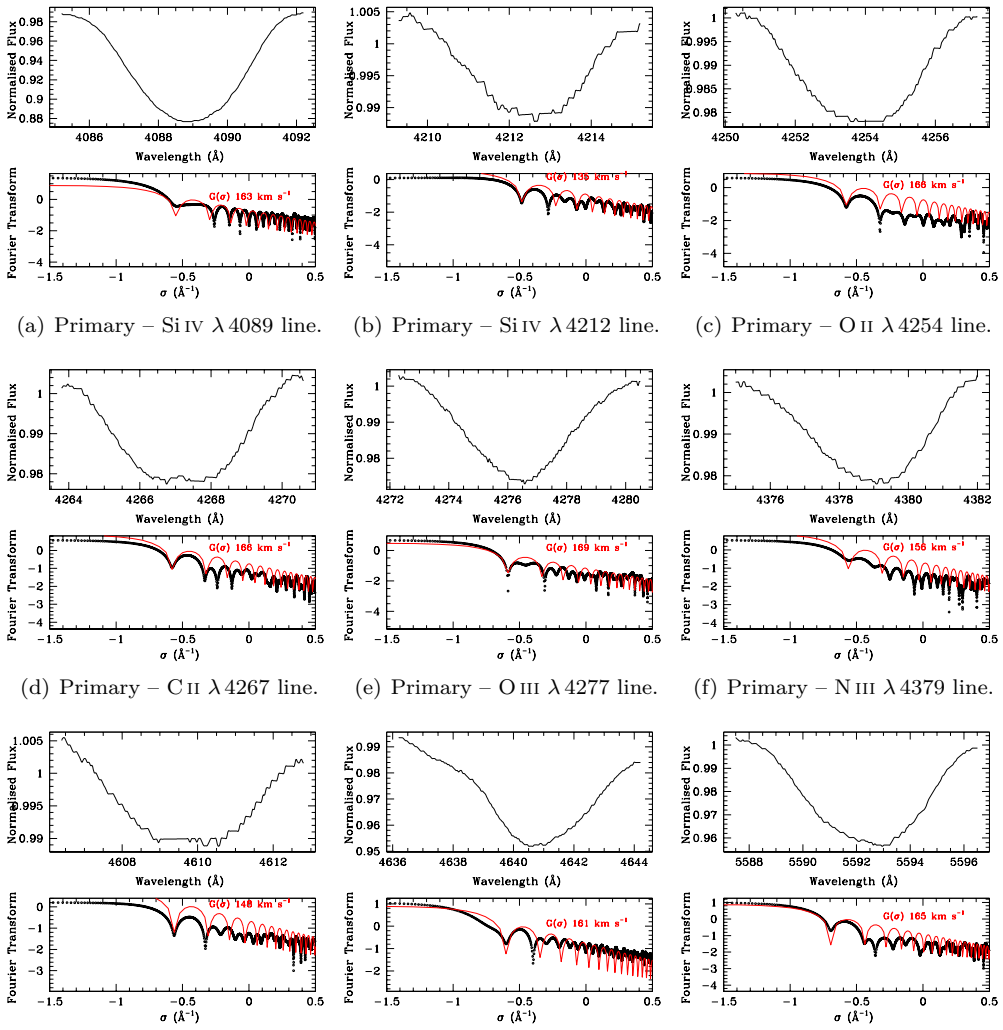

(a) Primary – Si IV λ 4089 line. (b) Primary – Si IV λ 4212 line. (c) Primary – O II λ 4254 line.

(d) Primary – C II λ 4267 line. (e) Primary – O III λ 4277 line. (f) Primary – N III λ 4379 line.

(g) Primary – O II λ 4610 line. (h) Primary – N III λ 4641 line. (i) Primary – O III λ 5592 line.

Figure 2.24. Fourier transforms of line profiles of HD 152219 (panels (a) to (z)). *Top row:* Line profiles of the separated spectra obtained after application of the brightness ratio for the primary and secondary stars. *Bottom row:* Fourier transform of these lines (in black) and best-match rotational profile (in red).

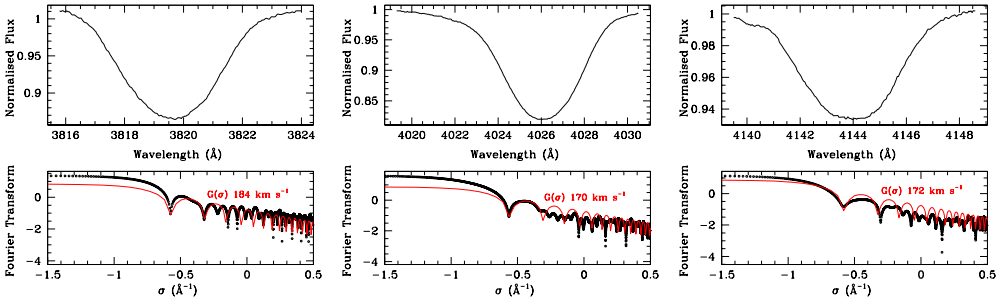

(j) Primary – He I λ 3820 line. (k) Primary – He I λ 4026 line. (l) Primary – He I λ 4144 line.

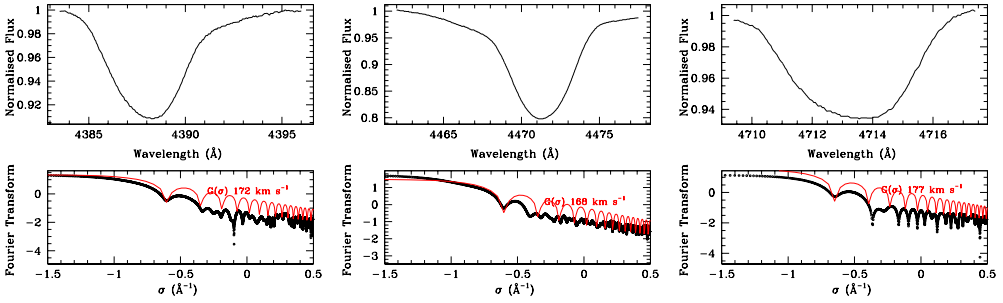

(m) Primary – He I λ 4387 line. (n) Primary – He I λ 4471 line. (o) Primary – He I λ 4713 line.

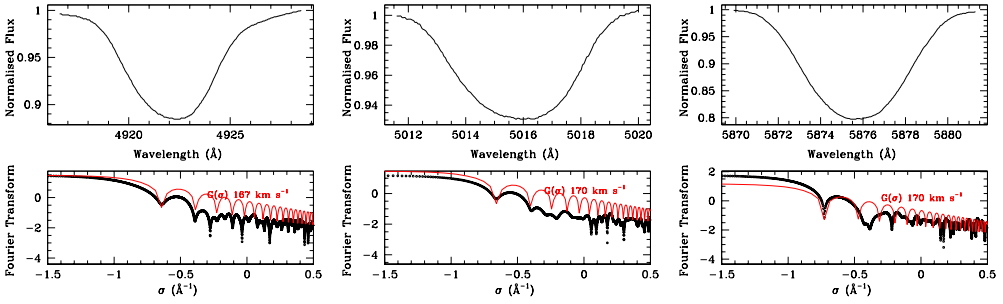

(p) Primary – He I λ 4922 line. (q) Primary – He I λ 5016 line. (r) Primary – He I λ 5876 line.

Figure 2.24. Continued.

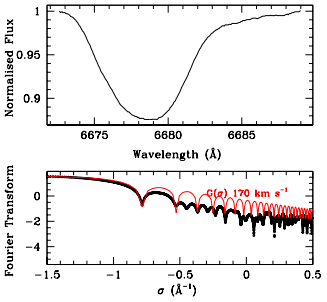

(s) Primary – He I λ 6678 line.

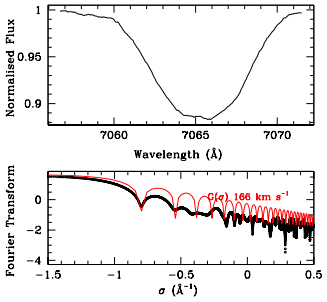

(t) Primary – He I λ 7065 line.

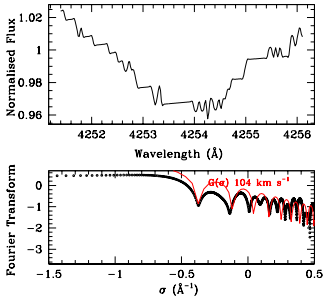

(u) Secondary – O II λ 4254 line.

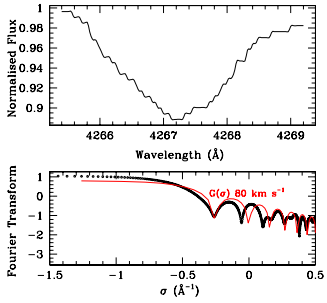

(v) Secondary – C II λ 4267 line.

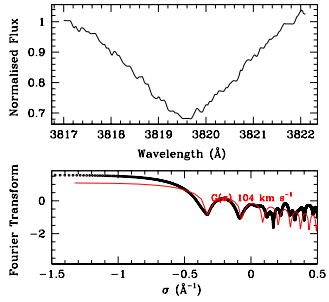

(w) Secondary – He I λ 3820 line.

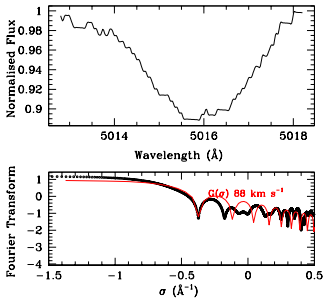

(x) Secondary – He I λ 5016 line.

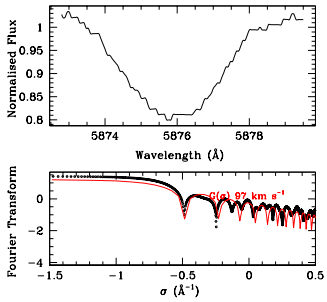

(y) Secondary – He I λ 5876 line.

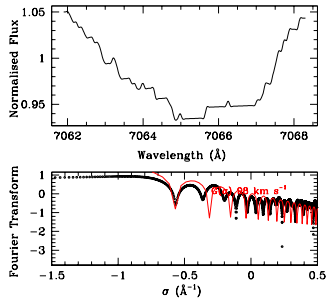

(z) Secondary – He I λ 7065 line.

Figure 2.24. Continued.

Table 2.24. Best-fit projected rotational velocities as derived from the disentangled spectra of HD 152219 and comparison with values coming from the literature.

Line	$v_{\rm eq} \sin i_{\rm rot}$ (km s^{-1})	
	Primary	Secondary
Si IV 4089	163	...
Si IV 4212	135	...
O II 4254	166	104
C II 4267	166	80
O III 4277	169	...
N III 4379	156	...
O II 4610	148	...
N III 4641	161	...
O III 5592	165	...
He I 3820	184	104
He I 4026	170	...
He I 4144	172	...
He I 4387	172	...
He I 4471	168	...
He I 4713	177	...
He I 4922	167	...
He I 5016	170	88
He I 5876	170	97
He I 6678	170	...
He I 7065	166	98
Mean (metallic lines)	159 ± 11	92 ± 17
Mean (He I lines)	171 ± 5	97 ± 7
Mean (all lines)	166 ± 10	95 ± 9
Conti & Ebbets (1977)	250	...
Levato & Morrell (1983)	160	...
Sana et al. (2006)		
He I lines	190 ± 10	...
Si IV 4089	150 ± 10	...
O III 5592	175 ± 10	...
He II 4542	130 ± 10	...
He II 4686	160 ± 10	...

We determined the effective temperature while searching for the overall best fit of the He I and He II lines. The main diagnostic lines are the He I $\lambda\,4471$ and He II $\lambda\,4542$ lines as these lines are usually found in strong absorption for all O spectral types. However, we observed that the strength of the He I $\lambda\,4471$ line was usually underestimated while the other He I lines were well-adjusted. As mentioned by several authors (Voels et al. 1989; Herrero et al. 1992), the He I $\lambda\,4471$ line suffers from dilution effects because this line forms in more external layers of the stellar atmosphere than the other He I lines and is thus more affected by luminosity effects. However, given the luminosity class of the primary star, it seems rather unlikely that the dilution effect is responsible for the observed discrepancy, since this effect is usually noticeable in the case of late supergiant O-type stars (Voels et al. 1989; Herrero et al. 1992). The He II $\lambda\,4542$ line is heavily blended, and hence, cannot

be used here. The He I λ 4121 line is blended with the Si IV λ 4116 line, and hence, difficult to adjust precisely. The He I λ 4144 line is well-isolated but the mechanism of its formation is uncertain and might suffer from the same problem as He I λ 4471. Hence, this line is also discarded for the determination of the effective temperature. The He II λ 5412 line is not a good indicator either as it is affected by the stellar wind (Herrero et al. 1992). The most reliable He I lines are the λ 4026, 4388, 4713, and 4922 lines. However, the He I λ 4713 line is not very sensitive to a small change in effective temperature and cannot be used to fine tune the value of this parameter, whilst the He I λ 4388 line is blended with the N III λ 4379 line. The He I λ 4026 line is blended with He II λ 4026, meaning that a small change in effective temperature does not affect this line, especially since He I λ 4026 reaches its maximum intensity at spectral type O9. Hence, we adjusted the effective temperature on the He I λ 4922 line and inferred a value of $30\,900 \pm 1000$ K. With this effective temperature, the He I $\lambda\lambda$ 4026, 4388, 4713, 4922 lines as well as the He II λ 4200 line are perfectly adjusted, but the He I λ 5876 line is not well-reproduced.

To determine the surface gravity of the primary star, we adjusted the wings of the Balmer lines Hβ, Hγ, Hδ, and H I $\lambda\lambda$ 3835, 3890. We excluded the Balmer line Hε as it is not correctly reproduced by the disentangling code because of the blend with the interstellar Ca II line. We derived a value of $\log g_{\rm spectro} = 3.60 \pm 0.10$.

The surface chemical abundances (in number compared to H) of C, N, and O should be adjusted on corresponding lines, and we decided to set the abundances of the other elements, including He, to solar abundances as taken from Asplund et al. (2009).
The oxygen abundance was determined by adjusting the O III λ 5592 line as this is the only oxygen line not blended with other lines. The best fit is obtained for an abundance O/H of $(8.50 \pm 0.50) \times 10^{-4}$. The primary star therefore seems to have a highly enhanced oxygen abundance compared to solar. The corresponding synthetic `CMFGEN` spectrum displays, however, a series of O III absorption lines ($\lambda\lambda$ 4368, 4396, 4448, 4454, 4458) that are not present in the observed spectra (neither before nor after disentangling). These lines are not correctly reproduced by the model, as already pointed out in the case of HD 152248 (see discussion in Section 2.2.1.5) and were not considered for the determination of the oxygen abundance. The `CMFGEN` spectrum also displays the O III λ 5508 line, which is, however, not present in the stellar spectrum. The O II λ 4070 and 4185 are correctly reproduced. However, these lines are blended with C III λ 4070 and 4187 lines, respectively, and should therefore be considered with caution. Altogether, it is rather unlikely and impossible to certify that the oxygen abundance is different from solar and we decided to finally set the oxygen abundance to solar.
The carbon abundance was adjusted on the C III λ 4070 line. We obtained a depleted carbon abundance of $(7.00 \pm 1.00) \times 10^{-5}$ compared to solar. This value has to be taken with caution for the same reason as for the oxygen lines. Indeed, C III λ 4070 is blended with O II λ 4070. We note that the C III $\lambda\lambda$ 4647-51 blend and the C III λ 5696 are not well reproduced by our model. These lines are known to be problematic because their formation processes are complex and are controlled by a number of far-UV lines (Martins & Hillier 2012). As a result, the strength and nature of C III $\lambda\lambda$ 4647-51 and C III λ 5696 critically depend on subtle details of the stellar atmosphere model. We therefore decided not to consider these lines in our fitting procedure. We further note that the C IV λ 5801 and λ 5812 lines are not

well reproduced either by our model. These two lines are usually problematic and rarely correctly reproduced (F. Martins 2019, private communication, see also Raucq et al. 2017). Therefore, we did not use these lines to adjust the carbon abundance. Given the difficulties to properly adjust the carbon abundance, we finally decided to set its value to solar.
Finally, we could not determine the nitrogen abundance as the N III $\lambda\lambda$ 4510-4530 complex is completely absent from the stellar spectrum whilst the $\lambda\lambda$ 4634-4640 complex is heavily blended with Si IV, O II, and C III lines, and the N III λ 4379 line is heavily blended with the C III λ 4379 line. We therefore set the nitrogen abundance N/H to solar.

Regarding the wind parameters, the clumping parameters were fixed: The volume filling factor f_1 was set to 0.1, and the f_2 parameter was set to 100 km s^{-1}. The β parameter of the velocity law was fixed to the value of 0.9 as suggested by Muijres et al. (2012) for an O9 V type star. We fixed the value of v_∞ to 1930 km s^{-1} as determined from the *IUE* spectra (see Section 2.3.1.5). Regarding the mass-loss rate, the main diagnostic lines in the optical domain are Hα and He II λ 4686. We inferred a value of $\dot{M} = 6\times10^{-8}\,M_\odot\,\mathrm{yr}^{-1}$.

The stellar and wind parameters of the best-fit `CMFGEN` model atmosphere are summarised in Table 2.25. The normalised disentangled spectra of the primary star of HD 152219 are illustrated in Figure 2.25 along with the best-fit `CMFGEN` adjustment.

Table 2.25. Stellar and wind parameters of the best-fit `CMFGEN` model atmosphere derived from the separated spectra of HD 152219.

Parameter	Value	
	Primary	Secondary
$T_{\rm eff}$ (K)	$30\,900 \pm 1000$	$23\,500 \pm 1000$
$\log g_{\rm spectro}$ (cgs)	3.60 ± 0.10	3.92 ± 0.10
$v_{\rm macro}$ (km s^{-1})	120 ± 10	50 ± 10
$v_{\rm micro}$ (km s^{-1})	15 ± 3	8 ± 2
$\dot{M}$ ($M_\odot$ yr^{-1})	6.0×10^{-8}	1.0×10^{-10}
$\dot{M}_{\rm unclumped}$ ($M_\odot$ yr^{-1})^a	1.9×10^{-7}	3.2×10^{-10}
v_∞ (km s^{-1})	1930 (fixed)	2250 ± 50
f_1	0.1 (fixed)	0.1 (fixed)
f_2 (km s^{-1})	100 (fixed)	100 (fixed)
β	0.90 (fixed)	(fixed)
$R_{\rm spectro}$ ($R_\odot$)	$9.7^{+1.8}_{-1.5}$	$3.7^{+0.8}_{-0.7}$
$M_{\rm spectro}$ ($M_\odot$)	$13.7^{+5.9}_{-5.3}$	$4.1^{+2.0}_{-1.9}$

Notes. $^a\dot{M}_{\rm unclumped} = \dot{M}/\sqrt{f_1}$.

Secondary star We proceeded differently for the secondary star. Since the O III λ 5592 line is not present in the spectrum of the secondary star, we had to rely on He I and Balmer lines to adjust the macroturbulence velocity. Hence, we adjusted $v_{\rm macro}$, the effective temperature, and the surface gravity simultaneously, in an iterative manner. We inferred a value of $v_{\rm macro} = 50 \pm 10$ km s^{-1}.

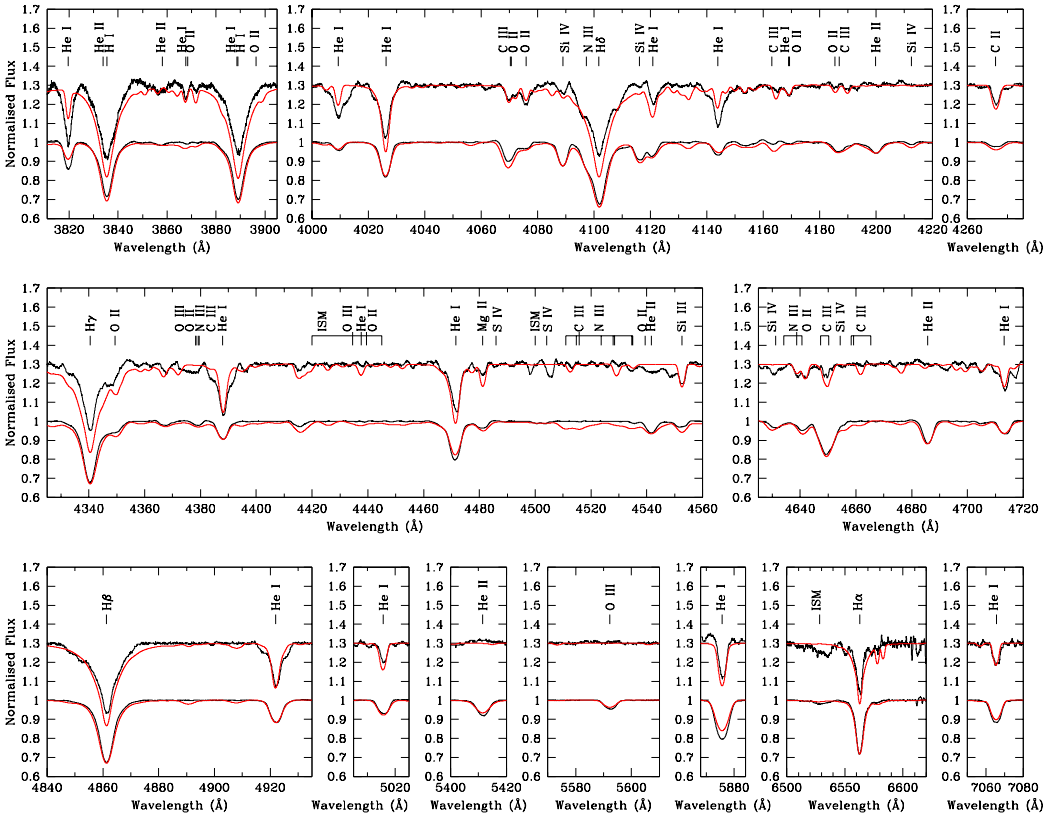

Figure 2.25. Normalised disentangled spectra (in black) of the primary and secondary stars of HD 152219 (the spectrum of the secondary star is shifted by +0.2 in the y-axis for convenience) together with the respective best-fit `CMFGEN` model atmosphere (in red).

As for the primary star, we determined the effective temperature mainly based on the He I λ 4922 line. We found a value of $23\,500 \pm 1000$ K. With this effective temperature, the He I $\lambda\lambda$ 4026, 4471, 5016, 5876 lines are overestimated whilst the He I $\lambda\lambda$ 4388, 4713, 7065 lines are underestimated.

The surface gravity should be obtained by adjusting the wings of the Balmer lines Hβ, Hγ, Hδ, and H I $\lambda\lambda$ 3835, 3890. However, in the present case, the wings, as well as the depths, of the Balmer lines are systematically overestimated, whatever the value of $\log g$. Hence, we decided to assume $\log g_{\rm spectro} = 3.92 \pm 0.10$ as inferred by Sana (2009). With this value, the wings of all hydrogen lines are overestimated.

We set the microturbulence velocity to $10\,{\rm km\,s^{-1}}$, as suggested by Cazorla et al. (2017) for such types of stars. The surface chemical abundances (in number compared to H) of all elements, including C, N, and O, were set to solar abundances as taken from Asplund et al. (2009).

Regarding the wind parameters, the clumping parameters f_1 and f_2 were fixed to the same values as for the primary star. We fixed the β parameter of the velocity law to the value of 1.1 (Lefever et al. 2010). The mass-loss rate was adjusted based on the Hγ and Hα lines. We inferred a value of $\dot{M} = (5.0 \pm 1.0) \times 10^{-10}\,M_\odot\,\mathrm{yr}^{-1}$. We found for the wind terminal velocity a value of $v_\infty = 2040 \pm 30\,\mathrm{km\,s}^{-1}$ based on the adjustment of the strength of the Hα line.

The stellar and wind parameters of the best-fit `CMFGEN` model atmosphere are summarised in Table 2.25. The normalised disentangled spectra of the secondary star are illustrated in Figure 2.25 along with the best-fit `CMFGEN` adjustment.

Spectroscopic radii and masses The bolometric magnitudes of the stars $M_{\mathrm{bol},1} = -7.46^{+0.31}_{-0.37}$ and $M_{\mathrm{bol},2} = -4.17^{+0.38}_{-0.43}$ were computed through the relations recalled in Section 2.1.4. We further obtained bolometric luminosities $L_{\mathrm{bol},1}$ of $7.74^{+2.66}_{-2.18} \times 10^4 L_\odot$ and $L_{\mathrm{bol},2}$ of $3.72^{+1.48}_{-1.29} \times 10^3 L_\odot$ for the primary and secondary stars, respectively. From the relation between bolometric luminosity, radius, and effective temperature, we inferred spectroscopic radii $R_{\mathrm{spectro},1} = 9.7^{+1.8}_{-1.5}\,R_\odot$ and $R_{\mathrm{spectro},2} = 3.7^{+0.8}_{-0.7}\,R_\odot$ for the primary and secondary stars, respectively. Using the surface gravities determined with `CMFGEN`, we obtained spectroscopic masses $M_{\mathrm{spectro},1} = 13.7^{+5.9}_{-5.3}\,M_\odot$ and $M_{\mathrm{spectro},2} = 4.1^{+2.0}_{-1.9}\,M_\odot$ for the primary and secondary stars, respectively.

2.3.2. Radial velocity analysis

Our total radial velocities dataset consists of the ninety-three radial velocities determined as part of the disentangling process of the FEROS observations (see Table 2.21) complemented with forty-six primary radial velocities coming from the literature (see Table 2.26). Sixteen primary radial velocities are taken from Hill et al. (1974), one from Conti et al. (1977), four from Levato & Morrell (1983), three from Perry et al. (1990), eight from García & Mermilliod (2001), eight from Stickland & Lloyd (2001), and six CAT+CES radial velocities from Sana et al. (2006). We discarded the third datapoint from the Perry et al. (1990) dataset (marked with an asterisk in Table 2.26) as it was found to be offset by about $80\,\mathrm{km\,s}^{-1}$ from the most-likely orbital solution[7] (see also Sana et al. 2006). Likewise, we also discarded the last four points of García & Mermilliod (2001) (marked with an asterisk in Table 2.26) as these were shown to be discrepant. In total, we ended up with a series of hundred thirty-four primary radial velocity data points spanning about thirty-eight years. For the Hill et al. (1974), Conti et al. (1977), Levato & Morrell (1983), Perry et al. (1990), and García & Mermilliod (2001) data, we adopted the errors on the radial velocities quoted by these authors. For the *IUE* data from Stickland & Lloyd (2001) and for the CAT/CES data of Sana et al. (2006), we estimated the errors to $5\,\mathrm{km\,s}^{-1}$, corresponding to the dispersions of the radial velocity points over the orbital solution. For the radial velocities derived from the spectral disentangling, we adopted the errors obtained from the dispersion of the radial velocities for the various spectral domains (see Section 2.3.1.2 for detailed explanations, and Table 2.21). We did not use the secondary radial velocities in the determination of the apsidal motion

[7] We actually think that this discrepancy comes from a typographic error in Perry et al. (1990). Indeed, Perry et al. (1990) infers a value of $40\,\mathrm{km\,s}^{-1}$ for this data point while the theoretical radial velocity curve indicates a value of $-40\,\mathrm{km\,s}^{-1}$. However, we have no mean to verify this assertion and we hence decided to discard this point.

rate as these data are only available for the most recent observations and are subject to larger errors than the primary radial velocities.

Table 2.26. Journal of the literature radial velocity measurements of HD 152219. Column 1 gives the heliocentric Julian date (HJD) of the observations. Column 2 gives the radial velocity RV_1 of the primary star. Column 3 gives the estimated error Δ on RV_1. Column 4 provides the reference of the measurement.

Date (HJD) -2 400 000	RV_1 (km s^{-1})	Δ (km s^{-1})	Ref.	Date (HJD) -2 400 000	RV_1 (km s^{-1})	Δ (km s^{-1})	Ref.
40 808.540	83.1	9.9	[1]	39 958.773*	40.0	6.0	[4]
40 808.719	82.4	6.7	[1]	49 910.751	-61.6	4.9	[5]
40 809.508	-55.5	7.7	[1]	49 912.721	45.5	3.9	[5]
40 809.610	-63.5	5.6	[1]	49 914.499	-132.9	4.5	[5]
40 810.475	-139.3	3.7	[1]	49 915.513	14.9	3.6	[5]
40 810.590	-134.1	8.1	[1]	50 593.600*	-145.2	3.9	[5]
40 810.694	-137.9	8.2	[1]	50 595.536*	78.9	7.6	[5]
40 811.573	-4.8	4.1	[1]	50 597.900*	-149.9	5.2	[5]
40 812.558	101.4	7.3	[1]	50 598.792*	-51.2	2.6	[5]
40 813.519	-13.4	3.5	[1]	50 179.023	57.2	5.0	[6]
40 813.631	-52.0	9.5	[1]	50 180.012	15.3	5.0	[6]
40 814.633	-138.8	8.2	[1]	50 180.956	-140.4	5.0	[6]
40 815.474	-34.3	1.5	[1]	50 181.983	-106.3	5.0	[6]
40 815.565	-33.6	3.2	[1]	50 182.974	29.5	5.0	[6]
40 815.675	-36.1	5.2	[1]	50 184.050	39.8	5.0	[6]
40 816.619	75.2	5.0	[1]	50 185.007	-119.3	5.0	[6]
42 529.89	66.3	3.8	[2]	50 185.983	-135.1	5.0	[6]
43 647.788	-57.3	4.3	[3]	50 995.660	-118.6	5.0	[7]
43 648.834	54.1	6.1	[3]	50 996.591	-3.6	5.0	[7]
43 649.839	76.6	7.8	[3]	50 997.608	92.3	5.0	[7]
43 650.898	-110.6	3.7	[3]	50 998.595	14.8	5.0	[7]
39 949.817	-124.0	5.0	[4]	50 999.603	-120.9	5.0	[7]
39 950.796	-16.0	5.0	[4]	51 000.572	-32.2	5.0	[7]

References. [1] Hill et al. (1974), [2] Conti et al. (1977), [3] Levato & Morrell (1983), [4] Perry et al. (1990), [5] García & Mermilliod (2001), [6] Stickland & Lloyd (2001), [7] Sana et al. (2006).
Notes. The observations marked with an asterisk * were discarded for the radial velocity analysis (see main text).

We adjusted the primary radial velocities using Equation (2.30). We explicitly accounted for secular variations of the argument of periastron, through the relation (2.36). As already mentioned for HD 152248 in Section 2.2.2, the radial velocities of different spectral lines potentially yield slightly different apparent systemic velocities (see also Table 3 of Sana et al. 2006). We therefore adjusted the systemic velocity of each subset of our total dataset so as to minimise the sum of the residuals of the data about the curve given by equation (2.30). We simultaneously adjusted the six free parameters (K_1, $P_{\rm orb}$, e, T_0, ω_0, and $\dot{\omega}$) to find the best-fit to the whole set of radial velocity data by scanning the parameter space in a systematic way. The results are given in Table 2.27. The projections of the six-dimensional parameter space onto two-dimensional planes, as well as the best-fit solution, are illustrated in Figure 2.26. The best fit of the radial velocity time series is achieved for an apsidal

motion rate of $(1.198 \pm 0.300)^\circ\,\mathrm{yr}^{-1}$. The rather large uncertainty on this value is due to the small eccentricity of the orbit. Within the error bars, our value overlaps with that derived by Mayer et al. (2008), $(1.64 \pm 0.18)^\circ\,\mathrm{yr}^{-1}$, based on the then available literature radial velocities and ASAS-3 photometry.

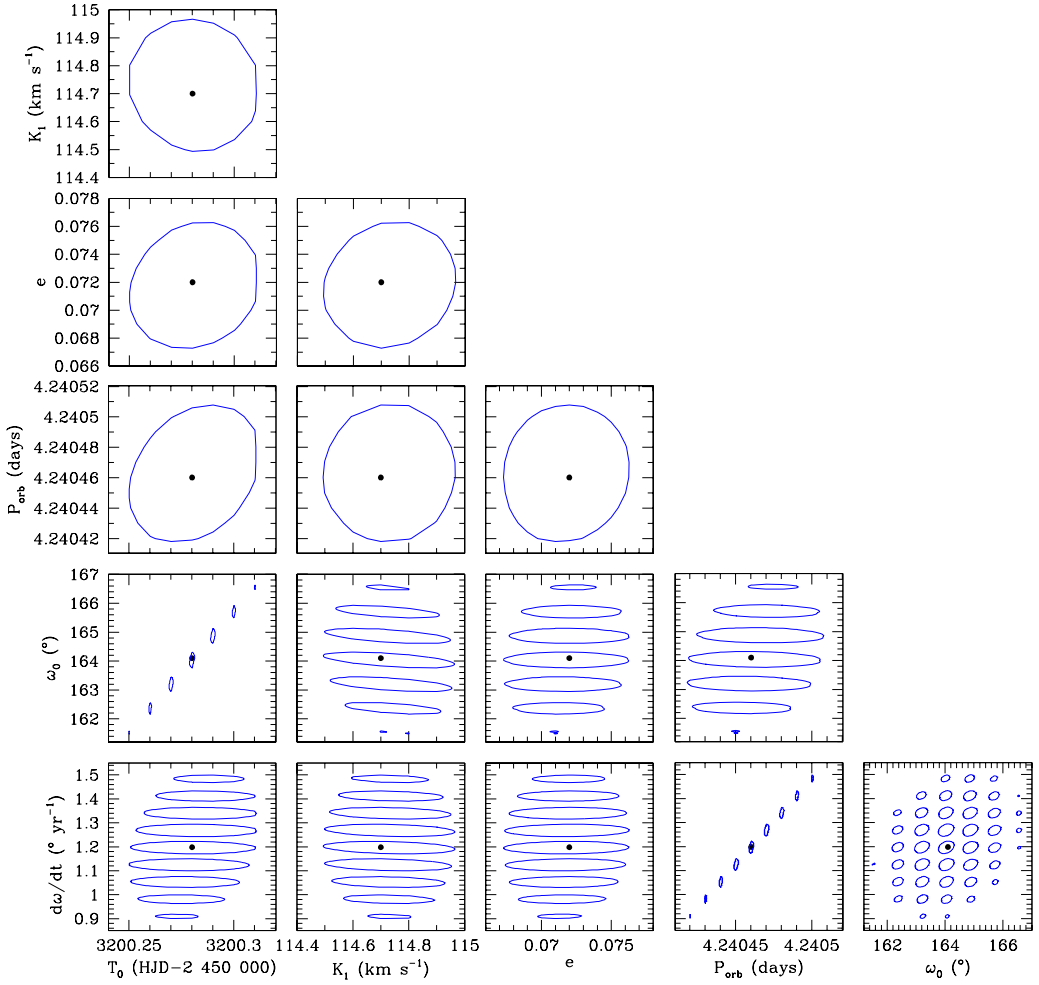

Figure 2.26. Confidence contours for the best-fit parameters obtained from the adjustment of the full set of hundred thirty-four primary radial velocity data of HD 152219 with Equations (2.30) and (2.36). The best-fit solution is shown in each panel by the black filled dot. The corresponding 1σ confidence level is shown by the blue contour. Figure taken from Rosu et al. (2022a).

We determined the mass ratio $q = m_2/m_1$ of HD 152219 by applying the linear relation between the primary and secondary radial velocities, given by Equation (2.33), to the radial velocities obtained in the disentangling process. We obtained a value $q = 0.413 \pm 0.004$. We then built an SB2 orbital solution for the binary system. Our best-fit parameters and their $1\,\sigma$ errors are listed in Table 2.27. The best fit of the radial velocity data is illustrated

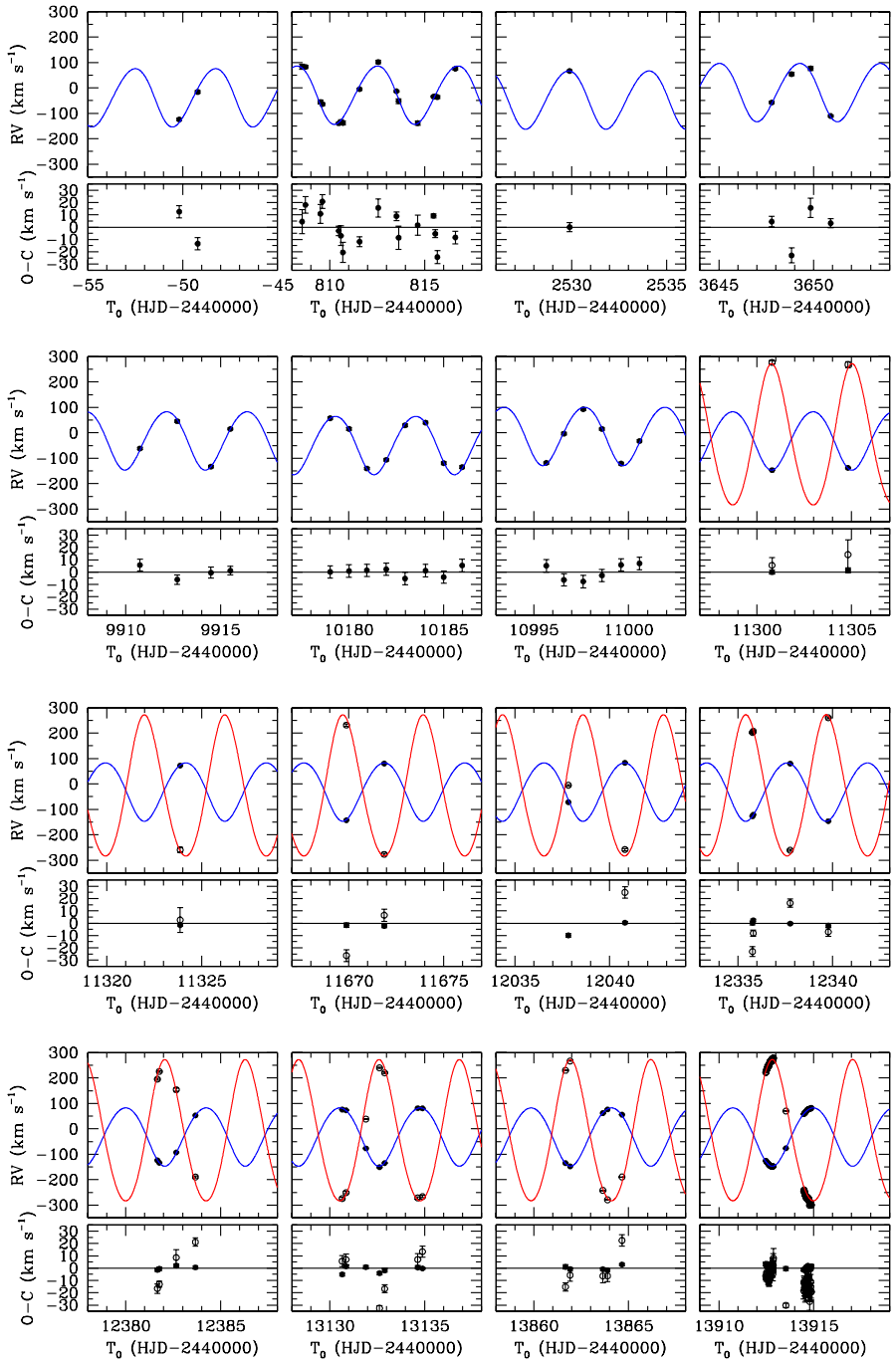

Figure 2.27. Comparison between the measured radial velocities of the primary (filled dots) and secondary (open dots, when available) stars of HD 152219 with the radial velocities expected from Equations (2.30), (2.33), and (2.36) with the best-fit parameters given in Table 2.27 (in blue for the primary star and in red for the secondary star). Figure taken from Rosu et al. (2022a).

in Figure 2.27. From the He I lines, Sana et al. (2006) inferred a slightly smaller mass ratio ($q = 0.395 \pm 0.003$), a higher eccentricity ($e = 0.082 \pm 0.011$), a smaller semi-amplitude of the primary radial velocity curve ($K_1 = 110.7 \pm 0.7\,\mathrm{km\,s^{-1}}$), and consequently a larger semi-amplitude of the secondary radial velocity curve ($K_2 = 279.9 \pm 1.7\,\mathrm{km\,s^{-1}}$). These differences likely arise due to the two-Gaussian fit used by Sana et al. (2006) to establish the radial velocities.

Table 2.27. Best-fit orbital parameters of HD 152219 obtained with Equations (2.30), (2.33), and (2.36).

Parameter	Primary RVs
P_{orb} (d)	$4.24046^{+0.00005}_{-0.00004}$
e	$0.072^{+0.004}_{-0.005}$
$\dot{\omega}$ ($^\circ\,\mathrm{yr}^{-1}$)	1.198 ± 0.300
ω_0 ($^\circ$)	164.1 ± 2.6
T_0 (HJD$-2\,450\,000$)	$3\,200.28^{+0.02}_{-0.03}$
$q = m_2/m_1$	0.413 ± 0.004
K_1 ($\mathrm{km\,s^{-1}}$)	$114.7^{+0.3}_{-0.2}$
K_2($\mathrm{km\,s^{-1}}$)	277.7 ± 2.9
$a_1 \sin i$ ($R_\odot$)	9.59 ± 0.03
$a_2 \sin i$ ($R_\odot$)	23.22 ± 0.24
$m_1 \sin^3 i$ ($M_\odot$)	18.64 ± 0.47
$m_2 \sin^3 i$ ($M_\odot$)	7.70 ± 0.12
χ^2_ν	2.72

2.3.3. Photometric analysis

This section is devoted to the photometric analysis of the binary system HD 152219. The set of observational photometric data we used is introduced. Light curve analysis by means of the `Nightfall` code is performed. The apsidal motion is reviewed in light of this photometric analysis.

2.3.3.1. Observational data

Five public databases report photometric observations of the binary system HD 152219. However, only two of them were useful in the present context. Indeed, whilst the white light observations collected with the Optical Monitor Camera (Mas-Hesse et al. 2003) onboard the INTEGRAL spacecraft are too scarce, and hence, useless to perform any meaningful analysis of the light curve, the Hipparcos/Tycho data (Gaia Collaboration 2018) have too large uncertainties, and the All-Sky Automated Survey for Supernovae (ASAS-SN, Kochanek et al. 2017) data are saturated as the magnitude of HD 152219 in the visible band $m_V \sim 7.57$. The only two remaining datasets are the All Sky Automated Survey (ASAS-3, Pojmański & Maciejewski 2004) V-band data (used by Otero & Wils (2005) to discover the existence of

eclipses) and the data collected by the Transiting Exoplanet Survey Satellite (TESS, Ricker et al. 2015). We refer to Section 2.2.4.1 for the description of the ASAS-3 and TESS Surveys.

Regarding the ASAS-3 data, we adopted the 4 pixel aperture data and discarded the observations taken before HJD 2 452 455 (Mayer et al. 2008). The ASAS-3 light curve shows a significant number of obvious outliers. To get rid of those, we built a mean light curve from normal data points computed for phase bins of 0.01 and applied a $1.25\,\sigma$ clipping to the data about this mean light curve. In this way, most of the points that were off by 0.05 mag or more from the mean magnitude were removed. The few remaining outliers were associated with phase bins containing very few data points. The phase-folded ASAS-3 light curve is illustrated in Figure 2.28 adopting the orbital period derived in Section 2.3.2 (see Table 2.27).

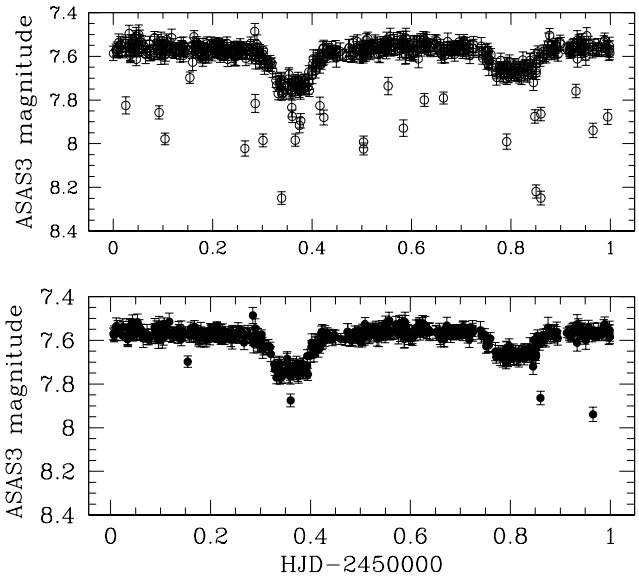

Figure 2.28. Phase-folded ASAS-3 light curve of HD 152219 using the orbital period given in Table 2.27. *Top panel:* Raw ASAS-3 data. *Bottom panel:* ASAS-3 data after the $1.25\,\sigma$ clipping. Figure taken from Rosu et al. (2022a).

TESS observed HD 152219 with camera 1 during sector 12 (between 21 May and 19 June 2019, hereafter TESS-12) and sector 39 (between 27 May and 24 June 2021, hereafter TESS-39). We extracted the 2-minutes high-cadence TESS-12 light curve from the Mikulski Archive for Space Telescopes (MAST) portal[8]. Both background-corrected aperture photometry and photometry obtained after removal of trends correlated to spacecraft and instrumental effects, so-called PDC photometry, are provided. We only kept the data points with a quality flag of 0, and we discarded the data taken immediately before the gap between the two spacecraft orbits. We extracted the TESS-39 light curve with a 10-

[8] `http://mast.stsci.edu`

minutes cadence from the full frame images (FFI) using the Lightkurve[9] `Python` software. We evaluated the background level in three different ways: We restricted ourselves to those pixels in a 50×50 pixels cutout that were below the median flux, and applied a principal analysis including two or five components (see Figure 2.29). The observations taken after HJD 2 459 386 were discarded due to their large dispersion. Because HD 152219 was located near the edge of the CCDs during sector 12, we also extracted the 30-minutes cadence light curve from the FFI using the Lightkurve `Python` software, restricting the source region to the central $(21'')^2$ pixel, and evaluated the background level as for the TESS-39 data. The results were in agreement with those coming from the PDC photometry. In total, we ended up with 11 944 and 3411 data points for TESS-12 and TESS-39, respectively. The formal photometric accuracy ranges between 0.34 and 0.38 mmag.

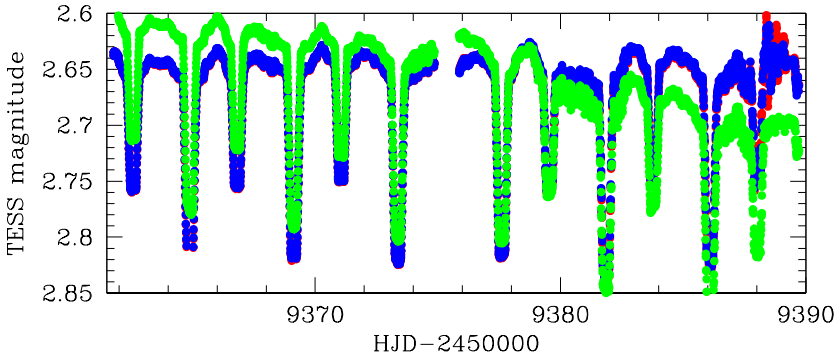

Figure 2.29. TESS-39 light curves of HD 152219 when the background level is evaluated by restricting ourselves to those pixels of a 50×50 pixels cutout that were below the median flux (green), or by applying a principal component analysis including two (blue) or five (red) components.

Both the ASAS-3 and TESS data are contaminated by nearby sources. Indeed, the region around HD 152219 is rather crowded: Within a radius of $1'$, we found two stars having a magnitude difference in the I-band compared to HD 152219 ($m_I = 7.27$) of less than 4 mag. The two contaminators are the β Cep variable CPD-41° 7706 (V 945 Sco) and CPD-41° 7712, located at $38.5''$ and $54.0''$, respectively, and having magnitudes in the I-band m_I of 9.26 and 8.84, respectively (Sung et al. 1998). In the extreme case where all the light from both sources would contaminate the photometry of HD 152219, the third light contribution would amount to ~ 0.28. If only all the light from the nearest neighbour would contaminate the photometry of HD 152219, the third light contribution would amount to ~ 0.16. Both the masks adopted for the extraction of the TESS light curves and the FFI suggest a third light contribution amounting to 0.09. The PDC pipeline automatically corrects the light curve for a constant third light contribution of this level, meaning that the TESS-12 photometry should be free of third light. However, the FFI is not corrected for the third light contribution, and hence, the TESS-39 photometry should still contain a non-zero third light contribution. Non-orbital variations are observed in both TESS light curves. To reduce these variations, we constructed a mean light curve consisting of normal points computed for phase bins of 0.01 (see Figure 2.30).

[9] `https://docs.lightkurve.org`

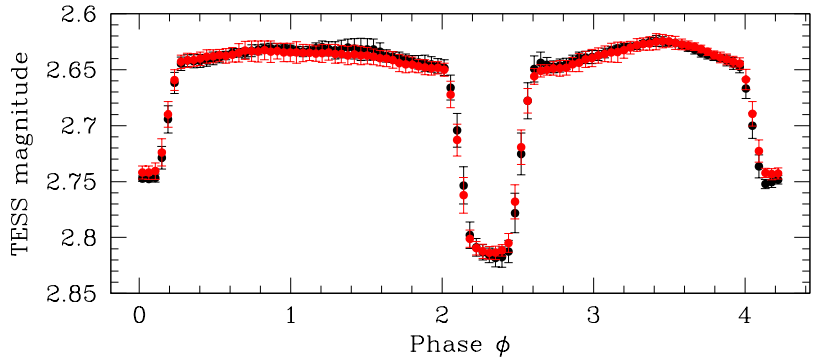

Figure 2.30. Phase-folded mean TESS-12 (in black) and TESS-39 (in red) light curves of HD 152219 consisting of normal points computed for phase bins of 0.01, using the orbital period given in Table 2.27.

2.3.3.2. Light curve analysis

We analysed the light curves of HD 152219 with the `Nightfall` code version 1.92 (see Section 2.1.9 for detailed explanations about the code). Following the results of our radial velocity analysis (see Section 2.3.2), we set the mass ratio q to 0.413 and the eccentricity e to 0.072. The effective temperature of the primary star was fixed to 30 900 K as derived from the `CMFGEN` analysis (see Section 2.3.1.6). We did not fix the effective temperature of the secondary star to 23 500 K as derived from the `CMFGEN` analysis (see Section 2.3.1.6) as the solutions obtained in this way were unable to reproduce the primary eclipse; we decided to leave this parameter free in the light curve analysis. We adopted a quadratic limb-darkening law. Reflection effects were accounted for by considering the mutual irradiation of all pairs of surface elements of the two stars (Hendry 1992). The five free parameters to adjust were the effective temperature of the secondary star $T_{\rm eff,2}$, the Roche lobe filling factors of both stars $f_{\rm P}$ and $f_{\rm S}$, the inclination of the orbit i, and the longitude of periastron ω. For the TESS-12 and TESS-39 data, we can assume that ω is constant over the duration of each TESS sector as the light curves were obtained over sufficiently short time intervals. The TESS-12 data offer the best coverage of the two eclipses and is also more reliable than the TESS-39 and ASAS-3 data due to the shorter cadence at which data were collected. Thence, we decided to proceed as follows: We adjusted the five free parameters on the TESS-12 light curve assuming a third light contribution $I_3 = 0$. We then used these results to adjust the ASAS-3 and TESS-39 light curves allowing for ω only to vary in order to offer a test of our apsidal motion rate determination performed in Section 2.3.2.

The best-fit parameters obtained through the adjustment of the TESS-12 light curve are given in Table 2.28 while the best fit is illustrated in Figure 2.31. Within the error bars, the light ratio in the V-band between the secondary and primary stars, of 0.084 as estimated by the `Nightfall` code, is compatible with the value inferred from spectroscopy (see Section 2.3.1.3). We estimated the error bars on the parameters by scanning the five-dimensional parameter space in a systematic way. For this purpose, we used the χ^2

Table 2.28. Parameters of the best-fit `Nightfall` model for the TESS-12 light curve of HD 152219.

Parameter	Value
I_3	0 (fixed)
$T_{\rm eff,2}$ (K)	$21\,697^{+370}_{-340}$
$f_{\rm P}$	0.711 ± 0.009
$f_{\rm S}$	0.418 ± 0.005
i (°)	$89.58^{+0.42}_{-2.28}$
ω (°)	$192.4^{+3.4}_{-9.4}$
χ^2_ν	0.376

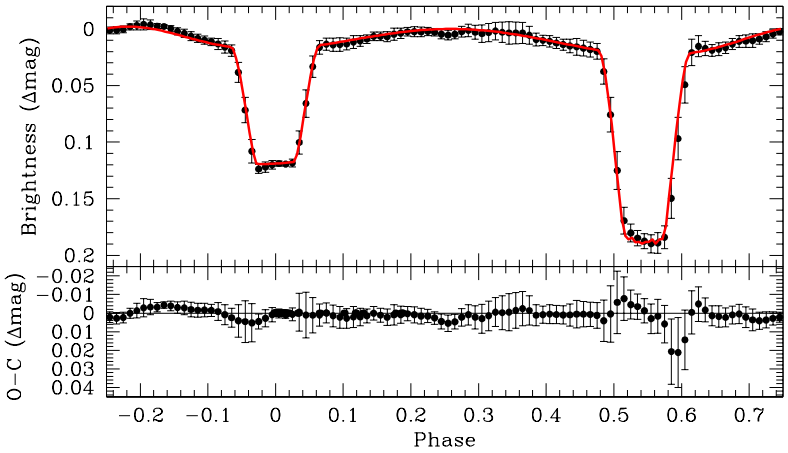

Figure 2.31. *Upper panel:* Best-fit `Nightfall` solution of the TESS-12 light curve of HD 152219. *Lower panel:* Residuals over the best-fit solution. Figure taken from Rosu et al. (2022a).

mapping functionality implemented in `Nightfall` that scans two parameters at a time while fixing the other three to their best-fit values. The 1σ confidence contours were then computed in each two-dimensional plane adopting $\Delta\chi^2 = 2.30$ as appropriate for two free parameters and are plotted in Figure 2.32. To get an estimate of the error bars on each parameter, we then adopted the largest contour on the considered parameter in order to account for correlations. As recalled in Section 1.2.2, in the case of a near circular orbit seen under an inclination of 90°, the depths of the eclipses are set by the ratio between the effective temperatures of the two stars. The uncertainties on the primary effective temperature (determined in Section 2.3.1.6) should propagate in the determination of the secondary effective temperature. In order to get an estimate of this error propagation, we computed two best-fit models of the TESS-12 light curve with `Nightfall` fixing $T_{\rm eff,1}$ to its best-fit value $\pm 1\sigma$, that is to say, to 31 900 and 29 900 K, respectively, and leaving $T_{\rm eff,2}$ as the only free parameter, all other parameters being fixed to their best-fit value as given in Table 2.28. We obtained $T_{\rm eff,2} = 22\,320$ and 21 047 K, respectively, values that differ from

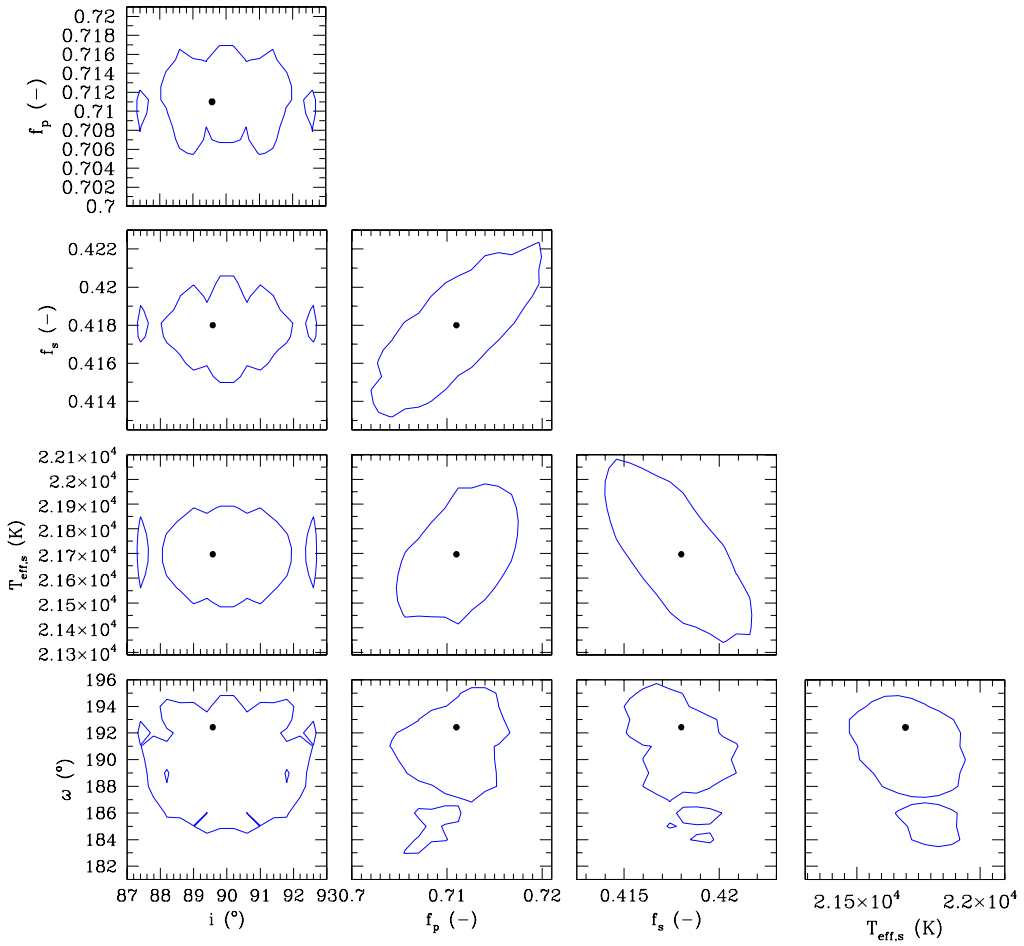

Figure 2.32. Confidence contours for the best-fit parameters obtained from the adjustment of the TESS-12 light curve of HD 152219 with the `Nightfall` code. The best-fit solution (i.e. with a third light contribution $I_3 = 0$) is shown in each panel by the black dot, while the corresponding 1σ confidence level is shown by the blue contour. Figure taken from Rosu et al. (2022a).

the best-fit value by +623 and −650 K, respectively. These differences are smaller than the 1000 K error bar on the primary effective temperature. Still, to be conservative, we adopted an error bar of 1000 K on the secondary effective temperature too.

For the sake of completeness, we scanned the parameter space for the third light contribution from 0 to 0.28 with a step of 0.01 and searched for the best-fit of the TESS-12 light curve for each value of I_3. The results are given in Table 2.29. The main difference between all these adjustments lies in the Roche lobe filling factor of the secondary star (see Figure 2.33). The formally best adjustment, as judged by its χ^2_ν, is achieved for a third light contribution of 0.19, as shown in Figure 2.33. Yet, we stress that the quality of the fit is not

extremely sensitive to the assumed value of I_3 and that values of I_3 significantly larger than 0 lead to secondary radii that are not consistent with our spectroscopic analysis.

Table 2.29. Parameters of the best-fits `Nightfall` models for the TESS-12 light curve of HD 152219 for a grid of third light contributions. Column 1 gives the contribution of the third light, as a fraction of the total brightness of the system. Column 2 gives the effective temperature of the secondary star. Columns 3 and 4 give the Roche lobe filling factor of the primary and secondary stars, respectively. Columns 5 and 6 give the orbital inclination and the argument of periastron, respectively. Column 7 gives the reduced χ^2_ν of the adjustment.

I_3	$T_{\rm eff,2}$ (K)	$f_{\rm P}$	$f_{\rm S}$	i (°)	ω (°)	χ^2_ν
0	21 697	0.711	0.418	89.58	192.43	0.376
0.01	21 600	0.711	0.422	89.98	190.09	0.371
0.02	21 660	0.717	0.427	89.49	189.21	0.367
0.03	21 739	0.709	0.427	89.59	190.25	0.364
0.04	21 658	0.714	0.432	89.68	189.92	0.354
0.05	21 599	0.716	0.436	89.74	190.25	0.350
0.06	21 733	0.716	0.438	89.75	189.76	0.345
0.07	21 670	0.721	0.443	89.80	189.66	0.346
0.08	21 841	0.721	0.446	89.22	190.11	0.344
0.09	21 747	0.721	0.448	89.25	190.39	0.341
0.10	21 708	0.725	0.455	88.51	188.68	0.337
0.11	21 745	0.726	0.458	88.57	188.36	0.332
0.12	21 764	0.724	0.461	89.29	187.78	0.327
0.13	21 857	0.725	0.465	89.76	187.57	0.332
0.14	21 764	0.724	0.468	90.00	187.22	0.329
0.15	21 683	0.730	0.475	89.60	188.54	0.324
0.16	21 914	0.726	0.474	89.62	188.67	0.328
0.17	21 857	0.732	0.481	89.49	189.00	0.327
0.18	21 818	0.730	0.484	90.00	189.82	0.325
0.19	21 806	0.732	0.490	88.38	187.84	0.323
0.20	21 804	0.733	0.495	89.76	190.17	0.328
0.21	21 894	0.739	0.501	88.50	186.58	0.329
0.22	21 869	0.738	0.504	88.15	188.78	0.331
0.23	21 857	0.734	0.507	89.49	188.81	0.336
0.24	22 009	0.738	0.511	89.63	187.91	0.338
0.25	21 923	0.737	0.517	89.76	186.48	0.338
0.26	21 890	0.740	0.523	89.86	187.03	0.344
0.27	21 954	0.740	0.528	89.93	186.60	0.350
0.28	22 056	0.743	0.531	89.78	188.83	0.356

We note that our best-fit value of the inclination is not compatible, even within the error bars, with the one, of $72 \pm 3°$, inferred by Mayer et al. (2008) from their analysis of the ASAS-3 data. Notwithstanding, adopting their value of the inclination, together with our best-fit values for the other free parameters, yields a light curve that is inconsistent with the total primary eclipse. Indeed, the total primary eclipse puts a stringent constraint on the inclination of the system as we determined that a minimum value of 80° is required.

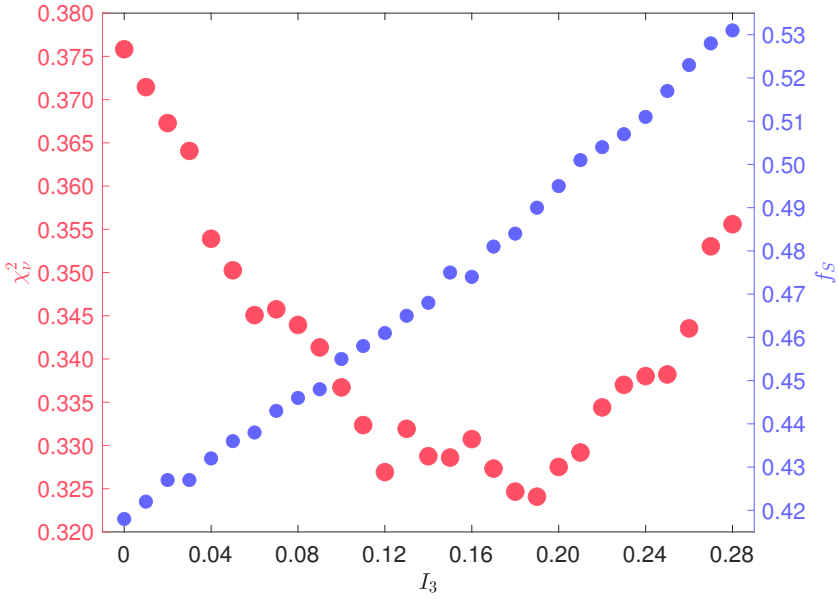

Figure 2.33. Values of the reduced χ^2_ν (*left axis*) and secondary Roche lobe filling factor f_S (*right axis*) as a function of the third light contribution I_3 for the best-fit `Nightfall` adjustments of the TESS-12 photometry of HD 152219.

The combination of our best-fit orbital inclination with the minimum semi-major axis and minimum stellar masses inferred from the radial velocity curves (see Section 2.3.2) yields a semi-major axis a of $32.81 \pm 0.24\,R_\odot$ and individual absolute masses of $18.64 \pm 0.47\,M_\odot$ and $7.70 \pm 0.12\,M_\odot$ for the primary and secondary stars, respectively. These absolute masses are higher than those derived from the spectroscopic analysis (see Section 2.3.1.6) though the primary mass is compatible within the error bars. From these values, we inferred photometric values of the surface gravities for the primary and secondary stars: $\log g_1 = 3.76 \pm 0.02$ and $\log g_2 = 4.19 \pm 0.01$. These values are higher than those derived from spectroscopy (see discussion in Section 2.3.1.6). The photometric radii of the primary and secondary stars $R_1 = 9.40^{+0.14}_{-0.15}\,R_\odot$ and $R_2 = 3.69 \pm 0.06\,R_\odot$ agree with the spectroscopic radii within the error bars (see Section 2.3.1.6). We then inferred bolometric luminosities $L_{\rm bol,1} = (7.26 \pm 0.97) \times 10^4\,L_\odot$ and $L_{\rm bol,2} = (2.73 \pm 0.51) \times 10^3\,L_\odot$ for the primary and secondary stars, respectively. These values are compatible within the error bars with those derived from spectroscopy (see Section 2.3.1.6). Table 2.30 lists the physical parameters expressed in so-called nominal solar units as adopted by the International Astronomical Union (Prša et al. 2016b). We note that the conventional solar units used throughout this analysis agree with these nominal values.

Assuming the rotational axes of the stars are orthogonal to the orbital plane, we can combine the best-fit values of the inclination and stellar radii with the projected rotational velocities of the stars determined in Section 2.3.1.4 to derive rotational periods of 2.86 ± 0.18

Table 2.30. Physical parameters of the components of HD 152219 as derived from the photometric analysis.

Parameter	Value	
	Primary	Secondary
$m_{\rm photo}$ ($\mathcal{M}_\odot^{\rm N}$)	18.64 ± 0.47	7.70 ± 0.12
$R_{\rm equiv}$ ($\mathcal{R}_\odot^{\rm N}$)	$9.40^{+0.14}_{-0.15}$	3.69 ± 0.06
a ($\mathcal{R}_\odot^{\rm N}$)	32.81 ± 0.2	
$\log g_{\rm photo}$ (cgs)	3.76 ± 0.02	4.19 ± 0.01
$L_{\rm bol,photo}$ ($\mathcal{L}_\odot^{\rm N}$)	$(7.26 \pm 0.97) \times 10^4$	$(2.73 \pm 0.51) \times 10^3$

and 1.97 ± 0.19 days for the primary and secondary stars, respectively. The ratio between rotational angular velocity and instantaneous orbital angular velocity at periastron amounts to 1.28 ± 0.08 for the primary star and to 1.86 ± 0.18 for the secondary star. We conclude that pseudo-synchronisation is about to be achieved in the system for the primary star but is far from being achieved for the secondary star.

2.3.3.3. Apsidal motion

The light curves of a binary system being sensitive to the apsidal motion, they can in principle be used to determine the apsidal motion rate of the system (see Section 1.2.2.5). However, in the case of HD 152219, as in the case of HD 152248 (see Section 2.2.4.3), the time span of the photometric observations is much shorter than the total time span of the spectroscopic observations. Consequently, we decided to use the photometric observations as a consistency check of the apsidal motion rate determined based on the radial velocities (see Section 2.3.2). For this purpose, we adjusted the TESS-39 light curve fixing all parameters to the best-fit values obtained for the TESS-12 light curve, allowing for ω only to vary. As explained in Section 2.3.3.1, the TESS-39 data might be contaminated by an unknown third light contribution. Therefore, we also left the third light contribution free for the adjustment of the light curve. Adopting the 1σ contour for the two-parameter space, plotted in Figure 2.34, the best-fit adjustment is achieved for $\omega = (192.5^{+3.8}_{-6.1})^\circ$ and $I_3 = 0.032^{+0.015}_{-0.014}$, and has $\chi^2_\nu = 0.395$ (see Table 2.31). We note that the depth of the secondary eclipse was not well-reproduced for a zero third light contribution. The TESS-39 light curve is plotted in Figure 2.35 together with the best-fit adjustment. The evolution of ω as a function of time as inferred from the radial velocity analysis is plotted in Figure 2.36, together with the TESS-12 and TESS-39 results. Both TESS results agree with the results inferred from the global fit of the radial velocities within the error bars.

Regarding the ASAS-3 data, the total time span of the observations is too long to assume a constant value of ω throughout the campaign. We divided the ASAS-3 dataset in seven separate sets of observations and performed the adjustment of each dataset separately. As for the TESS-39 light curve, we fixed all parameters to the best-fit values obtained for the TESS-12 light curve and allowed for ω and I_3 only to vary. The best-fit solutions are given in Table 2.31 and plotted in Figure 2.36. It is clearly evident that the ASAS-3 data are too

sparsely sampled to determine meaningful epoch-dependent values of ω and are therefore useless in this purpose.

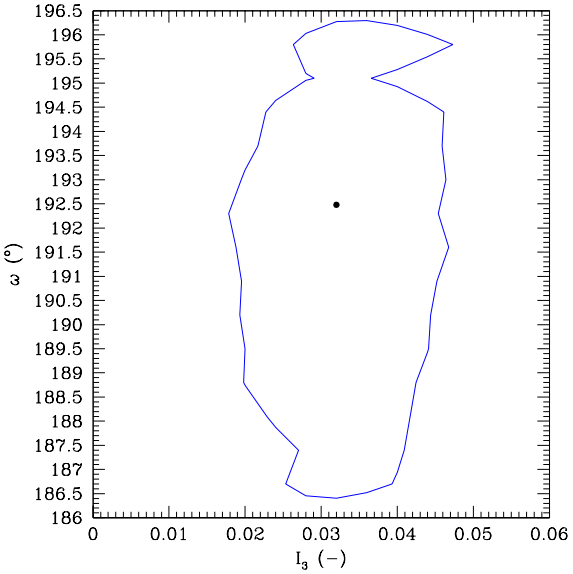

Figure 2.34. Confidence contour for the best-fit parameters obtained from the adjustment of the TESS-39 light curve of HD 152219 with the `Nightfall` code. The best-fit solution is shown by the black dot, while the corresponding 1σ confidence level is shown by the blue contour.

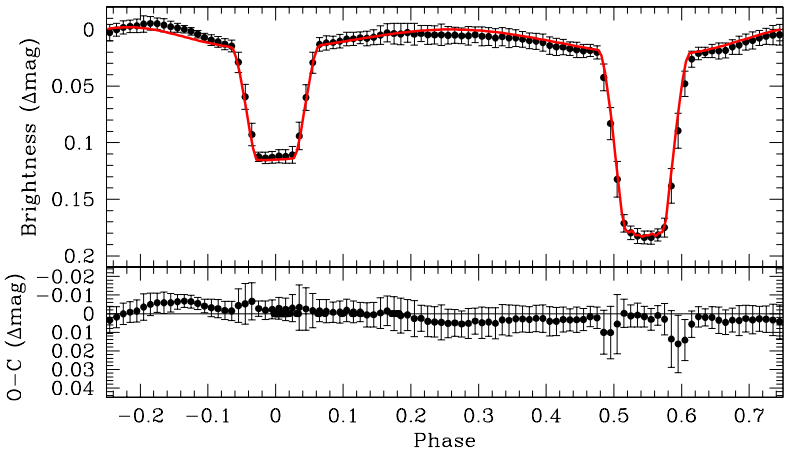

Figure 2.35. *Upper panel:* Best-fit `Nightfall` solution of the TESS-39 light curve of HD 152219. *Lower panel:* Residuals over the best-fit solution. Figure taken from Rosu et al. (2022a).

Table 2.31. Best-fit values of ω and I_3 from the photometry of HD 152219. Column 1 gives the mid-epoch of the observation. Columns 2 and 3 give the total number of observational data and the total time span of the campaign, respectively. Column 4 gives information about the instrumentation. Columns 5, 6, and 7 give the values of ω, I_3, and χ^2_ν, respectively, of the best-fit adjustment.

Epoch (HJD)	N	Δt (d)	Instrumentation	ω (°)	I_3	χ^2_ν
2 452 795.7	71	281.6	ASAS-3	170.7	0.191	1.048
2 453 112.8	33	157.8	ASAS-3	184.7	0.046	1.468
2 453 527.2	73	270.6	ASAS-3	201.1	0.001	10.901
2 453 868.7	37	225.6	ASAS-3	166.2	0.140	0.431
2 454 256.2	69	258.6	ASAS-3	171.1	0.112	1.449
2 454 626.7	117	275.6	ASAS-3	187.3	0	2.294
2 454 981.2	48	260.6	ASAS-3	169.2	0	1.362
2 458 641.4	11 944	23.0	TESS-12	192.4	0 (fixed)	0.376
2 459 374.4	3411	25.2	TESS-39	192.5	0.032	0.395

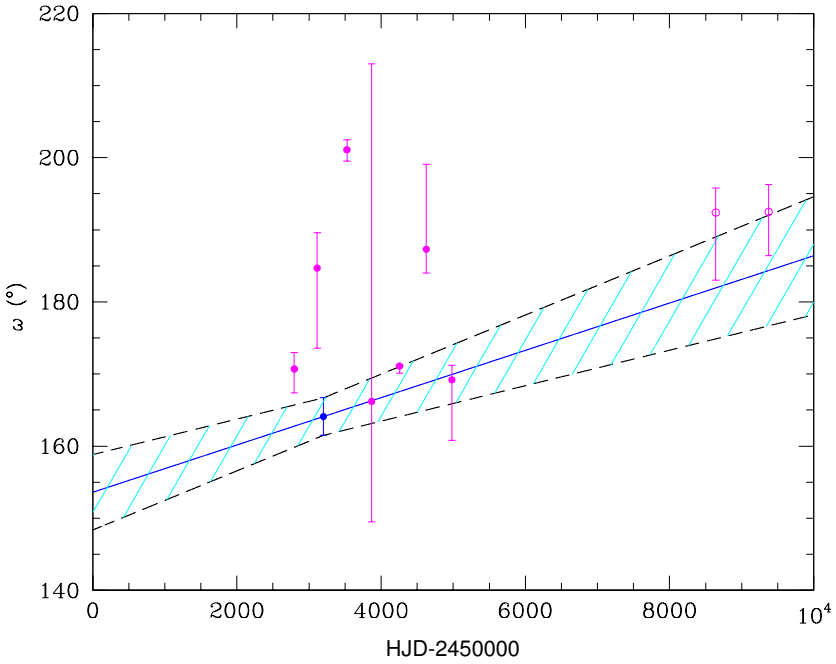

Figure 2.36. Values of ω as a function of time inferred from the photometric light curves and the radial velocities of HD 152219. The pink filled symbols and the pink open symbols correspond to the data of the fits of the ASAS-3 photometry, and the TESS-12 and TESS-39 photometry, respectively. The blue dot indicates the ω_0 value obtained from the global fit of all radial velocity data. The solid blue line corresponds to our best-fit value of $\dot{\omega}$ inferred from the radial velocities, and the hatched cyan zone corresponds to the range of values according to the 1σ uncertainties on ω_0 and $\dot{\omega}$ (see Table 2.27).

As a second consistency check, we computed the phase difference $\Delta\phi$ between the primary and secondary eclipses for the TESS-12, TESS-39, and combined ASAS-3 data. We adjusted a second-order polynomial to the eclipses and found values of 0.451 ± 0.004, 0.454 ± 0.004, and 0.452 ± 0.010 for these three sets of data, respectively. These results were further confirmed by both the `Nightfall` results and the computation of the first order moment of the eclipses. We computed the phase difference as a function of ω from Equations (1.10) and (1.11) expected from the radial velocity analysis, adopting the eccentricity given in Section 2.3.2. The resulting curve is plotted in Figure 2.37 together with the photometric data. Within the error bars, the observational values of $\Delta\phi$ agree with the results inferred from the radial velocities. If we further adopt the value of ω inferred from the radial velocity analysis at the time of the TESS-12 observations, we find an eccentricity of $0.070^{+0.006}_{-0.005}$ which is compatible within the error bars with the eccentricity determined from the radial velocity analysis. This is illustrated in Figure 2.38, where the solutions of Equations (1.10) and (1.11) in the (ω, e)-plane are plotted together with the values expected for the TESS-12 observations. Altogether, these results enforce the coherence between the radial velocity and photometric analyses.

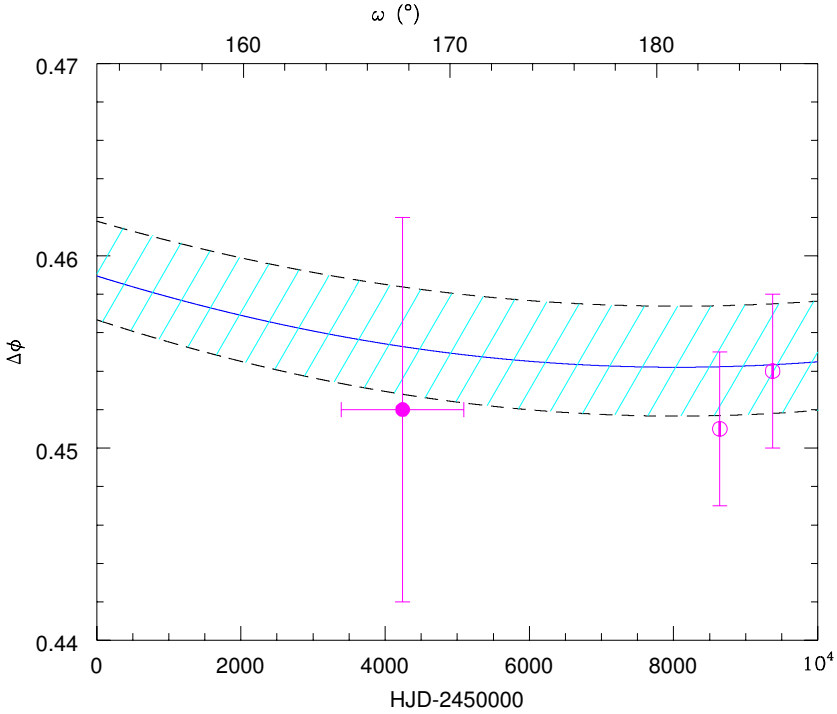

Figure 2.37. Values of the phase difference $\Delta\phi$ between the primary and secondary eclipses as a function of time and ω inferred from the photometric light curves and the radial velocities of HD 152219. The pink filled symbol and the pink open symbols correspond to the data of the fits of the ASAS-3 photometry, and the TESS-12 and TESS-39 photometry, respectively. The solid blue line corresponds to our best-fit value of $\Delta\phi$ inferred from the radial velocities, and the hatched cyan zone corresponds to the range of values according to the 1σ uncertainties on the eccentricity (see Table 2.27). Figure taken from Rosu et al. (2022a).

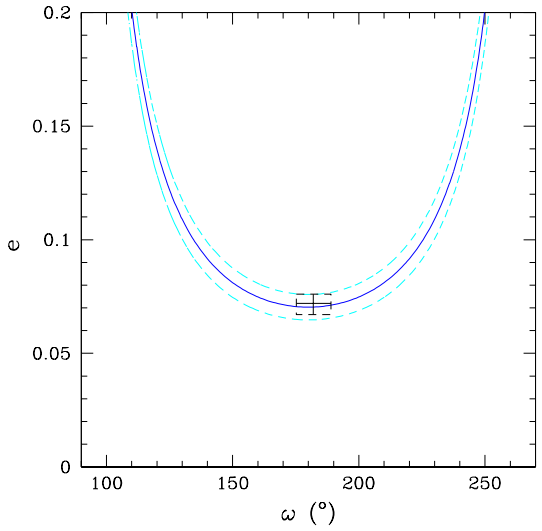

Figure 2.38. Solutions of Equations (1.10) and (1.11) in the (ω, e)-plane as inferred from the radial velocity analysis (in blue) together with the 1σ uncertainties (in cyan, see Table 2.27) of HD 152219. The value expected for the TESS-12 observations, with its error bars, is depicted in black.

2.3.4. Evidence for the Rossiter-McLaughlin effect

The signature of the Rossiter-McLaughlin effect in HD 152219 was first reported by Sana (2009) from the analysis of the He II λ 4686 line (see his figures). He reported maximum radial velocity deviations of $\pm 26\,\mathrm{km\,s^{-1}}$, with nearly equal amplitudes in both the positive and negative directions. This effect is observed during the eclipse of the primary star by the secondary star. It takes its origin from the fact that when the secondary star passes in front of the primary star in our line of sight, assuming a prograde orbit, it first eclipses the parts of the primary star that produce the blue wings of the spectral lines. Consequently, the line centroids are shifted to the red. Likewise, near the end of the eclipse, the secondary star eclipses the parts of the primary star that produce the red wings of the spectral lines and, consequently, the line centroids are shifted to the blue. Given that the radial velocities are estimated based on the centroids of the spectral lines, their values are thereby affected.

The Rossiter-McLaughlin effect can in principle be used as a test of the misalignment between the stellar rotation axis and the normal to the orbital plane (see e.g. Hosokawa 1953; Ohta et al. 2005; Giménez 2006; Albrecht et al. 2007). In the present case, we searched for a possible misalignment of the primary stellar rotation axis. We designed a `Fortran` code to determine the Rossiter-McLaughlin effect for a grid of values for the angle α between the primary stellar rotation axis and the normal to the orbital plane and the angle i_{rot} between the primary stellar rotation axis and the line joining the centre of the binary system and the observer. We adopted the orbital inclination derived in the photometric analysis (see Section 2.3.3.2) and the projected rotational velocity $v_{\mathrm{eq}} \sin i_{\mathrm{rot}}$ given in Section 2.3.1.4. We computed synthetic line profiles adopting the quadratic limb darkening law of Claret (2000) and we assumed spherically symmetric stars

characterised by the radii derived in the photometric analysis (see Section 2.3.3.2). We used the first order moment of the line profile to get an estimate of the centroids of the lines.

We were unfortunately unable to confront our derived amplitudes to those reported by Sana (2009), as our maximum amplitude of the Rossiter-McLaughlin effect is of $19\,\mathrm{km\,s^{-1}}$, that is to say, almost 27% smaller than the one derived by Sana (2009). This discrepancy might come from the fact that whilst we used the first moment to get an estimate of the centroids of the lines, Sana (2009) fitted a Gaussian profile to determine the radial velocities of the lines. Owing to the highly non-Gaussian shapes of the lines during eclipses, the Gaussian fitting yields a different amplitude of the Rossiter-McLaughlin effect than our method. This amplitude difference is difficult to reproduce as it requires the knowledge of the wavelength range over which the Gaussian fitting was performed. Nonetheless, considering the fact that the maximum radial velocity deviations have the same amplitude in both positive and negative sides allowed us to exclude values of α between 15° and 165°.

2.3.5. HD 152219 in a nutshell

We have reanalysed the eccentric massive binary HD 152219. We reconstructed the individual spectra of the components using our disentangling code. We reassessed the spectral classification of the stars and found spectral types O9.5 III and B1-2 V-III for the primary and secondary stars, respectively. Projected rotational velocities of 166 ± 10 and $95 \pm 9\,\mathrm{km\,s^{-1}}$ were derived for the primary and secondary stars, respectively. The analysis of these spectra by means of the `CMFGEN` model atmosphere code further allowed us to determine the stellar and wind properties of the system, notably the effective temperature, $T_{\mathrm{eff},1} = 30\,900 \pm 1000\,\mathrm{K}$, of the primary star.

The orbital inclination, the secondary effective temperature, and the Roche-lobe filling factors of both stars were constrained through the analysis of the light curve by means of the `Nightfall` code. We determined an inclination of $(89.58^{+0.42}_{-2.28})°$ and a secondary effective temperature of $21\,697 \pm 1000\,\mathrm{K}$. Mean stellar radii of $9.40^{+0.14}_{-0.15}$ and $3.69 \pm 0.06\ \mathcal{R}^{\mathrm{N}}_{\odot}$ were inferred for the primary and secondary stars, respectively. Masses of 18.64 ± 0.47 and $7.70 \pm 0.12\ \mathcal{M}^{\mathrm{N}}_{\odot}$ were obtained for the primary and secondary stars, respectively. Radial velocity data from the literature and redetermined in this paper allowed us to establish a rate of apsidal motion of $(1.198 \pm 0.300)°\,\mathrm{yr^{-1}}$, an eccentricity of $0.072^{+0.004}_{-0.005}$, and an orbital period of $4.24046^{+0.00005}_{-0.00004}$ days. We further showed that the longitude of periastron derived based on the photometric observations, either through the fit of the light curves or the fit of the times of photometric minima, were in agreement with the values derived from the radial velocity analysis, enforcing the robustness of the present analysis. The analysis of the Rossiter-McLaughlin effect constrained the misalignment angle of the primary stellar rotation axis with respect to the normal to the orbital plane to a value of $\alpha \leq 15°$, or equivalently, $\alpha \geq 165°$.

The properties of HD 152219 render the system an interesting target to study tidally-induced apsidal motion from a theoretical point of view. In Chapter 3, we use stellar evolution models to determine theoretical rates of apsidal motion and compare them to the observed rate.

2.4. The high rate apsidal motion binary: CPD-41° 7742

The methodology presented in Chapter 1, Section 1.2.3, highlighted in orange in Figure 1.9, is applied to the binary system CPD-41° 7742. The spectroscopic analysis is performed in Section 2.4.1, where the reconstruction of the individual components spectra together with the establishment of their radial velocities are performed by means of a disentangling code. Subsequent analyses of these spectra are carried out to reassess the spectral classification of the stars and to determine their properties as well as their wind characteristics. The radial velocity measurements of the binary system are analysed in Section 2.4.2 to determine notably the orbital period of the system. The optical photometry is analysed in Section 2.4.3 by means of the `Nightfall` binary star code, and the phase shifts between the primary and secondary eclipses are used to infer the rate of apsidal motion and the orbital eccentricity of the system. The orbital parameters and physical properties are derived in Section 2.4.4. The main conclusions are drawn in Section 2.4.5. The most important results of this section are presented in Rosu et al. (2022b).

2.4.1. Spectroscopic analysis

This section is devoted to the spectral analysis of the binary system CPD-41° 7742. The extensive set of observational spectroscopic data we used is introduced. Spectral disentangling is performed to reconstruct the individual spectra as well as to determine the radial velocities of the stars over the orbital cycle. The spectral classification is reassessed and the projected rotational velocities are derived for both stars. The fundamental properties of the stars and their winds are constrained through the fit of the individual spectra with synthetic `CMFGEN` spectra.

2.4.1.1. Observational data

The set of spectroscopic data of CPD-41° 7742 in the optical domain consists of hundred sixty-six medium-high resolution spectra collected between May 1999 and September 2017. Twenty-six out of these were obtained with the FEROS Spectrograph between May 1999 and April 2002. We refer to Section 2.2.1.1 for more information about the instrumentation. Exposure times of the observations were of thirty minutes, resulting in typical signal to noise ratio of 150 and 180 at 4200 Å and 6000 Å, respectively. The FEROS pipeline of the `MIDAS` software was used to reduce the FEROS data. Forty-one spectra were obtained with the High Accuracy Radial velocity Planet Searcher (HARPS) spectrograph attached to the Cassegrain focus of the ESO 3.6 m telescope in La Silla during five consecutive nights in April 2009. The HARPS instrument has a spectral resolving power of 115 000 (Mayor et al. 2003). Its detector consists of a mosaic of two CCDs detectors that have all together 4096×4096 pixels of $15 \times 15\,\mu$m. The wavelength domain, covered by seventy-two orders, ranges from 3780 to 6910 Å, with a small gap between 5300 and 5330 Å. Exposure times of the observations were 300 seconds. The remaining ninety-nine spectra were obtained with the GIRAFFE spectrograph mounted on the ESO Very Large Telescope (VLT) at Cerro Paranal (Pasquini et al. 2002), between April and September 2017. The GIRAFFE instrument has a spectral

resolving power of 6300 and its EEV CCD detector has 2048×4096 pixels of $15 \times 15\,\mu$m. The wavelength domain ranges from 3950 to 4572 Å. Exposure times of the observations range between 220 and 595 seconds. Both HARPS and GIRAFFE spectra provided in the archive were already reduced using the dedicated pipelines. The pre-processing of all these observations was performed following the methodology outlined in Section 2.1.1.

2.4.1.2. Spectral disentangling

The spectral disentangling was performed following the methodology outlined in Section 2.1.2. For the cross-correlation, we used `TLUSTY` synthetic spectra having $T_{\rm eff} = 30\,000$ K, $\log g = 3.75$, and $v_{\rm eq} \sin i_{\rm rot} = 160\,{\rm km\,s^{-1}}$ for the primary star and $T_{\rm eff} = 21\,000$ K, $\log g = 4.00$, and $v_{\rm eq} \sin i_{\rm rot} = 160\,{\rm km\,s^{-1}}$ for the secondary star. The initial input values for the radial velocities were estimated using a Gaussian fitting of the He I λ 4026 line on the spectra.

Contrary to HD 152248 and HD 152219 (see discussions in Sections 2.2.1.2 and 2.3.1.2, respectively), we could use, in the case of CPD-41° 7742, all the available spectra, even those taken near conjunction phase. Indeed, we verified that the spectra taken near conjunction phase did not bias the reconstruction of the spectra of the binary components by comparing the reconstructed spectra with and without the observations taken near conjunction phase. Like in the case of HD 152219 (see Section 2.3.1.2), the Hα and He II λ 4686 lines are not seen in emission and there is therefore no problem of reconstruction of these lines.

The spectral disentangling was performed separately over the following eight wavelength domains: A0 [3810:3920] Å, A1 [3990:4400] Å, A2 [4300:4565] Å, A3 [4570:5040] Å, A4 [5380:5860] Å, A5 [5832:5885] Å, A6 [6450:6720] Å, and A7 [7025:7095] Å. The GIRAFFE spectra only cover the A1 and A2 domains, the HARPS spectra cover all domains except for the A7 domain, whilst the FEROS spectra cover all wavelength domains. As in the cases of HD 152248 and HD 152219, the presence of interstellar lines or diffuse interstellar bands close to spectral lines in the spectral domain A4 affects the quality of the resulting reconstructed spectra. In this case, the disentangling code erroneously associated some of the line flux of the non-moving interstellar medium to the stars. In addition, an insufficient number of spectral lines – especially lines of the secondary star – are present in the A4 and A5 domains. These two situations can affect the determination of the stellar radial velocities. Therefore, we proceeded as follows: We first processed the wavelength domains (A0, A1, A2, A3, A6, and A7) for which the code was able to reproduce the individual spectra and simultaneously estimate the radial velocities of the stars. We present the convergence of the radial velocities as a function of the number of iterations in the A1-domain for the primary and secondary stars in Figure 2.39. The convergence is effectively ensured after sixty iterations, as advocated in Section 2.1.2.2. We observed the same trend for the five other domains. We then computed a weighted-average mean of the stellar radial velocities. The radial velocities from the individual wavelength domains were weighted according to the number of strong primary lines present in these domains (three lines for A0, six lines for A1, three lines for A2, four lines for A3, two lines for A6, and one line for A7). The radial velocities obtained for each wavelength domain are presented as a function of the phase, adopting the orbital period derived from the radial velocity analysis in Section 2.4.2,

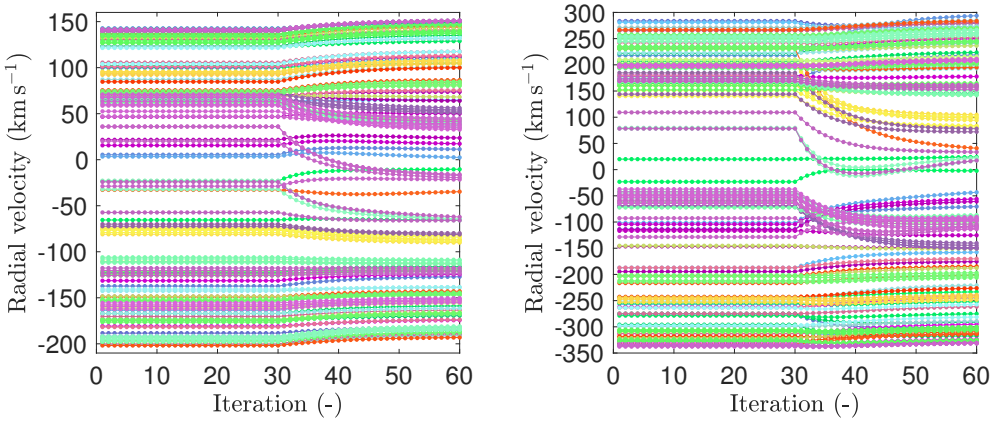

(a) Primary star. (b) Secondary star.

Figure 2.39. Convergence of the radial velocities as a function of the number of iterations in the disentangling method applied in the A1-domain for (a) the primary star and (b) the secondary star of CPD-41° 7742. Each line corresponds to one particular spectrum.

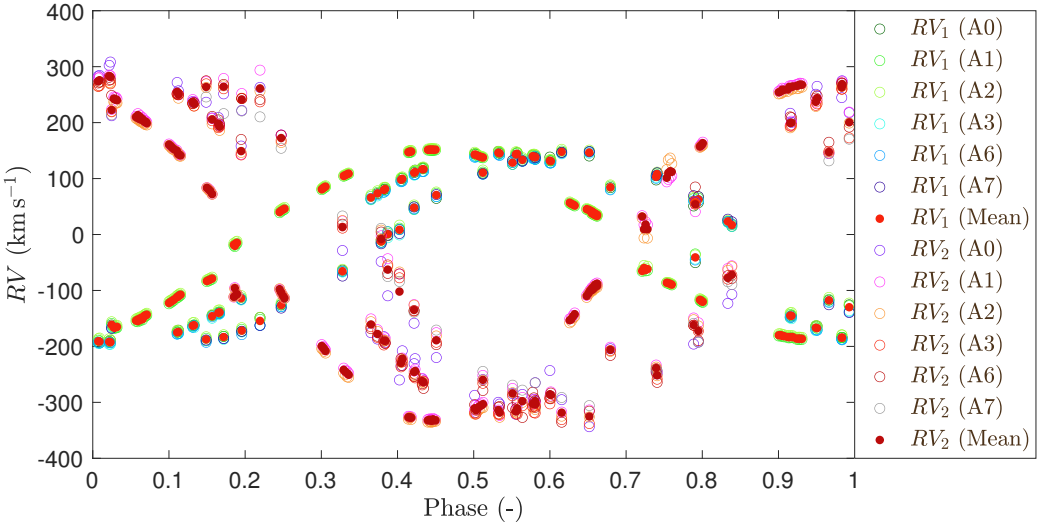

Figure 2.40. Radial velocities of both stars of CPD-41° 7742 as a function of the phase obtained for each of the six wavelength domains A0, A1, A2, A3, A6, and A7 and mean value of the radial velocities over these six domains. The observational phase is computed with the orbital period determined in Section 2.4.2, Table 2.37.

in Figure 2.40 together with the mean value over the six domains. The differences in radial velocities mainly come from the fact that these are estimated on different lines which form in different layers of the stellar atmosphere, therefore having a different velocity. The resulting radial velocities of both stars are reported in Table 2.32 together with their 1σ errors. We finally performed the disentangling on the remaining two domains (A4 and A5) with the radial velocities fixed to these weighted averages, and, for the A4 domain only, using a version of the code designed to deal with a third spectral component.

2.4.1.3. Spectral classification and absolute magnitudes

The reconstructed spectra of the binary components of CPD-41° 7742 allowed us to reassess the spectral classification of the stars.

For the primary star, we used Conti's criterion (Conti & Alschuler 1971) complemented by Mathys (1988, see Table 2.1 in Section 2.1.3) to determine the spectral type of the star. We found that $\log W'$ amounts to 0.58 ± 0.01, which corresponds to spectral type O9.5. We complemented this criterion with Sota's criteria (Sota et al. 2011, 2014, see Table 2.2 in Section 2.1.3) based on the ratios between the intensities of several lines: The ratio He II λ 4542/He I λ 4388 amounts to 0.66 ± 0.01, the ratio He II λ 4200/He I λ 4144 amounts to 0.75 ± 0.01 and the ratio Si III λ 4552/He II λ 4542 amounts to 0.44 ± 0.01. All three ratios being lower than unity, the spectral type O9.7 is clearly excluded and the spectral type O9.5 is confirmed. To assess the luminosity class of the primary star, we used Conti's criterion (Conti & Alschuler 1971, see Table 2.4 in Section 2.1.3) and found that $\log W''$ amounts to 0.08 ± 0.01, which corresponds to the main sequence luminosity class V. This is confirmed by the appearance of the spectral lines Si IV λ 4116 and He I λ 4121 of the same strength and weaker than Hδ in line with expectations for luminosity class V (see the spectral atlas of Gray (2009) for spectral type O9).

For the secondary star, we used the spectral atlas of Gray (2009). As He II lines are absent in the spectrum, spectral type O is excluded. Qualitatively, the ratio between the strengths of the He I λ 4471 and Mg II λ 4481 lines suggests a spectral type between B1 V and B3 V. This statement is confirmed by the fact that the Si II $\lambda\lambda$ 4128-32 lines are only marginally present but should be clearly visible for spectral types later than B2.5. In addition, the Si IV λ 4089 line is clearly visible but weaker than the Si III λ 4552 line, suggesting a spectral type B1, with an uncertainty of one spectral type. However, using the spectral atlas of Walborn & Fitzpatrick (1990), a B2 V class is favoured as the strengths of the He I $\lambda\lambda$ 4387, 4471 lines are nearly identical, the strength of the O II λ 4416 line is much weaker than the strength of the He I λ 4387 line, and the strength of the He I λ 4713 line exceeds those of the O II $\lambda\lambda$ 4639-42, N II λ 4630, and C III λ 4647 lines. Regarding the luminosity class, the ratio of the strengths of the Si III λ 4552 and He I λ 4387 lines suggests a main-sequence star (class V). Furthermore, the O II λ 4348 line is barely visible, the O II λ 4416 line is weak, and the Balmer lines are wide, which confirms that the secondary star is of luminosity class V. In conclusion, the secondary star is a B1–2 V star, in agreement with previous studies (see discussion in Section 1.3.3).

The brightness ratio in the visible domain was estimated based on the ratio between the EWs of the spectral lines of the secondary star and `TLUSTY` synthetic spectra of similar effective temperatures. We did not apply this technique to the primary star because the

Table 2.32. Journal of the spectroscopic observations of CPD-41° 7742. Column 1 gives the heliocentric Julian date (HJD) of the observations at mid-exposure. Column 2 gives the observational phase ϕ computed with the orbital period determined in Section 2.4.2, Table 2.37. Columns 3 and 4 give the radial velocities RV_1 and RV_2 of the primary and secondary stars, respectively, with their 1σ uncertainties. Column 5 provides information about the instrumentation.

HJD $-2\,450\,000$	ϕ	RV_1 (km s^{-1})	RV_2 (km s^{-1})	Instrumentation
1299.843	0.172	-183.3 ± 1.2	264.2 ± 5.7	ESO 1.5 m + FEROS
1300.841	0.581	138.3 ± 1.4	-303.7 ± 4.1	ESO 1.5 m + FEROS
1301.847	0.993	-129.9 ± 2.3	200.5 ± 8.9	ESO 1.5 m + FEROS
1302.847	0.403	8.5 ± 2.5	-102.0 ± 28.1	ESO 1.5 m + FEROS
1304.841	0.219	-154.4 ± 2.5	261.1 ± 12.0	ESO 1.5 m + FEROS
1327.863	0.652	146.7 ± 1.4	-325.2 ± 5.6	ESO 1.5 m + FEROS
1668.928	0.387	0.5 ± 1.8	-62.7 ± 9.9	ESO 1.5 m + FEROS
1669.791	0.741	108.2 ± 1.0	-251.6 ± 3.0	ESO 1.5 m + FEROS
1669.923	0.795	62.8 ± 1.5	-172.3 ± 6.2	ESO 1.5 m + FEROS
1670.787	0.149	-187.6 ± 1.3	263.7 ± 5.6	ESO 1.5 m + FEROS
1670.901	0.196	-171.8 ± 1.5	241.5 ± 4.7	ESO 1.5 m + FEROS
1671.800	0.564	133.5 ± 1.1	-298.0 ± 4.7	ESO 1.5 m + FEROS
1671.926	0.615	147.8 ± 1.1	-318.4 ± 5.2	ESO 1.5 m + FEROS
1672.782	0.966	-117.6 ± 1.2	147.4 ± 2.2	ESO 1.5 m + FEROS
1672.925	0.025	-161.3 ± 1.5	222.5 ± 3.3	ESO 1.5 m + FEROS
2037.792	0.512	110.4 ± 1.1	-259.8 ± 3.6	ESO 1.5 m + FEROS
2037.887	0.551	128.4 ± 1.1	-283.8 ± 4.0	ESO 1.5 m + FEROS
2039.783	0.328	-65.6 ± 0.8	13.2 ± 7.8	ESO 1.5 m + FEROS
2039.907	0.379	-12.4 ± 1.0	-8.1 ± 7.3	ESO 1.5 m + FEROS
2040.788	0.739	103.2 ± 1.4	-238.7 ± 2.1	ESO 1.5 m + FEROS
2040.908	0.789	61.2 ± 2.1	-161.7 ± 6.8	ESO 1.5 m + FEROS
2337.860	0.451	70.6 ± 1.7	-189.0 ± 6.8	ESO 1.5 m + FEROS
2338.794	0.834	23.5 ± 0.5	-77.7 ± 9.2	ESO 1.5 m + FEROS
2381.723	0.422	48.1 ± 1.3	-135.0 ± 5.0	ESO 1.5 m + FEROS
2382.741	0.839	16.9 ± 0.8	-71.9 ± 7.9	ESO 1.5 m + FEROS
2383.738	0.247	-126.1 ± 1.1	172.4 ± 2.7	ESO 1.5 m + FEROS
4924.888	0.365	66.0 ± 1.5	-160.8 ± 4.4	ESO 3.6 m + HARPS
4924.909	0.374	73.6 ± 1.5	-177.8 ± 3.4	ESO 3.6 m + HARPS
4925.655	0.679	84.4 ± 1.4	-206.1 ± 2.0	ESO 3.6 m + HARPS
4925.927	0.791	-40.9 ± 2.8	53.9 ± 5.6	ESO 3.6 m + HARPS
4926.708	0.111	-174.9 ± 1.1	255.0 ± 3.1	ESO 3.6 m + HARPS
4926.712	0.112	-174.2 ± 1.0	250.0 ± 1.6	ESO 3.6 m + HARPS
4926.758	0.131	-163.0 ± 1.0	237.1 ± 1.6	ESO 3.6 m + HARPS
4926.762	0.133	-162.1 ± 1.3	233.9 ± 1.7	ESO 3.6 m + HARPS
4926.820	0.157	-146.0 ± 1.0	205.5 ± 1.7	ESO 3.6 m + HARPS
4926.840	0.165	-139.9 ± 1.2	198.0 ± 2.7	ESO 3.6 m + HARPS
4926.844	0.166	-139.0 ± 1.0	192.8 ± 1.3	ESO 3.6 m + HARPS
4926.913	0.195	-113.9 ± 1.2	149.0 ± 3.7	ESO 3.6 m + HARPS
4927.661	0.501	142.9 ± 1.2	-310.6 ± 4.8	ESO 3.6 m + HARPS
4927.665	0.503	142.5 ± 1.2	-314.1 ± 3.6	ESO 3.6 m + HARPS
4927.737	0.532	146.2 ± 1.0	-313.7 ± 3.1	ESO 3.6 m + HARPS
4927.741	0.534	145.1 ± 1.1	-318.4 ± 3.6	ESO 3.6 m + HARPS

Table 2.32. Continued.

HJD $-2\,450\,000$	ϕ	RV_1 (km s^{-1})	RV_2 (km s^{-1})	Instrumentation
4927.793	0.555	143.1 ± 1.2	-316.4 ± 1.8	ESO 3.6 m + HARPS
4927.797	0.557	144.3 ± 1.2	-311.2 ± 3.4	ESO 3.6 m + HARPS
4927.847	0.577	140.0 ± 1.3	-302.6 ± 2.8	ESO 3.6 m + HARPS
4927.851	0.579	139.0 ± 1.5	-301.8 ± 4.6	ESO 3.6 m + HARPS
4927.855	0.581	138.0 ± 1.1	-297.7 ± 6.4	ESO 3.6 m + HARPS
4927.902	0.600	131.9 ± 1.5	-285.5 ± 8.2	ESO 3.6 m + HARPS
4927.905	0.601	131.1 ± 1.1	-286.8 ± 2.4	ESO 3.6 m + HARPS
4928.676	0.917	-145.4 ± 1.6	199.8 ± 2.0	ESO 3.6 m + HARPS
4928.672	0.915	-144.9 ± 1.4	199.3 ± 3.9	ESO 3.6 m + HARPS
4928.754	0.949	-166.7 ± 1.5	237.1 ± 3.1	ESO 3.6 m + HARPS
4928.758	0.951	-167.3 ± 1.2	243.7 ± 4.4	ESO 3.6 m + HARPS
4928.837	0.983	-184.4 ± 1.2	262.9 ± 4.1	ESO 3.6 m + HARPS
4928.838	0.983	-184.4 ± 1.1	269.0 ± 2.7	ESO 3.6 m + HARPS
4928.896	0.007	-190.8 ± 1.4	273.5 ± 3.6	ESO 3.6 m + HARPS
4928.900	0.009	-191.3 ± 1.4	275.8 ± 3.2	ESO 3.6 m + HARPS
4928.896	0.007	-190.8 ± 1.4	273.5 ± 3.6	ESO 3.6 m + HARPS
4928.900	0.009	-191.3 ± 1.4	275.8 ± 3.2	ESO 3.6 m + HARPS
4928.931	0.022	-191.7 ± 1.4	283.1 ± 4.2	ESO 3.6 m + HARPS
4928.935	0.023	-192.5 ± 1.2	281.6 ± 5.6	ESO 3.6 m + HARPS
4929.811	0.382	79.7 ± 1.3	-189.6 ± 2.2	ESO 3.6 m + HARPS
4929.815	0.384	81.5 ± 1.3	-190.1 ± 2.1	ESO 3.6 m + HARPS
4929.866	0.405	97.8 ± 1.3	-229.7 ± 2.2	ESO 3.6 m + HARPS
4929.870	0.406	99.5 ± 1.1	-222.1 ± 3.1	ESO 3.6 m + HARPS
4929.908	0.422	110.4 ± 1.3	-245.8 ± 3.3	ESO 3.6 m + HARPS
4929.911	0.423	111.7 ± 1.5	-243.9 ± 5.0	ESO 3.6 m + HARPS
4929.934	0.432	116.6 ± 1.2	-261.9 ± 2.3	ESO 3.6 m + HARPS
4929.938	0.434	116.7 ± 1.3	-263.8 ± 1.6	ESO 3.6 m + HARPS
7845.767	0.059	-154.7 ± 1.1	213.5 ± 2.4	ESO VLT + GIRAFFE
7845.774	0.062	-152.7 ± 1.1	210.1 ± 2.4	ESO VLT + GIRAFFE
7845.782	0.065	-151.2 ± 1.2	206.2 ± 2.6	ESO VLT + GIRAFFE
7919.650	0.329	104.6 ± 0.5	-241.8 ± 2.8	ESO VLT + GIRAFFE
7919.655	0.331	106.0 ± 0.5	-245.3 ± 2.5	ESO VLT + GIRAFFE
7919.661	0.334	107.8 ± 0.4	-247.7 ± 3.2	ESO VLT + GIRAFFE
7919.666	0.336	108.9 ± 0.5	-250.6 ± 2.2	ESO VLT + GIRAFFE
7920.685	0.753	-86.2 ± 0.3	101.4 ± 6.9	ESO VLT + GIRAFFE
7920.690	0.755	-86.8 ± 0.6	110.1 ± 11.0	ESO VLT + GIRAFFE
7920.696	0.758	-88.2 ± 0.5	113.1 ± 11.1	ESO VLT + GIRAFFE
7920.701	0.760	-89.6 ± 0.5	112.0 ± 6.9	ESO VLT + GIRAFFE
7926.534	0.150	-83.1 ± 1.0	83.7 ± 0.2	ESO VLT + GIRAFFE
7926.540	0.152	-81.6 ± 1.0	80.7 ± 0.5	ESO VLT + GIRAFFE
7926.545	0.154	-80.2 ± 0.9	77.8 ± 0.3	ESO VLT + GIRAFFE
7926.551	0.157	-78.6 ± 1.1	72.1 ± 0.1	ESO VLT + GIRAFFE
7929.683	0.440	151.5 ± 0.6	-332.1 ± 1.5	ESO VLT + GIRAFFE
7929.688	0.442	151.6 ± 0.3	-331.1 ± 1.4	ESO VLT + GIRAFFE
7929.694	0.444	151.5 ± 0.8	-332.6 ± 1.5	ESO VLT + GIRAFFE
7929.699	0.446	151.5 ± 0.8	-330.3 ± 1.6	ESO VLT + GIRAFFE

Table 2.32. Continued.

HJD $-2\,450\,000$	ϕ	RV_1 ($\mathrm{km\,s^{-1}}$)	RV_2 ($\mathrm{km\,s^{-1}}$)	Instrumentation
7932.578	0.626	56.8 ± 0.6	-153.1 ± 2.2	ESO VLT + GIRAFFE
7932.583	0.628	54.8 ± 0.6	-151.4 ± 1.7	ESO VLT + GIRAFFE
7932.589	0.630	53.4 ± 0.7	-146.2 ± 1.5	ESO VLT + GIRAFFE
7932.594	0.633	51.7 ± 0.6	-142.4 ± 2.0	ESO VLT + GIRAFFE
7934.725	0.506	140.5 ± 0.6	-309.5 ± 2.4	ESO VLT + GIRAFFE
7934.730	0.508	139.5 ± 0.6	-307.0 ± 2.4	ESO VLT + GIRAFFE
7934.736	0.510	138.3 ± 0.6	-305.2 ± 2.3	ESO VLT + GIRAFFE
7934.741	0.512	137.7 ± 0.5	-303.2 ± 3.0	ESO VLT + GIRAFFE
7946.706	0.414	147.2 ± 0.9	-326.6 ± 1.6	ESO VLT + GIRAFFE
7946.709	0.415	147.5 ± 0.8	-326.4 ± 0.5	ESO VLT + GIRAFFE
7946.712	0.417	148.3 ± 0.8	-327.0 ± 0.1	ESO VLT + GIRAFFE
7946.715	0.418	148.3 ± 0.9	-327.4 ± 1.5	ESO VLT + GIRAFFE
7947.640	0.797	-116.8 ± 0.9	157.2 ± 0.7	ESO VLT + GIRAFFE
7947.643	0.798	-118.1 ± 1.0	159.1 ± 0.8	ESO VLT + GIRAFFE
7947.646	0.799	-119.4 ± 0.9	160.4 ± 0.9	ESO VLT + GIRAFFE
7947.649	0.801	-120.2 ± 1.1	163.3 ± 1.6	ESO VLT + GIRAFFE
7950.644	0.028	-166.5 ± 1.1	243.0 ± 2.8	ESO VLT + GIRAFFE
7950.647	0.029	-166.2 ± 1.0	241.3 ± 3.0	ESO VLT + GIRAFFE
7950.651	0.031	-165.7 ± 1.2	241.6 ± 3.2	ESO VLT + GIRAFFE
7950.654	0.032	-165.1 ± 1.3	240.0 ± 2.3	ESO VLT + GIRAFFE
7955.622	0.067	-146.1 ± 0.9	202.6 ± 1.7	ESO VLT + GIRAFFE
7955.625	0.068	-145.1 ± 1.0	201.2 ± 2.1	ESO VLT + GIRAFFE
7955.628	0.070	-144.4 ± 1.1	201.6 ± 1.2	ESO VLT + GIRAFFE
7955.631	0.071	-143.2 ± 1.2	199.0 ± 1.5	ESO VLT + GIRAFFE
7957.713	0.924	-186.1 ± 1.0	265.7 ± 2.4	ESO VLT + GIRAFFE
7957.719	0.926	-186.1 ± 1.2	266.5 ± 2.6	ESO VLT + GIRAFFE
7957.724	0.928	-186.2 ± 1.2	268.2 ± 2.1	ESO VLT + GIRAFFE
7957.730	0.931	-186.4 ± 1.2	267.7 ± 2.1	ESO VLT + GIRAFFE
7963.514	0.301	80.8 ± 0.6	-199.2 ± 2.3	ESO VLT + GIRAFFE
7963.518	0.302	82.6 ± 0.7	-202.1 ± 1.5	ESO VLT + GIRAFFE
7963.522	0.304	84.3 ± 0.7	-204.8 ± 1.9	ESO VLT + GIRAFFE
7963.526	0.305	85.6 ± 0.7	-208.1 ± 1.8	ESO VLT + GIRAFFE
7971.685	0.648	45.3 ± 0.5	-109.9 ± 1.2	ESO VLT + GIRAFFE
7971.691	0.651	44.3 ± 0.4	-105.1 ± 0.9	ESO VLT + GIRAFFE
7971.696	0.653	42.8 ± 0.4	-100.4 ± 0.8	ESO VLT + GIRAFFE
7971.702	0.655	41.1 ± 0.3	-99.3 ± 1.0	ESO VLT + GIRAFFE
7982.576	0.110	-112.1 ± 1.2	149.7 ± 0.8	ESO VLT + GIRAFFE
7982.580	0.112	-110.9 ± 1.3	144.2 ± 0.5	ESO VLT + GIRAFFE
7982.584	0.114	-108.7 ± 1.1	142.7 ± 1.1	ESO VLT + GIRAFFE
7982.588	0.115	-107.5 ± 1.2	141.3 ± 0.6	ESO VLT + GIRAFFE
7998.551	0.655	40.5 ± 0.5	-96.2 ± 1.3	ESO VLT + GIRAFFE
7998.556	0.657	38.8 ± 0.3	-93.6 ± 0.8	ESO VLT + GIRAFFE
7998.561	0.659	37.4 ± 0.2	-89.6 ± 1.1	ESO VLT + GIRAFFE
7998.567	0.662	35.3 ± 0.4	-88.0 ± 1.1	ESO VLT + GIRAFFE
8001.590	0.900	-180.0 ± 1.2	254.4 ± 1.5	ESO VLT + GIRAFFE
8001.596	0.903	-179.9 ± 1.1	255.8 ± 1.9	ESO VLT + GIRAFFE

Table 2.32. Continued.

HJD $-2\,450\,000$	ϕ	RV_1 ($\mathrm{km\,s^{-1}}$)	RV_2 ($\mathrm{km\,s^{-1}}$)	Instrumentation
8001.601	0.905	-181.1 ± 1.1	258.9 ± 2.4	ESO VLT + GIRAFFE
8001.607	0.907	-181.7 ± 1.1	258.6 ± 1.6	ESO VLT + GIRAFFE
8001.619	0.912	-183.3 ± 1.1	259.4 ± 1.6	ESO VLT + GIRAFFE
8001.624	0.914	-183.4 ± 1.3	263.9 ± 1.5	ESO VLT + GIRAFFE
8001.630	0.917	-183.2 ± 1.1	263.8 ± 2.2	ESO VLT + GIRAFFE
8001.635	0.919	-183.4 ± 1.1	264.6 ± 1.7	ESO VLT + GIRAFFE
8003.593	0.721	-65.1 ± 0.7	32.3 ± 1.3	ESO VLT + GIRAFFE
8003.599	0.724	-59.9 ± 2.2	9.6 ± 7.4	ESO VLT + GIRAFFE
8003.604	0.726	-63.4 ± 1.5	17.9 ± 4.5	ESO VLT + GIRAFFE
8003.610	0.728	-61.8 ± 2.4	9.5 ± 7.5	ESO VLT + GIRAFFE
8004.518	0.100	-122.4 ± 1.3	160.9 ± 0.8	ESO VLT + GIRAFFE
8004.523	0.102	-120.5 ± 1.3	158.4 ± 0.9	ESO VLT + GIRAFFE
8004.528	0.104	-118.8 ± 1.2	155.4 ± 1.0	ESO VLT + GIRAFFE
8004.534	0.107	-116.3 ± 1.2	152.5 ± 0.7	ESO VLT + GIRAFFE
8014.489	0.185	-18.2 ± 1.2	-111.6 ± 0.2	ESO VLT + GIRAFFE
8014.492	0.186	-20.2 ± 1.2	-95.8 ± 0.7	ESO VLT + GIRAFFE
8014.496	0.188	-15.8 ± 1.3	-108.0 ± 0.1	ESO VLT + GIRAFFE
8014.499	0.189	-14.7 ± 1.2	-106.4 ± 0.1	ESO VLT + GIRAFFE
8017.559	0.443	151.6 ± 0.9	-332.1 ± 1.1	ESO VLT + GIRAFFE
8017.565	0.445	151.4 ± 0.8	-332.5 ± 0.8	ESO VLT + GIRAFFE
8017.570	0.447	151.3 ± 0.8	-331.7 ± 1.2	ESO VLT + GIRAFFE
8017.576	0.450	151.7 ± 0.7	-332.1 ± 0.8	ESO VLT + GIRAFFE
8019.517	0.245	40.1 ± 1.0	-97.7 ± 0.4	ESO VLT + GIRAFFE
8019.522	0.247	42.5 ± 1.1	-103.6 ± 0.1	ESO VLT + GIRAFFE
8019.528	0.250	44.6 ± 1.0	-109.6 ± 0.1	ESO VLT + GIRAFFE
8019.533	0.252	46.1 ± 1.1	-113.9 ± 0.0	ESO VLT + GIRAFFE
8020.517	0.655	38.0 ± 0.5	-98.2 ± 0.8	ESO VLT + GIRAFFE
8020.523	0.657	36.1 ± 0.4	-96.7 ± 1.0	ESO VLT + GIRAFFE
8020.528	0.659	34.6 ± 0.3	-93.7 ± 1.0	ESO VLT + GIRAFFE
8020.534	0.662	33.1 ± 0.4	-91.8 ± 1.2	ESO VLT + GIRAFFE
8021.498	0.057	-153.8 ± 1.3	210.1 ± 1.1	ESO VLT + GIRAFFE
8021.503	0.059	-152.1 ± 1.2	208.5 ± 1.2	ESO VLT + GIRAFFE
8021.509	0.061	-150.8 ± 1.1	206.5 ± 1.5	ESO VLT + GIRAFFE
8021.514	0.063	-149.1 ± 1.2	205.4 ± 1.9	ESO VLT + GIRAFFE

uncertainties on the brightness ratio determined in this manner are on the order of the contribution of the secondary star, as it was already observed in the case of HD 152219 (see Section 2.3.1.3). For this purpose, we used the Hβ, He I $\lambda\lambda$ 4026, 4144, 4471, 4922, 5016, 5876 lines (see Table 2.33). The ratio $\mathrm{EW_{TLUSTY}/EW_{sec}} = (l_1 + l_2)/l_2$ is equal to 6.73 ± 1.02, 6.62 ± 0.94, 6.42 ± 0.89, 6.24 ± 0.97, and 5.97 ± 0.87 for $T_{\rm eff}$ of 20 000, 21 000, 22 000, 23 000, and 24 000 K, respectively. As these values are very similar, we took the value for the TLUSTY spectrum of 22 000 K, which corresponds to the temperature of a B1.5 V star as inferred by Humphreys & McElroy (1984), and derived a value for l_2/l_1 of 0.18 ± 0.03. This brightness ratio is applied to the reconstructed spectra of the stars through the relations (2.7) and (2.8) recalled in Section 2.1.2.2.

Table 2.33. Equivalent widths of the lines used to determine the brightness ratio in the visible domain of the binary system CPD-41° 7742 based on the secondary star. Column 1 provides the line used, Column 2 indicates the EWs of the secondary spectral lines, and Columns 3 to 7 indicate the ratio between the EWs of TLUSTY spectral lines and the secondary spectral lines for TLUSTY spectra of 20 000, 21 000, 22 000, 23 000, and 24 000 K, respectively.

Line	EW_{sec}	$\frac{EW_{TLUSTY}}{EW_{sec}}$ (20 000 K)	$\frac{EW_{TLUSTY}}{EW_{sec}}$ (21 000 K)	$\frac{EW_{TLUSTY}}{EW_{sec}}$ (22 000 K)	$\frac{EW_{TLUSTY}}{EW_{sec}}$ (23 000 K)	$\frac{EW_{TLUSTY}}{EW_{sec}}$ (24 000 K)
Hβ	0.51	8.31	8.02	7.65	7.85	7.32
He I λ 4026	0.18	6.83	6.76	6.57	6.31	5.96
He I λ 4144	0.10	5.82	5.74	5.54	5.28	4.89
He I λ 4471	0.18	6.64	6.61	6.45	6.32	6.22
He I λ 4922	0.12	7.76	7.55	7.44	7.06	6.71
He I λ 5016	0.05	6.37	6.28	6.02	5.70	5.62
He I λ 5876	0.12	5.41	5.37	5.29	5.18	5.09
Mean	/	6.73 ± 1.02	6.62 ± 0.94	6.42 ± 0.89	6.24 ± 0.97	5.97 ± 0.87

The third *Gaia* data release (EDR3, Gaia Collaboration 2021) quotes a parallax of $\varpi = 0.6452 \pm 0.0231$ mas, corresponding to a distance of 1489^{+64}_{-61} pc (Bailer-Jones et al. 2021). From this distance, we derived a distance modulus of 10.87 ± 0.09. Zacharias et al. (2013) reported mean V and B magnitudes of 8.80 and 9.02, respectively. For these two values, we estimated errors of 0.01. Adopting a value of -0.26 ± 0.01 for the intrinsic colour index $(B-V)_0$ of an O9.5 V star (Martins & Plez 2006) and assuming the reddening factor in the V-band R_V equal to 3.3 ± 0.1 for NGC 6231 (Sung et al. 1998), we obtained an absolute magnitude in the V-band of the binary system $M_V = -3.65 \pm 0.12$. The brightness ratio then yields individual absolute magnitudes $M_{V,1} = -3.47 \pm 0.12$ and $M_{V,2} = -1.63 \pm 0.19$ for the primary and secondary stars, respectively.

Comparing the magnitude obtained for the primary star to those reported by Martins & Plez (2006) shows that the primary is slightly less luminous than a 'typical' O9.5 V star. Likewise, comparing the magnitude obtained for the secondary star to those reported by Humphreys & McElroy (1984) shows that the secondary is fainter than expected for B1–2 V type stars. These comparisons clearly rule out luminosity classes III-II for both stars.

2.4.1.4. Projected rotational velocities

The projected rotational velocities of both stars were derived using the Fourier transform method as explained in Section 2.1.6. We applied this method to thirteen well-isolated spectral lines of the primary star which are expected to be free of blends, five metallic lines and eight He I lines, and to nine well-isolated lines of the secondary star, three metallic lines and six He I lines. The results are presented in Table 2.34, and the Fourier transforms are illustrated for the different lines in Figure 2.41 for the primary and secondary stars. The mean $v_{eq} \sin i_{rot}$ computed on metallic lines alone or on all the lines agree very well. We adopted a mean $v_{eq} \sin i_{rot}$ of 140 ± 7 km s^{-1} for the primary star and of 89 ± 7 km s^{-1} for the secondary star. The value of $v_{eq} \sin i_{rot}$ for the primary star agrees with the value obtained by Levato & Morrell (1983).

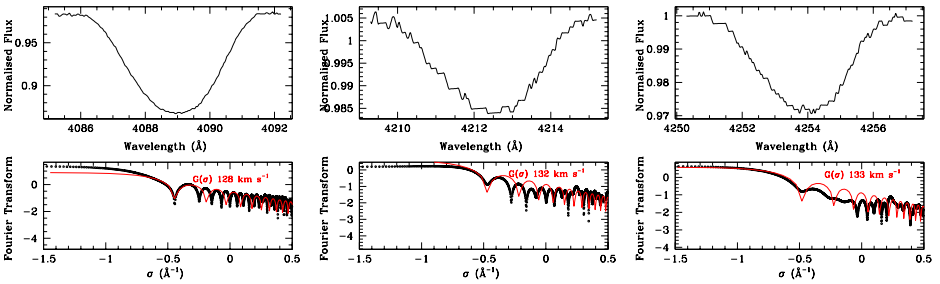

(a) Primary – Si IV λ 4089 line. (b) Primary – Si IV λ 4212 line. (c) Primary – O II λ 4254 line.

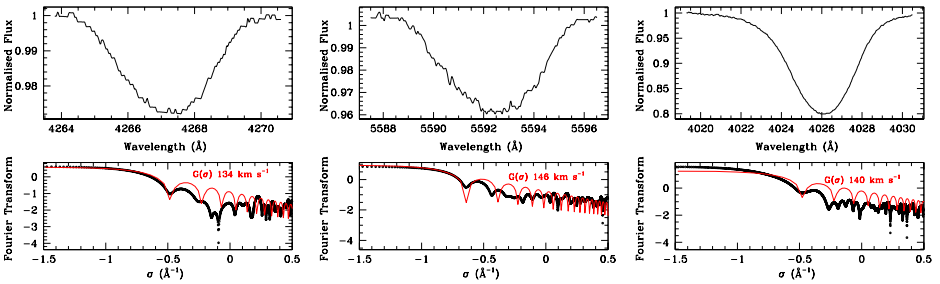

(d) Primary – C II λ 4267 line. (e) Primary – O III λ 5592 line. (f) Primary – He I λ 4026 line.

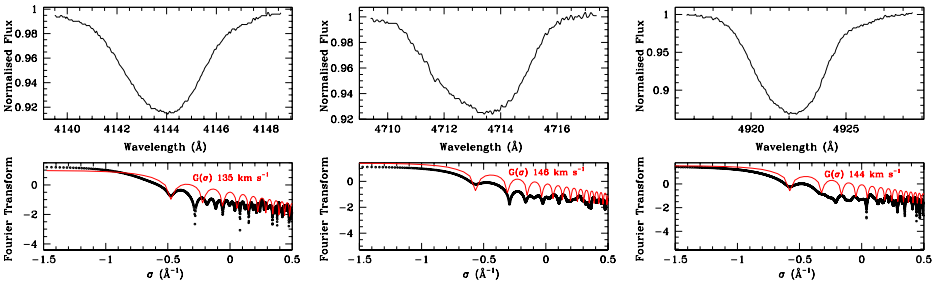

(g) Primary – He I λ 4144 line. (h) Primary – He I λ 4713 line. (i) Primary – He I λ 4922 line.

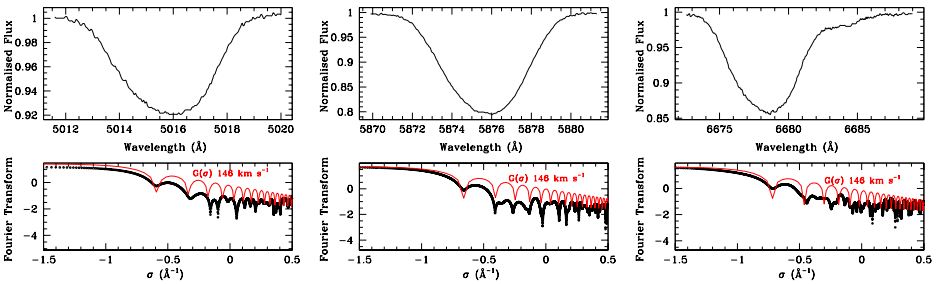

(j) Primary – He I λ 5016 line. (k) Primary – He I λ 5876 line. (l) Primary – He I λ 6678 line.

Figure 2.41. Fourier transforms of line profiles of CPD-41° 7742 (panels (a) to (s)). *Top row:* Line profiles of the separated spectra obtained after application of the brightness ratio for the primary and secondary stars. *Bottom row:* Fourier transform of these lines (in black) and best-match rotational profile (in red).

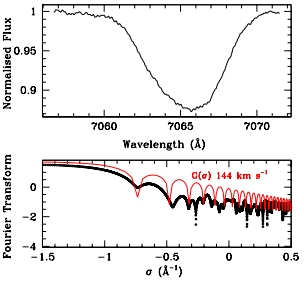

(j) Primary – He I λ 7065 line.

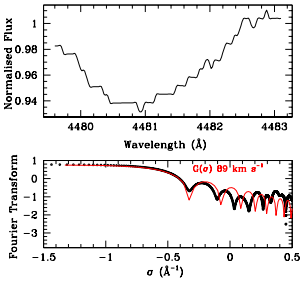

(k) Secondary – Mg II λ 4481 line.

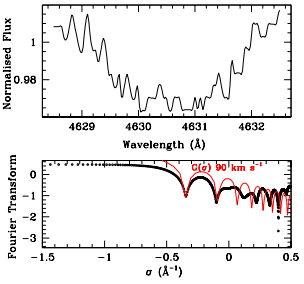

(l) Secondary – Si IV λ 4631 line.

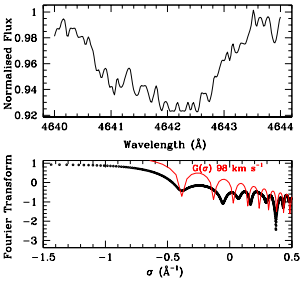

(m) Secondary – N III λ 4641 line.

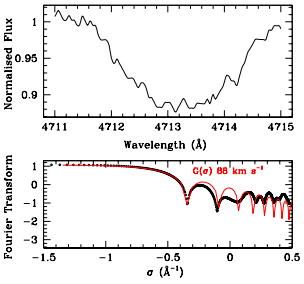

(n) Secondary – He I λ 4713 line.

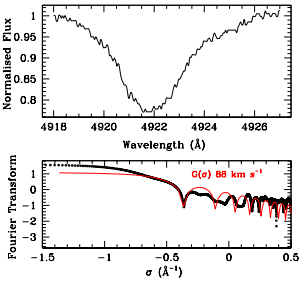

(o) Secondary – He I λ 4922 line.

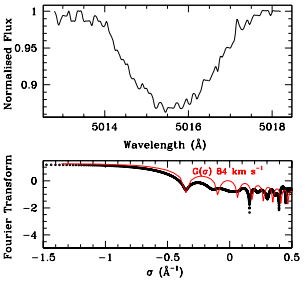

(p) Secondary – He I λ 5016 line.

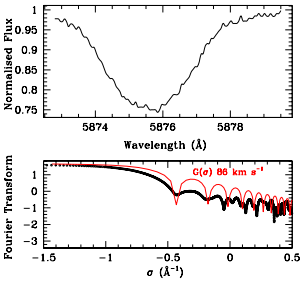

(q) Secondary – He I λ 5876 line.

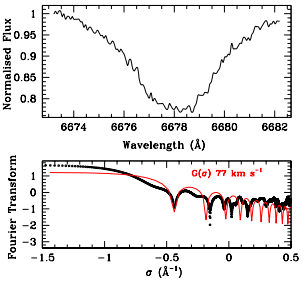

(r) Secondary – He I λ 6678 line.

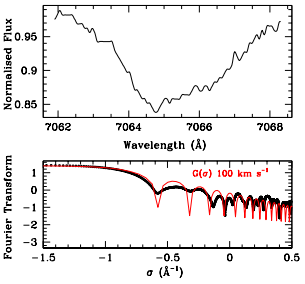

(s) Secondary – He I λ 7065 line.

Figure 2.41. Continued.

Table 2.34. Best-fit projected rotational velocities as derived from the disentangled spectra of CPD-41° 7742.

Line	$v_{\rm eq} \sin i_{\rm rot}$ (km s^{-1})	
	Primary	Secondary
Si IV λ 4089	128	...
Si IV λ 4212	132	...
O II λ 4254	133	...
C II λ 4267	134	...
Mg II λ 4481	...	89
Si IV λ 4631	...	90
N III λ 4641	...	98
O III λ 5592	146	...
He I λ 4026	140	...
He I λ 4144	135	...
He I λ 4713	146	88
He I λ 4922	144	88
He I λ 5016	146	84
He I λ 5876	146	86
He I λ 6678	146	77
He I λ 7065	144	100
Mean (metallic lines)	135 ± 7	92 ± 5
Mean (He I lines)	143 ± 4	87 ± 7
Mean (all lines)	140 ± 7	89 ± 7
Levato & Morrell (1983)	130	...

Notes. The value quoted by Levato & Morrell (1983) was obtained by visual comparison with the standards given by Slettebak et al. (1975).

2.4.1.5. Model atmosphere fitting

We used the projected rotational velocities determined previously to broaden the `CMFGEN` spectra. The stellar and wind parameters were then adjusted following the procedure outlined by Martins (2011).

Primary star First of all, we adjusted the macroturbulence velocity on the wings of the O III λ 5592 and Balmer lines and we derived a value of $v_{\rm macro} = 100 \pm 10\,{\rm km\,s^{-1}}$. We inferred a value of $14 \pm 3\,{\rm km\,s^{-1}}$ for the microturbulence velocity based on the adjustment of the metallic lines.

We determined the effective temperature while searching for the best fit of the He I and He II lines. We observed the same problems as for the primary star of HD 152219 (see discussion in Section 2.3.1.6) and we hence proceeded similarly. We adjusted the effective temperature on the He I λ 4922 line and inferred a value of $31\,800 \pm 1000$ K. With this effective temperature, the He I $\lambda\lambda$ 4026, 4713, 4922 lines as well as the He II λ 4200 line are perfectly adjusted. The He I λ 5876 line is not well-reproduced, as already observed for HD 152219 (see Section 2.3.1.6).

We determined the surface gravity by adjusting the wings of the Balmer lines Hβ, Hγ, Hδ, and H I $\lambda\lambda$ 3835, 3890. We derived $\log g_{\rm spectro} = 3.76 \pm 0.10$.

The surface chemical abundances (in number compared to H) of all elements, including C, N, and O, were set to solar abundances as taken from Asplund et al. (2009) for the same reasons as for HD 152219 (see discussion in Section 2.3.1.6).

Regarding the wind parameters, the clumping parameters were fixed: The volume filling factor f_1 was set to 0.1, and the f_2 parameter was set to 100 km s^{-1}. The β parameter of the velocity law was fixed to the value of 1.1 as suggested by Muijres et al. (2012) for an O9.5 V type star. In principle, the wind terminal velocity could be derived from the Hα line. However, because of the degeneracy between the wind parameters, we decided to fix the value of v_∞ to 2380 km s^{-1} as inferred by Sana et al. (2005). Regarding the mass-loss rate, the main diagnostic lines in the optical domain are Hα and He II λ 4686. We inferred a value of $\dot{M} = (5.0 \pm 1.0) \times 10^{-8}\, M_\odot\,{\rm yr}^{-1}$ based on the Hα line but could not reproduce correctly the He II λ 4686 line.

The stellar and wind parameters of the best-fit `CMFGEN` model atmosphere are summarised in Table 2.35. The normalised disentangled spectra of the primary star of CPD-41° 7742 are illustrated in Figure 2.42 along with the best-fit `CMFGEN` adjustment.

Table 2.35. Stellar and wind parameters of the best-fit `CMFGEN` model atmosphere derived from the separated spectra of CPD-41° 7742.

Parameter	Value	
	Primary	Secondary
$T_{\rm eff}$ (K)	$31\,800 \pm 1000$	$26\,000 \pm 1000$
$\log g_{\rm spectro}$ (cgs)	3.76 ± 0.10	4.00 ± 0.10
$v_{\rm macro}$ (km s^{-1})	100 ± 10	50 ± 10
$v_{\rm micro}$ (km s^{-1})	14 ± 3	10 ± 3
$\dot{M}$ ($M_\odot$ yr^{-1})	$(5.0 \pm 1.0) \times 10^{-8}$	$(5.0 \pm 1.0) \times 10^{-10}$
$\dot{M}_{\rm unclumped}$ ($M_\odot$ yr^{-1})^a	$(1.6 \pm 0.3) \times 10^{-7}$	$(1.6 \pm 0.3) \times 10^{-9}$
v_∞ (km s^{-1})	2380 (fixed)	2040 ± 30
f_1	0.1 (fixed)	0.1 (fixed)
f_2 (km s^{-1})	100 (fixed)	100 (fixed)
β	1.10 (fixed)	1.10 (fixed)
$R_{\rm spectro}$ ($R_\odot$)	$6.06^{+0.85}_{-0.76}$	$2.95^{+0.49}_{-0.45}$
$M_{\rm spectro}$ ($M_\odot$)	$7.72^{+2.80}_{-2.62}$	$3.18^{+1.28}_{-1.21}$

Notes. $^a \dot{M}_{\rm unclumped} = \dot{M}/\sqrt{f_1}$.

Secondary star We proceeded differently for the secondary star. Again, we had to rely on He I and Balmer lines to adjust the macroturbulence velocity, the effective temperature, and the surface gravity simultaneously, in an iterative manner. We inferred a value of $v_{\rm macro} = 50 \pm 10$ km s^{-1}.

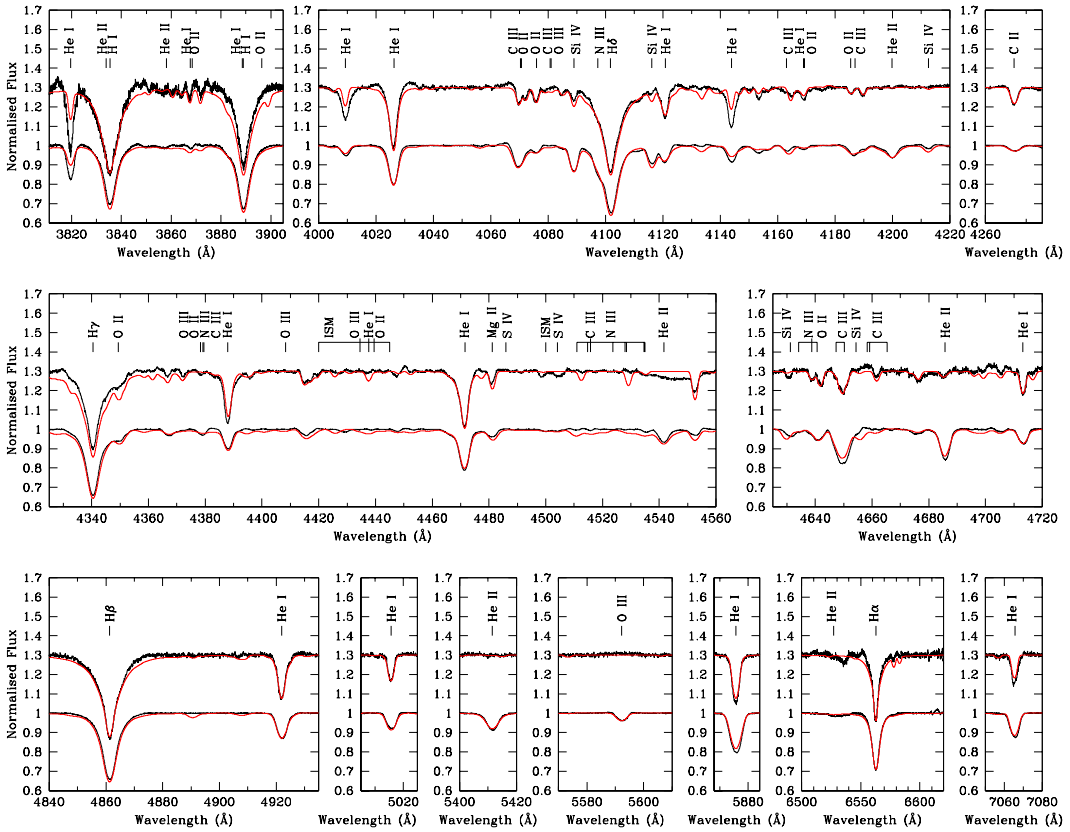

Figure 2.42. Normalised disentangled spectra (in black) of the primary and secondary stars of CPD-41° 7742 (the spectrum of the secondary star is shifted by +0.3 in the y-axis for convenience) together with the respective best-fit `CMFGEN` model atmosphere (in red).

As for the primary star, we determined the effective temperature mainly based on the He I λ 4922 line. We found a value of 26 000 $\pm$ 1000 K. With this effective temperature, the He I $\lambda\lambda$ 4471, 4713, 5016 lines are also perfectly adjusted. However, the He I λ 4026 line is slightly overestimated whilst the He I $\lambda\lambda$ 4388, 5876, 7065 lines are slightly underestimated.

We estimated the surface gravity through the adjustment of the wings of the Balmer lines Hβ, Hγ, Hδ, and H I $\lambda\lambda$ 3835, 3890. We derived $\log g_{\rm spectro} = 4.00 \pm 0.10$. With this value, the wings of Hβ, Hδ, and H I λ 3835 are perfectly adjusted whilst the wings of the two other lines are overestimated.

As for the secondary star of HD 152219, we set the microturbulence velocity to 10 km s^{-1}, as suggested by Cazorla et al. (2017) for such types of stars. The surface chemical abundances (in number compared to H) of all elements, including C, N, and O, were set to solar as taken from Asplund et al. (2009).

Regarding the wind parameters, the clumping parameters f_1 and f_2 were fixed to the same values as for the primary star. We fixed the β parameter of the velocity law to 1.1 (Lefever et al. 2010). The mass-loss rate was adjusted based on the Hγ and Hα lines. We inferred a value of $\dot{M} = (5.0 \pm 1.0) \times 10^{-10}\,M_\odot\,\mathrm{yr}^{-1}$. We found for the wind terminal velocity a value of $v_\infty = 2040 \pm 30\,\mathrm{km\,s}^{-1}$ based on the adjustment of the strength of the Hα line.

The stellar and wind parameters of the best-fit `CMFGEN` model atmosphere are summarised in Table 2.35. The normalised disentangled spectra of the secondary star of CPD-41° 7742 are illustrated in Figure 2.42 along with the best-fit `CMFGEN` adjustment.

Spectroscopic radii and masses The bolometric magnitudes of the stars $M_{\mathrm{bol},1} = -6.42^{+0.16}_{-0.15}$ and $M_{\mathrm{bol},2} = -3.98 \pm 0.22$ were computed through the relations recalled in Section 2.1.4. We further obtained bolometric luminosities $L_{\mathrm{bol},1}$ of $2.96^{+0.42}_{-0.41} \times 10^4 L_\odot$ for the primary star and $L_{\mathrm{bol},2}$ of $3.13^{+0.65}_{-0.64} \times 10^3 L_\odot$ for the secondary star. From the relation between bolometric luminosity, radius, and effective temperature, we inferred spectroscopic radii $R_{\mathrm{spectro},1} = 5.66^{+0.54}_{-0.53}\,R_\odot$ and $R_{\mathrm{spectro},2} = 2.76^{+0.36}_{-0.35}\,R_\odot$ for the primary and secondary stars, respectively. The surface gravities determined with `CMFGEN` were corrected to account for the impact of the centrifugal force and the radiation pressure to first order such that $\log g_C$ equals to 3.84 ± 0.08 for the primary star and to 4.03 ± 0.09 for the secondary star. Spectroscopic masses $M_{\mathrm{spectro},1} = 8.1 \pm 2.2\,M_\odot$ and $M_{\mathrm{spectro},2} = 3.0 \pm 1.0\,M_\odot$ were then deduced for the primary and secondary stars, respectively.

2.4.2. Radial velocity analysis

The total dataset of radial velocities consists of our 166 primary and secondary radial velocities determined as part of the disentangling process of the FEROS, HARPS, and GIRAFFE observations (see Table 2.32) complemented by thirty-seven primary and nine secondary radial velocities coming from the literature (see Table 2.36). For the primary star, there are sixteen radial velocities from Hill et al. (1974), four from Levato & Morrell (1983), three from Perry et al. (1990), eight from García & Mermilliod (2001), and six from Sana et al. (2003, their CAT data). The secondary radial velocities come from García & Mermilliod (2001), three values, and from Sana et al. (2003), six values. As reported by Sana et al. (2003), some of the Julian dates quoted by García & Mermilliod (2001) were wrong by one day. These dates were corrected and reported by Sana et al. (2003) and we therefore adopted these corrected dates in the present analysis. In total, we ended up with a series of 203 primary radial velocity data points spanning about forty-nine years and 175 secondary radial velocity data points spanning about twenty-two years. We adopted the following values for the uncertainties on the primary radial velocities[10]: $10\,\mathrm{km\,s}^{-1}$ for the data of Hill et al. (1974), Levato & Morrell (1983), and García & Mermilliod (2001), $15\,\mathrm{km\,s}^{-1}$ for the data of Perry et al. (1990), and $5\,\mathrm{km\,s}^{-1}$ for the CAT data of Sana et al. (2003). For the radial velocities derived from the spectral disentangling, we adopted formal errors of $5\,\mathrm{km\,s}^{-1}$, as the small errors derived as part of the disentangling method would bias the adjustment given our high number of radial velocities compared to those coming

[10] We did not adopt the error quoted by these authors, if they exist, as they were often found to be underestimated compared to our best-fit solution.

Table 2.36. Journal of the literature radial velocity measurements of CPD-41° 7742. Column 1 gives the heliocentric Julian date (HJD) of the observations. Columns 2 and 3 give the radial velocities RV_1 and RV_2 of the primary and secondary stars, respectively, with their estimated error bars. Column 4 provides the reference of the measurements.

Date (HJD) -2 400 000	RV_1 ($\mathrm{km\,s^{-1}}$)	RV_2 ($\mathrm{km\,s^{-1}}$)	Ref.	Date (HJD) -2 400 000	RV_1 ($\mathrm{km\,s^{-1}}$)	RV_2 ($\mathrm{km\,s^{-1}}$)	Ref.
39 959.792	47.0 ± 9.0	...	[1]	43 647.711	13.3 ± 6.0	...	[3]
40 018.810	-92.0 ± 13.0	...	[1]	43 648.775	-125.0 ± 4.0	...	[3]
40 019.833	0.0 ± 11.0	...	[1]	43 649.765	144.0 ± 4.8	...	[3]
40 807.734	-114.0	...	[2]	43 650.789	-164.0 ± 3.5	...	[3]
40 808.632	166.4	...	[2]	49 912.743	36.5 ± 3.6	...	[4]
40 809.479	-55.5	...	[2]	49 914.521	127.5 ± 3.2	...	[4]
40 809.568	-98.8	...	[2]	49 915.538	-127.8 ± 4.1	145.5 ± 4.6	[4]
40 809.690	-132.2	...	[2]	49 967.537	-94.8 ± 4.0	...	[4]
40 810.532	-40.6	...	[2]	50 593.680	6.6 ± 4.3	...	[4]
40 812.486	-166.2	...	[2]	50 594.726	-129.2 ± 6.0	193.0 ± 7.8	[4]
40 812.642	-142.9	...	[2]	50 596.827	-162.8 ± 5.3	195.9 ± 10.0	[4]
40 813.481	145.8	...	[2]	50 597.811	115.8 ± 4.9	...	[4]
40 813.587	145.0	...	[2]	50 995.723	119.4	-271.8	[5]
40 813.703	151.0	...	[2]	50 996.654	-82.6	-82.6	[5]
40 814.510	-129.5	...	[2]	50 997.669	-79.7	26.7	[5]
40 815.500	-9.4	...	[2]	50 998.657	84.4	-226.8	[5]
40 815.595	21.3	...	[2]	50 999.664	-185.9	231.2	[5]
40 817.479	-150.4	...	[2]	51 000.642	126.4	-278.2	[5]
40 817.677	-71.3	...	[2]				

References. [1] Perry et al. (1990), [2] Hill et al. (1974), [3] Levato & Morrell (1983), [4] García & Mermilliod (2001) corrected by Sana et al. (2003), [5] Sana et al. (2003).

from the literature. Since the secondary radial velocities are only available for the most recent data and are subject to larger errors than the primary radial velocities, we did not use them in the determination of the rate of apsidal motion.

We adjusted the primary radial velocity data using Equation (2.30) explicitly accounting for the secular variation of the argument of periastron, through the relation (2.36). As already mentioned for HD 152248 (Section 2.2.2) and HD 152219 (Section 2.3.2), the radial velocities of different spectral lines potentially yield slightly different apparent systemic velocities. We therefore adjusted the systemic velocity of each subset of our total dataset so as to minimise the sum of the residuals of the data about the curve given by Equation (2.30). To find the values of the six free parameters (K_1, $P_{\rm orb}$, e, T_0, ω_0, and $\dot{\omega}$) that provide the best fit to the whole set of primary radial velocity data, we scanned the parameter space in a systematic way. The projections of the six-dimensional parameter space onto the two-dimensional planes are illustrated in Figure 2.43. We observe a strong degeneracy between the different parameters of the fit, as shown by the numerous local minima. We are therefore not able to derive a unique solution with sufficient accuracy, at least without the prior knowledge of one of these parameters.

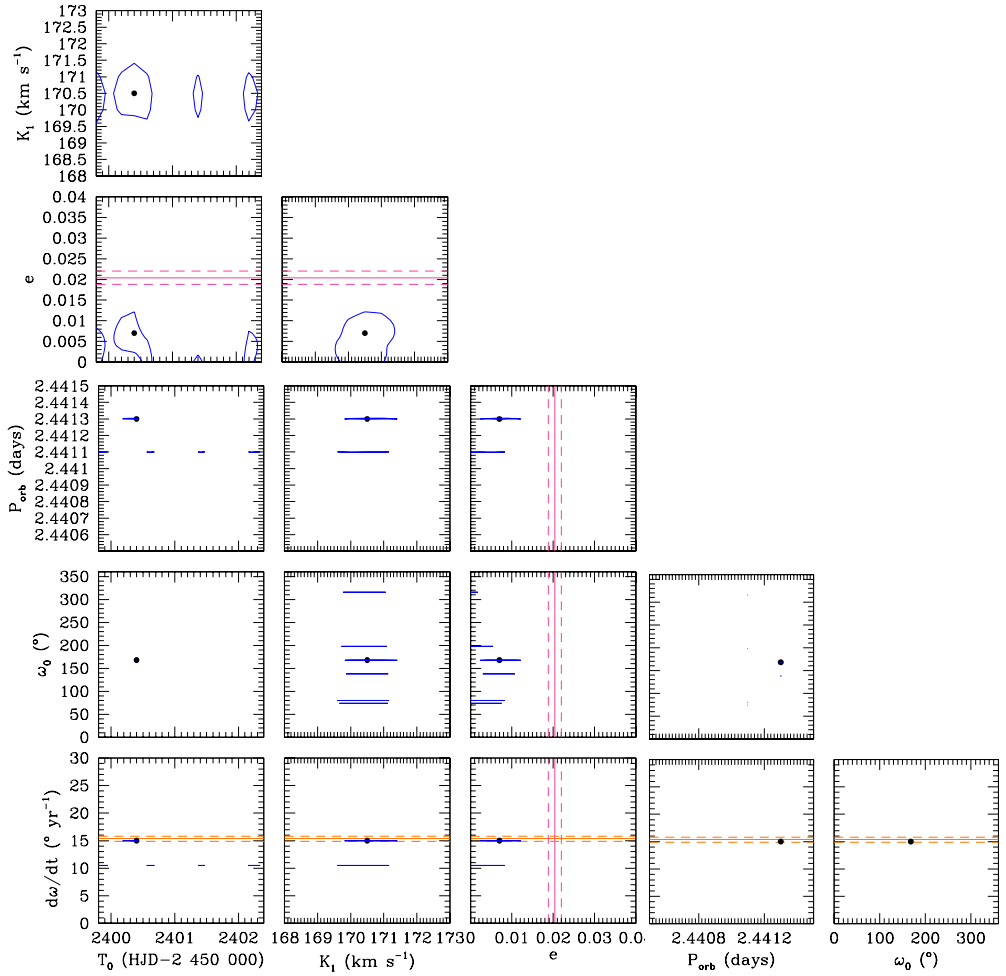

Figure 2.43. Confidence contours for the best-fit parameters obtained from the adjustment of the primary radial velocity data of CPD-41°7742. The best-fit solution is shown in each panel by the black filled dot. The corresponding $1\,\sigma$ confidence level is shown by the blue contour. For comparison, the value of the apsidal motion rate (respectively eccentricity) and its error bars as derived in Section 2.4.3.3 are shown in orange (respectively pink) respectively by the solid and dashed lines. Figure taken from Rosu et al. (2022b).

To solve this issue, we fixed the eccentricity and the apsidal motion rate to the values of 0.0204 and $15.38°\,\mathrm{yr}^{-1}$ as derived from the analysis of the times of photometric minima (see Section 2.4.3.3), and left the four other parameters free. As Figure 2.43 indicates, this value of $\dot{\omega}$ is in agreement with one local minimum of the global adjustment of the radial velocities, while the eccentricity is not. The projections of the remaining four-dimensional parameter space onto two-dimensional planes are illustrated in Figure 2.44. The corresponding orbital parameters are given in Table 2.37. Figure 2.45 illustrates the best fit of the radial velocity data at twelve different epochs.

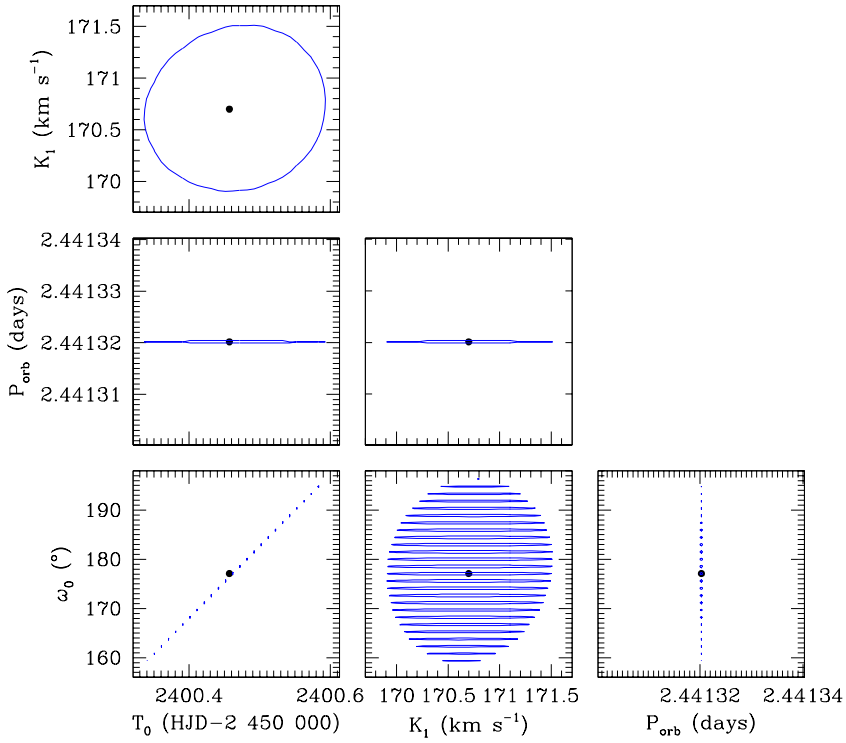

Figure 2.44. Confidence contours for the best-fit parameters obtained from the adjustment of the primary radial veolicity data of CPD-41°7742 when the eccentricity and the apsidal motion rate are fixed to the values of 0.0204 and 15.38° yr^{-1} as derived from the analysis of the times of photometric minima (see Section 2.4.3.3). The best-fit solution is shown in each panel by the black filled dot. The corresponding 1 σ confidence level is shown by the blue contour. Figure taken from Rosu et al. (2022b).

We determined the mass ratio $q = m_2/m_1$ of CPD-41° 7742 by applying Equation (2.33) to the radial velocities obtained in the disentangling process and we derived a value $q = 0.562 \pm 0.006$. We used this result to build an SB2 orbital solution for CPD-41° 7742. Our best-fit parameters and their 1σ errors are listed in Table 2.37.

We note that the mass ratio we found is slightly higher than the value of 0.555 ± 0.005 quoted by Sana et al. (2003) from the He I lines but is compatible with this value within the error bars. We further note that our semi-amplitudes of the primary and secondary radial velocity curves are higher than those derived by Sana et al. (2003, see Table 1.1 in Section 1.3.3). These differences are likely due to the two-Gaussian fit used by Sana et al. (2003) to establish their radial velocities.

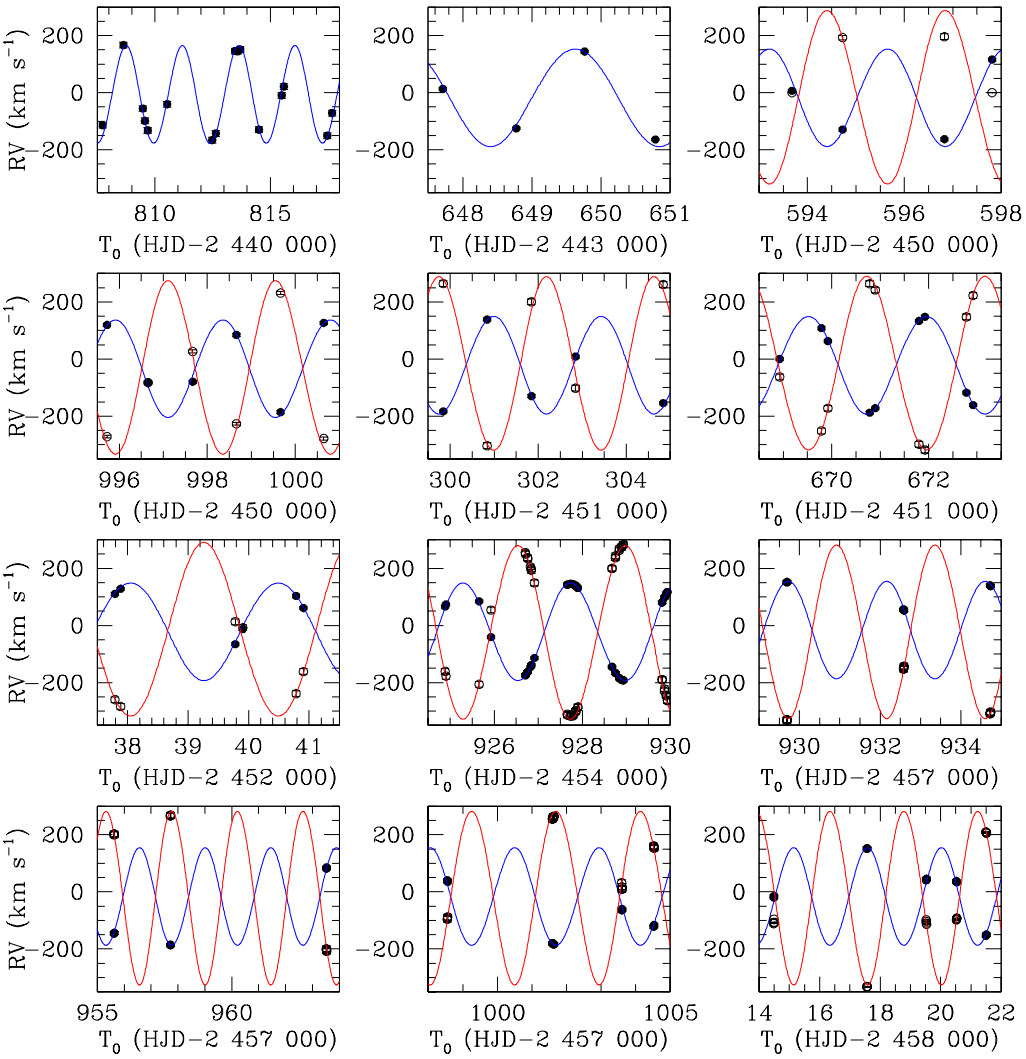

Figure 2.45. Comparison between the measured radial velocities of the primary (filled dots) and secondary (open dots, when available) of CPD-41° 7742 with the orbital solution from Table 2.37. The blue and red lines represent the fitted radial velocity curves of the primary and secondary stars, respectively. The top panels correspond to the data from Hill et al. (1974, *left*), Levato & Morrell (1983, *middle*), and García & Mermilliod (2001, *right*). The left panel on the second row yields the CAT/CES data from Sana et al. (2003). All other panels correspond to the radial velocities derived in the present analysis. Figure taken from Rosu et al. (2022b).

Table 2.37. Best-fit orbital parameters of CPD-41°7742 obtained from the adjustment of the radial velocity data.

Parameter	Primary RVs
$P_{\rm orb}$ (d)	2.441320 ± 0.000001
e	0.0204 (fixed)
$\dot{\omega}$ ($^\circ\,{\rm yr}^{-1}$)	15.38 (fixed)
ω_0 ($^\circ$)	$177.1^{+19.0}_{-18.0}$
T_0 (HJD)	$2\,452\,400.46 \pm 0.12$
$q = m_2/m_1$	0.562 ± 0.006
K_1 (km s^{-1})	170.7 ± 0.8
K_2 (km s^{-1})	303.7 ± 3.5
$a_1 \sin i\,(R_\odot)$	8.23 ± 0.06
$a_2 \sin i\,(R_\odot)$	14.64 ± 0.12
$m_1 \sin^3 i\,(M_\odot)$	17.27 ± 0.49
$m_2 \sin^3 i\,(M_\odot)$	9.71 ± 0.29
χ^2_ν	2.028

2.4.3. Photometric analysis

This section is devoted to the photometric analysis of the binary system CPD-41° 7742. The set of photometric data we used is introduced. Light curve analysis by means of the `Nightfall` code is performed. The phase shifts between the primary and secondary eclipses are used to infer the rate of apsidal motion and the orbital eccentricity of the system.

2.4.3.1. Observational data

Several sets of photometric data are available for CPD-41° 7742. However, only three of them were useful in the present context. Indeed, whilst the ASAS-SN data are saturated as the magnitude of CPD-41° 7742 in the visible band $m_V \sim 8.8$, the ASAS-3 data are heavily contaminated by the nearby brighter source HD 152248, and the Asteroid Terrestrial-impact Last Alert System (ATLAS) data are of very poor quality.

Between 22 March and 19 April 1997, the binary system was observed with the 0.6 m Bochum telescope at La Silla observatory. Data were collected with two narrow-band filters, one centred on the He II λ 4686 line, the other one centred at 6051 Å (Royer et al. 1998). In the following, we will refer to these data as Bochum 4686 and Bochum 6051, respectively. These data were previously used by Sana et al. (2005), and we refer to this paper for details about the observations and the instrument characteristics.

The second set of photometric observations consists of *uvby* Strömgren data obtained at ESO/La Silla with the Danish 1.54 m telescope equipped with either a LORAL 2048×2048 CCD chip (observations between June and July 2000) or an EEV/MAT 2048×4096 CCD chip (observations between March and July 2001) in the framework of the Long-Term

Photometry of Variables project (Sterken 1983, 1994). Data reduction was carried out by Bouzid et al. (2005) and we refer to this paper for more detailed information.

The system was also recently observed by TESS during sectors 12 (i.e. between 21 May and 19 June 2019, hereafter TESS-12) and 39 (i.e. between 27 May and 24 June 2021, hereafter TESS-39). The cadence was 30 minutes for TESS-12 and 10 minutes for TESS-39. We built light curves for this system using aperture photometry extracted with the Python package `Lightkurve`. The source extraction was done in the single central pixel of a 50×50 pixel image (cutout) to avoid as much as possible contamination from neighbouring sources. As a background mask, we used pixels with fluxes below the median flux. Several corrections for background contamination were tried: a simple median of the background pixels as well as a principal component analysis with two (pca-2) or five (pca-5) components. Only the first one could be done for TESS-12 while all three methodologies led to similar results for TESS-39 and we adopted the pca-5 result in this case. All data points with errors larger than the mean of the errors plus three times their 1σ dispersion were discarded. The TESS fluxes were converted into magnitudes and the mean magnitude in each sector was subtracted. The time intervals that showed a long-term (instrumental) trend were discarded: for TESS-12, we removed the data taken during the first half of the sector (i.e. before the satellite's perigee gap); for TESS-39, we skipped data taken within about two days of the beginning or end of the sector and around the perigee gap.

2.4.3.2. Light curve analysis

We analysed the light curves of CPD-41° 7742 by means of the `Nightfall` code version 1.92 (see Section 2.1.9 for detailed explanations about the code). As the Bochum and *uvby* observations are not polluted by the presence of another star in the field, there is no need to include any third light in the model. The TESS observations are, however, polluted by the presence of the massive binary HD 152248 in the field, and hence, a third light contribution needs to be included in the model for these observations. The period of the system was fixed to the instantaneous sidereal period $P_{\rm ecl}$ as computed with Equation (2.40). For the value of $P_{\rm orb}$ given in Table 2.37 and the values of e and $\dot{\omega}$ given in Table 2.42, $P_{\rm ecl}$ ranges between 2.440609 and 2.440637 days.

The existence of apsidal motion in the system and the different levels of third light contamination of the various datasets prevent us from performing a simultaneous analysis of all photometric data. Hence, we performed the analysis of the four datasets (Bochum 6051 and 4686, *uvby*, TESS-12, and TESS-39) separately. The dates of primary minima were directly adjusted on the phase-folded light curve. We obtained 2 450 553.544, 2 451 932.48551, 2 458 629.5717, and 2 459 361.7536 HJD for the Bochum, *uvby*, TESS-12, and TESS-39 photometry, respectively.

The photometric data collected with the Bochum telescope cover an interval of twenty-eight days, which is short enough to neglect any change of ω. We fixed the effective temperatures of the stars to the values derived from the `CMFGEN` analysis (see Table 2.35 and Section 2.4.1.5). We fixed the mass ratio to the value derived from the radial velocity analysis (see Table 2.37). We were thus left with five parameters to adjust: i, e, $f_{\rm P}$, $f_{\rm S}$, and ω. We

performed a series of adjustments of the light curves fixing the eccentricity to values ranging from 0.008 to 0.031. The resulting values of i, ω, $f_{\rm P}$, $f_{\rm S}$, and χ^2 are shown in Figure 2.46. This series of tests allows us to put a constraint on the lower bound of the eccentricity only. In this way, the best-fit Roche-lobe filling factor of the primary star ($\simeq 0.73$) was systematically smaller than that of the secondary star ($\simeq 0.83$), leading to $f_{\rm S}/f_{\rm P} = 1.14$. With the stellar temperatures fixed to their values derived from the spectroscopic analysis, this result is at odds with the spectroscopic brightness ratio that rather implies $R_1/R_2 = 2.05 \pm 0.45$ and thus $f_{\rm S}/f_{\rm P} = 0.63 \pm 0.14$.

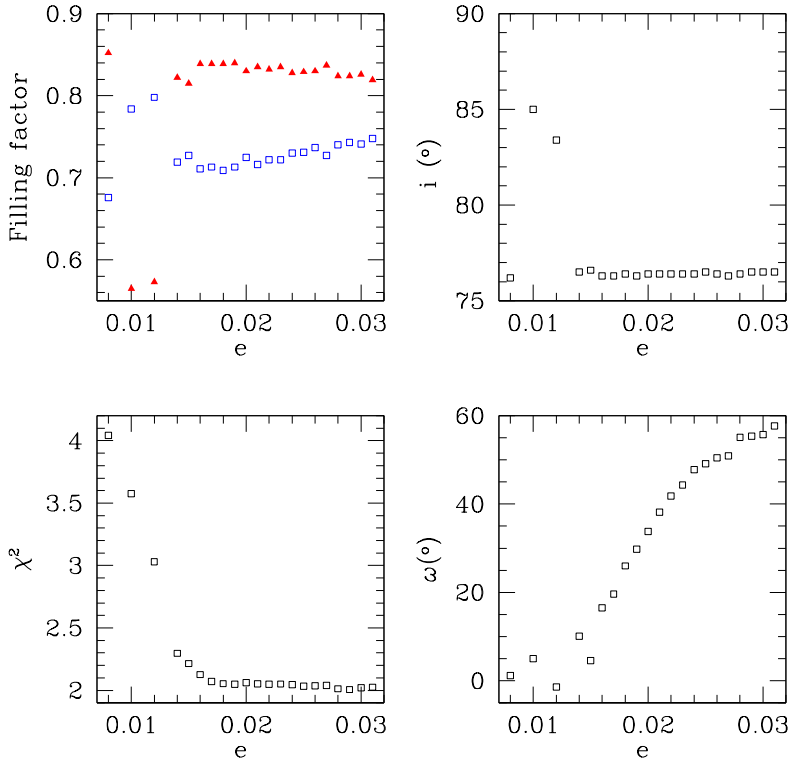

Figure 2.46. Best-fit values of the `Nightfall` adjustment of the Bochum 6051 and 4686 photometric data of CPD-41° 7742 for different values of the eccentricity: $f_{\rm P}$ and $f_{\rm S}$ (blue open rectangles and red filled triangles, *top left panel*), i (*top right panel*), χ^2_ν (*bottom left panel*), and ω (*bottom right panel*).

To solve this issue, we explored a grid of models where we varied the value of $f_{\rm P}$ between 0.80 and 0.90 and fixed $f_{\rm S}$ in such a way that the ratio $f_{\rm S}/f_{\rm P}$ is equal to the spectroscopic value or this value $\pm 1\,\sigma$. Figure 2.47 shows the values of χ^2_ν and i as a function of the fixed eccentricity for the different values of $f_{\rm P}$ and $f_{\rm S}$. These tests indicate that the best-fit solutions are obtained when $f_{\rm S}$ is at the higher end of the *authorised* range and for $f_{\rm P}$ values near 0.81. The evolutions of χ^2_ν and i are plotted as a function of the eccentricity for the different values of $f_{\rm P}$ and such that the ratio $f_{\rm S}/f_{\rm P} = 0.77$ in Figure 2.48.

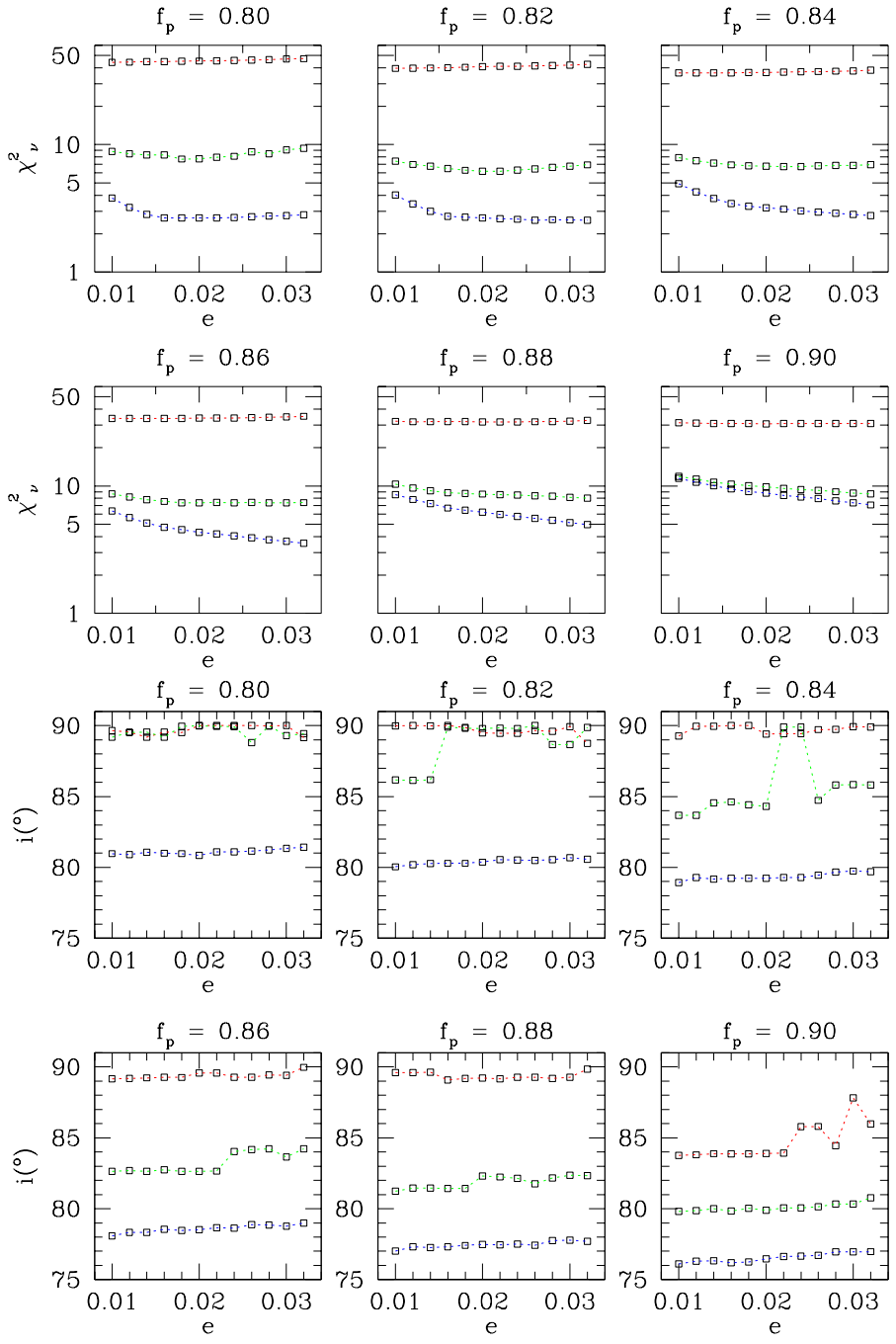

Figure 2.47. Best-fit i and χ^2_ν values of the `Nightfall` adjustments of the Bochum 6051 and 4686 photometric data of CPD-41° 7742 for different values of e, f_P, and the ratio $f_\mathrm{S}/f_\mathrm{P}$ (0.49, 0.63, and 0.77 in red, green, and blue, respectively).

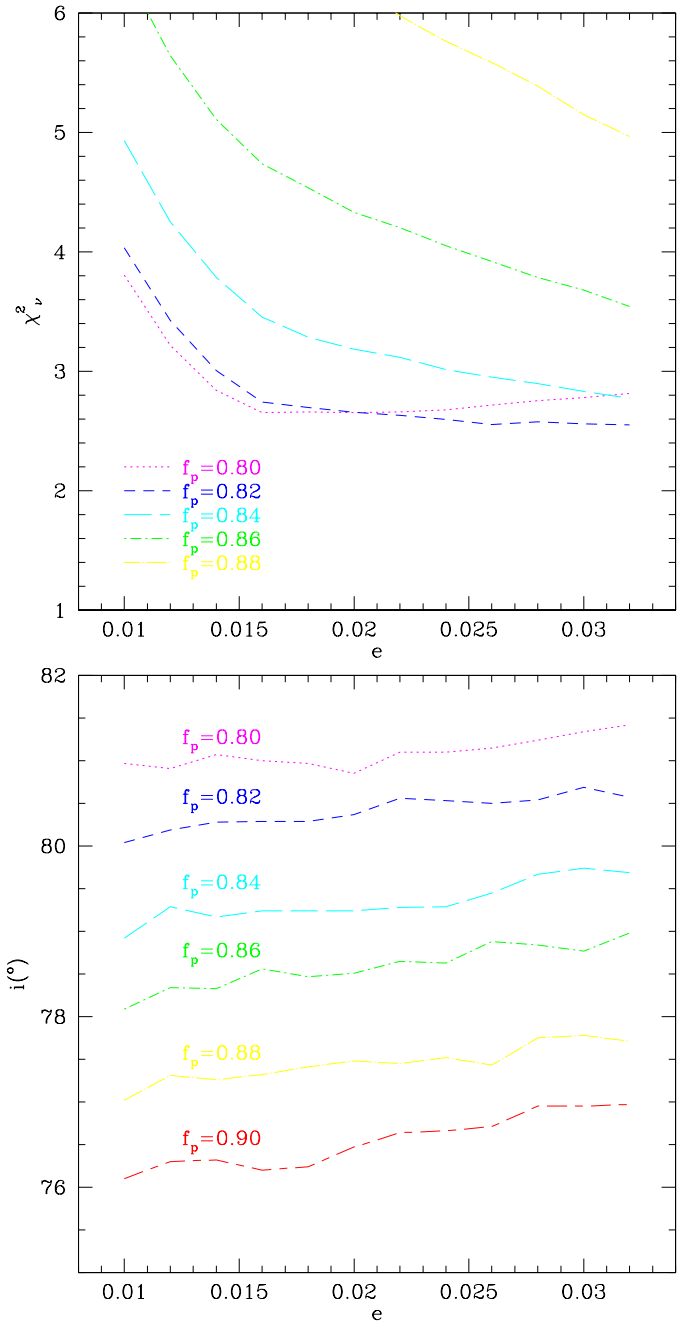

Figure 2.48. Evolution of χ^2_ν (*top panel*) and i (*bottom panel*) as a function of the eccentricity for different values of $f_{\rm P}$ and a ratio $f_{\rm S}/f_{\rm P} = 0.77$ for the `Nightfall` adjustments of the Bochum 6051 and 4686 photometric data of CPD-41° 7742.

To account for the fact that the spectroscopic temperatures are subject to some uncertainties, we then started exploring another grid of models for $f_{\rm P}$ between 0.80 and 0.84, but this time leaving $f_{\rm S}$ and the secondary's effective temperature as free parameters. The main results of this approach are summarised in Table 2.38. The 1σ and 90% confidence contours in the $(f_{\rm P}, e)$-plane are shown in Figure 2.49 and the best-fit light curve is shown in Figure 2.50. The eclipse depths of both eclipses of the two Bochum datasets are given in Table 2.39.

Table 2.38. Best-fit parameters of the `Nightfall` adjustment of the Bochum 6051 and 4686 photometric data of CPD-41° 7742.

Parameter	Value
q	0.562 (fixed)
$T_{\rm eff,1}$ (K)	31 800 (fixed)
$T_{\rm eff,2}$ (K)	$24\,098^{+50}_{-100}$
$f_{\rm P}$	$0.820^{+0.007}_{-0.008}$
$f_{\rm S}$	$0.604^{+0.003}_{-0.007}$
i (°)	$82.0^{+0.6}_{-0.5}$
e	$0.022^{+0.005}_{-0.006}$
ω (°)	$40.4^{+14.2}_{-28.0}$
χ^2_ν	1.87

Table 2.39. Time at mid-exposure and depths of the primary and secondary eclipses for the photometric observations of CPD-41° 7742.

Filter	Time (HJD)	Eclipse depth (mag)	
		Primary	Secondary
Bochum 6051	2 450 544.8142	0.255	0.384
Bochum 4686	2 450 546.8402	0.248	0.391
u-band	2 451 911.7223	0.237	0.400
v-band	2 451 911.7094	0.243	0.396
b-band	2 451 911.7205	0.246	0.391
y-band	2 451 911.7251	0.251	0.386
TESS-12	2 458 646.4641	...	...
TESS-39	2 459 373.9463	...	...

Notes. We do not provide the eclipse depths of the TESS-12 and TESS-39 data as the TESS light curves are diluted by a residual contamination of third light.

Compared to solutions with the secondary effective temperature fixed, the quality of the fits is improved. The secondary star's best-fit photometric temperature is lower than the spectroscopic value by about 2000 K (i.e. twice the estimated error on the spectroscopic value). Yet, it should be noted that the primary spectroscopic temperature also has an uncertainty of 1000 K which is not accounted for in the photometric fits. Since the photometric

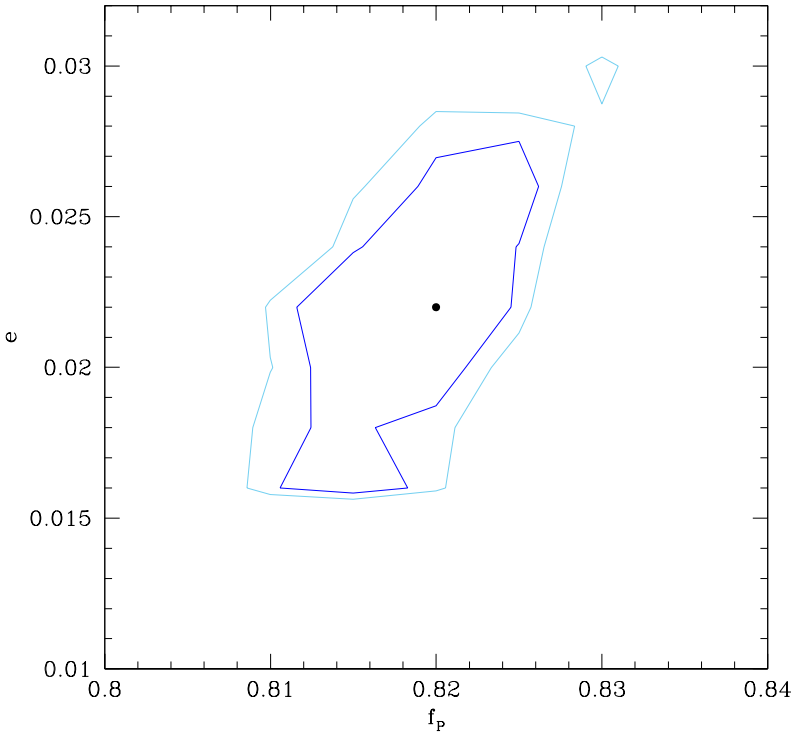

Figure 2.49. Confidence contours of the best-fit solutions to the Bochum 6051 and 4686 photometry of CPD-41° 7742 in the $(f_{\rm P}, e)$-plane. The best-fit solution is shown by the black filled dot. The corresponding 1σ and 90% confidence levels are shown by the dark and light blue contours, respectively. Figure taken from Rosu et al. (2022b).

solution is mostly sensitive to the ratio of the temperatures, increasing the primary effective temperature by 1000 K (i.e. 1σ of the spectroscopic value) actually leads to a secondary effective temperature of 24 960 K. This latter is lower than the spectroscopic value by 1040 K (i.e. a bit more than the estimated error on the spectroscopic value). For consistency, in the following, we adopt an error of 1000 K on the secondary effective temperature. The V-band brightness ratio of the two stars for these solutions, which amounts to $\simeq 0.20$, is in excellent agreement with the spectroscopic value. Hence, the issue mentioned above can be solved this way. The value of 0.0204 for the eccentricity derived from the analysis of the times of photometric minima (see Section 2.4.3.3) is fully consistent with the best estimate obtained here.

Finally, we analysed the *uvby*, TESS-12, and TESS-39 photometric observations fixing all parameters to their best-fit values (see Table 2.38) except for e fixed to the value of 0.0204 (see Section 2.4.3.3), and for ω that was left as a free parameter. For the *uvby* photometry, the best fit gives $\omega = (84.6^{+0.7}_{-0.5})^\circ$ and is plotted in Figure 2.50. The four light curves are well-adjusted. In order to check if our best-fit solution is robust and not biased by the best-fit solution of the Bochum photometry, we performed three additional adjustments of the

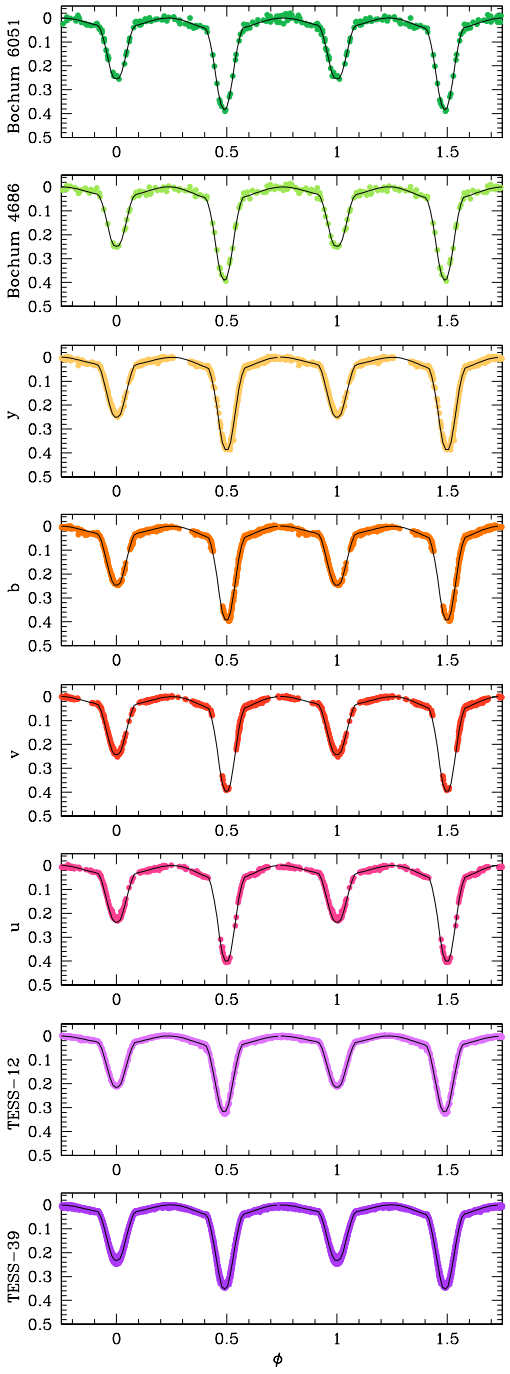

Figure 2.50. Best-fit solution to the Bochum 6051 and 4686, *uvby*, TESS-12, and TESS-39 photometric data of CPD-41° 7742. The light curves have been phase-folded using $P_{\rm ecl}$. Figure taken from Rosu et al. (2022b).

uvby photometry: For all three cases, in addition to ω, the secondary effective temperature was left free; for two of them, the secondary Roche lobe filling factor was also left free; and for one of them, the inclination was left as a free parameter too. The results are given in Table 2.40. The reduced χ^2_ν decreases slightly as more free parameters are adopted, but the best-fit values of the parameters do not change significantly, which ensures that our best-fit solution with all parameters fixed except for ω is robust. The eclipse depths of both eclipses of the photometric datasets are given in Table 2.39. Regarding the TESS-12 and TESS-39 data, we left ω and the third light contribution I_3 as free parameters of the adjustment and obtained $\omega = (347.0^{+3.0}_{-5.0})^\circ$, $I_3 = 0.147 \pm 0.010$, $\chi^2_\nu = 694.4$, and $\omega = (43.4^{+6.6}_{-3.4})^\circ$, $I_3 = 0.071 \pm 0.012$, $\chi^2_\nu = 347.0$, respectively. We note that the large values of χ^2_ν have no physical sense and arise because of the underestimate of the errors on the TESS data. The best fits are shown in Figure 2.50. As the eclipses of the TESS light curves are diluted by the residual contamination of third light, we cannot compare their depths to those of the Bochum and *uvby* photometric data.

Table 2.40. Best-fit parameters of the *uvby* photometry of CPD-41° 7742.

Parameter	Value			
	Case I	Case II	Case III	Case IV
i (°)	82.0 (fixed)	82.0 (fixed)	82.0 (fixed)	$80.8^{+0.9}_{-0.4}$
f_S	0.604 (fixed)	0.604 (fixed)	$0.593^{+0.003}_{-0.001}$	$0.613^{+0.012}_{-0.015}$
$T_{\rm eff,2}$ (K)	24 098 (fixed)	$23\,408^{+110}_{-100}$	$23\,726^{+50}_{-200}$	$23\,700^{+200}_{-160}$
ω (°)	$84.6^{+0.7}_{-0.5}$	$84.0^{+0.7}_{-1.1}$	$85.8^{+1.5}_{-2.3}$	$87.7^{+1.7}_{-2.3}$
χ^2_ν	0.857	0.638	0.556	0.534

2.4.3.3. Times of photometric minima

We used the times of minima of the photometric observations to determine the apsidal motion rate of the system. We computed the phase difference between the primary and secondary eclipses for the different sets of observations. We adjusted a second-order polynomial as well as a Gaussian to the eclipses for the Bochum 6051 and 4686, *uvby*, TESS-12, and TESS-39 separately, and found the values given in Table 2.41.

Table 2.41. Phase differences given by Equation (1.9) between the primary and secondary eclipses for the photometric observations of CPD-41° 7742.

Filter	$\Delta\phi$
Bochum 6051 & 4686	0.5109 ± 0.0010
uvby-bands	0.5011 ± 0.0008
TESS-12	0.5132 ± 0.0007
TESS-39	0.5099 ± 0.0007

We then computed the phase difference between the times of the secondary and primary eclipses, respectively t_2 and t_1, following Equation (1.12). We adjusted this curve to the

observations explicitly accounting for the apsidal motion rate $\dot{\omega}$ through the variation of ω with time. This is illustrated in Figure 2.51. The best-fit adjustment (summarised in Table 2.42) is obtained for $e = 0.0204 \pm 0.0016$, $\dot{\omega} = (15.38^{+0.42}_{-0.51})^\circ\,\mathrm{yr}^{-1}$, $\omega = (28.75^{+5.63}_{-6.38})^\circ$ at the time of the Bochum observations, and $\chi_\nu = 0.1539$. The projections of the three-dimensional parameter space onto the two-dimensional planes are illustrated in Figure 2.52.

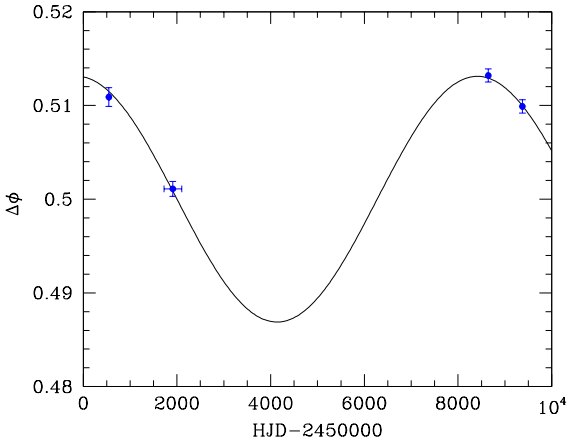

Figure 2.51. Values of the phase difference $\Delta\phi$ between the primary and secondary eclipses as a function of time inferred from the times of photometric minima of the light curves of CPD-41° 7742. The blue symbols correspond to the data of the fits of the Bochum 6051 and 4686, *uvby*, TESS-12, and TESS-39 photometry. The solid line corresponds to our best-fit value of $\Delta\phi$ from Equation (1.12). Figure taken from Rosu et al. (2022b).

Table 2.42. Best-fit parameters of the adjustment of the phase differences between the primary and secondary eclipses for the photometric observations of CPD-41° 7742.

Parameter	Value
e	0.0204 ± 0.0016
$\dot{\omega}$ ($^\circ\,\mathrm{yr}^{-1}$)	$15.38^{+0.42}_{-0.51}$
T_0 (HJD – 2 450 000)	553.544
ω_0 ($^\circ$)	$28.75^{+5.63}_{-6.38}$
χ^2_ν	0.1539

2.4.4. Orbital and physical parameters

The best-fit parameters obtained from the adjustment of the radial velocities (see Table 2.37), the Bochum light curves (see Table 2.38), and the adjustment of the times of photometric minima (see Table 2.42) are combined to finally establish the orbital and physical parameters of CPD-41° 7742. A semi-major axis of $23.09 \pm 0.16\,R_\odot$ is inferred for the system. Absolute masses for the primary and secondary stars $M_1 = 17.8 \pm 0.5\,M_\odot$

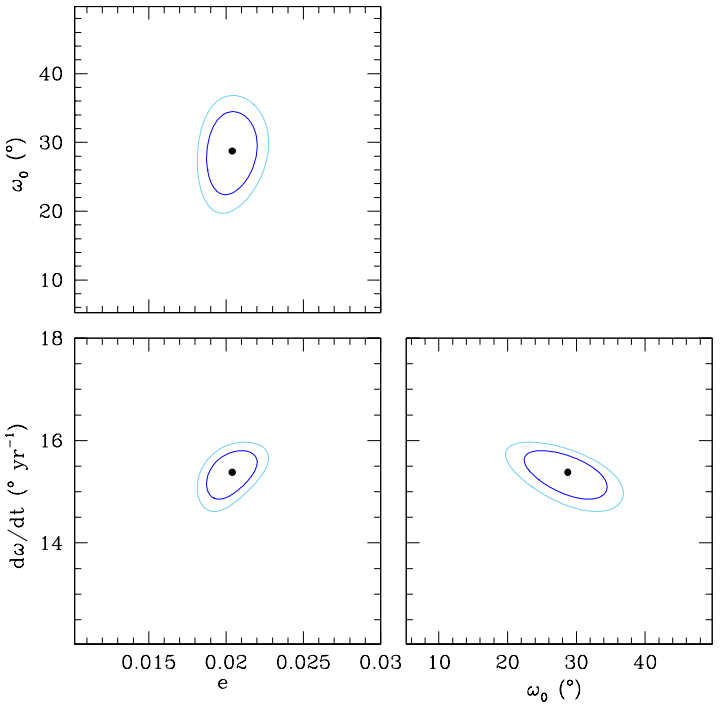

Figure 2.52. Confidence contours for the best fit obtained from the adjustment of the phase differences between the times of the secondary and primary eclipses of CPD-41° 7742 using Equation (1.12). The best-fit solution is shown in each panel by the black filled dot. The corresponding 1σ and 99% confidence levels are shown by the dark and light blue contours, respectively. Figure taken from Rosu et al. (2022b).

and $M_2 = 10.0 \pm 0.3\,M_\odot$, as well as absolute radii for the primary and secondary stars $R_1 = 7.57 \pm 0.09\,R_\odot$ and $R_2 = 4.29^{+0.04}_{-0.06}\,R_\odot$ are derived. This leads to photometric values of the surface gravities of the primary and secondary stars of $\log g_1 = 3.93 \pm 0.02$ and $\log g_2 = 4.17 \pm 0.02$. As expected, the absolute masses and the surface gravities are higher than those derived from the spectroscopic analysis (see discussion in Section 2.4.1.5). From the photometric stellar radii, the primary effective temperature derived in Section 2.4.1.5, and the secondary effective temperature derived in Section 2.4.3.2, we inferred bolometric luminosities $L_{\rm bol,1} = (5.28^{+0.67}_{-0.68}) \times 10^4\,L_\odot$ and $L_{\rm bol,2} = 5.58^{+0.93}_{-0.94} \times 10^3\,L_\odot$ for the primary and secondary stars, respectively. These values are larger than those derived from the spectroscopic analysis (see Section 2.4.1.5). If we further assume the stellar rotational axes to be aligned with the normal to the orbital plane, the combination of the orbital inclination, the stellar radii, and the projected rotational velocities of the stars derived in Section 2.4.1.4 yields rotational periods for the primary and secondary stars $P_{\rm rot,1} = 2.71 \pm 0.14$ days and $P_{\rm rot,2} = 2.42 \pm 0.19$ days. The ratio between rotational angular velocity and instantaneous orbital angular velocity at periastron amounts to 0.86 ± 0.04 for the primary star and to 0.97 ± 0.08 for the secondary star. Pseudo-synchronisation is achieved for the secondary star and about to be achieved for the primary star.

2.4.5. CPD-41° 7742 in a nutshell

We have completely reanalysed the eccentric massive binary CPD-41° 7742 from an observational point of view. We reconstructed the individual spectra of the components using our disentangling code. We reassessed the spectral classification of the stars and found spectral types O9.5 V and B1–2 V for the primary and secondary stars, respectively. Projected rotational velocities of 140 ± 7 and 89 ± 7 km s^{-1} were derived for the primary and secondary stars, respectively. The analysis of these spectra by means of the `CMFGEN` model atmosphere code further allowed us to determine the stellar and wind properties of the system, notably the effective temperature, $T_{\rm eff,1} = 31\,800 \pm 1000$ K, of the primary star.

The orbital inclination, the secondary effective temperature, and the Roche-lobe filling factors of both stars were constrained through the analysis of the light curve by means of the `Nightfall` code. We determined an inclination of $(82.0^{+0.6}_{-0.5})^\circ$ and a secondary effective temperature of 24 098 ± 1000 K. Mean stellar radii of 7.57 ± 0.09 and $4.29^{+0.04}_{-0.06}$ $\mathcal{R}^{\rm N}_\odot$ were inferred for the primary and secondary stars, respectively. Masses of 17.8 ± 0.5 and 10.0 ± 0.3 $\mathcal{M}^{\rm N}_\odot$ were obtained for the primary and secondary stars, respectively. Radial velocity data from the literature and redetermined in this paper allowed us to infer an orbital period of 2.441320 ± 0.000001 days. The adjustment of the phase differences between the times of secondary and primary minima of the eclipses of the different sets of photometric observations explicitly accounting for the apsidal motion allowed us to establish a rate of apsidal motion of $(15.38^{+0.42}_{-0.51})^\circ$ yr^{-1} and an eccentricity of 0.0204 ± 0.0016. We hence solved the inconsistency highlighted by Sana et al. (2005) and Bouzid et al. (2005) discussed in Section 1.3.3 between the longitude of periastron inferred through the radial velocity analysis on the one hand and the photometric analysis on the other hand.

The high apsidal motion rate of CPD-41° 7742 renders the system an interesting target to study tidally-induced apsidal motion from a theoretical point of view. In Chapter 3, we use stellar evolution models to determine theoretical rates of apsidal motion and compare them to the observed rate.

2.5. The revisited binary: HD 152218

The massive binary system HD 152218 – also known as V 1007 Sco – is briefly revisited here in light of the newly available TESS photometric data compared to our first analysis of this system (Rauw et al. 2016). The stellar and orbital parameters of HD 152218 (taken from the radial velocity analysis of Rauw et al. 2016) are summarised in Table 2.43. The most important results of this section are presented in Rosu et al. (2022b).

Table 2.43. Observational properties of the binary system HD 152218 taken from Rauw et al. (2016).

Parameter	Value	
	Primary	Secondary
M ($M_\odot$)	19.8 ± 1.5	15.0 ± 1.1
R ($R_\odot$)	$8.4^{+1.1}_{-1.0}$	$7.8^{+1.0}_{-1.6}$
$T_{\rm eff}$ (K)	$33\,400 \pm 1000$	$29\,900 \pm 1000$
$P_{\rm rot}$ (d)	$2.69^{+0.37}_{-0.34}$	$2.56^{+0.48}_{-0.63}$
e	$0.280^{+0.010}_{-0.008}$	
i ($^\circ$)	$66.3^{+3.0}_{-3.3}$	
$P_{\rm orb}$ (d)	5.60445 ± 0.00005	
$\dot{\omega}$ ($^\circ$ yr^{-1})	$2.04^{+0.23}_{-0.24}$	

Notes. There was a small typo in the secondary rotational period in Rauw et al. (2016) that we corrected here.

HD 152218 was observed by TESS during the same sectors as CPD-41° 7742 (i.e. sectors 12 and 39). We performed an extraction of the light curves with a 30-minutes and 10-minutes cadences for TESS-12 and TESS-39, respectively. For this purpose, we used the `Lightkurve` software and followed the reduction steps explained in Section 2.4.3.1 for the binary CPD-41° 7742. We adopted the pca-5 for the background subtraction for both sectors. This results in a total of 1257 and 3705 data points for TESS-12 and TESS-39, respectively.

We analysed the light curves of HD 152218 with the `Nightfall` code, version 1.92 (see Section 2.1.9 for detailed explanations about the code). We fixed the effective temperatures, the eccentricity, and the orbital period to the values quoted by Rauw et al. (2016, see Table 2.43). The only free parameters were the orbital inclination, the longitude of periastron, and the Roche lobe filling factors of the two stars. The best-fit adjustments are given in Table 2.44 (we note that the large values of χ^2_ν have no physical sense and arise because of the underestimate of the errors on the TESS data) and illustrated in Figure 2.53.

The values of the longitude of periastron expected at the times of the TESS-12 and TESS-39 observations from the apsidal motion rate derived based on the radial velocity analysis of Rauw et al. (2016) amount to $(135.8^{+5.4}_{-5.7})^\circ$ and $(139.9^{+5.9}_{-6.1})^\circ$, respectively. Whilst the value of ω inferred for the TESS-12 light curve is compatible within the error bars, this is not the case for the TESS-39 light curve. In addition, the value of ω should be larger for

Table 2.44. Best-fit parameters of the TESS photometry of HD 152218.

Parameter	Value	
	TESS-12	TESS-39
Epoch (HJD)	2 458 638.98	2 459 375.68
i (°)	$68.06^{+0.6}_{-0.40}$	$66.09^{+1.60}_{-0.40}$
$f_{\rm P}$	$0.673^{+0.020}_{-0.022}$	$0.680^{+0.035}_{-0.028}$
$f_{\rm S}$	$0.679^{+0.026}_{-0.023}$	$0.721^{+0.028}_{-0.036}$
ω (°)	$132.2^{+0.6}_{-1.1}$	$124.9^{+0.8}_{-1.2}$
χ^2_ν	1042.8	437.8

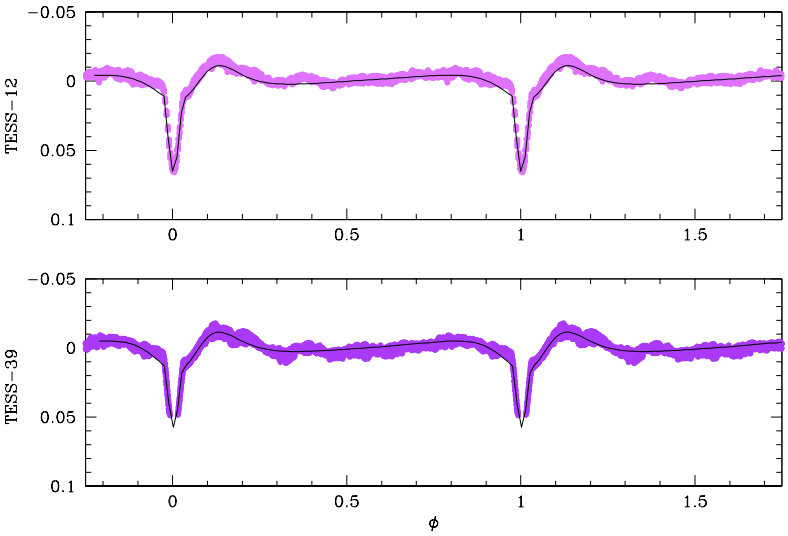

Figure 2.53. Best-fit solution to the TESS-12 and TESS-39 photometry of HD 152218. The light curves have been phase-folded with $P_{\rm ecl} = 5.60415$ days computed using Equation (2.40). Figure taken from Rosu et al. (2022b).

the TESS-39 light curve than for the TESS-12 one.

In the case of HD 152218, the fact that there is a single eclipse leads to a degeneracy between the primary and secondary Roche lobe filling factors, and the orbital inclination that can shift the formally best-fit solution to values of the Roche lobe filling factors that are inconsistent with the spectroscopic brightness ratio. To overcome this difficulty, we scanned the parameter space fixing $i, f_{\rm P}$, and $f_{\rm S}$ to the values that, considering Figure 6 of Rauw et al. (2016), give a brightness ratio in accordance with the spectroscopic value and are acceptable (at 1σ) with the ASAS-3 photometry. In this way, ω was the only free parameter of the adjustment. The results are summarised in Table 2.45. The combination of parameters that give acceptable results in terms of χ^2_ν give ω values ranging from 125.5° to 133.8° for the TESS-12 data and from 129.2° to 137.9° for the TESS-39 data.

These values are in agreement, within the error bars, with those expected from the spectroscopic apsidal motion rate. These solutions all predict an inclination between 67° and 69°.

Table 2.45. Best-fit values of the adjustments of the TESS-12 and TESS-39 light curves of HD 152218. Columns 1 and 2 give the values (fixed) of the Roche lobe filling factors of the primary and secondary stars. Column 3 gives the value (fixed) of the inclination. Columns 4 and 5 (respectively 6 and 7) give the values of the longitude of periastron and the reduced χ^2_ν of the adjustment for the TESS-12 (respectively TESS-39) light curve.

			TESS-12		TESS-39	
f_P (fixed)	f_S (fixed)	i (°, fixed)	ω (°)	χ^2_ν	ω (°)	χ^2_ν
0.61	0.71	68.5	305.48	1134.4	309.19	460.4
0.63	0.68	69.0	312.09	1092.3	311.68	470.1
0.63	0.73	68.0	312.06	1110.2	311.86	466.1
0.65	0.67	69.0	313.79	1114.3	317.79	475.8
0.65	0.76	67.0	312.42	1310.3	311.55	528.6
0.67	0.65	69.0	313.75	1119.9	317.89	475.7
0.67	0.78	65.5	305.24	1374.4	311.34	530.3
0.69	0.61	69.0	311.68	1118.1	311.64	470.8
0.69	0.66	68.5	318.15	1165.1	317.88	483.0
0.69	0.80	65.0	311.38	1848.6	312.14	678.5
0.71	0.59	69.5	318.10	1246.9	317.94	507.8
0.71	0.68	67.0	305.93	1131.3	311.71	450.8
0.71	0.84	63.5	307.47	2625.5	312.93	966.1
0.73	0.61	68.5	315.06	1268.2	317.77	522.0
0.73	0.70	66.2	310.92	1273.4	311.93	495.0
0.73	0.83	63.5	313.48	2686.9	312.80	979.2
0.75	0.62	68.2	320.60	1607.9	318.71	630.3
0.75	0.72	65.5	312.74	1535.5	312.62	596.6
0.75	0.81	63.0	306.72	2227.8	306.88	814.8
0.77	0.63	67.0	312.29	1583.4	312.28	621.2
0.77	0.74	64.8	313.51	1963.7	313.48	762.2
0.77	0.80	63.2	313.35	2553.4	313.35	923.8
0.79	0.64	66.0	308.86	1810.6	311.55	672.0
0.79	0.76	63.7	313.19	2394.2	313.19	885.5
0.79	0.78	63.5	313.63	2753.9	312.96	1031.8
0.74	0.71	66.3	313.88	1451.1	317.79	592.4

We therefore conclude that the previously reported apsidal motion rate derived by Rauw et al. (2016) is confirmed by the new photometric data.

Chapter 3

Larger Convective Cores Than Usually Considered

"You investigate for curiosity, because it is unknown, not because you know the answer."

(Richard Feynman)

The apsidal motion rate depends upon many properties of the binary stars, notably the way the mass is distributed inside each star, that is to say, the density stratification between its core and external layers, which is summarised in a global parameter called the internal structure constant of the star. Stellar structure and evolution models aim at reproducing the internal structure and global properties of the stars. Confronting observationally determined properties and stellar evolution models allows us to infer constraints on the mixing processes occurring inside the stars as well as on the age of the binary stars. The apsidal motion equations and their link to the internal structure constant are provided in Section 3.1. The stellar structure and evolution codes `Clés` *and* `GENEC` *are described in Section 3.2. Each of the binaries considered here is analysed in a different way and therefore has its own dedicated section, respectively Section 3.3, 3.4, 3.5, and 3.6.*

Contents

3.1. Precession of the line of apsides

In a close eccentric binary, the tidal deformation of the stars leads to stellar gravitational fields that are no longer spherically symmetric. This situation induces a slow precession of the line of apsides, known as apsidal motion (Schmitt et al. 2016, and references therein). The apsidal motion occurs at a rate $\dot{\omega}$, which is a function of the internal structure of the two stars (e.g. Shakura 1985; Claret & Giménez 2010). More specifically, the contribution of a binary component to the binary's rate of apsidal motion is directly proportional to the star's internal structure constant k_2 (Shakura 1985). This parameter is a sensitive indicator of the density stratification inside the star, and its value changes significantly as the star evolves away from the main sequence. Measuring $\dot{\omega}$ thus provides precious information about the internal structure of the binary components. This is even more important for massive stars for which such information is rather scarce (Bulut & Demircan 2007).

In Section 3.1.1, we present the equations of apsidal motion under the assumption that the stellar rotation axes are aligned with the normal to the orbital plane and that only the contributions arising from the second-order harmonic distorsions of the potential are considered. The internal structure constant is introduced in Section 3.1.2. We develop the apsidal motion equations when higher-order terms are considered in Section 3.1.3 and when a misalignment of the rotation axes with respect to the normal to the orbital plane is considered in Section 3.1.4.

3.1.1. Apsidal motion equations

In the simple two-body case, the rate of apsidal motion is given by the sum of a classical Newtonian contribution (N) and a general relativistic correction (GR):

$$\dot{\omega} = \dot{\omega}_{\rm N} + \dot{\omega}_{\rm GR}. \tag{3.1}$$

The classical Newtonian contribution is the dominant term in the majority of non-degenerate binary systems; A few exceptions where the general relativistic correction is quite large are discussed in Baroch et al. (2021, and references therein).

The classical Newtonian contribution to the apsidal motion takes its origin in the non-Keplerian terms of the gravitational potentials of the stars. These terms stem from the non-spherical shape of the stars as a result of both the stellar rotation and the presence of the companion. Indeed, tidal interactions take their origin in the gravitational attraction existing between the two stars and in the stellar rotations which are not synchronised with the orbital motion. The amplitude of the deformation of a star in response to these tidal interactions depends on the way the mass is distributed in the stellar interior. Provided that the stellar rotation axes are aligned with the normal to the orbital plane[1], the Newtonian term can be expressed according to Sterne (1939), where we only consider the contributions

[1] A more general form of the expression of the Newtonian contribution to the apsidal motion accounting for the rotation axis misalignment is presented in Section 3.1.4.

arising from the second-order harmonic distorsions of the gravitational potential[2]:

$$\dot{\omega}_{\rm N} = \frac{2\pi}{P_{\rm orb}}\left[15f(e)\left\{k_{2,1}q\left(\frac{R_1}{a}\right)^5 + \frac{k_{2,2}}{q}\left(\frac{R_2}{a}\right)^5\right\} + g(e)\left\{k_{2,1}(1+q)\left(\frac{R_1}{a}\right)^5\left(\frac{P_{\rm orb}}{P_{\rm rot,1}}\right)^2 + k_{2,2}\,\frac{1+q}{q}\left(\frac{R_2}{a}\right)^5\left(\frac{P_{\rm orb}}{P_{\rm rot,2}}\right)^2\right\}\right], \tag{3.2}$$

where a is the semi-major axis, $q = M_2/M_1$ is the mass ratio[3], $k_{2,1}$ and $k_{2,2}$ are the internal structure constants of the primary and secondary stars, respectively, $P_{\rm rot,1}$ and $P_{\rm rot,2}$ are the rotational periods of the primary and secondary stars, respectively, and f and g are functions of the orbital eccentricity expressed by the following relations:

$$\begin{cases} f(e) = \dfrac{1 + \frac{3e^2}{2} + \frac{e^4}{8}}{(1-e^2)^5}, \\ g(e) = \dfrac{1}{(1-e^2)^2}. \end{cases} \tag{3.3}$$

The Newtonian term is itself the sum of the effects induced by tidal and rotational deformations.

The general relativistic contribution to the rate of apsidal motion, when only the quadratic corrections are taken into account, is given by the expression

$$\dot{\omega}_{\rm GR} = \frac{2\pi}{P_{\rm orb}}\frac{3G(M_1+M_2)}{c^2 a(1-e^2)} = \left(\frac{2\pi}{P_{\rm orb}}\right)^{5/3}\frac{3(G(M_1+M_2))^{2/3}}{c^2(1-e^2)}, \tag{3.4}$$

where G is the gravitational constant and c is the speed of light (Shakura 1985).

With $\dot{\omega}$ and $\dot{\omega}_{\rm GR}$ derived from observations (as all terms appearing in the right-hand side of Equation (3.4) are known from observations), the Newtonian contribution can be evaluated through Equation (3.1). In the right-hand side of Equation (3.2), all terms can be inferred observationally, except for the internal structure constants of the stars. It is impossible to isolate the internal structure constants of the stars to observationally determine their values as the system is underdetermined, except if $k_{2,1} = k_{2,2}$, in which case the two stars are identical (i.e. they share the same mass, radius, and effective temperature) and the binary system is a twin system. Indeed, in this case, Equation (3.1) reduces to

$$\dot{\omega} = \frac{4\pi}{P_{\rm orb}}k_2\left(\frac{R_*}{a}\right)^5\left[15f(e) + g(e)P_{\rm orb}^2\left(\frac{1}{P_{\rm rot,1}^2} + \frac{1}{P_{\rm rot,2}^2}\right)\right] + \left(\frac{2\pi}{P_{\rm orb}}\right)^{5/3}\frac{3(2GM_*)^{2/3}}{c^2(1-e^2)}, \tag{3.5}$$

where we adopted the following notations:

$$R_1 = R_2 \equiv R_*, \quad M_1 = M_2 \equiv M_*, \quad k_{2,1} = k_{2,2} \equiv k_2. \tag{3.6}$$

[2] Higher-order contributions to the apsidal motion are presented in Section 3.1.3.
[3] In this Chapter, we adopted capital letters for the masses, in opposition to the previous Chapters.

Such twin cases are scarce, but offer a unique opportunity to observationally constrain the k_2 value. The massive binary HD 152248, presented in Section 3.3, is one such case where the k_2 value could be inferred observationally.

However, in the general case of two different stars, the internal structure constant cannot be determined from an observational point of view. Nonetheless, we can rewrite Equation (3.2) in the form

$$\dot{\omega}_{\rm N} = c_1 k_{2,1} + c_2 k_{2,2}, \tag{3.7}$$

where c_1 and c_2 are two known functions depending on the stellar parameters. We can then define a weighted-average value of the internal structure constant for the system

$$\bar{k}_2 = \frac{c_1 k_{2,1} + c_2 k_{2,2}}{c_1 + c_2} = \frac{\dot{\omega}_{\rm N}}{c_1 + c_2}. \tag{3.8}$$

All terms appearing in the right-hand side of Equation (3.8) are known from observations, hence is $\bar{k}_2$ also.

3.1.2. Internal structure constant k_2

The internal structure constant, also known as the apsidal motion constant, is a measure of the internal mass distribution of the star, that is to say, the density contrast between the core and the external layers of the star. Its expression is given by

$$k_2 = \frac{3 - \eta_2(R_*)}{4 + 2\,\eta_2(R_*)}, \tag{3.9}$$

where $\eta_2(R_*)$ is the logarithmic derivative of the surface harmonic of the distorted star expressed in terms of the ellipticity ϵ_2 and evaluated at the stellar surface R_*:

$$\eta_2(R_*) = \left.\frac{d\ln\epsilon_2}{d\ln r}\right|_{r=R_*}, \tag{3.10}$$

which is the solution of the Clairaut-Radau differential equation

$$r\frac{d\eta_2(r)}{dr} + \eta_2^2(r) - \eta_2(r) + 6\frac{\rho(r)}{\bar{\rho}(r)}\left(\eta_2(r) + 1\right) - 6 = 0 \tag{3.11}$$

with the boundary condition $\eta_2(0) = 0$ (Hejlesen 1987). In this expression, r is the current radius at which the equation is evaluated, $\rho(r)$ is the density at distance r from the centre, and $\bar{\rho}(r)$ is the mean density within the sphere of radius r. An homogeneous sphere of constant density has a k_2 equal to 0.75 whilst the k_2 of a massive star having a very dense core and a diluted atmosphere can take a value as low as 10^{-4} (see e.g. Rosu et al. 2020a, 2022a). During stellar evolution, the external layers become more and more diluted compared to the stellar core, hence k_2 decreases with time, making this quantity a good indicator of stellar evolution.

3.1.2.1. A look inside the star

The internal structure constant is a simple algebraic equation of the η_2 function evaluated at the stellar surface (see Equation (3.9)). Since η_2 is computed from the integration of the Clairaut-Radau equation throughout the stellar interior (see Equation (3.11)), we can look at the evolution of η_2 inside the star, from the centre to the surface, in order to identify the layers that contribute the most to η_2. In this context, it is instructive to consider an approximation suggested by Fitzpatrick (2016), which helps us highlight the parameters contributing the most to η_2. The Clairaut-Radau equation can be written in the form known as Radau's equation:

$$\frac{d}{dr}\left[\bar{\rho}(r)r^5[1+\eta_2(r)]^{1/2}\right] = 5\bar{\rho}(r)r^4\psi(\eta_2), \tag{3.12}$$

where

$$\psi(\eta_2) = \frac{1+\eta_2/2-\eta_2^2/10}{(1+\eta_2)^{1/2}}. \tag{3.13}$$

If $\eta_2 \lesssim 1.5$, then $\psi(\eta_2) \approx 1$ is roughly constant (see Figure 3.1).

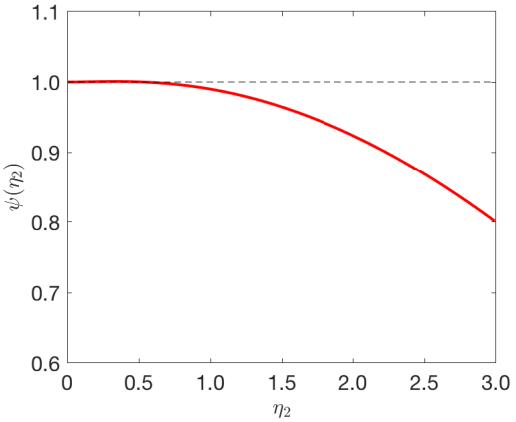

Figure 3.1. Evolution of $\psi(\eta_2)$ as a function of η_2.

Hence, Equation (3.12) reduces to

$$\frac{d}{dr}\left[\bar{\rho}(r)r^5[1+\eta_2(r)]^{1/2}\right] \approx 5\bar{\rho}(r)r^4, \tag{3.14}$$

where the right-hand side is now independent of η_2. In this case,

$$[1+\eta_2(R)]^{1/2} = \frac{5}{\bar{\rho}(R)R^5}\int_0^R \bar{\rho}(r)r^4\, dr \tag{3.15}$$

(Fitzpatrick 2016). Replacing the mean density with its expression in terms of the mass and

the radius, and expressing the term $\bar{\rho}(r)$ through its integral expression, we get

$$[1+\eta_2(R)]^{1/2} = \frac{5}{MR^2}\int_0^R \left(\int_0^r 4\pi r'^2 \rho(r')\ dr'\right) r\ dr. \tag{3.16}$$

Performing the integration by parts, we get

$$[1+\eta_2(R)]^{1/2} = \frac{10\pi}{MR^2}\int_0^R \rho(r) r^2 (R^2-r^2)\ dr. \tag{3.17}$$

In terms of the mean density, this last equation is equivalent to

$$\begin{aligned}[1+\eta_2(R)]^{1/2} &= \frac{15}{2\bar{\rho}(R)R^5}\int_0^R \rho(r) r^2 (R^2-r^2)\ dr \\ &= \frac{15}{2\bar{\rho}(R)}\int_0^1 \rho(r)\left(\frac{r}{R}\right)^2\left(1-\left(\frac{r}{R}\right)^2\right)\ d\frac{r}{R}.\end{aligned} \tag{3.18}$$

This equation expresses that a change in η_2 – and hence a change in k_2 – can be related to a change in the function $\rho(r)r^2(R^2-r^2)$. The evolution of the normalised[4] density inside the star as well as the normalised function $\rho(r)\left(\frac{r}{R}\right)^2\left(1-\left(\frac{r}{R}\right)^2\right)$ are presented in the top panels of Figure 3.2, for `Clés` models with an initial mass of 31.0 $M_\odot$, overshooting parameter $\alpha_{\rm ov}$ from 0.10 to 0.40, no turbulent diffusion, mass-loss rate scaling factor $\xi = 1$, metallicity $Z = 0.015$, and ages of 3, 4, and 5 Myr (see Section 3.2.1 for a description of the `Clés` code and the definition of the different parameters). As a reminder, the approximation under which Equation (3.18) is valid is $\eta_2 \lesssim 1.5$, which is not satisfied for all the radii inside the star; This is shown in the bottom left-hand panel of Figure 3.2, which represents the evolution of η_2 inside the star as computed with Equation (3.11). Nonetheless, this relation can be used as a first approximation, at least for the centre of the star, that is to say, up to a radius of $\sim 0.2-0.4$ depending on the age of the star. In the bottom right-hand panel of Figure 3.2, we show the evolution of the derivative of η_2 with respect to the radius, $\frac{d\eta_2}{dr}$. The peak in $\frac{d\eta_2}{dr}$ happens at a slightly higher radius than the peak in the function $\rho(r)r^2(R^2-r^2)$, indicating the direct – though not perfect – correlation between the two quantities. This peak happens at a radius close to the junction between the convective core and the radiative envelope in the overshooting region.

3.1.3. Higher-order terms in $\dot{\omega}$

In this section, we look at the higher-order contributions to the rate of apsidal motion due to tidal distortion. The first two contributions are $\dot{\omega}_3$ and $\dot{\omega}_4$, which can be expressed as

$$\dot{\omega}_3 = \frac{56\pi}{P_{\rm orb}} f_3(e)\left(k_{3,1} q\left(\frac{R_1}{a}\right)^7 + k_{3,2}\frac{1}{q}\left(\frac{R_2}{a}\right)^7\right) \tag{3.19}$$

[4] By normalised, we mean divided by $\frac{M_*}{R_*^3}$, which is a proxy for the mean stellar density where M_* and R_* are the mass and the radius of the star, respectively, expressed in cgs units.

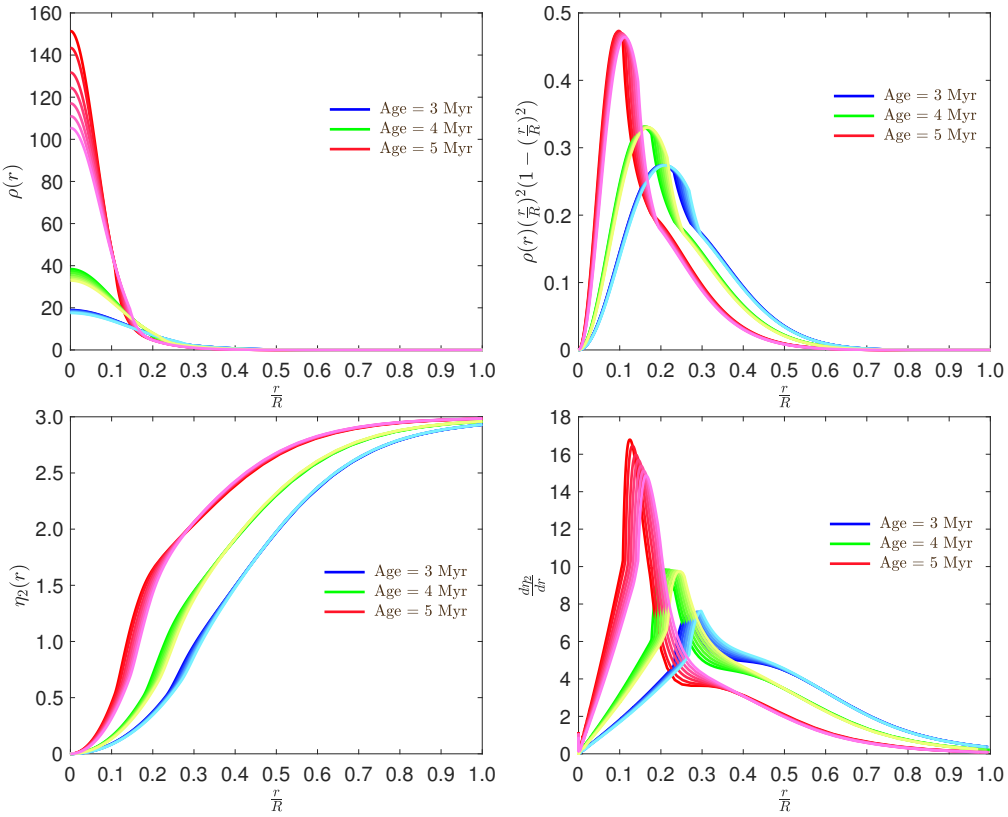

Figure 3.2. Evolution of the normalised density (*top left panel*), the normalised function $\rho(r)\left(\frac{r}{R}\right)^2\left(1-\left(\frac{r}{R}\right)^2\right)$ (*top right panel*), η_2 (*bottom left panel*), and $\frac{d\eta_2}{dr}$ (*bottom right panel*) inside the star for `Clés` models with an initial mass of $31.0\,M_\odot$, assuming no turbulent diffusion, $\xi = 1$, and $Z = 0.015$. Each colour range corresponds to a different age: The models of 3, 4, and 5 Myr are depicted in blue, green, and red declinations, respectively. For each colour range, the darkest shade corresponds to $\alpha_{\rm ov} = 0.10$ while the lightest one corresponds to $\alpha_{\rm ov} = 0.40$; all the intermediate shades span the range from $\alpha_{\rm ov} = 0.10$ to 0.40 in steps of 0.05. The bottom panels correspond to the results obtained from the numerical integration of Equation (3.11). Figure adapted from Rosu et al. (2020a).

and

$$\dot{\omega}_4 = \frac{90\pi}{P_{\rm orb}} f_4(e) \left(k_{4,1} q \left(\frac{R_1}{a}\right)^9 + k_{4,2} \frac{1}{q} \left(\frac{R_2}{a}\right)^9 \right), \tag{3.20}$$

where

$$f_3(e) = \frac{1 + \frac{15}{4}e^2 + \frac{15}{8}e^4 + \frac{5}{64}e^6}{(1-e^2)^7} \tag{3.21}$$

and

$$f_4(e) = \frac{1 + 7e^2 + \frac{35}{4}e^4 + \frac{35}{16}e^6 + \frac{7}{128}e^8}{(1-e^2)^9}, \tag{3.22}$$

as shown by Sterne (1939). In these two expressions, the internal structure constants k_3 and k_4 of the stars are defined by

$$k_j = \frac{j + 1 - \eta_j(R_*)}{2(j + \eta_j(R_*))}, \tag{3.23}$$

where the η_j are solutions of the second-order differential equation

$$r\frac{d\eta_j(r)}{dr} + \eta_j^2(r) - \eta_j(r) + 6\frac{\rho(r)}{\bar{\rho}(r)}\left(\eta_j(r) + 1\right) - j(j+1) = 0 \tag{3.24}$$

with the boundary condition $\eta_j(0) = j - 2$ (Hejlesen 1987). Hejlesen (1987) showed that these higher-order terms are negligible compared to the Newtonian and general relativistic terms presented in Section 3.1.1. We indeed confirmed this statement: We computed k_3, k_4, $\dot{\omega}_3$, and $\dot{\omega}_4$ for `Clés` models for the binary system HD 152248. We adopted an initial mass of 30.0 $M_\odot$ and values of the overshooting parameter ranging from 0.10 to 0.40. The results are presented in Figures 3.3 and 3.4 for k_3 and k_4 and for $\dot{\omega}_3$ and $\dot{\omega}_4$, respectively. For each model, $\dot{\omega}_3$ and $\dot{\omega}_4$ contribute a maximum amount of $(6 \times 10^{-5})^\circ\,\mathrm{yr}^{-1}$ and $(6 \times 10^{-6})^\circ\,\mathrm{yr}^{-1}$, respectively, to the rate of apsidal motion. These values are, respectively, three and four orders of magnitude below the actual precision on the value of the observed rate of apsidal motion (see Section 2.2.5). Hence, we can ignore these two contributions, $\dot{\omega}_3$ and $\dot{\omega}_4$, when computing the theoretical rate of apsidal motion.

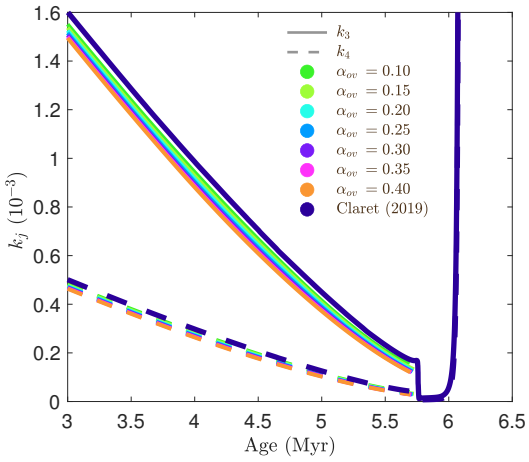

Figure 3.3. Evolution as a function of the stellar age of the internal structure constants k_3 and k_4 of the star for `Clés` models with an initial mass of 30.0 $M_\odot$ and an overshooting parameter of 0.10 (green), 0.15 (light green), 0.20 (cyan), 0.25 (light blue), 0.30 (purple), 0.35 (pink), and 0.40 (orange). The dark blue line represents the Claret (2019) model for an initial mass of 30.0 $M_\odot$.

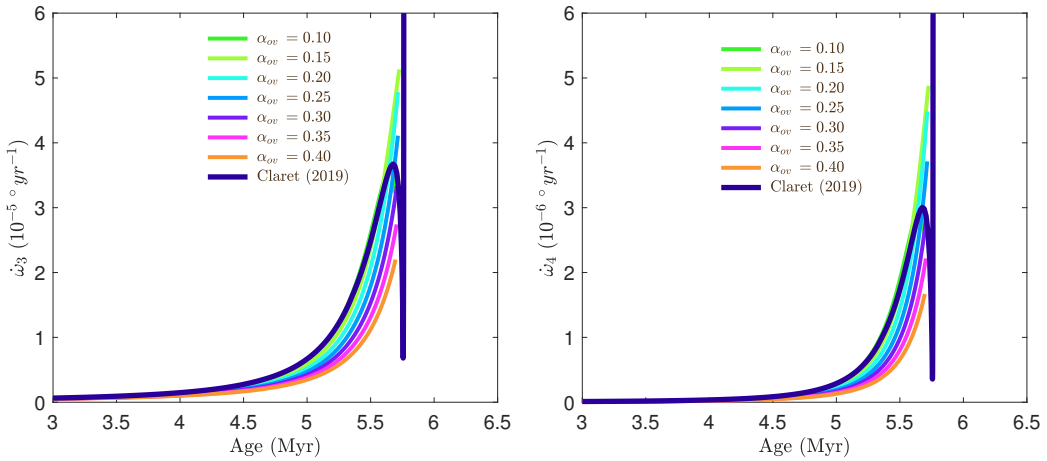

Figure 3.4. Evolution as a function of the stellar age of the third and fourth-order contributions to the apsidal motion rate of the binary as computed with Equations (3.19) and (3.20) for `Clés` models with an initial mass of 30.0 $M_\odot$ and an overshooting parameter of 0.10 (green), 0.15 (light green), 0.20 (cyan), 0.25 (light blue), 0.30 (purple), 0.35 (pink), and 0.40 (orange). The dark blue line represents the Claret (2019) model with an initial mass of 30.0 $M_\odot$.

3.1.4. Rotation axes misalignment

The general expression of the Newtonian contribution to the total rate of apsidal motion when the rotation axes are randomly oriented is given by Equation (3) of Shakura (1985):

$$\begin{aligned}\dot{\omega}_{\rm N} = \frac{2\pi}{P_{\rm orb}}\Bigg[& 15 f(e)\left\{k_{2,1} q \left(\frac{R_1}{a}\right)^5 + \frac{k_{2,2}}{q}\left(\frac{R_2}{a}\right)^5\right\} \\ & - \frac{g(e)}{(\sin i)^2}\Bigg\{k_{2,1}(1+q)\left(\frac{R_1}{a}\right)^5\left(\frac{P_{\rm orb}}{P_{\rm rot,1}}\right)^2 \\ & \left[\cos\alpha_1\left(\cos\alpha_1 - \cos\beta_1\cos i\right) + \frac{1}{2}(\sin i)^2\left(1 - 5(\cos\alpha_1)^2\right)\right] \\ & + k_{2,2}\frac{1+q}{q}\left(\frac{R_2}{a}\right)^5\left(\frac{P_{\rm orb}}{P_{\rm rot,2}}\right)^2 \\ & \left[\cos\alpha_2\left(\cos\alpha_2 - \cos\beta_2\cos i\right) + \frac{1}{2}(\sin i)^2\left(1 - 5(\cos\alpha_2)^2\right)\right]\Bigg\}\Bigg],\end{aligned} \tag{3.25}$$

where α_1 (respectively α_2) is the angle between the primary (respectively secondary) star rotation axis and the normal to the orbital plane, and β_1 (respectively β_2) is the angle between the primary (respectively secondary) star rotation axis and the line joining the binary centre and the observer.

We define the function $F_{\alpha,j}$ (with $j = 1, 2$ for the primary and secondary stars, respectively) as

$$F_{\alpha,j} = \cos\alpha_j \left(\cos\alpha_j - \cos\beta_j \cos i\right) + \frac{1}{2}\sin^2 i \left(1 - 5\cos^2\alpha_j\right). \tag{3.26}$$

We define θ as the azimutal angle of the rotation axes of the stars, such that $\theta = 0°$ and $180°$ correspond to the cases where the rotation axes $\mathbf{r}$, the line of sight $\mathbf{l}$, and the normal to the orbital plane $\mathbf{n}$ lie in the same plane (see Figure 3.5).

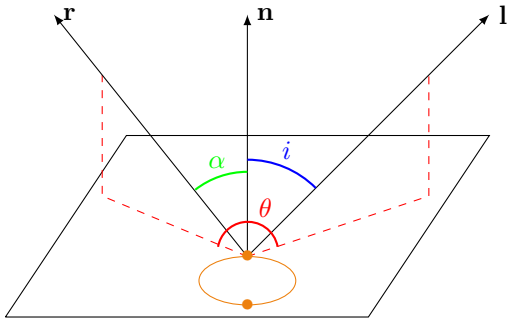

Figure 3.5. Definition of the azimutal angle θ. The plane depicted is the plane of the binary orbit; the binary orbit is depicted in orange. The two stars are symbolised by the two orange dots. The vectors $\mathbf{r}, \mathbf{l}$, and $\mathbf{n}$ are the rotation axis of the star, the line of sight, and the normal to the orbital plane, respectively, while the angles i and α are the orbital inclination and the angle between the stellar rotation axis and the normal to the orbital plane. Figure taken from Rosu et al. (2020a).

We can express $\cos\beta_j$ in terms of the inclination and α_j using the cosine relationship in spherical trigonometry:

$$\cos\beta_j = \cos i \cos\alpha_j + \sin i \sin\alpha_j \cos\theta. \tag{3.27}$$

Replacing in Equation (3.26) $\cos\beta_j$ by its expression given by Equation (3.27) gives us an expression for $F_{\alpha,j}$ which depends upon the inclination, α_j, and θ only. We can further show that $F_{\alpha,j}$ takes its extremum values for $\theta = 0°$ and $180°$. Assuming that $\theta = 180°$, we get $\beta_j = i + \alpha_j$.

We define the quantities

$$C_{\mathrm{mis},j} = -\frac{1}{(\sin i)^2}\left(1 + \frac{M_j}{M_{3-j}}\right)\left(\frac{R_j}{a}\right)^5 \left(\frac{P_{\mathrm{orb}}}{P_{\mathrm{rot},j}}\right)^2 F_{\alpha,j} \tag{3.28}$$

such that Equation (3.25) now writes

$$\dot{\omega}_{\mathrm{N}} = \frac{2\pi}{P_{\mathrm{orb}}}\left[15 f(e)\left\{k_{2,1} q \left(\frac{R_1}{a}\right)^5 + \frac{k_{2,2}}{q}\left(\frac{R_2}{a}\right)^5\right\} + g(e)\left\{k_{2,1} C_{\mathrm{mis},1} + k_{2,2} C_{\mathrm{mis},2}\right\}\right]. \tag{3.29}$$

3.1.4.1. Special case of a twin system

In the special case of a twin system, adopting the notations given by Equation (3.6) and further assuming the rotation axes of the two stars to be parallel, and defining

$$\begin{cases} \alpha_1 = \alpha_2 \equiv \alpha, \\ \beta_1 = \beta_2 \equiv \beta, \end{cases} \tag{3.30}$$

Equation (3.25) simplifies to

$$\dot{\omega}_{\rm N} = \frac{4\pi}{P_{\rm orb}} k_2 \left(\frac{R_*}{a}\right)^5 \left[15 f(e) - \frac{g(e)}{\sin^2 i} P_{\rm orb}^2 \left(\frac{1}{P_{\rm rot,1}^2} + \frac{1}{P_{\rm rot,2}^2} \right) \left[\cos\alpha \left(\cos\alpha - \cos\beta \cos i \right) + \frac{1}{2} \sin^2 i \left(1 - 5\cos^2\alpha \right) \right] \right], \tag{3.31}$$

whilst the function $F_\alpha \equiv F_{\alpha,1} = F_{\alpha,2}$ reduces to

$$F_\alpha = \cos\alpha \left(\cos\alpha - \cos\beta \cos i \right) + \frac{1}{2} \sin^2 i \left(1 - 5\cos^2\alpha \right). \tag{3.32}$$

With

$$\cos\beta = \cos i \cos\alpha + \sin i \sin\alpha \cos\theta, \tag{3.33}$$

we get

$$F_\alpha = \cos\alpha \left(\cos\alpha - \cos^2 i \cos\alpha - \cos i \sin i \sin\alpha \cos\theta \right) + \frac{1}{2} \sin^2 i \left(1 - 5\cos^2\alpha \right). \tag{3.34}$$

F_α takes its extremum values for $\theta = 0°$ and $180°$, in which cases it reduces to

$$F_{\alpha,\pm} = \sin^2 i \left(\frac{1}{2} - \frac{3}{2} \cos^2\alpha \right) \pm \frac{1}{4} \sin(2i) \sin(2\alpha), \tag{3.35}$$

where the plus and minus signs correspond to $\theta = 180°$ and $0°$, respectively.

3.1.4.2. Sub-critical rotation

One may wonder whether the condition of sub-critical rotation velocity leads to a restriction on the values of the putative misalignment angle α between the rotational and orbital axes. In fact, the stellar rotation rate $\Omega_{\rm rot}$ cannot exceed the critical value $\Omega_{\rm crit}$, which corresponds to a situation where the centrifugal force at the equator equals the effective gravity (i.e. the gravity corrected for the effect of radiation pressure):

$$\Omega_{\rm rot} \leq \Omega_{\rm crit} = \sqrt{\frac{G\,M_*}{R_*^3} \left(1 - \Gamma_e\right)}. \tag{3.36}$$

Here, the Eddington factor is given by

$$\Gamma_e = \frac{\kappa_e\, L_*}{4\,\pi\, c\, G\, M_*}. \tag{3.37}$$

We take the electron scattering opacity to be $\kappa_e \simeq 0.34\,\mathrm{cm^2\,g^{-1}}$ (e.g. Sanyal et al. 2015), implying $\Gamma_e = 2.6\,10^{-5}\,\frac{L_*\,M_\odot}{L_\odot\,M_*}$. Condition (3.36) translates into an upper limit on the equatorial rotational velocity

$$v_{\rm eq} \leq \sqrt{\frac{G\,M_*}{R_*}\,\left(1 - \frac{\kappa_e\, L_*}{4\,\pi\, c\, G\, M_*}\right)} \tag{3.38}$$

or

$$v_{\rm eq} \leq 436.7\,\sqrt{\frac{M_*\,R_\odot}{M_\odot\,R_*}\,\left(1 - 2.6\,10^{-5}\,\frac{L_*\,M_\odot}{L_\odot\,M_*}\right)}\,\mathrm{km\,s^{-1}}. \tag{3.39}$$

Using the observational value of the projected rotational velocity $v_{\rm eq}\sin i_{\rm rot} \equiv v_{\rm eq}\sin\beta$, Equation (3.39) allows us to put a constraint on the value of the angle β that then translates into a condition on the angle α through Equation (3.27) if we fix a value for θ.

3.2. Stellar structure and evolution codes

Stellar structure and evolution models aim at reproducing the internal structure of stars for a given set of initial parameters (or physical conditions) and for different evolutionary stages. In this way, we can follow the evolution with time of global stellar parameters (for instance the mass, radius, effective temperature, bolometric luminosity), as well as internal stellar parameters (for instance the size of the convective core, the density profile inside the star, and the central concentration of metals, among others).

Several stellar evolution codes exist in the scientific community. To cite only a few examples, the Code Liégeois d'Évolution Stellaire (`Clés`, developed and maintained by Richard Scuflaire at the STAR Institute at the University of Liège, Scuflaire et al. 2008), the Geneva Stellar evolution code (`GENEC`, developed and maintained at the University of Geneva, Eggenberger et al. 2008), the Modules for Experiments in Stellar Astrophysics code (`MESA`, developed and maintained at the University of California, Paxton et al. 2011), the Bonn code (developed and maintained at the University of Bonn, Brott et al. 2011).

Each stellar evolution code has its own characteristics and specificities but the general physics implemented in these codes is usually very similar, just as the physical ingredients. For massive stars, which are our concern here, the stellar atmosphere can either be computed separately from the interior models and added as a boundary condition (as in `Clés`) or directly with the stellar interior (as in `GENEC`).

For the purpose of the present work, we used both the `Clés` and `GENEC` codes. We describe their main characteristics and specificities in Sections 3.2.1 and 3.2.2, respectively.

3.2.1. `Clés` code

The `Clés` code allows us to build stellar structure and evolution models from the Hayashi track to the beginning of the helium combustion phase for low-mass ($M_\star \leq 1.2\,M_\odot$) stars, and up to the asymptotic giant branch phase for intermediate-mass ($1.2\,M_\odot \leq M_\star \leq 8\,M_\odot$) and high-mass ($M_\star \geq 8\,M_\odot$) stars. For the present study, we used version 19.1 of the `Clés` code.

The standard version of `Clés` uses `OPAL` opacities (Iglesias & Rogers 1996) combined with those of Ferguson et al. (2005) at low temperatures. The solar chemical composition is adopted from Asplund et al. (2009). The equation of state is implemented according to Cassisi et al. (2003), and the rates of nuclear reactions are implemented according to Adelberger et al. (2011). Mixing in convective regions is parameterised according to the mixing length theory (MLT, Cox & Giuli 1968). In this framework, two distinct physical lengths are given by the mixing length: the average distance travelled by convective elements before dissolving and the average size of these convective elements (Cox & Giuli 1968). The mixing length is generally assumed to be proportional to the pressure scale height H_p:

$$l = \alpha_{\mathrm{MLT}} H_p, \tag{3.40}$$

where $\alpha_{\rm MLT}$ is a proportionality coefficient that usually ranges between 1 and 2 (Renzini 1987). The `Clés` code computes the interior models; the atmosphere is computed separately and added to the model as a boundary condition. The important mass-loss via radiation pressure-driven stellar winds is implemented by default through the prescription of Vink et al. (2001) but the user has the possibility to scale this quantity by a multiplicative factor ξ or even to chose another formalism if deemed appropriate. We note that the Vink et al. (2001) recipe has been found to often over-predict the mass-loss rate of O-type stars (Sundqvist et al. 2019, and references therein).

For massive stars, the internal mixing is restricted to the convective core unless overshooting or/and turbulent mixing is/are introduced in the models. Indeed, at the formal convective core edge, only the buoyancy vanishes, but not necessarily the velocity of convective motions. Thus, to some extent, convection has to penetrate, or overshoot, into the surrounding stable layers. Whilst the convective elements are accelerated in the convective core, they undergo deceleration in the overshooting region (Renzini 1987). The problem is therefore to determine the extension of this overshooting region (Renzini 1987).
In `Clés`, instantaneous overshooting displaces the boundary of a mixed region from r_c to $r_{\rm ov}$, as given by the following step-function:

$$r_{\rm ov} = r_c + \alpha_{\rm ov} \min(H_p(r_c), h), \tag{3.41}$$

where h is the thickness of the convective zone,

$$H_p(r_c) = \frac{P(r_c)}{\rho(r_c) g(r_c)} \tag{3.42}$$

is the pressure scale height taken at the edge of the convective core as given by the Schwarzschild or Ledoux criterion, $P(r_c)$, $\rho(r_c)$, and $g(r_c)$ are the pressure, density, and local gravity at the edge of the convective core, respectively, and $\alpha_{\rm ov}$ is the overshooting parameter chosen by the user. In the stellar interior, some small perturbations might sometimes grow and generate macroscopic motions. For massive stars, the Ledoux criterion for convective instability is adopted. It defines wether these perturbations will develop or not and is expressed as

$$\nabla_{\rm rad} < \nabla_{\rm ad} + \frac{\phi}{\delta} \nabla_\mu, \tag{3.43}$$

where

$$\nabla \equiv \frac{d \ln T}{d \ln P}, \tag{3.44}$$

$$\nabla_\mu \equiv \frac{d \ln \mu}{d \ln P}, \tag{3.45}$$

$$\phi = \frac{\partial \ln \rho}{\partial \ln \mu}, \tag{3.46}$$

and

$$\delta = -\frac{\partial \ln \rho}{\partial \ln T}. \tag{3.47}$$

$\nabla_{\rm ad}$ is the internal gradient when the moving cells do not exchange any heat with the

surrounding medium, $\nabla_{\rm rad}$ is the thermal gradient necessary to carry the convective and radiative energies by radiation, and μ is the mean molecular weight. In the absence of a chemical gradient, $\nabla_\mu = 0$ and the Schwarzschild stability criterion

$$\nabla_{\rm rad} < \nabla_{\rm ad} \tag{3.48}$$

is recovered.
The classical step-function given by Equation (3.41) is adopted to prevent the models from having a region of extra mixing larger than the initial size of the convective core. Adding core overshooting results in the enlargement of the centrally mixed core leading, therefore, to an extended main-sequence lifetime of the star as more fuel is available for the hydrogen fusion.

The overshooting parameter $\alpha_{\rm ov}$ is poorly constrained. We refer to Renzini (1987) for a critical examination of various versions of the mixing-length theory approach to overshooting. While some studies suggest that $\alpha_{\rm ov}$ could take a value of 0.30 for stars more massive than $4\,M_\odot$ (Claret 2007; Claret & Torres 2016, 2019), there is currently no consensus on the value of this parameter for massive stars, except that it is most likely larger than or equal to 0.20. Claret (2019) showed based on their `MESA` models that $\alpha_{\rm ov}$ saturates around a value of 0.20 for stars more massive than $2\,M_\odot$ but their sample stopped at $4.5\,M_\odot$. In the present analysis, we explored values of $\alpha_{\rm ov}$ up to 0.40 in our `Clés` models for the binary systems HD 152248, HD 152219, CPD-41° 7742, and HD 152218 (see Sections 3.3, 3.4, 3.5, and 3.6, respectively), and showed evidence for the need of high $\alpha_{\rm ov}$ values. Tkachenko et al. (2020) reached the same conclusion from the analysis of their sample of stars based on `MESA` models. Martinet et al. (2021) suggested to use a value of $\alpha_{\rm ov} = 0.20$ for their `GENEC` rotating models for stars having a mass of $9\,M_\odot$ or higher. We emphasise here that different analyses using different stellar evolution codes with different prescriptions of the mixing processes reach the same qualitative conclusion that strong internal mixing is required.

Turbulent transport can be taken into account in the models. It is modelled as a diffusion process by adding a pure diffusion term of the form

$$-\,D_T \frac{\partial \ln X_i}{\partial r}, \tag{3.49}$$

with a positive turbulent diffusion coefficient D_T (in $\mathrm{cm^2\,s^{-1}}$), to each element's diffusion velocity, which tends to reduce its abundance gradient (Richer et al. 2000). In this expression, r is the radius and X_i is the mass fraction of element i at that point. The turbulent diffusion coefficient D_T takes the following expression:

$$D_T = D_{\rm turb} \left(\frac{\rho}{\rho_0} \right)^n + D_{\rm ct}, \tag{3.50}$$

where $D_{\rm turb}$, n, and $D_{\rm ct}$ are chosen by the user. No microscopic diffusion is introduced in the models. In the present analysis, we adopted a constant D_T value throughout the star, that is to say, we set $n = 0$. We emphasise that the values of D_T in massive stars are unconstrained.

Rotational mixing is not included in the `Clés` code, but its effect on the internal structure can be simulated by means of the turbulent diffusion (see Section 3.3.4).

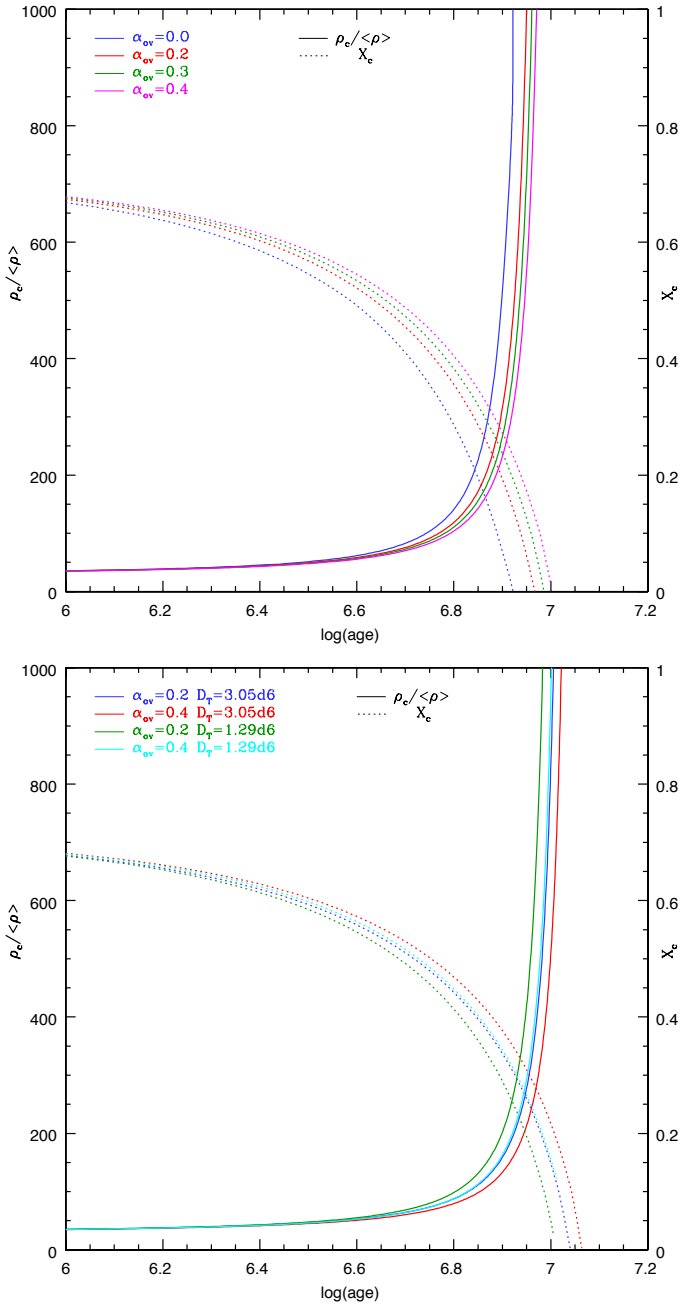

Figure 3.6. Evolution as a function of the stellar age of the ratio between the central density ρ_c and the mean density inside the star $<\rho>$ (solid lines) as well as the central hydrogen mass fraction X_c (dashed lines) for different models with an initial mass of 19.0 $M_\odot$ having different values of the overshooting parameter and turbulent diffusion coefficient.

All three mechanisms, the overshooting, the turbulent diffusion, and the rotational mixing, by enlarging the convective core and bringing more unprocessed material into the convective core, increase the main-sequence lifetime of the star. The additional mixing leads to a reduced mass concentration at a given age. This is illustrated in Figure 3.6 where the ratio between the central density ρ_c and the mean density inside the star $<\rho>$ as well as the central hydrogen mass fraction X_c are plotted as a function of the stellar age for different models with an initial mass of $19.0\,M_\odot$ having different values of the overshooting parameter and turbulent diffusion coefficient. In the bottom panel of Figure 3.6 – and here we anticipate the discussion in Section 3.3.2 – we highlight two models that are degenerate, namely those having $\alpha_{\rm ov} = 0.20$ and $D_T = 3.05 \times 10^6$ cm^2 s^{-1} and $\alpha_{\rm ov} = 0.40$ and $D_T = 1.29 \times 10^6$ cm^2 s^{-1}. However, despite this degeneracy between the models, the profiles of the hydrogen mass fraction are different, as illustrated in Figure 3.7. The ξ parameter has a negligible impact on the evolution of the ratio $\rho_c/<\rho>$ and of X_c (see Figure 3.8).

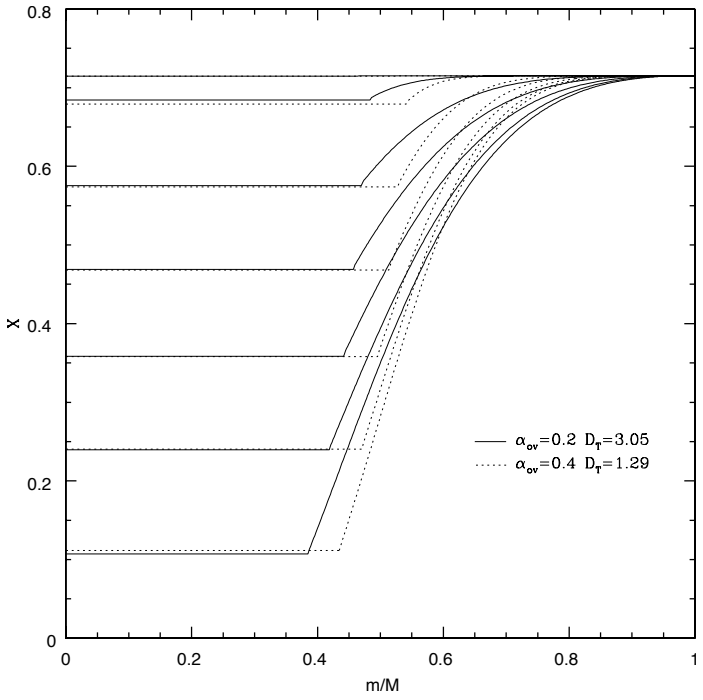

Figure 3.7. Evolution as a function of the reduced mass of the hydrogen mass fraction X at different stages of evolution for two models with an initial mass of $19.0\,M_\odot$, having $\alpha_{\rm ov} = 0.20$ and $D_T = 3.05 \times 10^6$ cm^2 s^{-1} (solid lines) and $\alpha_{\rm ov} = 0.40$ and $D_T = 1.29 \times 10^6$ cm^2 s^{-1} (dashed lines), respectively.

In the context of the present study, the main limitation of the code resides in the fact that the star is assumed to be single. Therefore, the putative influence of binarity on the internal structure of the stars is not taken into account. We will return to this point in Section 3.3.4.

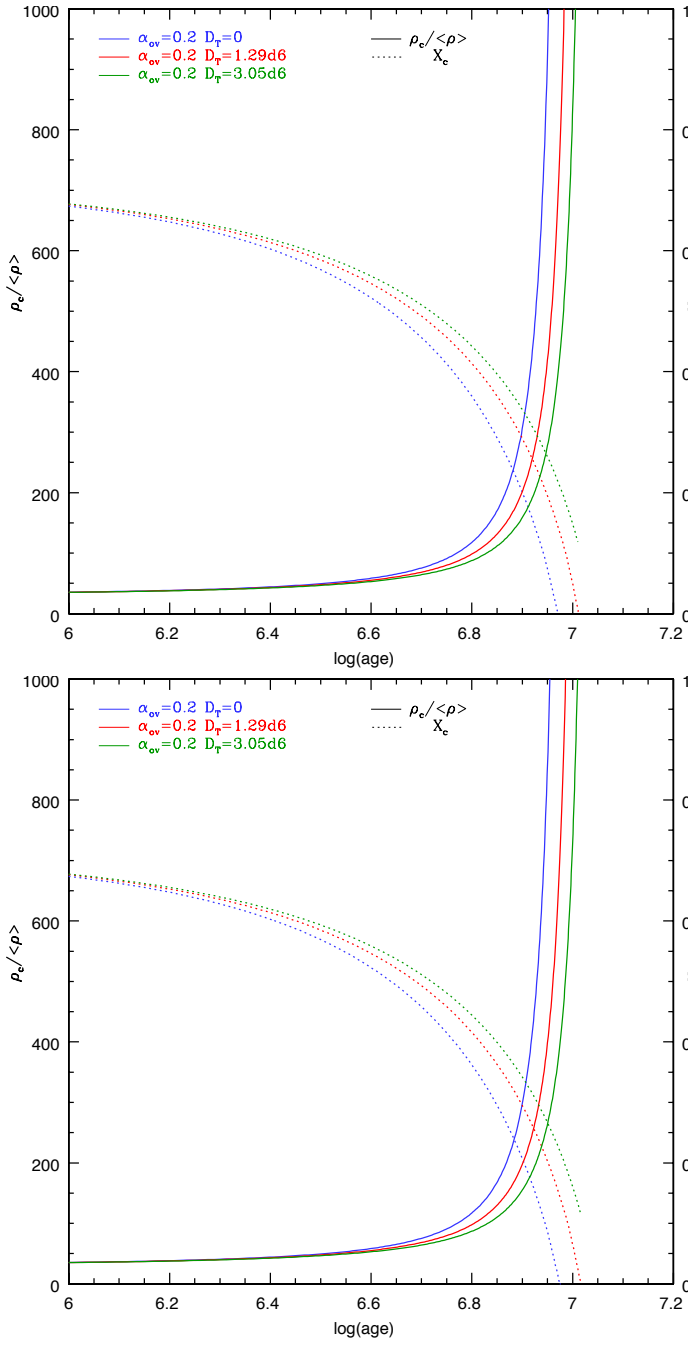

Figure 3.8. Evolution as a function of the stellar age of the ratio between the central density ρ_c and the mean density inside the star $<\rho>$ (solid lines) as well as the central hydrogen mass fraction X_c (dashed lines) for different models with an initial mass of 19.0 $M_\odot$, $\alpha_{\rm ov} = 0.20$, and having different values of the turbulent diffusion coefficient. *Top panel:* $\xi = 1$. *Bottom panel:* $\xi = 2$.

For our reference models, we adopted an hydrogen mass fraction $X = 0.715$ and a metallicity $Z = 0.015$, in accordance with Asplund et al. (2009), but we also investigated the influence of the metallicity and helium abundance. For the overshooting, we adopted $\alpha_{\rm ov} = 0.20$ as a reference. Since there are no obvious constraints on $\alpha_{\rm ov}$, we considered values from 0.10 to 0.40 depending on the cases and identified the impact of this parameter on the evolution of the stars and its interrelation with the turbulent diffusion.

Best-fit models were determined through a Levenberg-Marquardt minimisation implemented following Press et al. (1992) in a `Fortran` routine called `min-Clés`. This routine determines the combination of the `Clés` models' free parameters, including, notably, the initial mass and the stellar age, which allow for the best reproduction of a set of the star's currently observed properties. Other parameters, such as ξ or D_T, were also used as free parameters depending on the case. The constraints were fixed by the observational values of the mass, the radius, and, depending on the case, the effective temperature and the luminosity. We note here that at the time of the study of the first binary system, namely HD 152248, the computation of the internal structure constant for the stellar evolution models was not included yet in `Clés` and was thus performed a posteriori (see Section 3.3). This computation was introduced in `Clés` for the study of the other binary systems. Hence, we could add k_2 has a constraint of the models for the binary system HD 152219 (see Section 3.4).

3.2.2. `GENEC` code

`GENEC` is a one-dimensional code that accounts for the two-dimensional stellar surface deformation due to rotation. In its binary version, this code allows the inclusion of the effects of tidal interactions on the stellar structure, and thus on the k_2 value.

The changes in the stellar structure due to rotation is implemented following the prescriptions of Meynet & Maeder (1997). The transport of chemicals and angular momentum by meridional circulation and shears follows the descriptions of Zahn (1992), Maeder (1997), and Maeder & Zahn (1998). In convective regions, solid-body rotation is considered.

The `GENEC` code exists in two versions: the *single* version for an isolated star (Eggenberger et al. 2008) and the *binary* version for a star belonging to a binary system (Song et al. 2013). The binary version of the code currently follows the evolution of the stars until the onset of mass transfer. It accounts for the mixing induced by tidal interactions (Song et al. 2013) but does not account for the temporal modulation of these effects due to the eccentricity.

The mass-loss rate is implemented through the Vink et al. (2001) prescription and the overshooting is parameterised as in the `Clés` code (see Section 3.2.1). In `GENEC`, as in `Clés`, the Ledoux criterion for convection is used.

3.2.3. Computation of k_2 for the models

We solved the differential equation (3.11) for the set of stellar structure models considered in this paper. For this purpose, we used a `Fortran` code that implements a fourth-order Runge-Kutta method with step doubling. The code was validated against polytropic models and was already used in the study of the apsidal motion of the massive binary HD 152218 (Rauw et al. 2016). This code was not included yet in `Clés` at the time of the study of HD 152248.

As the `Clés` models do not account for the rotation of the stars, we followed Claret (1999) in correcting a posteriori the derived k_2 by an amount

$$\delta(\log k_2) = -0.87\lambda_s \tag{3.51}$$

with

$$\lambda_s = \frac{2\Omega_s^2 R^3}{3GM}, \tag{3.52}$$

where Ω_s is the observational angular rotational velocity of the star, computed based on the projected rotational velocity of the stars, the inclination of the orbit, and the observational stellar radius. By default, unless explicitly stated otherwise, this correction was applied to the outcome of the models presented in this work, except for those `GENEC` models that explicitly account for the effect of rotation.

3.3. The twin binary: HD 152248

Using our re-derived parameters of HD 152248 (see Section 2.2), we inferred values of $(1.680^{+0.064}_{-0.083})^\circ\,\mathrm{yr}^{-1}$ and $(0.163\pm0.001)^\circ\,\mathrm{yr}^{-1}$, respectively, for the Newtonian and general relativistic contributions to the total observational rate of apsidal motion using Equations (3.1), (3.2), and (3.4). Taking advantage of the twin nature of the system, and assuming both stars have the same internal structure constant, a value for the observational internal structure constant $k_{2,\mathrm{obs}}$ of 0.0010 ± 0.0001 was then inferred for both stars. The set of observationally determined properties of the binary is summarised in Table 3.1.

Table 3.1. Set of observationally determined properties of the binary system HD 152248 used for the `Clés` analysis, for which we adopted symmetric uncertainties.

Parameter	Value
M ($M_\odot$)	29.5 ± 0.5
R ($R_\odot$)	15.07 ± 0.12
T_{eff} (K)	$34\,000 \pm 1000$
L_{bol} ($L_\odot$)	$(2.73 \pm 0.32) \times 10^5$
$k_{2,\mathrm{obs}}$	0.0010 ± 0.0001
$\dot{\omega}_{\mathrm{obs}}$ ($^\circ\,\mathrm{yr}^{-1}$)	1.843 ± 0.083

This section is divided as follows. In Section 3.3.1, we search for best-fit models of the system using the `min-Clés` routine and we solve for the apsidal motion constants and the theoretical rate of apsidal motion for the set of `Clés` models that best reproduce the observed stellar parameters. We investigate the influence of various prescriptions for the internal mixing in Section 3.3.2 and of the metallicity in Section 3.3.3. In Section 3.3.4, we build single- and binary-star evolution models with `GENEC` in order to assess the impact of tidal interactions and stellar rotation on the internal structure of the stars. We discuss the impact of a rotation axis misalignment and of a putative ternary component in Section 3.3.5. Finally, we present our conclusions in Section 3.3.6. The most important results of this section are presented in Rosu et al. (2020a).

3.3.1. Preliminary analysis

Our observational study of HD 152248 led to the determination of a number of stellar parameters that can be compared to the predictions of the evolutionary models (see Table 3.1). As an illustration, we present in Figure 3.9 the evolution, as a function of the stellar age, of the mass, the radius, the effective temperature, the luminosity, the internal structure constant, and the ensuing rate of apsidal motion computed with Equation (3.1) for three `Clés` models with initial masses $M_{\mathrm{init}} = 30.0$, 31.0, and $32.0\,M_\odot$, mass-loss according to the Vink et al. (2001) recipe (i.e. with $\xi = 1$), $Z = 0.015$, $\alpha_{\mathrm{ov}} = 0.20$, and no turbulent diffusion. The observational value of the corresponding parameter and its error bars are represented. The evolution of the parameters for a model with an initial mass of $30.0\,M_\odot$ according to Claret (2019) is also presented for comparison. We note that Claret (2019) applied a scaling factor $\xi = 0.1$ to the mass-loss rate computed with the Vink et al. (2001)

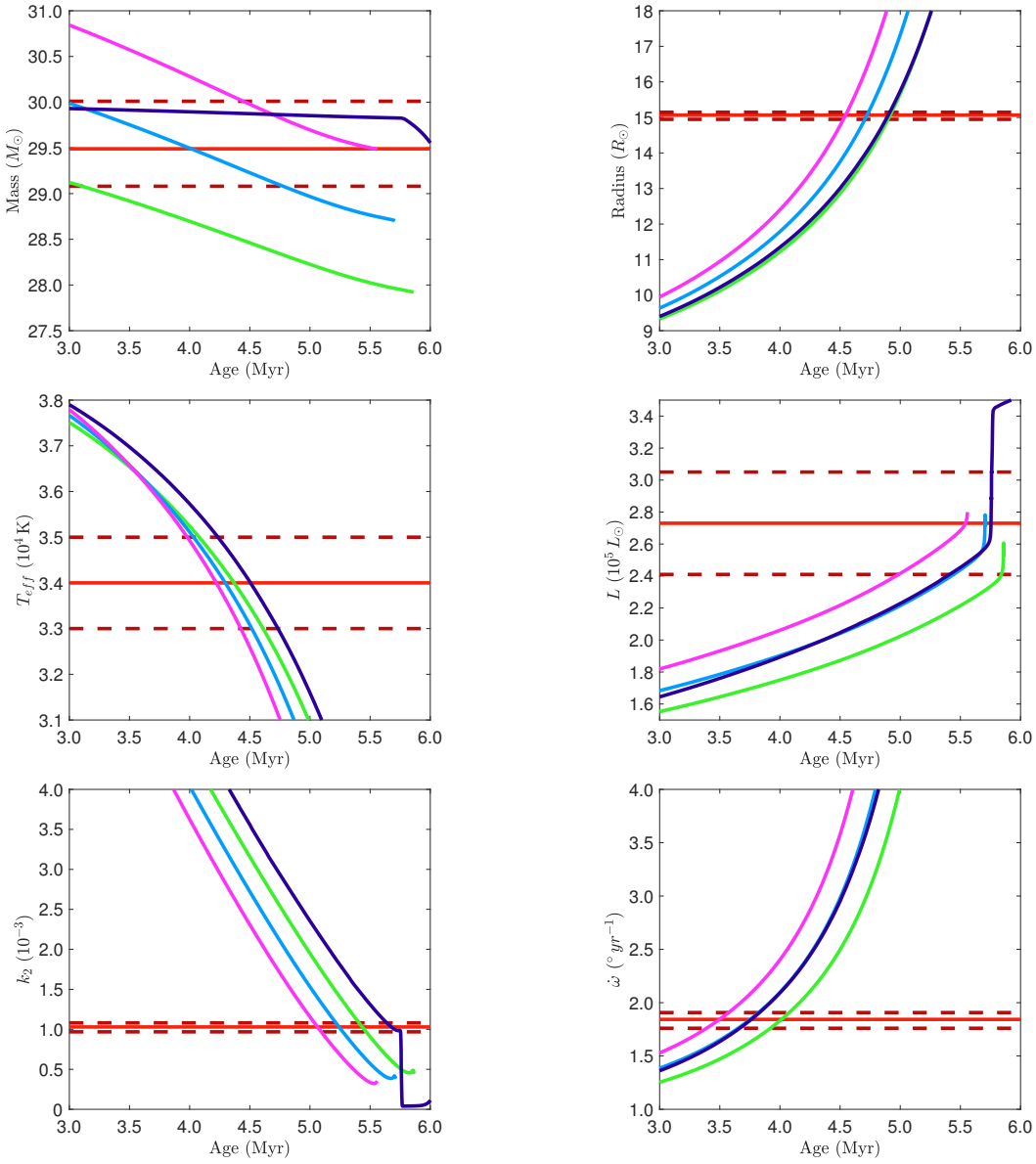

Figure 3.9. Evolution as a function of the stellar age of the mass (*top left panel*), radius (*top right panel*), effective temperature (*middle left panel*), luminosity (*middle right panel*), internal structure constant of the star (*bottom left panel*), and apsidal motion rate of the binary (as computed with Equation (3.1) assuming both stars are described with the same `Clés` model, *bottom right panel*) for `Clés` models with an initial mass of 30.0 (green), 31.0 (light blue), and 32.0 $M_\odot$ (pink), $\alpha_{\rm ov} = 0.20$, $\xi = 1$, $Z = 0.015$, and no turbulent diffusion. The observational value of the corresponding parameter and its error bars are represented by the solid red line and the dashed dark red horizontal lines, respectively. The dark blue line represents the Claret (2019) model with an initial mass of 30.0 $M_\odot$ and $\xi = 0.1$. Figure adapted from Rosu et al. (2020a).

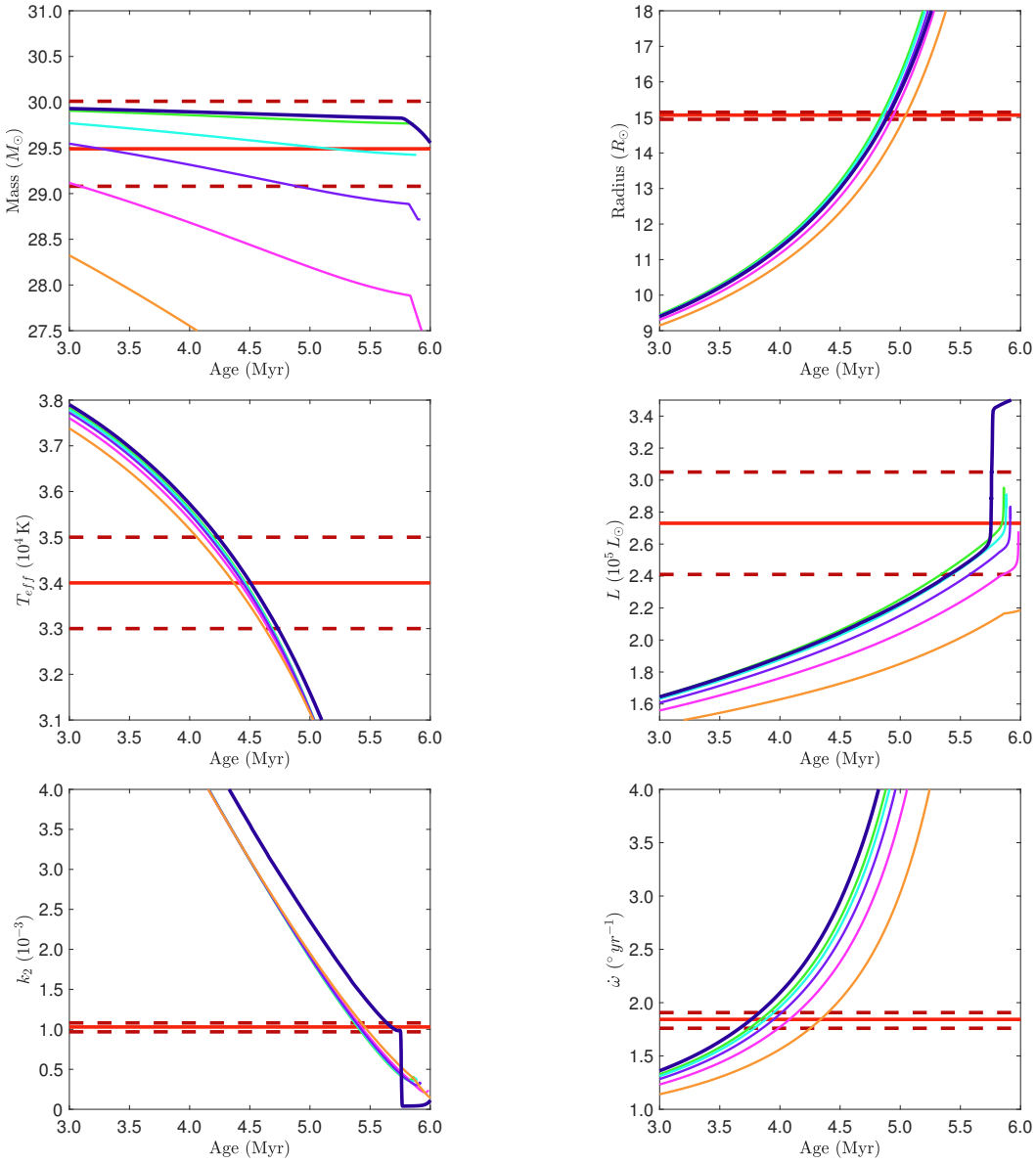

Figure 3.10. Evolution as a function of the stellar age of the mass (*top left panel*), radius (*top right panel*), effective temperature (*middle left panel*), luminosity (*middle right panel*), internal structure constant of the star (*bottom left panel*), and apsidal motion rate of the binary (as computed with Equation (3.1) assuming both stars are described with the same `Clés` model, *bottom right panel*) for `Clés` models with an initial mass of 30.0 $M_\odot$, $\alpha_{\rm ov} = 0.20$, $Z = 0.015$, no turbulent diffusion, and $\xi = 0.1$ (green), 0.25 (cyan), 0.50 (purple), 1 (pink), and 2 (orange). The observational value of the corresponding parameter and its error bars are represented by the solid red line and the dashed dark red horizontal lines, respectively. The dark blue line represents the Claret (2019) model with an initial mass of 30.0 $M_\odot$ and $\xi = 0.1$.

prescription. Using the same ξ and adopting the same initial mass in our `Clés` models, we recovered the same behaviour as predicted by the Claret (2019) model (see Figure 3.10).

We observe that, for a given `Clés` model, the crossing between the model value and the observational value (taking into account the uncertainties) does not happen at the same age for all the parameters. We note that it is difficult to reconcile the luminosity and k_2 on the one hand and all other parameters on the other hand. Indeed, both the luminosity and k_2 suggest a minimum stellar age of ~ 5.3 Myr, while the other parameters suggest ages of less than ~ 4.9 Myr. This is even clearer when looking at the evolutionary tracks of the three models in the Hertzsprung-Russell diagram in Figure 3.11. Indeed, none of these tracks crosses the observational box defined by the observational radius and effective temperature and their respective error bars. The three models that fit the k_2, represented by the three dots over-plotted on the corresponding tracks, lie well away from the two lines delimiting the range of acceptable radii. This issue is not solved by adopting other values for $\alpha_{\rm ov}$. This observation motivated us to use the `min-Clés` routine to search for a set of model parameters that best reproduce the observed values simultaneously (i.e. for a single value of the age).

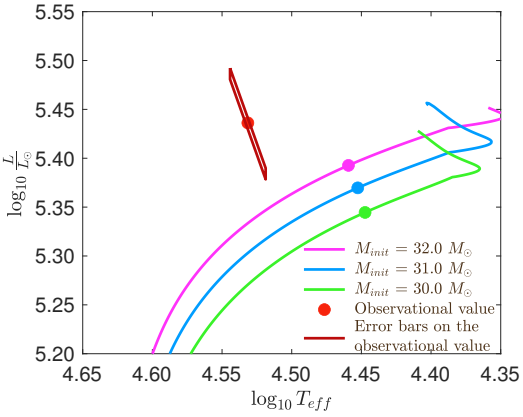

Figure 3.11. Hertzsprung-Russell diagram: evolutionary tracks of `Clés` models with initial masses of 30.0 (green), 31.0 (light blue), and 32.0 $M_\odot$ (pink), $\alpha_{\rm ov} = 0.20$, $\xi = 1$, $Z = 0.015$, and no turbulent diffusion. The three dots over-plotted on the corresponding tracks correspond to the models that fit the observational k_2. The observational value is represented by the red point and its error bars are represented by the dark red parallelogram. Figure adapted from Rosu et al. (2020a).

As a first step, we requested the `Clés` model to simultaneously reproduce the observed radius and mass with the mass-loss computed according to the Vink et al. (2001) recipe (i.e. with $\xi = 1$), and with $Z = 0.015$, $\alpha_{\rm ov} = 0.20$, and no turbulent diffusion. This model gave us $M_{\rm init} = 31.5\,M_\odot$ and an age of 4.65 Myr (Model I). However, this model clearly fails to reproduce the observed effective temperature, luminosity, and rate of apsidal motion (see Table 3.2). This confirms our observation regarding the difficulties involved in simultaneously fitting all the observed quantities. Adopting $\xi = 0.5$ leads to a larger discrepancy (Model III), whereas adopting $\xi = 2.0$ slightly improves the results (Model II).

Table 3.2. Parameters of some best-fit `Clés` models for HD 152248 discussed in Section 3.3.

Model	Age (Myr)	$M_{\rm init}$ ($M_\odot$)	M ($M_\odot$)	R ($R_\odot$)	$T_{\rm eff}$ (K)	L ($10^5\,L_\odot$)	$k_{2,\rm un.}$ (10^{-3})	k_2 (10^{-3})	$\dot{\omega}$ ($^\circ\,{\rm yr}^{-1}$)	$\dot{M}$ ($10^{-6}\,M_\odot\,{\rm yr}^{-1}$)	ξ	D_T ($10^7\,{\rm cm}^2\,{\rm s}^{-1}$)	$\alpha_{\rm ov}$	χ^2
Model I	4.65*	31.5*	29.5†	15.07†	32 209	2.20	2.26	2.09	3.581	0.58	1.0#	0.0#	0.20#	749.01
Model II	4.35*	34.0*	29.5†	15.07†	32 500	2.28	2.04	1.89	3.249	1.30	2.0#	0.0#	0.20#	490.66
Model III	4.80*	30.5*	29.5 †	15.07†	32 089	2.17	2.36	2.18	3.724	0.28	0.5#	0.0#	0.20#	877.50
Model IV	3.65*	44.9*	29.5†	15.07†	33 985†	2.73†	1.23	1.14	2.025	4.48	4.14*	0.0#	0.20#	8.03
Series V(1)	5.10*	32.6*	29.5†	15.07†	33 986†	2.73†	1.23	1.14	2.028	1.08	1.0#	1.91*	0.20#	8.31
Series V(2)	4.56*	36.1*	29.5†	15.07†	33 987†	2.73†	1.23	1.14	2.027	2.16	2.0#	1.34*	0.20#	8.21
Series V(3)	4.09*	40.0*	29.5†	15.07†	33 990†	2.73†	1.23	1.14	2.025	3.25	3.0#	0.74*	0.20#	8.10
Series VI(1)	5.13*	32.7*	29.5†	15.07†	33 989†	2.73†	1.24	1.15	2.040	1.08	1.0#	2.31*	0.10#	9.50
Series VI(2)	4.58*	36.2*	29.5†	15.07†	33 988†	2.73†	1.24	1.15	2.042	2.17	2.0#	1.73*	0.10#	9.63
Series VI(3)	4.12*	40.1*	29.5†	15.07†	33 979†	2.73†	1.25	1.15	2.050	3.24	3.0#	1.10*	0.10#	10.47
Series VII(1)	5.11*	32.6*	29.5†	15.07†	33 987†	2.73†	1.24	1.15	2.034	1.08	1.0#	2.10*	0.15#	8.92
Series VII(2)	4.57*	36.2*	29.5†	15.07†	33 985†	2.73†	1.24	1.15	2.036	2.16	2.0#	1.53*	0.15#	9.04
Series VII(3)	4.11*	40.1*	29.5†	15.07†	33 990†	2.73†	1.24	1.14	2.034	3.25	3.0#	0.92*	0.15#	8.87
Series VIII(1)	5.08*	32.6*	29.5†	15.07†	33 987†	2.73†	1.23	1.14	2.020	1.08	1.0#	1.73*	0.25#	7.61
Series VIII(2)	4.54*	36.1*	29.5†	15.07†	33 987†	2.73†	1.23	1.14	2.019	2.17	2.0#	1.16*	0.25#	7.54
Series VIII(3)	4.08*	40.0*	29.5†	15.07†	33 980†	2.73†	1.22	1.14	2.024	3.24	3.0#	0.56*	0.25#	7.93
Series IX(1)	5.07*	32.6*	29.5†	15.07†	33 986†	2.73†	1.23	1.13	2.014	1.08	1.0#	1.56*	0.30#	7.09
Series IX(2)	4.53*	36.1*	29.5†	15.07†	33 982†	2.73†	1.23	1.13	2.016	2.16	2.0#	0.99*	0.30#	7.32
Series IX(3)	4.07*	39.9*	29.5†	15.07†	33 992†	2.73†	1.22	1.13	2.007	3.25	3.0#	0.42*	0.30#	6.54
Series X(1)	5.06*	32.6*	29.5†	15.07†	33 987†	2.73†	1.22	1.13	2.008	1.08	1.0#	1.39*	0.35#	6.59
Series X(2)	4.52*	36.1*	29.5†	15.07†	33 987†	2.73†	1.22	1.13	2.006	2.17	2.0#	0.84*	0.35#	6.48
Series X(3)	4.07*	39.9*	29.5†	15.07†	33 995†	2.73†	1.22	1.12	1.997	3.26	3.0#	0.29*	0.35#	5.80
Series XI(1)	5.05*	32.6*	29.5†	15.07†	33 986†	2.73†	1.22	1.13	2.003	1.08	1.0#	1.23*	0.40#	6.26
Series XI(2)	4.51*	36.0*	29.5†	15.07†	33 987†	2.73†	1.22	1.12	2.000	2.17	2.0#	0.69*	0.40#	6.00
Series XI(3)	4.06*	39.9*	29.5†	15.07†	33 995†	2.73†	1.21	1.12	1.991	3.26	3.0#	0.16*	0.40#	5.30
Model XII	5.18*	32.8*	29.5†	15.07†	34 260†	2.82†	1.12	1.04†	1.857†	1.19	1.0#	$2.41^{+0.08\#}_{-0.08}$	0.20#	0.19
Model XIII	5.16*	32.8*	29.5†	15.07†	34 259†	2.82†	1.12	1.04†	1.858†	1.18	1.0#	$2.19^{+0.08\#}_{-0.07}$	0.25#	0.20
Model XIV	5.16*	32.7*	29.4†	15.07†	34 222†	2.81†	1.12	1.03†	1.854†	1.17	1.0#	$1.98^{+0.06\#}_{-0.06}$	0.30#	0.15
Model XV	5.14*	32.8*	29.5†	15.07†	34 234†	2.81†	1.12	1.03†	1.854†	1.18	1.0#	$1.79^{+0.07\#}_{-0.06}$	0.35#	0.14
Model XVI	5.12*	32.8*	29.5†	15.07†	34 231†	2.81†	1.12	1.04†	1.854†	1.17	1.0#	$1.60^{+0.05\#}_{-0.06}$	0.40#	0.14

Notes. Columns 1 and 2 give the name of the model and its current age. Column 3 lists the initial mass of the corresponding evolutionary sequence. Columns 4, 5, 6, and 7 give the current mass, radius, effective temperature, and luminosity of the model. Columns 8 and 9 yield the k_2 of the model respectively before and after applying the empirical correction for the effect of rotation of Claret (1999, Equation (3.51)). Column 10 gives the ensuing apsidal motion rate computed using Equation (3.1). Column 11 lists the mass-loss rate of the model. Columns 12, 13, and 14 give the mass-loss rate scaling factor, the turbulent diffusion coefficient, and the overshooting parameter of the model. Column 15 quotes the χ^2 of the model.
The *-symbol denotes free parameters of the models, the #-symbol denotes fixed parameters of the models, and the †-symbol denotes constraints of the models. All χ^2 have been computed based on M, R, $T_{\rm eff}$, L, k_2, and $\dot{\omega}$, but see the caveats of Andrae (2010) and Andrae et al. (2010).

As a second step, we requested the `Clés` model to simultaneously reproduce the observed mass, radius, and location in the Hertzsprung-Russell diagram for $Z = 0.015$, $\alpha_{\rm ov} = 0.20$, and no turbulent diffusion, but now allowing ξ to vary. These trials gave us $M_{\rm init} = 44.9\,M_{\odot}$, an age of 3.65 Myr, and a mass-loss scaling factor of $\xi = 4.14$ (Model IV). While this model predicts a rate of apsidal motion closer to the observational value than previous models (see Table. 3.2), the corresponding mass-loss rate of $4.48 \times 10^{-6}\,M_{\odot}\,{\rm yr}^{-1}$ exceeds the observational upper limit of the unclumped mass-loss rate ($2.5 \times 10^{-6}\,M_{\odot}\,{\rm yr}^{-1}$, see Section 2.2.1.5) by nearly a factor of two.

3.3.2. A ξ – $\alpha_{\rm ov}$ – D_T degeneracy

To overcome this problem, we investigated the influence of the turbulent diffusion and overshooting on the best-fit models. We requested the `Clés` models to simultaneously reproduce the observed mass, radius, and location in the Hertzsprung-Russell diagram for $\alpha_{\rm ov} = 0.20$ and $Z = 0.015$. In a first series of trials (Series V, see Table 3.2), we tested the impact of turbulent diffusion – leaving D_T as a free parameter – fixing ξ to 1, 2, and 3. Doing this, we found that models of equal quality, as far as the adjustment of the stellar parameters and of $\dot{\omega}$ is concerned, can be obtained for different pairs of D_T and ξ. To investigate this degeneracy between the two parameters, we performed six other series of trials (see Table 3.2) for different values of the overshooting parameter $\alpha_{\rm ov}$: 0.10 (Series VI), 0.15 (Series VII), 0.25 (Series VIII), 0.30 (Series IX), 0.35 (Series X), and 0.40 (Series XI). The left-hand panel of Figure 3.12 illustrates the degeneracy between these two parameters: Larger ξ values yield lower values of D_T for a given $\alpha_{\rm ov}$. Assuming a higher mass-loss rate means that the initial mass of the star is also higher. This in turn implies that when the star reaches the observed mass value, its convective core is larger than when a smaller mass-loss rate is applied. With a larger convective core, there is no need for a large turbulent mixing. Hence, if ξ increases, D_T decreases. The dispersions of the D_T values (for a given value of ξ) are large, but they also stem from the ranges of initial masses and ages that are found for each value of ξ.

These seven series of models also reveal the degeneracy between $\alpha_{\rm ov}$ and D_T: the larger the value of $\alpha_{\rm ov}$, the lower the value of D_T for a given value of ξ. If the overshooting parameter is increased, the mixing is enhanced and there is no need for a large turbulent mixing. These two parameters affect the stellar structure in a similar way, that is to say, they increase the mixing, which lowers the central concentration of metals (see Section 3.2.1). Hence, an increase in one of them leads to a decrease in the other. This degeneracy is also apparent in the left-hand panel of Figure 3.12.

The only difference between the models lies in the initial mass and current age of the star: the higher ξ, the higher the initial mass of the star and the lower its current age. This is expected since the mass-loss rate increases with ξ. For a given ξ, the couples of values $(\alpha_{\rm ov}, D_T)$ giving the best-fit to M, R, $T_{\rm eff}$, and L all yield stars of the same initial mass. But the higher $\alpha_{\rm ov}$ is, the lower the current age of the star is (see the right-hand panel of Figure 3.12). We also observe that for a given ξ, the higher the overshooting parameter $\alpha_{\rm ov}$, the lower the k_2 value and the ensuing $\dot{\omega}$ of the best-fit model (see Figure 3.13). Altogether, these results highlight two main effects of a higher overshooting parameter:

It accelerates the evolution of the star and increases the density contrast between the core and the external layers of the star, thereby decreasing the internal structure constant k_2.

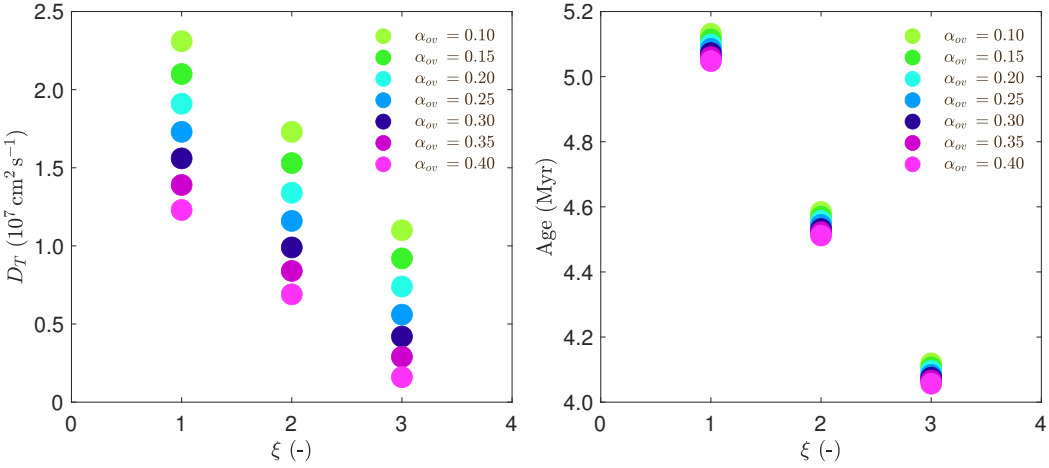

Figure 3.12. Degeneracy between the various mixing processes in the stellar interior for the best-fit `min-Clés` models: turbulent diffusion coefficient D_T (*left panel*) and current age of the star (*right panel*) as a function of the mass-loss rate scaling factor ξ for different values of $\alpha_{\rm ov}$. Figure adapted from Rosu et al. (2020a).

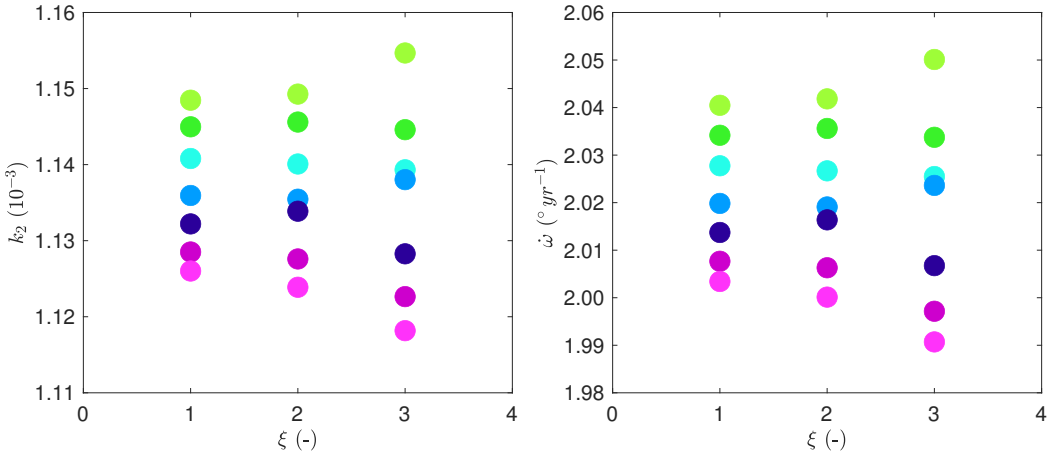

Figure 3.13. Internal structure constant k_2 (*left panel*) and apsidal motion rate $\dot{\omega}$ (*right panel*) as a function of the mass-loss rate scaling factor ξ for different values of $\alpha_{\rm ov}$ for the best-fit `min-Clés` models. The colour code is the same as in Figure 3.12. Figure adapted from Rosu et al. (2020a).

This degeneracy of the best-fit models is presented in the Hertzsprung-Russell diagram in Figure 3.14; here, the Series V(1), Series V(3), and Series XI(1) models are presented together with the observational box, which is defined by the observational radius and effective temperature and their respective error bars. A sequence of $M_{\rm init} = 33.0\,M_{\odot}$, $\alpha_{\rm ov} = 0.40$, $\xi = 1$, $Z = 0.017$, and $D_T = 1.54 \times 10^7\,{\rm cm^2\,s^{-1}}$ is also presented for comparison (see discussion in Section 3.3.3). While the sequences corresponding to the Series V(1) and XI(1) models are very similar, the sequence associated with Series V(3) model follows a very different track. Despite these differences, they all cross the observational box at some stage of their evolution.

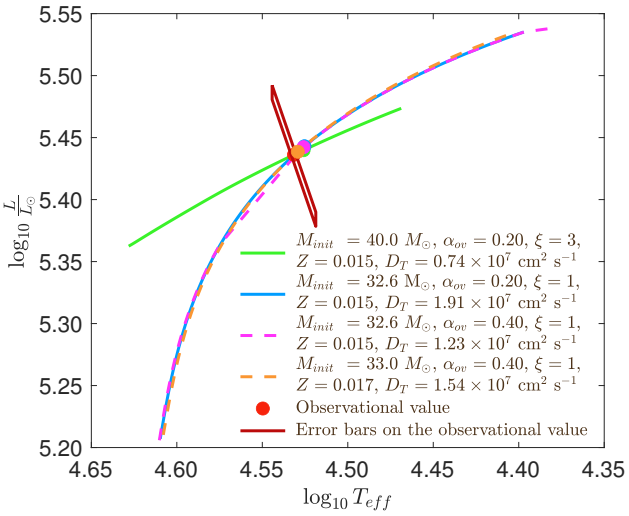

Figure 3.14. Hertzsprung-Russell diagram: evolutionary tracks of `Clés` models of $M_{\rm init} = 40.0\,M_{\odot}$, $\alpha_{\rm ov} = 0.20$, $\xi = 3$, $Z = 0.015$, and $D_T = 0.74 \times 10^7\,{\rm cm^2\,s^{-1}}$ (green, Series V(3)); $M_{\rm init} = 32.6\,M_{\odot}$, $\alpha_{\rm ov} = 0.20$, $\xi = 1$, $Z = 0.015$, and $D_T = 1.91 \times 10^7\,{\rm cm^2\,s^{-1}}$ (light blue, Series V(1)); $M_{\rm init} = 32.6\,M_{\odot}$, $\alpha_{\rm ov} = 0.40$, $\xi = 1$, $Z = 0.015$, and $D_T = 1.23 \times 10^7\,{\rm cm^2\,s^{-1}}$ (pink, Series XI(1)); and $M_{\rm init} = 33.0\,M_{\odot}$, $\alpha_{\rm ov} = 0.40$, $\xi = 1$, $Z = 0.017$, and $D_T = 1.54 \times 10^7\,{\rm cm^2\,s^{-1}}$ (orange). The dots over-plotted on the corresponding tracks correspond to the models that fit the observational k_2. The observational value is represented by the red point, and its error bars are represented by the dark red parallelogram. Figure adapted from Rosu et al. (2020a).

However, as can be seen in Table 3.2, none of these models is able to reproduce the observational k_2 and $\dot{\omega}$, since they predict values that are too high for these parameters. Since the rate of apsidal motion is the product of k_2, the fifth power of the radius, and a term which is identical for all previously computed models (since they all have the same mass and radius), the remaining discrepancy in $\dot{\omega}$ comes only from the discrepancy in k_2. This means that the models discussed so far have too low a density contrast between the core and the external stellar layers and therefore predict too large a value of k_2. This situation is reminiscent of the conclusion reached by several authors (Claret & Giménez 1992, 1993; Claret 1995, 1999, 2004, 2019), who also found that the theoretical k_2 in their models was often too large.

Hence, as a third step, we relaxed our constraints on the mass, radius, effective temperature, and luminosity to find a model that reproduces these four constraints within the error bars, as well as k_2 and $\dot{\omega}$. So far, we have considered the influence of three parameters: ξ, $\alpha_{\rm ov}$, and D_T. Having ξ larger than unity is rather unlikely (see discussion in Section 3.2.1), and from now on, we fix $\xi = 1$. Regarding $\alpha_{\rm ov}$, it is most likely larger than or equal to 0.20 (see discussion in Section 3.2.1), whilst the values of D_T are unconstrained.

All other parameters fixed, we need to increase $\alpha_{\rm ov}$ and/or D_T to obtain a less homogeneous (in terms of density stratification) star, and hence, a lower k_2 value and a lower $\dot{\omega}$. We performed five series (Series XII, XIII, XIV, XV, and XVI) of tests with $\xi = 1$ and the value of $\alpha_{\rm ov}$ fixed (to 0.20, 0.25, 0.30, 0.35, and 0.40, respectively). For each series, we ran six models with different values of D_T, starting from the best-fit value determined previously and adopting increasing values of D_T. We then used `min-Clés` to find the initial mass and current age of the model that best reproduces the observed mass, radius, effective temperature, and luminosity for this pair of $\alpha_{\rm ov}$ and D_T. The resulting values of M, R, $T_{\rm eff}$, L, k_2, and $\dot{\omega}$ are presented in Figure 3.15. For each individual model, we then computed a χ^2 based on the six parameters (M, R, $T_{\rm eff}$, L, k_2, and $\dot{\omega}$). For each series of models with the same $\alpha_{\rm ov}$, we determined the minimum of the χ^2 as a function of D_T by fitting a cubic spline to the χ^2 values of the six models. We re-normalised this function by its minimum so that the reduced $\chi^2_\nu = \chi^2/\chi^2_{\rm min}$ is now equal to 1 at minimum. The 1σ uncertainty on D_T was then estimated from the D_T values corresponding to $\chi^2_\nu = 2$ (but see the caveats in Andrae (2010) and Andrae et al. (2010)). The results are presented in Figure 3.16. In this way, we inferred couples of values for $\alpha_{\rm ov}$ and D_T, which allowed us to obtain the best-fit models in terms of $M, R, T_{\rm eff}, L, k_2$, and $\dot{\omega}$ (Models XII, XIII, XIV, XV, and XVI). These final models are summarised in Table 3.2.

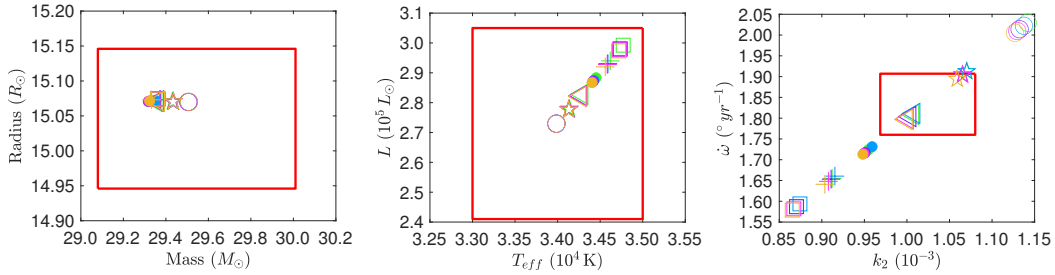

Figure 3.15. Position of the best-fit `min-Clés` models in the (M, R)-plane (*left panel*), in the ($T_{\rm eff}$, $L/L_\odot$)-plane (*middle panel*), and in the (k_2, $\dot{\omega}$)-plane (*right panel*) for the five Series (see text): XII ($\alpha_{\rm ov} = 0.20$, green), XIII ($\alpha_{\rm ov} = 0.25$, blue), XIV ($\alpha_{\rm ov} = 0.30$, violet), XV ($\alpha_{\rm ov} = 0.35$, pink), and XVI ($\alpha_{\rm ov} = 0.40$, orange). Each symbol corresponds to a different value of D_T: The lowest value (which corresponds to the best-fit of M, R, $T_{\rm eff}$, and L) is depicted by an open circle, while increasing values of D_T are depicted, in ascending order, by a star, an open triangle, a filled dot, a cross, and an open square. The red rectangle represents the observational box, that is to say, the range of observational values taking into account the error bars. Figure adapted from Rosu et al. (2020a).

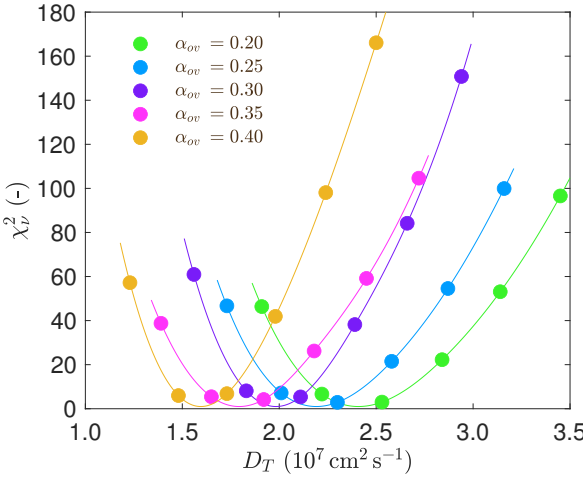

Figure 3.16. Reduced χ^2_ν as a function of D_T for the five Series (see text): XII ($\alpha_{\rm ov} = 0.20$, green), XIII ($\alpha_{\rm ov} = 0.25$, blue), XIV ($\alpha_{\rm ov} = 0.30$, violet), XV ($\alpha_{\rm ov} = 0.35$, pink), and XVI ($\alpha_{\rm ov} = 0.40$, orange). Figure adapted from Rosu et al. (2020a).

These five final models all give an initial mass for the star of $32.8 \pm 0.6\,M_\odot$ and a current age ranging from 5.12 to 5.18 Myr, which gives an age estimate of 5.15 ± 0.13 Myr for the stars. In order for the mass-loss rate and the turbulent diffusion to take less extreme values, the overshooting parameter has to take a high value of 0.40. If the mass-loss rates were higher than predicted by the Vink et al. (2001) recipe, the initial masses of the stars would be higher and their current age would be lower.

We note that the profiles of the normalised density, of the normalised function $\rho(r)\left(\frac{r}{R}\right)^2\left(1-\left(\frac{r}{R}\right)^2\right)$, of η_2, and of $\frac{d\eta_2}{dr}$ inside the star are not significantly affected by a modification of D_T (except for extreme values of D_T) with all other parameters fixed (see Figure 3.17). As it was already mentioned in Section 3.1.2.1 and outlined in Figure 3.2, a change in $\alpha_{\rm ov}$ with all other parameters fixed does not significantly affect these profiles either. These profiles are indeed mainly affected by the evolution of the star (i.e. its age).

3.3.3. Influence of the metallicity

Although there is a priori no observational evidence that HD 152248 would have a metallicity that significantly deviates from solar (see Section 1.3), we looked at the influence of the metallicity on the binary stars' parameters for the sake of completeness. We tested values for Z of 0.013, 0.014, 0.016, and 0.017 for models having $\xi = 1$ and different values of the overshooting parameter, namely 0.20, 0.25, 0.30, 0.35, and 0.40. We left the age, initial mass, and D_T as free parameters and constrained M, R, $T_{\rm eff}$, and L. The resulting values of these four parameters for the best-fit models were all in agreement with the observational values.

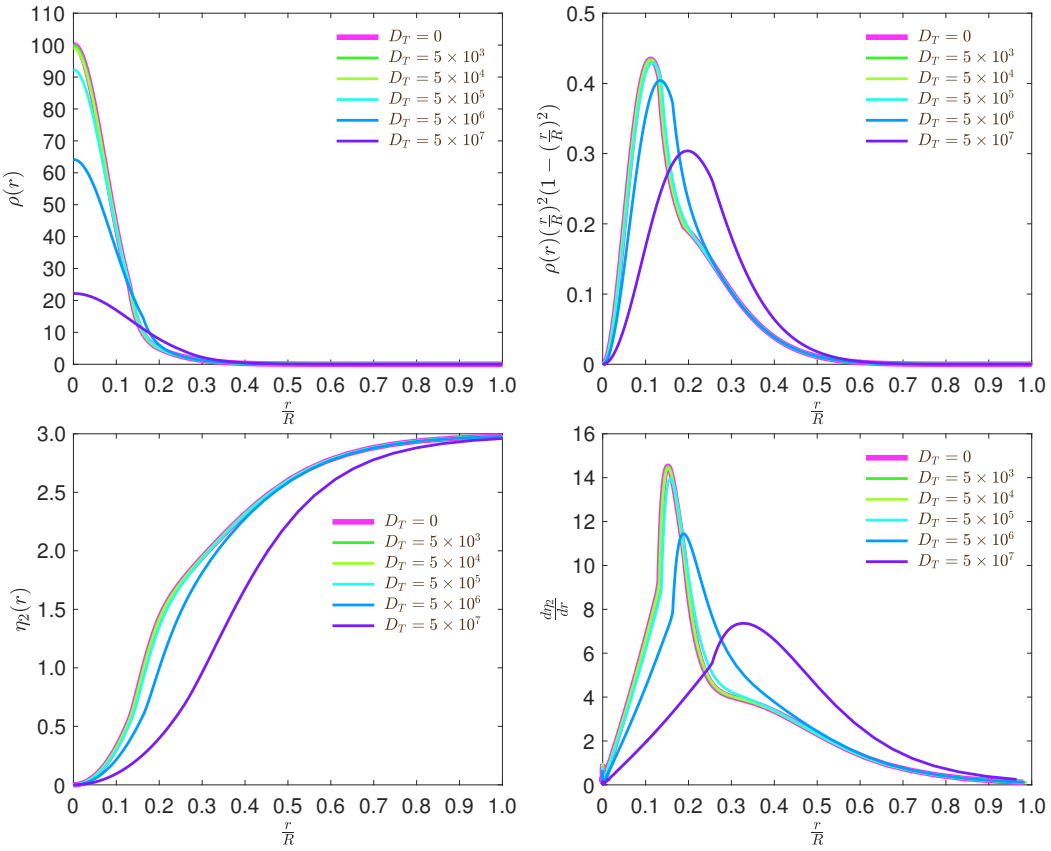

Figure 3.17. Evolution of the normalised density (*top left panel*), the normalised function $\rho(r)\left(\frac{r}{R}\right)^2\left(1-\left(\frac{r}{R}\right)^2\right)$ (*top right panel*), η_2 (*bottom left panel*), and $\frac{d\eta_2}{dr}$ (*bottom right panel*) inside the star for `Clés` models with an initial mass of $30.0\,M_\odot$, $\alpha_{\rm ov} = 0.20$, $\xi = 1$, $Z = 0.015$, and an age of 5 Myr. Each colour corresponds to a different value of D_T. The bottom panels correspond to the results obtained from the numerical integration of Equation (3.11).

The initial mass and the stellar age as well as the turbulent diffusion coefficient D_T are presented as a function of the overshooting parameter $\alpha_{\rm ov}$ for different values of the metallicity Z in Figure 3.18. For a given overshooting parameter $\alpha_{\rm ov}$, an increase in Z leads to an increase in D_T, a decrease in the current age, and an increase in the initial mass of the star. The increase in $M_{\rm init}$ with Z is expected since a higher Z value implies a higher mass-loss rate, and, combined with the fact that all models have similar ages, a higher initial mass is required. The impacts on the initial mass and on the age are nonetheless quite modest.

However, the impact of a modification of Z on the internal structure constant k_2 and on the apsidal motion rate $\dot{\omega}$ are much more significant, as Figure 3.19 indicates. For a given mass, increasing the metallicity increases the opacity. Hence, the radiative transport is less

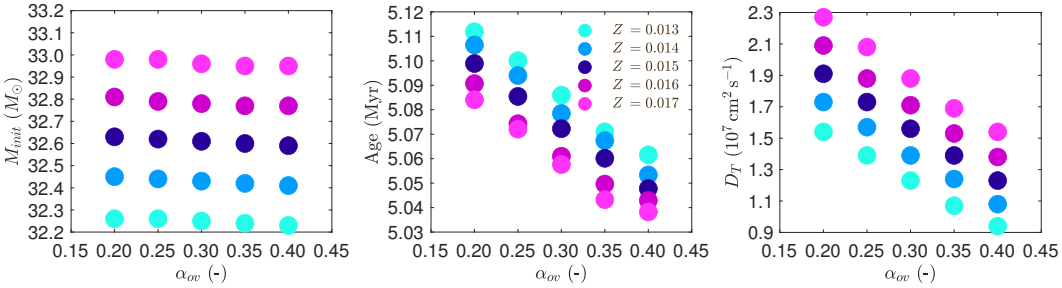

Figure 3.18. Initial mass $M_{\rm init}$ (*left panel*), current age of the star (*middle panel*), and turbulent diffusion coefficient D_T (*right panel*) of the best-fit `min-Clés` models as a function of $\alpha_{\rm ov}$ for different values of the metallicity Z. Figure adapted from Rosu et al. (2020a).

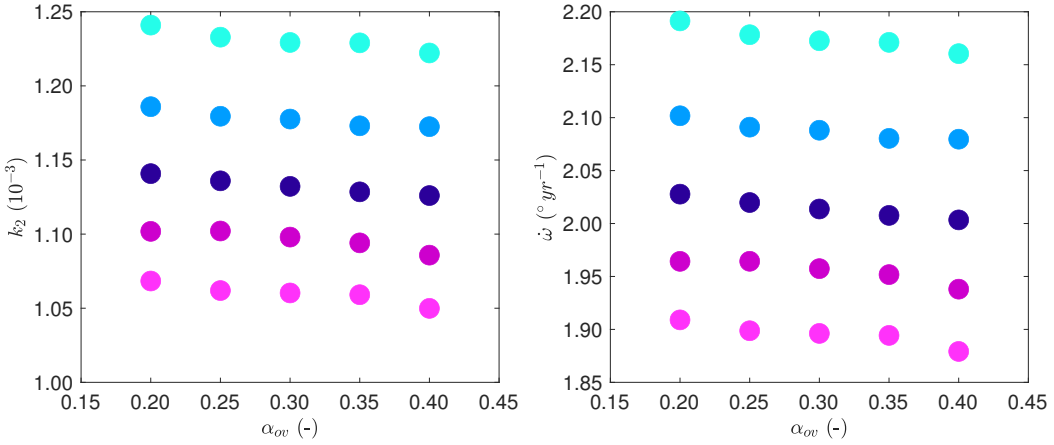

Figure 3.19. Internal structure constant k_2 (*left panel*) and apsidal motion rate $\dot{\omega}$ (*right panel*) of the best-fit `min-Clés` models as a function of $\alpha_{\rm ov}$ for different values of the metallicity Z. The colour code is the same as in Figure 3.18. Figure adapted from Rosu et al. (2020a).

efficient and both the effective temperature and luminosity decrease. Therefore, to satisfy the constraints on the mass, radius, effective temperature, and luminosity, the adjustments require an increase in D_T. Indeed, an increase in D_T induces an increase in the luminosity, which compensates for the decrease in luminosity induced by an enhanced metallicity. The decrease in k_2 with metallicity directly follows from the increased mass of the convective core with turbulent diffusion, which in turn induces a higher density contrast inside the star[5]. The decrease in $\dot{\omega}$ with Z directly follows from the decrease in k_2. We note that the modification of the various parameters with metallicity is not a direct consequence of the modification of the metallicity, but is rather an indirect consequence following from the modification of the turbulent diffusion with metallicity. The degeneracy between Z and D_T is illustrated in the Hertzsprung-Russell diagram in Figure 3.14 for an evolutionary sequence

[5] This will be discussed in details in Section 3.3.4, and especially in Figure 3.23, where the extent of the convective core is seen as the central region of constant X.

of $M_{\rm init} = 33.0\,M_\odot$, $\alpha_{\rm ov} = 0.40$, $Z = 0.017$, and $D_T = 1.54 \times 10^7\,{\rm cm^2\,s^{-1}}$. The evolutionary track of this sequence overlaps almost perfectly with the evolutionary track of a sequence of $M_{\rm init} = 32.6\,M_\odot$, $\alpha_{\rm ov} = 0.40$, $Z = 0.015$, and $D_T = 1.23 \times 10^7\,{\rm cm^2\,s^{-1}}$.

3.3.4. Binary star evolution models including stellar rotation

We built three sequences of stellar evolution models with `GENEC`: two sequences with the single version (`GENEC` single) and one sequence with the binary version (`GENEC` binary). All sequences assume an initial mass of $32.8\,M_\odot$, $\alpha_{\rm ov} = 0.20$, $\xi = 1$, $Z = 0.015$, and no turbulent diffusion. For the binary version and one single version (hereafter "single-v_{100}"), an initial equatorial rotational velocity $v_{\rm eq,ini}$ of $100\,{\rm km\,s^{-1}}$ was chosen considering that the orbital period corresponds to an equatorial rotational velocity of approximately $60\,{\rm km\,s^{-1}}$. For the second single version (hereafter "single-v_0"), we adopted $v_{\rm eq,ini} = 0\,{\rm km\,s^{-1}}$. The derived k_2 value of the single-v_0 model was corrected by the empirical correction proposed by Claret (1999, see Equation (3.51)). The binary star sequence reaches the mass transfer state at time $t = 5.34\,{\rm Myr}$. At this stage, we emphasise that the `Clés` and `GENEC` codes adopt different definitions for the zero age of the stars. While the age in `Clés` is computed including the pre-main-sequence phase, in `GENEC` the ages are taken from the ZAMS, where a model is considered to be on the ZAMS when 3‰ of the initial hydrogen content has been burned in the core.

In Figure 3.20 we present the evolution as a function of the stellar age of the mass, radius, effective temperature, luminosity, and internal structure constant of the star for these three `GENEC` models as well as the evolution of $\dot{\omega}$ as a function of the stellar age as computed with Equation (3.1), assuming both stars are described with the same `GENEC` model. Two `Clés` models with an initial mass of $32.8\,M_\odot$, $\alpha_{\rm ov} = 0.20$, $\xi = 1$, and $Z = 0.015$ – one with no turbulent diffusion and one with a turbulent diffusion coefficient $D_T = 2.41 \times 10^7\,{\rm cm^2\,s^{-1}}$ – are also shown for comparison. The observational value of the corresponding parameter and its error bars are also represented.

Large differences between the `GENEC` single-v_{100} and the `GENEC` single-v_0 models are observed. Indeed, for a given age, the `GENEC` single-v_{100} model is smaller and less massive, and has a higher effective temperature, luminosity, and a lower density contrast between the core and the external layers (i.e. a higher k_2). The higher degree of homogeneity (in terms of density) of the model with rotation is explained by the fact that the rotation induces additional mixing inside the star, which flattens the density and η profiles, from the core to the external layers. Indeed, for a given age, the peak of the function $\rho(r)\left(\frac{r}{R}\right)^2\left(1-\left(\frac{r}{R}\right)^2\right)$ happens further away from the centre of the star and is less steep when rotation is included in the model (not shown). Consequently, the same is observed for the $\frac{d\eta_2}{dr}$ profile inside the star. These effects are even more evident as the age of the model increases. The higher k_2 value does not compensate for the smaller radius of the star, and, consequently, the apsidal motion rate is significantly reduced compared to the `GENEC` single-v_0 model.

One important question to address here is whether the empirical correction proposed by Claret (1999) for k_2 (Equation (3.51)) to account for the effect of stellar rotation is

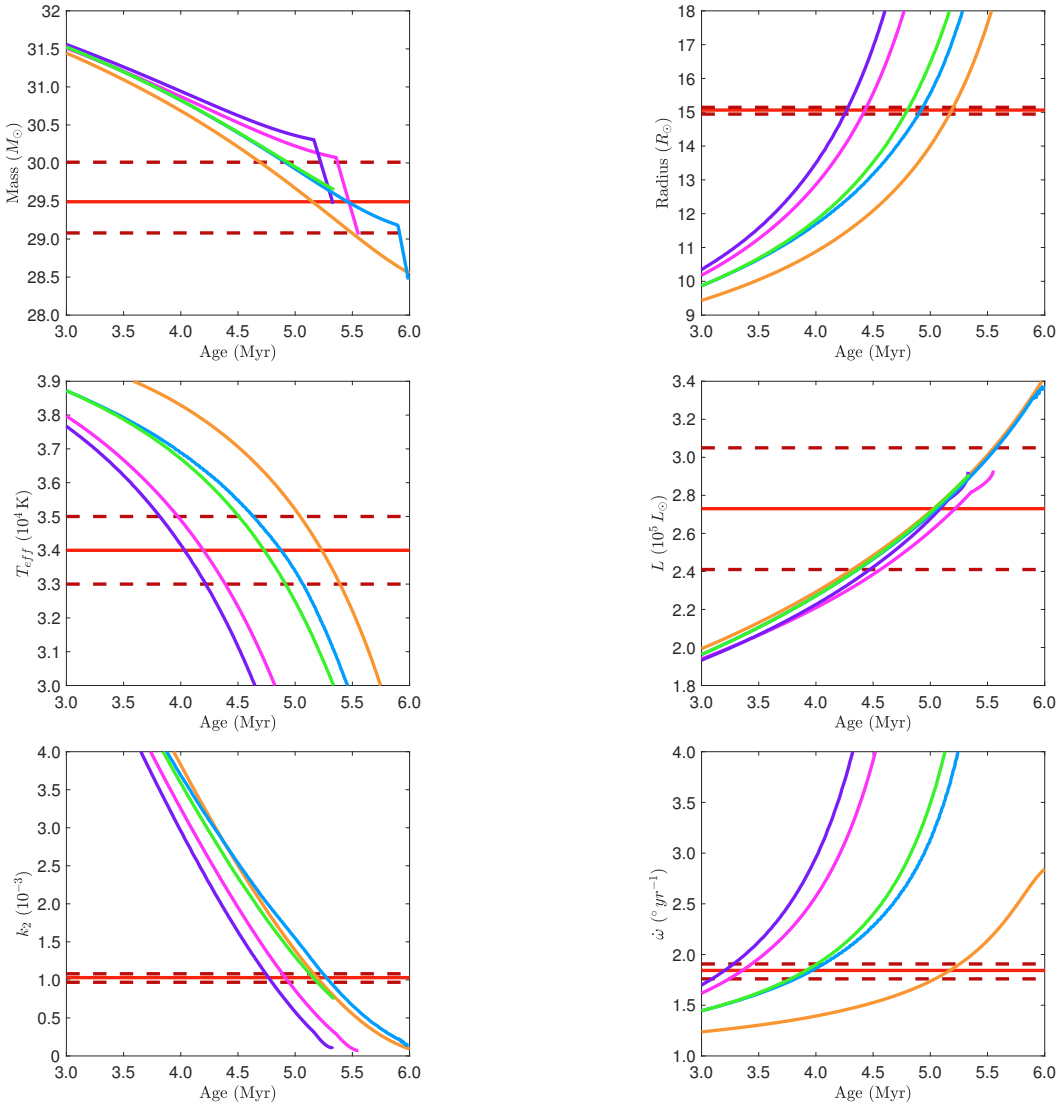

Figure 3.20. Evolution as a function of the stellar age of the mass (*top left panel*), radius (*top right panel*), effective temperature (*middle left panel*), luminosity (*middle right panel*), internal structure constant of the star (*bottom left panel*), and apsidal motion rate of the binary (as computed with Equation (3.1) assuming both stars are described with the same model, *bottom right panel*) for three `GENEC` models with an initial mass of $32.8\,M_\odot$, $\alpha_{\rm ov} = 0.20$, and $Z = 0.015$; the single version (blue) and the binary version (green) with initial rotational velocities $v_{\rm eq,ini} = 100\,{\rm km\,s^{-1}}$; and the single version (violet) with zero initial rotational velocity ($v_{\rm eq,ini} = 0\,{\rm km\,s^{-1}}$). Two `Clés` models with an initial mass of $32.8\,M_\odot$, $\alpha_{\rm ov} = 0.20$, and $Z = 0.015$, one with no turbulent diffusion (pink) and one with $D_T = 2.41 \times 10^7\,{\rm cm^2\,s^{-1}}$ (orange), are also presented for comparison. All models have $\xi = 1$. The observational values of the corresponding parameters and their error bars are represented by the solid red line and the dashed dark red horizontal lines, respectively. Figure adapted from Rosu et al. (2020a).

appropriate in this case. As explained by Claret (1999), the comparison of k_2 values between models with and without rotation applies to models of the same evolutionary state as measured by the hydrogen mass fraction in the core X_c. For models involving different physics, this implies that we have to compare models at different ages, as the age when a given value of X_c is reached strongly depends on the internal mixing processes. Hence, Figure 3.21 shows the evolution of k_2 as a function of X_c for the GENEC single-v_{100} and GENEC single-v_0 models as well as the GENEC single-v_0 model to which the empirical correction of Claret (1999) has not been applied (single-v_0, uncorrected). From these evolutions, we can assert that the empirical correction proposed by Claret (1999) for k_2 to account for the effect of stellar rotation is not sufficient for the stars considered here. The empirical correction effectively leads to a small reduction of k_2 for a given X_c, but, as Figure 3.21 indicates, this reduction is significantly smaller than the actual effect of rotation on k_2, especially during the early stages of the evolution.

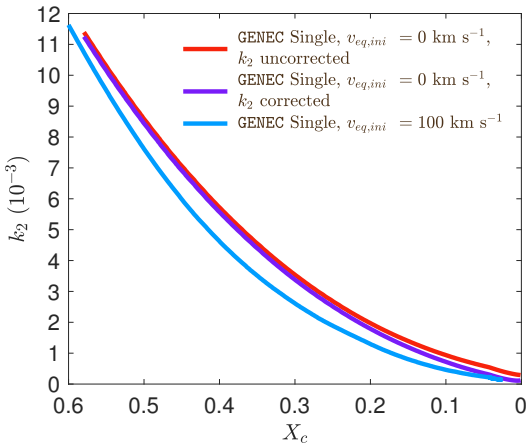

Figure 3.21. Evolution of k_2 as a function of the hydrogen mass fraction X_c inside the core for three GENEC models with an initial mass of 32.8 $M_\odot$, $\alpha_{ov} = 0.20$, $Z = 0.015$, and $\xi = 1$; the single version with initial rotational velocity $v_{eq,ini} = 100\,km\,s^{-1}$ (blue); the single version with zero initial rotational velocity ($v_{eq,ini} = 0\,km\,s^{-1}$, violet); and the single version with zero initial rotational velocity to which the empirical correction for k_2 of Claret (1999) has not been applied (red). Figure adapted from Rosu et al. (2020a).

Compared to the Clés model without turbulent diffusion, the GENEC single-v_0 model gives a slightly more massive, more voluminous, cooler, and more luminous star that has a higher density contrast between the core and the external layers. The higher radius dominates the smaller k_2, hence leading to a higher apsidal motion rate. The differences between the GENEC single-v_0 and Clés models are most probably due to inherent differences in the implementation of the codes. Comparing the Clés models with the GENEC single-v_{100} model gives an interesting result: The GENEC single-v_{100} model has an evolution in terms of absolute parameters of the stars intermediate between Clés models with and without turbulent diffusion.

This is even clearer when looking at the evolutionary tracks of the five models in the Hertzsprung-Russell diagram in Figure 3.22. Indeed, all the tracks, except the `GENEC` single-v_0 one and the `Clés` track without any turbulent diffusion, cross the observational box defined by the observational radius and effective temperature and their respective error bars. The five models that fit k_2 are represented by the five dots over-plotted on the corresponding tracks. All of these, except the one corresponding to the `Clés` model with enhanced turbulent diffusion, lie well above the range of acceptable radii. This highlights, again, the need for an enhanced turbulent mixing inside the stars to reproduce the small observational k_2 value. Nonetheless, the two `GENEC` models with rotation that fit the k_2 observational value are closer to the observational box than the `GENEC` model without rotation, suggesting that, at first glance, the stellar rotation acts on the stellar interior in the same way as the turbulent diffusion does.

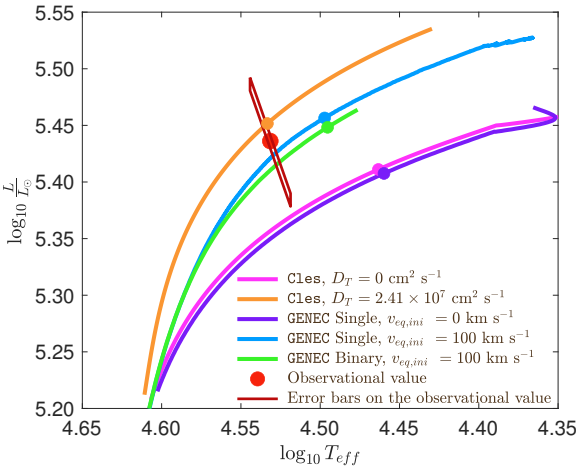

Figure 3.22. Hertzsprung-Russell diagram: evolutionary tracks of three `GENEC` models with an initial mass of 32.8 $M_\odot$, $\alpha_{ov} = 0.20$, $Z = 0.015$, and $\xi = 1$ for the single version (blue) and binary version (green) – both with initial rotational velocity $v_{\rm eq,ini} = 100\,{\rm km\,s^{-1}}$ – and the single version with zero initial rotational velocity ($v_{\rm eq,ini} = 0\,{\rm km\,s^{-1}}$, violet). Two `Clés` models with an initial mass of 32.8 $M_\odot$, $\alpha_{ov} = 0.20$, $Z = 0.015$, and $\xi = 1$ – one with no turbulent diffusion (pink) and one with $D_T = 2.41 \times 10^7\,{\rm cm^2\,s^{-1}}$ (orange) – are also presented for comparison. The dots over-plotted on the corresponding tracks correspond to the models that fit the observational k_2. The red point indicates the observationally determined value, while the dark red parallelogram indicates the associated error box. Figure adapted from Rosu et al. (2020a).

Figure 3.23 illustrates the hydrogen mass fraction profile inside the star for these five models at an age when the central mass fraction of hydrogen reaches a value of $X_c = 0.2$. The hydrogen profile of the `Clés` model with turbulent diffusion is closer to those of the `GENEC` models with rotation than that of the `GENEC` model without rotation. This suggests that there is a qualitative similarity in the effects caused by turbulent diffusion inside the star on the one hand and stellar rotation on the other hand. However, while the `Clés` model with enhanced turbulent diffusion has a hydrogen abundance at the stellar surface identical to the ones of the `Clés` model without turbulent diffusion and the `GENEC` model without

rotation, the surface hydrogen abundance of the two GENEC models with rotation are lower: Stellar rotation induces a decrease in X at the stellar surface. We therefore suspect that the high turbulent diffusion coefficient found for the stars in Section 3.3.2 could be partly attributed to the effect of stellar rotation, but further investigation is required to confirm this hypothesis. Comparing the GENEC single-v_{100} and GENEC binary curves, we observe that the inclusion of binarity in the code induces a reduction in the size of the convective core and an increase in the hydrogen mass fraction at the stellar surface.

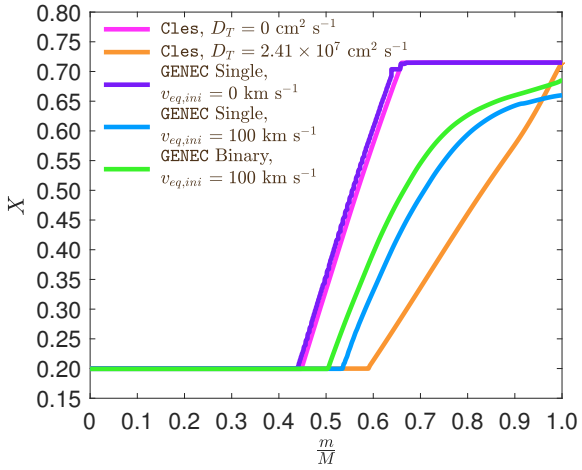

Figure 3.23. Evolution of the hydrogen mass fraction X as a function of the mass fraction inside the star for three GENEC models with an initial mass of 32.8 $M_\odot$, $\alpha_{\rm ov} = 0.20$, $Z = 0.015$, and $\xi = 1$; the single version (blue) and the binary version (green) with initial rotational velocities of $v_{\rm eq,ini} = 100\,{\rm km\,s^{-1}}$; and the single version (violet) with zero initial rotational velocity ($v_{\rm eq,ini} = 0\,{\rm km\,s^{-1}}$). Two Clés models with an initial mass of 32.8 $M_\odot$, $\alpha_{\rm ov} = 0.20$, $Z = 0.015$, and $\xi = 1$ – one without turbulent diffusion (pink) and one with $D_T = 2.41 \times 10^7\,{\rm cm^2\,s^{-1}}$ (orange) – are also presented for comparison. All models have a central fraction of hydrogen X_c of 0.2. Figure adapted from Rosu et al. (2020a).

We now compare the single-v_{100} and binary GENEC models and observe that the mass and the luminosity are not affected much: Until the onset of mass-transfer, both models have essentially identical masses and luminosities. For a given age, the binary model gives a slightly bigger and less homogeneous (in terms of density) star with a lower effective temperature than the single model. Again, the smaller value of k_2 does not compensate for the higher radius, and, consequently, the apsidal motion rate at a given age is slightly higher for the binary version. Due to the presence of a companion and the induced tidal interactions, a binary star does not evolve on the same timescale as a single star. Therefore, it is interesting to look at the evolution of k_2 as a function of the radius of the star rather than as a function of the age. In Figure 3.24, we present the evolution of k_2 as a function of the radius for the three GENEC models and the two Clés models. We observe that the single-v_{100} and binary GENEC models overlap perfectly, the Clés model with turbulent diffusion is closer to the two GENEC models with rotation, and the GENEC single-v_0 and the Clés model without turbulent diffusion overlap almost perfectly. This means that whatever the ages of the single-v_{100} and binary GENEC models, if they have the same radius then they have the

same k_2, and hence, the same density profile inside the star. As a consequence, the binarity property implemented in the code acts as if it would only change the age at which the star reaches a given state characterised by a given couple of values for R and k_2.

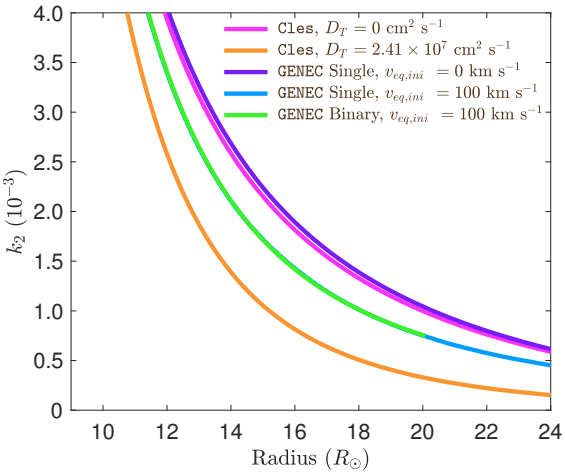

Figure 3.24. Evolution of k_2 as a function of the stellar radius for three `GENEC` models with an initial mass of $32.8\,M_\odot$, $\alpha_{\rm ov} = 0.20$, $Z = 0.015$ and $\xi = 1$; the single version (blue) and the binary version (green) with initial rotational velocities of $v_{\rm eq,ini} = 100\,{\rm km\,s^{-1}}$; and the single version with zero initial rotational velocity ($v_{\rm eq,ini} = 0\,{\rm km\,s^{-1}}$, violet). We note that the green and blue curves overlap perfectly until the green curve stops around $\sim 20\,R_\odot$. Two `Clés` models with an initial mass of $32.8\,M_\odot$, $\alpha_{\rm ov} = 0.20$, $Z = 0.015$, and $\xi = 1$ – one with no turbulent diffusion (pink) and one with $D_T = 2.41 \times 10^7\,{\rm cm^2\,s^{-1}}$ (orange) – are also presented for comparison. Figure adapted from Rosu et al. (2020a).

3.3.5. Additional effects

In this section, we analyse the impact of some effects that could bias our interpretation of the apsidal motion in terms of the internal structure constant. The inclusion of higher-order terms in the expression of the apsidal motion rate was shown to be negligible (see discussion in Section 3.1.3), hence we do not discuss it here. We consider the inclination of the stellar rotation axes with respect to the normal to the orbital plane (Section 3.3.5.1) and the possible action of a ternary component (Section 3.3.5.2).

3.3.5.1. Rotation axes misalignment

We refer here to the set of equations recalled in Section 3.1.4.1 for the special case of two identical stars and rotation axes parallel to each others. We represent $F_{\alpha,+}$ and $F_{\alpha,-}$ as a function of the angle α in Figure 3.25 for the specific case of $i = 67.6°$ (see Section 2.2.5). The minimum and maximum values of $F_{\alpha,-}$ are reached for $\alpha = 7.7°$ and $\alpha = 97.7°$, respectively, while the minimum and maximum values of $F_{\alpha,+}$ are reached for $\alpha = 172.3°$ and $\alpha = 82.3°$, respectively.

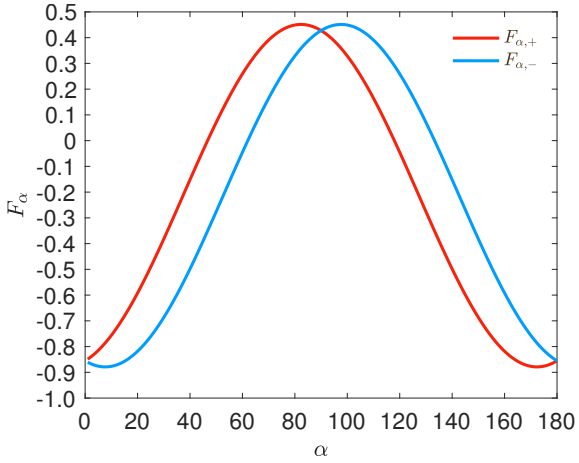

Figure 3.25. Behaviour of $F_{\alpha,+}$ (in red) and $F_{\alpha,-}$ (in blue), given by Equation (3.35), as a function of α, the angle between the rotation axes of the stars and the normal to the orbital plane. Figure adapted from Rosu et al. (2020a).

We compute the total (Newtonian plus general relativistic) apsidal motion rate as a function of the age for `Clés` models with an initial mass of $31.0\,M_\odot$ and $\alpha_{\rm ov} = 0.20$ for different angles α of the stellar rotation axes and assuming $\theta = 180°$. The results are presented in Figure 3.26. A small misalignment angle (up to approximately 30°) has nearly no impact on the value of the rate of apsidal motion. For a higher value of the misalignment angle, an effect on the rate of apsidal motion is clearly seen. In the extreme case ($\alpha = 82°$), the inferred age is increased by 0.5 Myr compared to the aligned case ($\alpha = 0°$). The small effect on the rate of apsidal motion induced by the misalignment of the stars' rotation axes is related to the fact that it only contributes to the term generated by the stellar rotation, a term that itself contributes, in the case of HD 152248, approximately 15% to the total Newtonian term.

One may wonder whether the condition of sub-critical rotation velocity leads to a restriction on the values of the putative misalignment angle α between the rotational and orbital axes, as discussed in Section 3.1.4.2. We used Equations (3.36) and (3.39) to enforce conditions on the equatorial rotational velocity for the stars: $v_{\rm eq} \leq 546\,{\rm km\,s^{-1}}$. Combining this result with the values of $v_{\rm eq} \sin\beta = 138\,{\rm km\,s^{-1}}$ and $137\,{\rm km\,s^{-1}}$ found for the primary and secondary stars, respectively (see Section 2.2.1.4), we obtain $\beta \geq 14.6°$. For an external observer, the impact of a putative misalignment angle α depends on the azimuthal angle θ between the plane defined by the orbital axes and our line of sight as well as the plane defined by the rotational and orbital axes through Equation (3.33). As shown in Section 3.1.4, the largest impact of α on the rate of apsidal motion corresponds to situations where θ is either 0° or 180°. For an azimuthal angle of $\theta = 0°$, the condition on β translates into $\alpha < 53°$ or $\alpha > 82.2°$. Likewise, for $\theta = 180°$, we obtain $\alpha < 97.8°$ or $\alpha > 127°$. These conditions do not rule out the values of α that produce the largest impact on $\dot{\omega}$. Hence, the condition of sub-critical rotation cannot be used to infer a general constraint on α.

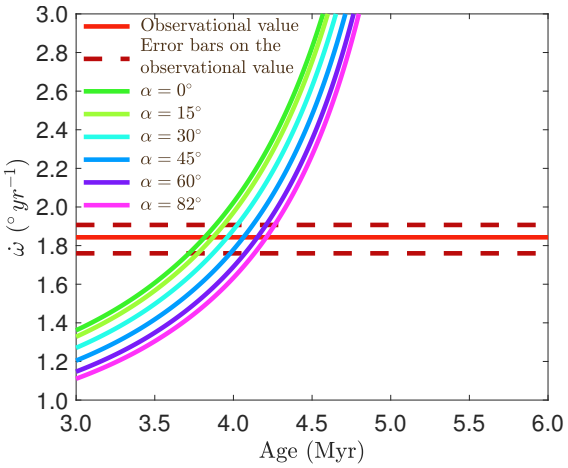

Figure 3.26. Evolution of the apsidal motion rate as a function of the stellar age for `Clés` models with an initial mass of $31.0\,M_\odot$, $\alpha_{\rm ov} = 0.20$, $\xi = 1$, $Z = 0.015$, and no turbulent diffusion for different misalignment angles α of the stellar rotation axes with respect to the normal to the orbital plane in the case where $\theta = 180°$. The cases of $\alpha = 0°, 15°, 30°, 45°, 60°$, and $82°$ are depicted in green, light green, cyan, blue, purple, and pink, respectively. The observational value of the apsidal motion rate and its error bars are represented by the solid red line and the dashed dark red horizontal lines, respectively. Figure adapted from Rosu et al. (2020a).

3.3.5.2. Action of a putative ternary star?

As pointed out by Borkovits et al. (2019), the picture of apsidal motion can become significantly more complicated in the case of a hierarchical triple system. What happens in these systems strongly depends on the relative orientation of the inner and outer orbital planes. If the two planes are essentially co-planar, the action of the ternary star on the inner binary can be summarised as an increase in the rate of apsidal motion compared to the value expected from the tidal interactions and relativistic effects (Borkovits et al. 2019; Bozkurt & Değirmenci 2007). In this case, the contribution of the ternary star to $\dot{\omega}$ would be positive (i.e. in the same direction as the Newtonian and general relativistic effects).

However, things can change significantly if the outer orbit is not co-planar with the inner one. Such systems are subject to the Kozai-Lidov mechanism. In these cases, the eccentricity of the inner binary undergoes cyclic variations (Söderhjelm 1982; Naoz et al. 2013; Borkovits et al. 2019). In addition, the line of apsides of the inner binary may either rotate or librate (Borkovits et al. 2019). In the former case, the contribution of the third star to the $\dot{\omega}$ of the inner binary can be positive or negative. Therefore, the action of a putative ternary star could actually bias the observational determination of the rate of apsidal motion (Borkovits et al. 2005, 2019).

Naoz et al. (2013) investigated the secular perturbations in hierarchical triple systems up to the octupole order. These authors showed that the relative importance of the octupole

term of the Hamiltonian compared to the quadrupole term is proportional to

$$\epsilon_M = \frac{M_1 - M_2}{M_1 + M_2} \frac{a_{\rm in}}{a_{\rm out}} \frac{e_{\rm out}}{1 - e_{\rm out}^2}, \tag{3.53}$$

where the quantities $a_{\rm in}$, $a_{\rm out}$, and $e_{\rm out}$ stand for the semi-major axis of the inner binary, the semi-major axis of the ternary star motion around the inner binary's centre of mass, and the eccentricity of the ternary star's orbit. Since the eclipsing binary of HD 152248 consists of two nearly identical stars (i.e. $M_1 = M_2$), we conclude that, in the present case, only the quadrupole term should be relevant. As a result, the rate of apsidal motion due to a putative ternary component would be given by Equation (A29) of Naoz et al. (2013):

$$\begin{aligned}\dot{\omega}_1 = 6\, C_2 \Bigg\{ & \frac{1}{G_1} \left[4 \cos^2 i_{\rm tot} + (5 \cos 2\omega_1 - 1)\left(1 - e_1^2 - \cos^2 i_{\rm tot}\right)\right] \\ & + \frac{\cos i_{\rm tot}}{G_2} \left[2 + e_1^2 \left(3 - 5 \cos 2\omega_1\right)\right] \Bigg\}. \end{aligned} \tag{3.54}$$

In this equation, the argument of periastron of the inner (short-period) binary is denoted with ω_1, while e_1 is the eccentricity of this orbit. G_1 and G_2 stand for the angular momentum of the inner and outer orbits. The angle $i_{\rm tot}$ is the mutual inclination between the angular momentum vectors of the inner and outer orbits. The constant C_2 gathers all the dependencies on the masses of the components and semi-major axes of the inner and outer orbits. This equation indicates that the rate of apsidal motion induced by the third star depends on the masses of all three components (via C_2) and the relative inclination of the inner and outer orbits, as well as on the value of ω_1 itself and on the amplitudes of the angular momentum vectors of the two orbits. Solving this equation therefore requires information about the third star and the outer orbit.

In Section 2.2.3, we searched for spectroscopic evidence of a ternary star in HD 152248. It was shown that (1) the disentangled spectra and the photometric light curves could be interpreted consistently without the need for a third light contribution, and that (2) the existing radial velocity data fail to reveal a reflex motion around the centre of mass of a triple system. Yet, both the residuals of the radial velocities about the orbital solution of the system accounting for the presence of apsidal motion and the dispersion of ω values inferred from the photometric data were quite large. While the former effect was attributed to the dynamical tidal deformations and the impact of wind interactions on the stellar atmospheres, we cannot completely rule out the possibility of the presence of a third star that would be less massive and less bright than the components of the eclipsing binary. However, we currently lack the information regarding the orbit of such a putative star that would be needed to compute its impact on the apsidal motion of the inner binary.

3.3.6. HD 152248 in a nutshell

We have analysed the eccentric massive binary HD 152248 and its apsidal motion from a theoretical point of view. We first built `Clés` stellar evolution models by constraining the mass, radius, effective temperature, and luminosity to the observational values. Assuming

no turbulent diffusion occurs inside the star and fixing the overshooting parameter $\alpha_{\rm ov}$ to a value of 0.20 gave rise to a model requiring an unrealistically high mass-loss rate scaling factor ξ. Considering different prescriptions for the internal mixing occurring inside the stars, we highlighted the well-known degeneracy between the effects of overshooting and turbulent diffusion. To reproduce k_2 and $\dot{\omega}$ along with the mass, radius, effective temperature, and luminosity required a significant internal mixing enhancement, either through overshooting or turbulent diffusion as both mechanisms lead to an enlargement of the convective core. However, further investigation is required to determine whether this enhanced turbulent diffusion, necessary to reproduce the low k_2 observational value, is physically representative of the stars. Indeed, the standard models, that is to say, models without enhanced turbulent mixing, that simultaneously fit the observational mass, radius, effective temperature, and luminosity all predict too large a k_2 value compared to the observations. The fact that standard models seem to predict stars that have a too low density contrast between the core and the external layers was already pointed out by previous studies (Claret 2019, and references therein), although mostly for lower-mass systems.

Assuming the mass-loss rate is described by the Vink et al. (2001) recipe, these results allowed us to determine an initial mass of both stars of $32.8 \pm 0.6\,M_{\odot}$ and a current age of 5.15 ± 0.13 Myr. A higher mass-loss rate would imply higher initial masses and younger current age of the stars. If the stars appeared to have a sub-solar metallicity, as advocated by some authors (Kilian et al. 1994; Baume et al. 1999), then their initial masses would be slightly smaller, their age slightly higher, and the required turbulent diffusion slightly lower.

We also investigated the impact of binarity and stellar rotation by means of single and binary `GENEC` models that account for stellar rotation. The binary version of this code takes into account the mixing induced by tidal interactions occurring inside a binary system. These tests revealed that the current evolutionary stage of HD 152248 can be described by single-star models and that the system has not yet gone through a mass-exchange episode; this is in line with the conclusions of Section 2.2. Furthermore, we suggest that the high turbulent diffusion required to reproduce the observations can be partly attributed to stellar rotation, but further investigation is required to confirm or infirm this hypothesis.

Finally, we analysed the impact of some effects that could bias our interpretation of the apsidal motion in terms of the internal structure constant. We considered the impact of a misalignment of the stellar rotation axes and deduced that unless the axes are inclined by an angle of at least $\sim 60°$ with respect to the normal to the orbital plane, the apsidal motion rate is not affected much. This comes from the fact that the rotation axis orientation with respect to the orbital plane only appears in the rotational term of the Newtonian contribution, a term which contributes an amount of only $\sim 15\%$ to the total apsidal motion rate in the case of HD 152248. Such a high inclination angle seems highly unlikely in a close eccentric binary where the two stars are on the point of reaching pseudo-synchronisation. Indeed, in Section 2.2.5, we inferred values of 0.87 ± 0.03 and 0.86 ± 0.04 for the ratios of rotational angular velocity to instantaneous orbital angular velocity at periastron for the primary star and secondary star, respectively. A far more severe impact could arise from the action of a third star if HD 152248 turned out to be a triple system, although there is currently no observational evidence for the existence of a third component in this system.

3.4. The slow motion binary: HD 152219

The set of observationally determined properties of the binary is recalled in Table 3.3. Using our re-derived parameters of HD 152219 (see Section 2.3), we inferred a value for $\dot{\omega}_{\rm GR}$ of $(0.159 \pm 0.002)^\circ\,{\rm yr}^{-1}$. As a consequence, the observational contribution of the Newtonian term $\dot{\omega}_{\rm N}$ amounts to $(1.039 \pm 0.300)^\circ\,{\rm yr}^{-1}$. In the case of HD 152219, it is impossible to observationally constrain the individual values of the internal structure constants of both stars. Nevertheless, we computed the weighted-average apsidal motion constant $\bar{k}_2$ for the binary system using Equation (3.8) and got $\bar{k}_2 = 0.00173 \pm 0.00052$. As the secondary star is smaller and less massive than the primary star, its k_2 value exceeds that of the primary. Therefore, we have $k_{2,1} < \bar{k}_2 < k_{2,2}$. Observationally, we have $\frac{c_1}{c_1+c_2} = 0.95$ and $\frac{c_2}{c_1+c_2} = 0.05$, meaning that $k_{2,1}$ has a much higher weight in the calculation of $\bar{k}_2$[6]. We further note – and here we anticipate the analysis performed in Section 3.4.2 – that if we make the hypothesis that $k_{2,1} = \bar{k}_2$, and if $k_{2,2}$ appears to be equal to $n * k_{2,1}$, then the ensuing error beyond the initial hypothesis amounts to $(n-1) * 5\%$.

Table 3.3. Set of observationally determined properties of the binary system HD 152219 used for the `Clés` analysis, for which we adopted symmetric uncertainties.

Parameter	Value	
	Primary	Secondary
M ($M_\odot$)	18.64 ± 0.47	7.70 ± 0.12
R ($R_\odot$)	9.40 ± 0.15	3.69 ± 0.06
$T_{\rm eff}$ (K)	$30\,900 \pm 1000$	$21\,697 \pm 1000$
$\bar{k}_2$	0.00173 ± 0.00052	

We built stellar evolution models for the massive binary HD 152219 with the version of the `Clés` code that includes the computation of the internal structure constant. We search for best-fit models of the system using the `min-Clés` routine and we solve for the apsidal motion constants and the theoretical rate of apsidal motion for the set of `Clés` models that best reproduce the observed stellar parameters in Sections 3.4.1, 3.4.2, 3.4.3, and 3.4.4. We investigate the influence of the metallicity and helium abundance in Section 3.4.5. We discuss the impact of a rotation axis misalignment in Section 3.4.6. Finally, we present our conclusions in Section 3.4.7. The most important results of this section are presented in Rosu et al. (2022a).

3.4.1. Preliminary analysis

In a first attempt to obtain stellar evolution models representative of both stars, we built two `Clés` models simultaneously, adopting the six corresponding constraints (M, R, and $T_{\rm eff}$ of both stars), and leaving the initial masses of the two stars and the age of the binary system as the only three free parameters. For both stars, we adopted $\xi = 1$, $\alpha_{\rm ov} = 0.30$, and no turbulent diffusion. The best-fit solution gives an age of 7.8 Myr, but none of the

[6] We note, however, that this does not imply that the product $\frac{c_1}{c_1+c_2}k_{2,1}$ contributes 95% to $\bar{k}_2$.

stellar parameters is correctly reproduced. Adding more free parameters would certainly help the convergence of the models but, due to degeneracies, might also lead to spurious solutions. Hence, we decided to proceed differently and to analyse both stars separately, keeping in mind that the ages of both stars have to match somehow.

As an illustration, we built two stellar evolutionary sequences, the first one with an initial mass of $19.0\,M_\odot$ and $\xi = 1$ which should represent the primary star, and the second one with an initial mass of $7.7\,M_\odot$ and $\xi = 0.1$ which should represent the secondary star. Both sequences assume $\alpha_{\rm ov} = 0.30$ and no turbulent diffusion. Whilst the stellar parameters of the

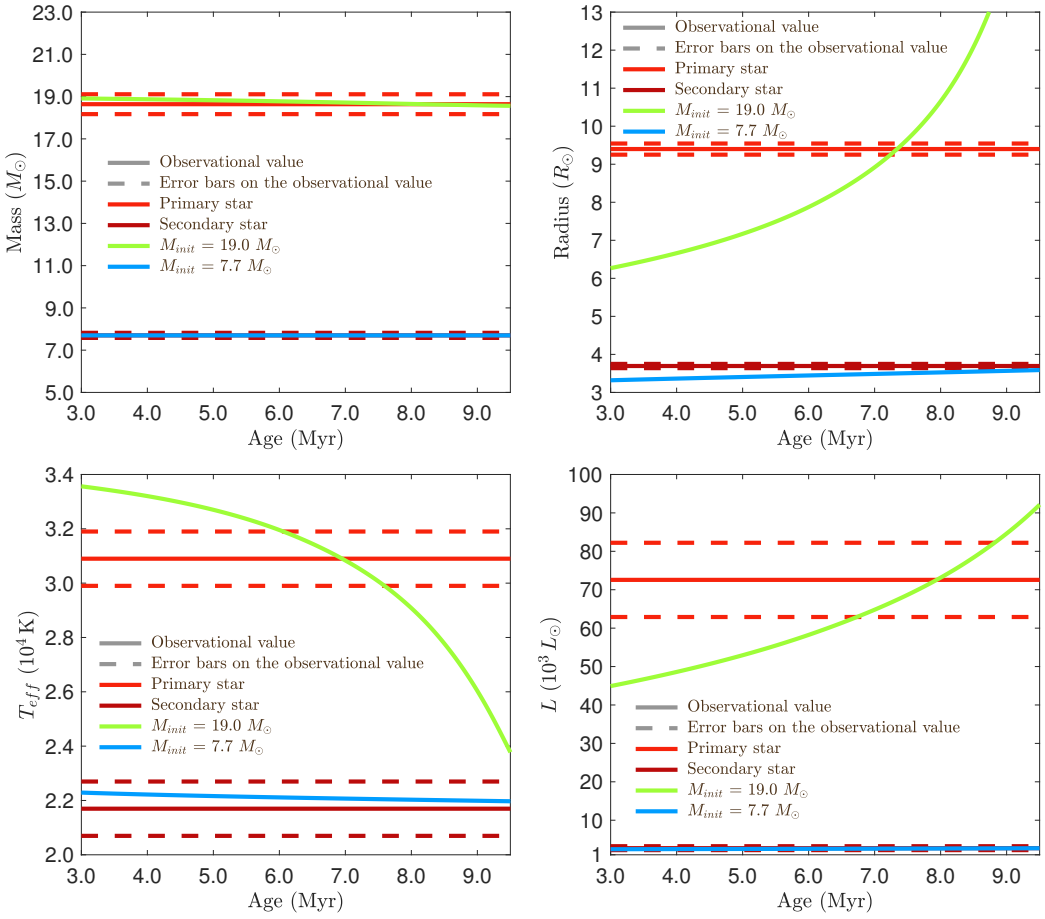

Figure 3.27. Evolution as a function of the stellar age of the mass (*top left panel*), radius (*top right panel*), effective temperature (*bottom left panel*), and luminosity (*bottom right panel*) of the stars for `Clés` models with an initial mass of $19.0\,M_\odot$ and $\xi = 1$ (green, primary star) and an initial mass of $7.7\,M_\odot$ and $\xi = 0.1$ (light blue, secondary star). The models have $\alpha_{\rm ov} = 0.30$, $Z = 0.015$, and no turbulent diffusion. The observational value of the corresponding parameter and its error bars are represented for the primary (respectively secondary) star by the solid red (respectively dark red) line and the dashed red (respectively dark red) horizontal lines, respectively.

primary star all cross the observational values, within the error bars, between 7 and 8 Myr, the stellar parameters of the secondary star cross the observational values, within the error bars, beyond 10 Myr (see Figure 3.27). This preliminary analysis already shows the difficulty to build consistent stellar evolutionary models for both stars but also coherent in terms of age. Yet, the importance of these two evolutionary sequences rather lies in Figure 3.28: The left panel shows the evolution as a function of the stellar age of the internal structure constants of both evolutionary sequences together with the weighted-average mean of k_2, while the right panel shows the evolution as a function of the stellar age of the apsidal motion contributions of both stars taken separately as well as the total apsidal motion of the binary system. This second panel clearly shows that the primary star contributes the most part to the binary apsidal motion, as expected. The evolution of $\bar{k}_2$ and $k_{2,1}$ overlap nearly perfectly, suggesting that $k_{2,1}$ dominates in $\bar{k}_2$. To quantify this assertion, we show in Figure 3.29 the evolution as a function of the age of the coefficients $\frac{c_1}{c_1+c_2}$ and $\frac{c_2}{c_1+c_2}$ appearing in Equation (3.8) for these two evolutionary sequences. The contribution of $k_{2,1}$ to $\bar{k}_2$ increases with time and, assuming an age older than 5 Myr, amounts to minimum 90%. These arguments, together with the fact that the stellar parameters of the primary star are better constrained than those of the secondary star, motivate us to first build stellar evolutions models for the primary star.

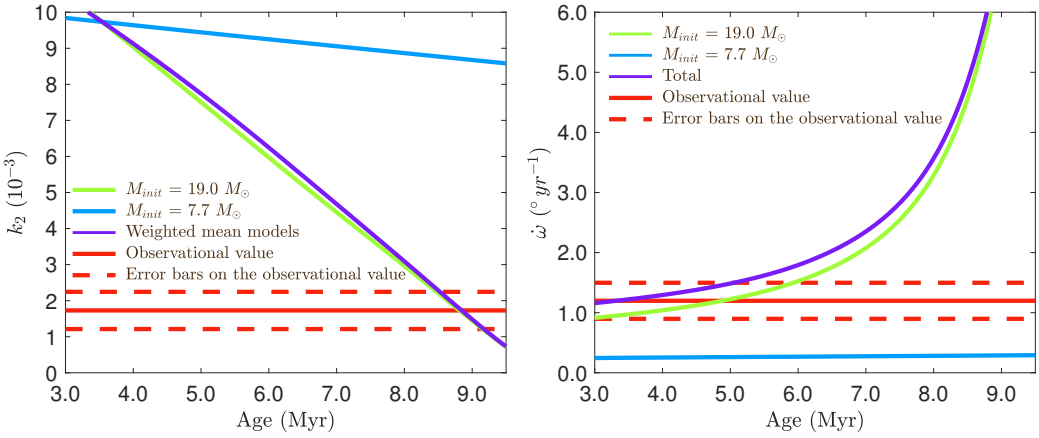

Figure 3.28. Evolution of k_2 and $\dot{\omega}$. *Left panel:* Evolution as a function of the stellar age of the internal structure constant (to which the empirical correction of Claret (1999, Equation (3.51)) has been applied) for `Clés` models with an initial mass of 19.0 $M_\odot$ and $\xi = 1$ ($k_{2,1}$, green) and an initial mass of 7.7 $M_\odot$ and $\xi = 0.1$ ($k_{2,2}$, blue), both models have $\alpha_{ov} = 0.30$ and no turbulent diffusion. The weighted-average mean of the k_2 values, computed using Equation (3.8), is also depicted ($\bar{k}_2$, purple). *Right panel:* Evolution as a function of the stellar age of the total apsidal motion rate (purple) and of the contributions of the two stars (green and blue). The observational value of the corresponding parameter and its error bars are represented by the solid red line and the dashed red horizontal lines, respectively. Figure adapted from Rosu et al. (2022a).

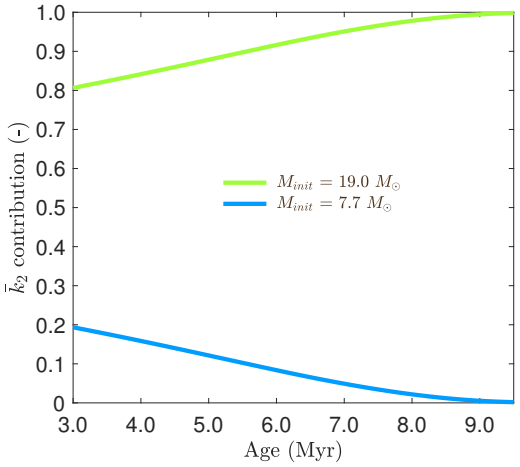

Figure 3.29. Evolution as a function of the stellar age of the contributions $\frac{c_1}{c_1+c_2}$ and $\frac{c_2}{c_1+c_2}$ to the weighted-average mean $\bar{k}_2$ of the internal structure constants $k_{2,1}$ and $k_{2,2}$ (to which the empirical correction of Claret (1999, Equation (3.51)) has been applied) for the models presented in Figure 3.28. Figure adapted from Rosu et al. (2022a).

3.4.2. Primary star

We built stellar evolution models for the primary star assuming the three constraints M, R, and $T_{\rm eff}$, and adopting at least the initial mass of the star and its age as free parameters. The first model (Model I) is built fixing $\xi = 1$ and $\alpha_{\rm ov} = 0.30$, and assuming no turbulent diffusion. The only free parameters are thus the initial mass and the current age of the star. This model gives $M_{\rm init} = 19.05\,M_\odot$ and an age of 7.30 Myr, but has a slightly lower effective temperature than observed, even though still within the error bars (see Table 3.4). We note that the χ^2 is computed based on $M, R, T_{\rm eff}$, and $k_{2,1} = \bar{k}_2$. Adopting $\alpha_{\rm ov} = 0.0$ gives even worse results in terms of M, R, and $T_{\rm eff}$. Without any mixing, the global parameters of the star cannot be reproduced accurately.

Hence, we subsequently investigated the influence of $\xi, \alpha_{\rm ov}$, and D_T on the best-fit models. In three series of models, Series II to IV, we fixed ξ to 1, 0.5, and 0.25, respectively. For each series, we built five models with different values of $\alpha_{\rm ov}$, namely 0.20, 0.25, 0.30, 0.35, and 0.40, while leaving D_T as an additional free parameter. The results are summarised in Table 3.4. Series II, III, and IV models have an initial mass of 19.00, 18.82, and 18.73 $M_\odot$, respectively, and an age between 7.81 and 7.88 Myr, 7.92 and 7.99 Myr, and 7.98 and 8.05 Myr, respectively. The age is lower for larger values of $\alpha_{\rm ov}$ and ξ. All these fifteen models correctly reproduce the three constraints M, R, and $T_{\rm eff}$, meaning that models of equal quality, as far as the adjustment of the three stellar parameters is concerned, can be obtained for different triplets of D_T, ξ, and $\alpha_{\rm ov}$. This $D_T - \xi - \alpha_{\rm ov}$ degeneracy (already highlighted for HD 152248 in Section 3.3.2) is illustrated in Figure 3.30.

Table 3.4. Parameters of some best-fit `Clés` models for HD 152219 discussed in Section 3.4.

Model	Age (Myr)	$M_{\rm init}$ ($M_\odot$)	M ($M_\odot$)	R ($R_\odot$)	$T_{\rm eff}$ (K)	$k_{2,\rm un.}$ (10^{-3})	k_2 (10^{-3})	$\dot{M}$ ($10^{-7} M_\odot\,{\rm yr}^{-1}$)	ξ	D_T ($10^6\,{\rm cm}^2\,{\rm s}^{-1}$)	$\alpha_{\rm ov}$	χ^2
Model I	7.30	19.05	18.74	9.39	30 383	4.3686	3.9670	0.66	1	$0.0^{\#}$	0.30	19.11
Series II(1)	7.88	19.00	18.64	9.40	30 900	3.8505	3.4936	0.82	1	2.12^{*}	0.20	11.68
Series II(2)	7.86	19.00	18.64	9.40	30 900	3.8467	3.4900	0.82	1	1.68^{*}	0.25	11.63
Series II(3)	7.84	19.00	18.64	9.40	30 900	3.8435	3.4871	0.82	1	1.29^{*}	0.30	11.59
Series II(4)	7.83	19.00	18.64	9.40	30 900	3.8405	3.4844	0.82	1	0.95^{*}	0.35	11.56
Series II(5)	7.81	19.00	18.64	9.40	30 900	3.8379	3.4821	0.82	1	0.65^{*}	0.40	11.53
Series III(1)	7.99	18.82	18.64	9.40	30 900	3.8507	3.4936	0.41	0.5	2.18^{*}	0.20	11.68
Series III(2)	7.97	18.82	18.64	9.40	30 900	3.8463	3.4896	0.41	0.5	1.75^{*}	0.25	11.63
Series III(3)	7.95	18.82	18.64	9.40	30 900	3.8437	3.4873	0.41	0.5	1.35^{*}	0.30	11.60
Series III(4)	7.94	18.82	18.64	9.40	30 900	3.8410	3.4849	0.41	0.5	1.00^{*}	0.35	11.57
Series III(5)	7.92	18.82	18.64	9.40	30 900	3.8384	3.4825	0.41	0.5	0.67^{*}	0.40	11.53
Series IV(1)	8.05	18.73	18.64	9.40	30 900	3.8511	3.4940	0.20	0.25	2.22^{*}	0.20	11.69
Series IV(2)	8.03	18.73	18.64	9.40	30 900	3.8463	3.4897	0.20	0.25	1.78^{*}	0.25	11.63
Series IV(3)	8.01	18.73	18.64	9.40	30 900	3.8434	3.4870	0.20	0.25	1.38^{*}	0.30	11.59
Series IV(4)	7.99	18.73	18.64	9.40	30 900	3.8413	3.4852	0.20	0.25	1.03^{*}	0.35	11.57
Series IV(5)	7.98	18.73	18.64	9.40	30 900	3.8385	3.4826	0.20	0.25	0.73^{*}	0.40	11.54
Model V	9.49	18.91	18.34	9.49	32 234	2.7753	2.5068	1.44	1	9.92^{*}	0.20	4.85
Model VI	9.57	18.91	18.32	9.51	32 298	2.7070	2.4432	1.49	1	9.67^{*}	0.25	4.90
Model VII	9.56	18.94	18.34	9.47	32 419	2.7089	2.4486	1.52	1	9.37^{*}	0.30	4.87
Model VIII	9.50	18.91	18.33	9.49	32 305	2.7179	2.4551	1.48	1	8.20^{*}	0.35	4.73
Model IX	9.54	18.86	18.28	9.49	32 266	2.6912	2.4298	1.46	1	7.53^{*}	0.40	4.69
Model $\rm I_S$	10.90	7.70	7.70	3.69	21 760	8.5115	8.2581	0.001	0.1	0.0^{*}	0.10	0.01
Model $\rm II_S$	11.15	7.70	7.70	3.69	21 789	8.4740	8.2217	0.001	0.1	0.0^{*}	0.15	0.01
Model $\rm III_S$	11.40	7.70	7.70	3.69	21 818	8.4379	8.1866	0.001	0.1	0.0^{*}	0.20	0.02
Model $\rm IV_S$	11.66	7.70	7.70	3.69	21 847	8.4029	8.1527	0.001	0.1	0.0^{*}	0.25	0.03
Model $\rm V_S$	11.89	7.70	7.70	3.69	21 875	8.3694	8.1201	0.001	0.1	0.0^{*}	0.30	0.04
Model $\rm VI_S$	12.18	7.70	7.70	3.69	21 903	8.3366	8.0883	0.001	0.1	0.0^{*}	0.35	0.05
Model $\rm VII_S$	12.45	7.70	7.70	3.69	21 930	8.3050	8.0576	0.001	0.1	0.0^{*}	0.40	0.06
Model Z+	8.17	19.09	18.64	9.40	30 900	3.4777	3.1553	1.04	1	3.51	0.30	7.63
Model X+	8.54	19.01	18.64	9.40	30 900	3.6527	3.3141	0.82	1	2.29	0.30	9.42
Model Z+X+	8.91	19.10	18.64	9.40	30 900	3.3245	3.0162	1.04	1	4.86	0.30	6.22
Model $\rm Z{+}_S$	15.36	7.70	7.70	3.69	21 697	8.0328	7.7938	0.001	0.1	1.81	0.30	0.01
Model $\rm X{+}_S$	14.13	7.70	7.70	3.69	21 697	8.1705	7.9274	0.001	0.1	0.11	0.30	0.01
Model $\rm Z{+}X{+}_S$	20.81	7.70	7.70	3.69	21 697	7.9312	7.6952	0.001	0.1	2.82	0.30	0.01

Notes. Columns 1 and 2 give the name of the model and its current age. Column 3 lists the initial mass of the corresponding evolutionary sequence. Columns 4, 5, and 6 give the current mass, radius, and effective temperature of the model. Columns 7 and 8 yield the k_2 of the model respectively before and after applying the empirical correction for the effect of rotation of Claret (1999, Equation (3.51)). Column 9 lists the mass-loss rate of the model. Columns 10, 11, and 12 give the mass-loss rate scaling factor, the turbulent diffusion coefficient, and the overshooting parameter of the model. Column 13 quotes the χ^2 of the model.

Models without and with subscript S correspond to the models of the primary star and secondary star, respectively. The Models Z+ and $\rm Z{+}_S$ have $Z = 0.020$, the Models X+ and $\rm X{+}_S$ have $X = 0.730$, and the Models Z+X+ and $\rm Z{+}X{+}_S$ have $Z = 0.020$ and $X = 0.730$.

For D_T, the *-symbol denotes it is a free parameter of the model, while the #-symbol denotes it is a fixed parameter of the model.

All χ^2 for the primary star have been computed based on $M, R, T_{\rm eff}$, and $k_{2,1}$. All χ^2 for the secondary star have been computed based on M, R, and $T_{\rm eff}$ only.

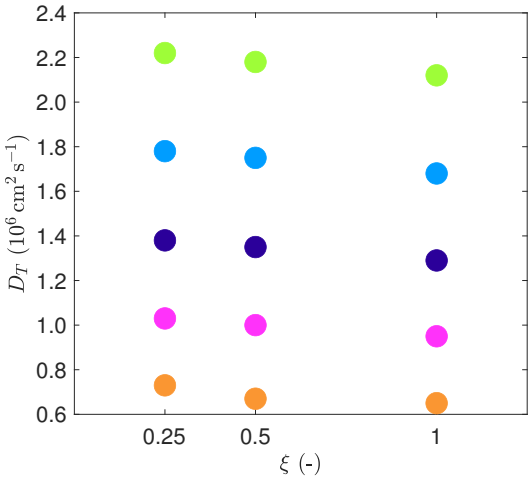

Figure 3.30. Degeneracy between the various processes in the stellar interior for the best-fit `min-Clés` models: turbulent diffusion coefficient D_T as a function of the mass-loss rate scaling parameter ξ for different values of the overshooting parameter $\alpha_{\rm ov}$. The colours stand for $\alpha_{\rm ov} = 0.20$ (green), 0.25 (blue), 0.30 (purple), 0.35 (pink), and 0.40 (orange). Figure adapted from Rosu et al. (2022a).

The biggest differences between Series II, III, and IV lie in the different initial masses and ages of the models. Indeed, the higher the ξ value, the higher the initial mass of the star, and hence, the lower its age when the star reaches the state defined by the observational parameters. Finally, all these models have a k_2 value almost two times higher than the $\bar{k}_2$ value. There is no significant difference in the k_2 value for models having the same $\alpha_{\rm ov}$ but a different ξ. However, for the models having the same ξ, k_2 decreases when $\alpha_{\rm ov}$ increases notably due to a more pronounced density variation at a radius close to the junction between the convective core and the radiative envelope in the overshooting region.

The degeneracy between the best-fit models is illustrated in the Hertzsprung-Russell diagram in Figure 3.31 where four evolutionary sequences are presented, together with Model I for comparison and the observational box defined by the observational radius and effective temperature and their respective errors. The evolutionary sequences are built based on the initial mass, ξ, $\alpha_{\rm ov}$, and D_T adopted from the Series II(1), II(5), III(1), and IV(1). The sequences corresponding to Series II(1) and II(5) are very similar, while the sequences corresponding to Series III(1) and IV(1) follow slightly different tracks. Nonetheless, all four sequences cross the observational box at the same point and follow very close paths near this point. The five dots over-plotted on each track represent the models having $k_{2,1} = \bar{k}_2$, which is, as already stated, the maximum value $k_{2,1}$ can take. These five models lie well beyond the observational box, confirming that the best-fit models have a too low density contrast between the core and the external layers. The filled triangles over-plotted on these tracks represent the models having $k_{2,1} = 0.00139$ (see Section 3.4.3 for the justification of this value). As expected, these models lie even further away from the observational box than those with $k_{2,1} = \bar{k}_2$.

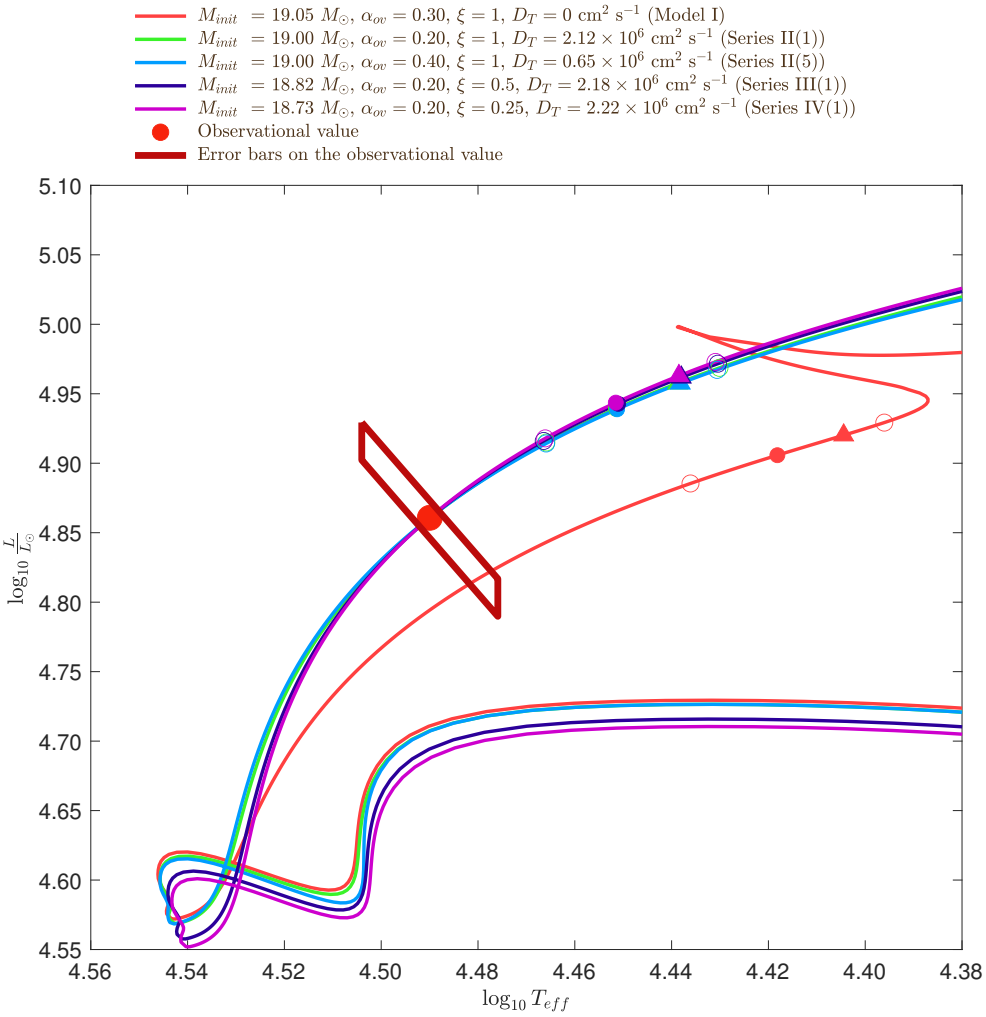

Figure 3.31. Hertzsprung-Russell diagram: evolutionary tracks of `Clés` models corresponding to the following best-fit models: Model I (coral), Series II(1) (green), Series II(5) (light blue), Series III(1) (dark blue), and Series IV(1) (plum). The dots and triangles over-plotted on the corresponding tracks indicate the models for which $k_{2,1}$ is equal to $\bar{k}_2$ and 0.00139, respectively, while the open circles correspond to the models for which $k_{2,1}$ is equal to $\bar{k}_2 \pm \Delta\bar{k}_2$. The observational value is represented by the red point, and its error bars are represented by the dark red parallelogram. Figure adapted from Rosu et al. (2022a).

All series predict mass-loss rates lower than observed. Since the observational $\dot{M}$ is poorly constrained, one cannot totally rule out the possibility of a ξ value different from 1. Yet, without any additional information, we decided, from now on, to restrict our analysis to models having $\xi = 1$.

We conclude that in order to find a model which reproduces M, R, and $T_{\rm eff}$ within their error bars, and which also satisfies the constraint that $k_{2,1} < \bar{k}_2$ within the error bars of $\bar{k}_2$, the value of D_T should be increased for a given value of $\alpha_{\rm ov}$. We computed five models (Models V to IX) with the value of $\alpha_{\rm ov}$ fixed to 0.20, 0.25, 0.30, 0.35, and 0.40, respectively, leaving the age, initial mass, and D_T as free parameters. Compared to previously computed models, one additional constraint is enforced: $k_{2,1} = \bar{k}_2$ within the error bars. The resulting models are reported in Table 3.4.

The masses and radii of all these models are within the error bars on these parameters. However, none of these models has an effective temperature and k_2 value compatible with the observational values: both parameters are overestimated. This highlights the difficulty to reconcile the observational and theoretical k_2 values, especially since $\bar{k}_2$ is only the upper-bound value on $k_{2,1}$. Requesting $k_{2,1}$ to be much lower than $\bar{k}_2$ would lead to an even more pronounced discrepancy.

Even though the mass and radius can be correctly reproduced within the error bars, it seems impossible to find a model reproducing both the effective temperature and the internal structure constant simultaneously. This issue is highlighted in the Hertzsprung-Russell diagram in Figure 3.32: Three evolutionary sequences are presented, together with the observational box. The evolutionary sequences are built based on the initial mass, ξ, $\alpha_{\rm ov}$, and D_T adopted from the Series II(1), Model V, and Model IX. As expected, the tracks corresponding to Models V and IX do not cross the observational box. The three dots over-plotted on each track represent the models having $k_{2,1} = \bar{k}_2$, while the filled triangles over-plotted on these tracks represent the models having $k_{2,1} = 0.00139$ (see Section 3.4.3 for the justification of this value). These six models lie well beyond the observational box, confirming that the best-fit models still have a too small density contrast between the core and the external layers. The two stars over-plotted on the tracks of Models V and IX correspond to the best-fit models given in Table 3.4 (we note that the one corresponding to Series II(1) perfectly matches the observational value).

3.4.3. Secondary star

We built stellar evolution models for the secondary star assuming the three constraints M, R, and $T_{\rm eff}$ and adopting the initial mass, the age, and the turbulent diffusion as free parameters. We built seven models (Models $\rm I_S$ to $\rm VII_S$) fixing $\xi = 0.1$ and adopting values for $\alpha_{\rm ov}$ of 0.10, 0.15, 0.20, 0.25, 0.30, 0.35, and 0.40. The resulting best-fit models are summarised in Table 3.4. All models reproduce perfectly the mass and radius, but slightly overestimate the effective temperature even though still within the error bars. All these models have an initial mass of $7.70\,M_\odot$ and an age ranging between 10.9 and 12.5 Myr. We observe that D_T converges towards a value of $0\,{\rm cm^2\,s^{-1}}$ for all models. Assuming Models IX and $\rm I_S$ correctly reproduce the primary and secondary stars, respectively, we get an apsidal motion rate of $1.8793^\circ\,{\rm yr^{-1}}$ for the binary system. This value is 57% higher than the observational value and is therefore incompatible with the observational results. Another problem lies in the fact that the ages of the best-fit models of the secondary star are incompatible with the range of ages derived for the primary star in Section 3.4.2. The internal structure constant of these models, corrected for the rotation of the star through Equation (3.51), amounts to

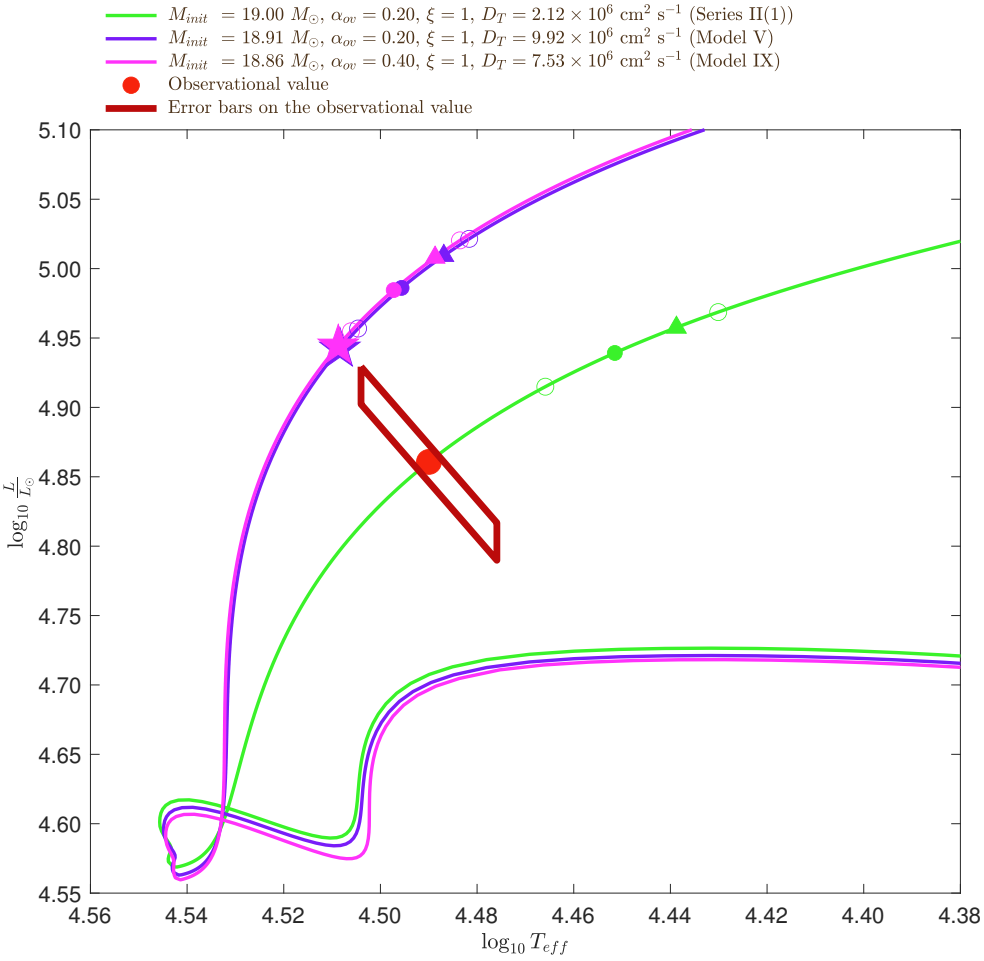

Figure 3.32. Hertzsprung-Russell diagram: evolutionary tracks of `Clés` models corresponding to the following best-fit models: Series II(1) (green), Model V (purple), and Model IX (pink). The dots and triangles over-plotted on the corresponding tracks correspond to the models for which $k_{2,1}$ is equal to $\bar{k}_2$ and 0.00139, respectively, while the open circles correspond to the models for which $k_{2,1}$ is equal to $\bar{k}_2 \pm \Delta\bar{k}_2$. The stars on the purple and pink tracks correspond to the best-fit models Model V and Model IX, respectively. The observational value is shown by the red point, and its error bars are represented by the dark red parallelogram. Figure adapted from Rosu et al. (2022a).

$\sim 8 \times 10^{-3}$. Assuming these models correctly reproduce the secondary star, then $k_{2,2} \sim 4.7\,\bar{k}_2$ and, making use of Equation (3.8), we deduce that $k_{2,1}$ should take the value of 0.00139. If it appeared that an enhanced mixing would be necessary to model the secondary star, then on the one hand $k_{2,2}$ would be lower and $k_{2,1}$ higher but, on the other hand, the age of the secondary star would be higher, thus reenforcing the age discrepancy between the primary and secondary stars.

3.4.4. Towards a common age of the stars?

In order to examine the age discrepancy raised in Section 3.4.3, we built series of evolutionary tracks with `Clés` for the two stars. We assumed $\alpha_{\rm ov} = 0.30$ for both stars. For the primary star, we assumed $\xi = 1$ and built twenty evolutionary tracks with an initial mass ranging from 17 to 21 $M_\odot$ with a step of 1 $M_\odot$ and a D_T value of 0, 2×10^6, 6×10^6, and 10×10^6 cm^2 s^{-1}. For the secondary star, we assumed $\xi = 0.1$ and built nine evolutionary tracks with an initial mass of 7.5, 7.7, and 8.0 $M_\odot$, and a D_T value of 0, 2×10^5, and 5×10^5 cm^2 s^{-1}.

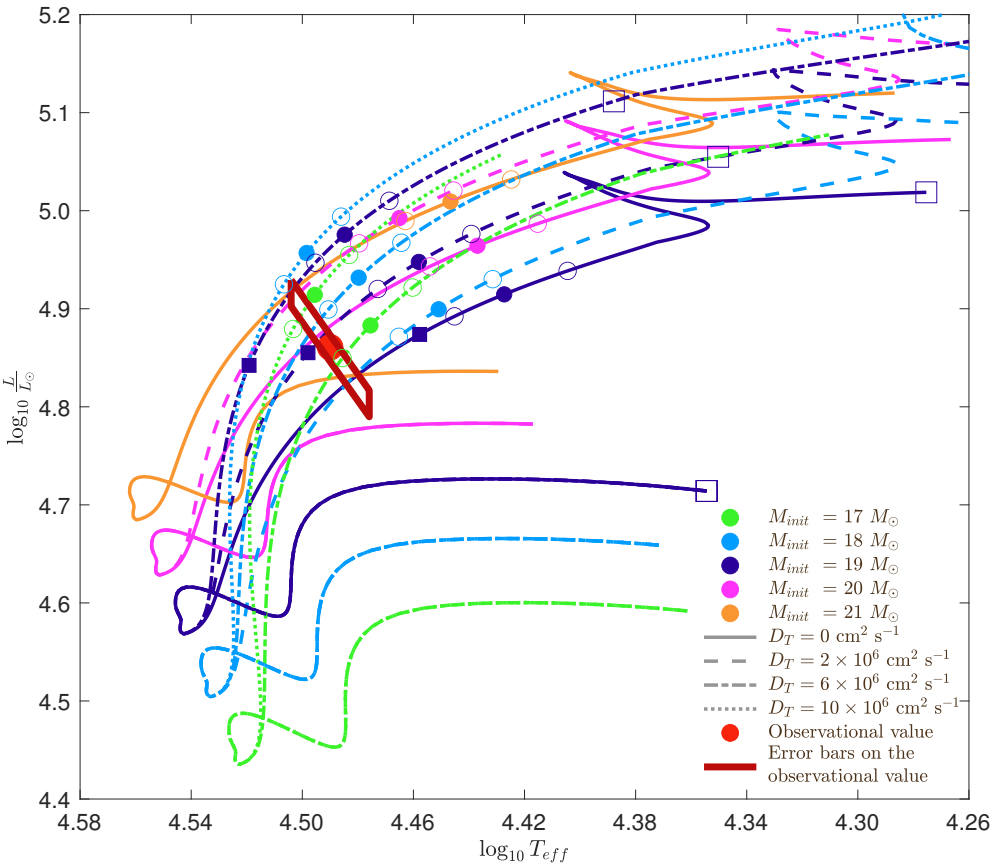

Figure 3.33. Hertzsprung-Russell diagram: evolutionary tracks of `Clés` models for the primary star of $M_{\rm init} = 17\,M_\odot$ (green), $18\,M_\odot$ (light blue), $19\,M_\odot$ (dark blue), $20\,M_\odot$ (pink), and $21\,M_\odot$ (orange), and $D_T = 0\,{\rm cm^2\,s^{-1}}$ (solid line), $2 \times 10^6\,{\rm cm^2\,s^{-1}}$ (dashed line), $6 \times 10^6\,{\rm cm^2\,s^{-1}}$ (dotted-dashed line), and $10 \times 10^6\,{\rm cm^2\,s^{-1}}$ (dotted line). All models have $\alpha_{\rm ov} = 0.30$ and $\xi = 1$. The dots over-plotted on the corresponding tracks correspond to the models for which $k_{2,1}$ is equal to $\bar{k}_2$, while the open circles correspond to the models for which $k_{2,1}$ is equal to $\bar{k}_2 \pm \Delta\bar{k}_2$. The filled and open squares over-plotted on the tracks having an initial mass of $19\,M_\odot$ correspond to the models for which the mass equals the observational value within the error bars. The observational value is represented by the red point, and its error bars are represented by the dark red parallelogram. Figure adapted from Rosu et al. (2022a).

Evolutionary tracks for the primary star are presented in the Hertzsprung-Russell diagram in Figure 3.33. In this figure, only the evolutionary tracks crossing (or nearly crossing) the observational box are presented. The models with an initial mass of 17 and 18 $M_\odot$ have a too low mass compared to observational, even within the error bars, and therefore do not fulfil the constraint on the mass. On the contrary, the models with an initial mass of 20 and 21 $M_\odot$ have too high a value of the mass compared to the observational one and, at best, fulfil the constraint on the mass at the very end of the main-sequence phase. Only the evolutionary tracks having an initial mass of 19 $M_\odot$ have a mass compatible with the observational value during the major part of the main-sequence phase – or at least when crossing (or nearly crossing) the observational box. During the main-sequence phase, the turbulent diffusion impacts the evolutionary tracks as follows: the higher the turbulent diffusion, the higher the bolometric luminosity of the star for a given effective temperature. Hence, for low-mass models (i.e. models with an initial mass of 17 and 18 $M_\odot$), only models with enhanced turbulent mixing cross the observational box, and only those having a D_T value of 6×10^6 and $10 \times 10^6\,\mathrm{cm^2\,s^{-1}}$ have a k_2 value (almost) compatible with $\bar{k}_2$ within the error bars when crossing the observational box. On the opposite, for the high-mass models (i.e. models with an initial mass of 20 and 21 $M_\odot$), only the models without or with a small D_T value cross the observational box, but none of them has a k_2 value compatible with $\bar{k}_2$ within the error bars when crossing the observational box. Regarding the models with an initial mass of 19 $M_\odot$, only those with D_T equal to 0, 2×10^6, and $6 \times 10^6\,\mathrm{cm^2\,s^{-1}}$ cross the observational box, but none of them has a k_2 value compatible with $\bar{k}_2$, though the track with $D_T = 6 \times 10^6\,\mathrm{cm^2\,s^{-1}}$ has a k_2 value very close to this value. These evolutionary sequences highlight the issue encountered in Section 3.4.2 about the difficulty to reconcile the mass, the radius, the effective temperature, and the internal structure constant of the star simultaneously.

Evolutionary tracks for the secondary star are presented in the Hertzsprung-Russell diagram in Figure 3.34. All these tracks cross the observational box defined by the radius and effective temperature at some point of their evolution. However, only the models with an initial mass of 7.7 $M_\odot$ have a mass compatible with the observation when crossing the observational box. Given that the mass-loss rate is negligible, only evolutionary tracks having an initial mass ranging between 7.58 and 7.82 $M_\odot$ are acceptable. Regarding the evolutionary track of initial mass 7.7 $M_\odot$ and $D_T = 0\,\mathrm{cm^2\,s^{-1}}$, the model closest to the observational value has a $k_{2,2}$ value approximately equal to $4.7\,\bar{k}_2$, confirming the value we found in Section 3.4.3. Within the observational box, the age of the star ranges from 10 to 14 Myr, well above the age of the best-fit models of the primary star of approximately 9.5 Myr. The filled 5-branch stars over-plotted on the tracks correspond to the models having an age of 9.5 Myr. These models are slightly below the observational box meaning that their stellar properties are not compatible with the observational values.

We inevitably come to the conclusion that we cannot find stellar evolution models for the two stars reproducing the stellar properties properly and having a compatible age at the same time. Whilst stellar evolution models have their intrinsic limitations, notably regarding the way the internal mixing is implemented, we might also have been biased by the observational data. There is no obvious issue arising from the spectroscopic and radial velocity analyses; Our determinations of the primary effective temperature and of the mass ratio, for example,

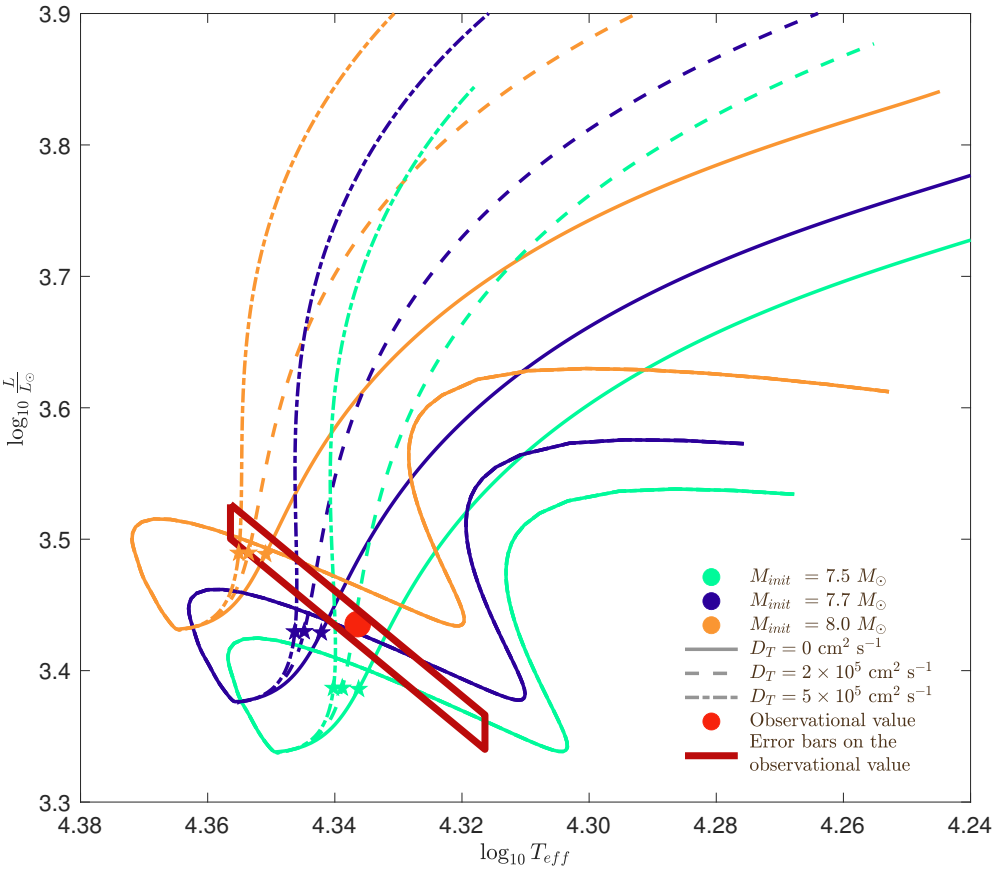

Figure 3.34. Hertzsprung-Russell diagram: evolutionary tracks of `Clés` models for the secondary star of $M_{\rm init} = 7.5\,M_\odot$ (water green), $7.7\,M_\odot$ (dark blue), and $8.0\,M_\odot$ (orange), and $D_T = 0\,{\rm cm^2\,s^{-1}}$ (solid line), $2 \times 10^5\,{\rm cm^2\,s^{-1}}$ (dashed line), and $5 \times 10^5\,{\rm cm^2\,s^{-1}}$ (dotted-dashed line). All models have $\alpha_{\rm ov} = 0.30$ and $\xi = 0.1$. The filled 5-branch stars over-plotted on the tracks correspond to the models for which the age is equal to the age of the best-fit models of the primary star (i.e. about 9.5 Myr). The observational value is represented by the red point, and its error bars are represented by the dark red parallelogram. Figure adapted from Rosu et al. (2022a).

should be robust. However, the situation is more complicated for photometry. For instance, the third light contribution might have been underestimated. The Roche lobe filling factors of the two stars and the effective temperature of the secondary star were determined based on the assumed value for the third light contribution. These parameters, and consequently also the radii of both stars, are not as reliable as their error bars might suggest. Yet, by taking $I_3 = 0$, we have actually the smallest possible radius of the secondary star, and larger radii would lead to even more severe age discrepancies than what we have found here.

3.4.5. Influence of the metallicity and helium abundance

As a last attempt to reconcile the ages of the primary and secondary stars in the models, we investigated the influence of a potential non-solar metallicity and helium abundance. Both the metallicity and the initial helium abundance affect the star essentially through a change in the opacity. The uncertainties in the opacity hence justify the influence analysis we performed here.

Regarding the metallicity, we built eight evolutionary sequences for the primary star, all having an initial mass of $19\,M_\odot$, $\alpha_{\rm ov} = 0.30$, and $\xi = 1$, but different values of Z, namely 0.010 and 0.020, and different values of D_T, namely 0, 2×10^6, 6×10^6, and $10 \times 10^6\,{\rm cm^2\,s^{-1}}$. These evolutionary tracks are presented in the Hertzsprung-Russell diagram in Figure 3.35 together with the evolutionary tracks for $Z = 0.015$ presented in Section 3.4.4. For more clarity, only the tracks crossing the observational box at some point of their evolution are shown. For $Z = 0.010$, only the two models with the lowest values of D_T cross the observational box, while for $Z = 0.020$, all models cross the observational box. In addition, all tracks have a mass compatible with the observational value when crossing the observational box. Compared to Figure 3.33, we observe that a higher metallicity has the same impact on the evolutionary tracks as a lower mass and/or lower D_T: The evolutionary track with $Z = 0.020$ and the highest value of D_T has now a value of $k_{2,1}$ compatible with $\bar{k}_2$ when it crosses the observational box.

Regarding the helium abundance, we built eight evolutionary sequences for the primary star, all having an initial mass of $19\,M_\odot$, $\alpha_{\rm ov} = 0.30$, $\xi = 1$, and $Z = 0.015$, but different values of X, namely 0.700 and 0.730, and different values of D_T, namely 0, 2×10^6, 6×10^6, and $10 \times 10^6\,{\rm cm^2\,s^{-1}}$. These evolutionary tracks are presented in the Hertzsprung-Russell diagram in Figure 3.36 together with the evolutionary tracks having $X = 0.715$ presented in Section 3.4.4. For more clarity, only the tracks crossing at some point of their evolution the observational box are shown. For all values of X, only the three models with the lowest values of D_T cross the observational box at some point of their evolution. In addition, all tracks have a mass compatible with the observational value when crossing the observational box. Compared to Figure 3.33, we observe that a higher X value, and hence, a lower helium abundance, has the same impact on the evolutionary tracks as a lower mass and/or lower D_T. The impact of a change in X is, however, smaller than that of a change in Z and none of the models has a $k_{2,1}$ compatible with $\bar{k}_2$ when crossing the observational box.

We then built three best-fit models for the primary star and the secondary star adopting the constraints on M, R, and $T_{\rm eff}$, fixing $\alpha_{\rm ov} = 0.30$ for both stars, and $\xi = 1$ for the primary star and 0.1 for the secondary star, and leaving the age, initial mass, and D_T as free parameters, for the three following couples of values for (X, Z): (0.715, 0.020), (0.730, 0.015), and (0.730, 0.020). The results are given in Table 3.4 under the names of Model Z+, X+, and Z+X+, respectively. All six models correctly reproduce the observational mass, radius, and effective temperature of the corresponding star. Regarding the three primary star models, compared to Series II(3), all models have a higher age, a slightly higher initial mass, and a higher turbulent diffusion coefficient D_T. Their lower $k_{2,1}$ value compared to Series II(3) make these three models better suited to reproduce the primary star. Regarding

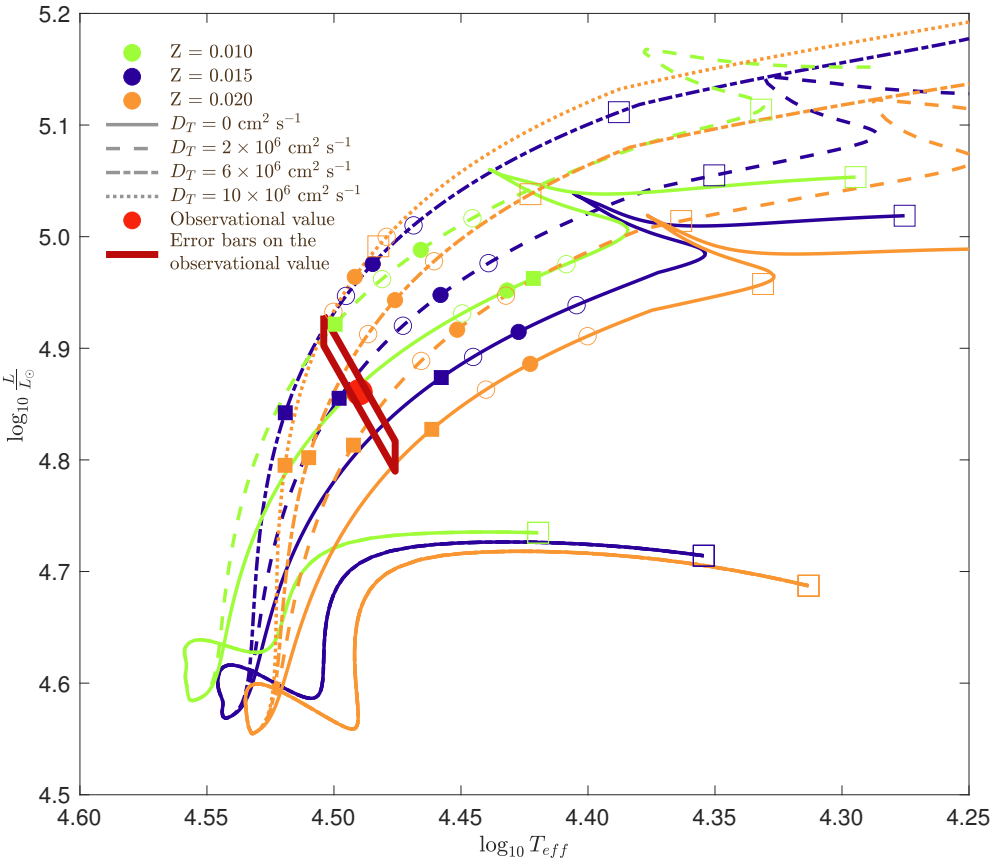

Figure 3.35. Hertzsprung-Russell diagram: evolutionary tracks of `Clés` models for the primary star having $M_{\rm init} = 19\,M_\odot$, $\alpha_{\rm ov} = 0.30$, $\xi = 1$, $X = 0.715$, $Z = 0.010$ (green), 0.015 (dark blue), and 0.020 (orange), and $D_T = 0\,{\rm cm^2\,s^{-1}}$ (solid line), $2 \times 10^6\,{\rm cm^2\,s^{-1}}$ (dashed line), $6 \times 10^6\,{\rm cm^2\,s^{-1}}$ (dotted-dashed line), and $10 \times 10^6\,{\rm cm^2\,s^{-1}}$ (dotted line). The dots over-plotted on the corresponding tracks correspond to the models for which $k_{2,1}$ is equal to $\bar{k}_2$, while the open circles correspond to the models for which $k_{2,1}$ is equal to $\bar{k}_2 \pm \Delta\bar{k}_2$. The filled and open squares over-plotted on the tracks correspond to the models for which the mass is equal to the observed value within the error bars. The observational value is represented by the red point, and its error bars are represented by the dark red parallelogram. Figure adapted from Rosu et al. (2022a).

the secondary star, compared to Model III$_{\rm S}$, the three models have a higher age, the same initial mass, and a higher D_T value, as well as a lower $k_{2,2}$ value. The evolutionary tracks corresponding to these best-fit models are presented in Figure 3.37 together with Series II(3) for the primary star and Model III$_{\rm S}$ for the secondary star. Compared to the models having a solar metallicity and helium abundance, the age discrepancy between the primary and secondary best-fit models is enhanced when higher metallicity or/and lower helium abundance is/are considered.

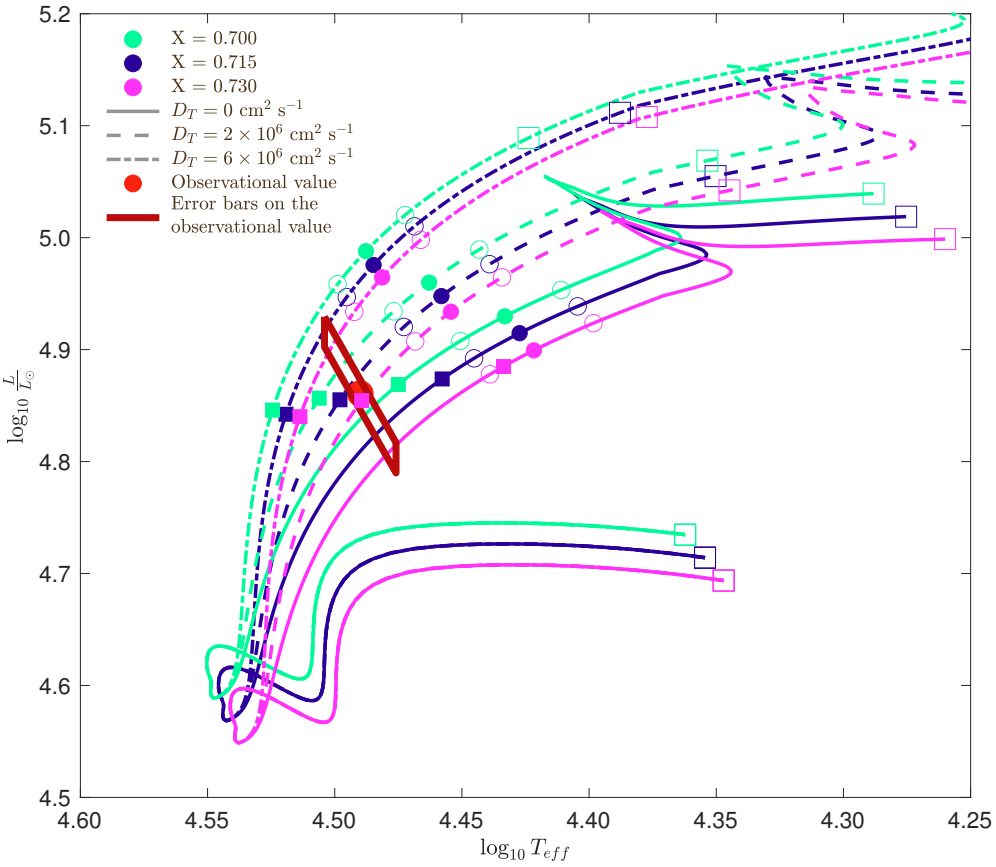

Figure 3.36. Hertzsprung-Russell diagram: evolutionary tracks of `Clés` models for the primary star having $M_{\rm init} = 19\,M_\odot$, $\alpha_{\rm ov} = 0.30$, $\xi = 1$, $Z = 0.015$, $X = 0.700$ (water green), 0.715 (dark blue), and 0.730 (pink), and $D_T = 0\,{\rm cm^2\,s^{-1}}$ (solid line), $2 \times 10^6\,{\rm cm^2\,s^{-1}}$ (dashed line), $6 \times 10^6\,{\rm cm^2\,s^{-1}}$ (dotted-dashed line), and $10 \times 10^6\,{\rm cm^2\,s^{-1}}$ (dotted line). The dots over-plotted on the corresponding tracks correspond to the models for which $k_{2,1}$ is equal to $\bar{k}_2$, while the open circles correspond to the models for which $k_{2,1}$ is equal to $\bar{k}_2 \pm \Delta\bar{k}_2$. The filled and open squares over-plotted on the tracks correspond to the models for which the mass is equal to the observed value within the error bars. The observational value is represented by the red point, and its error bars are represented by the dark red parallelogram. Figure adapted from Rosu et al. (2022a).

The increase in D_T with metallicity is explained in details in Section 3.3.3. In summary, an increase in metallicity, at a given mass, increases the opacity which in turn lowers the effectiveness of the radiative transport, and hence, decreases the effective temperature and luminosity. The same holds true for the increase in D_T with the decrease in helium abundance which is the direct consequence of an increase in the opacity with X. Since an increase in D_T leads to an increase in the luminosity, it compensates the decrease in $T_{\rm eff}$ and L induced by the enhanced metallicity. The turbulent diffusion increases the mass of the convective core; accordingly, k_2 decreases.

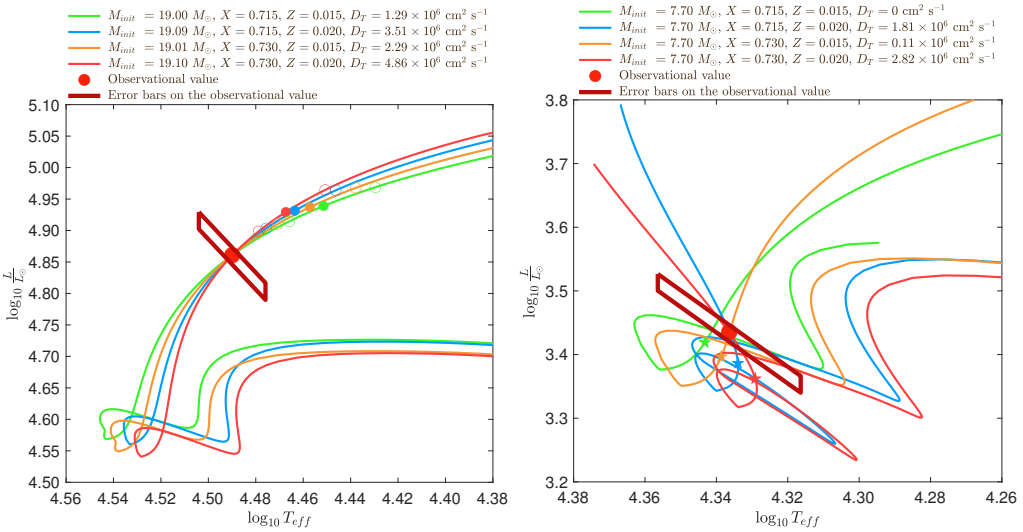

Figure 3.37. Hertzsprung-Russell diagram: evolutionary tracks of `Clés` models for the primary star (*left panel)* and secondary star (*right panel*) corresponding to the best-fit models listed in Table 3.4 together with Series II(3) for the primary star and Model III$_S$ for the secondary star. All models have $\alpha_{ov} = 0.30$, primary models have $\xi = 1$ while secondary models have $\xi = 0.1$. The dots over-plotted on the evolutionary tracks of the primary correspond to the models for which $k_{2,1}$ is equal to $\bar{k}_2$, while the open circles correspond to the models for which $k_{2,1}$ is equal to $\bar{k}_2 \pm \Delta\bar{k}_2$. The filled 5-branch stars over-plotted on the secondary tracks correspond to the models for which the age is equal to the age of the best-fit model of the primary star of same X and Z. The observational value is represented by the red point, and its error bars are represented by the dark red parallelogram. Figure adapted from Rosu et al. (2022a).

There is no observational evidence that HD 152219 would have a non-solar metallicity or helium abundance. Even though a higher metallicity and a subsolar helium abundance would improve the best-fit models of the primary star by allowing us to simultaneously satisfy the constraints on $M, R, T_{\rm eff}$, and $k_{2,1}$, such a high metallicity seems rather unlikely (see Section 1.3). At this stage, information is lacking to conclude that the metallicity and helium abundance of the star deviate from solar.

3.4.6. Discussion: what if the rotation axes were misaligned?

The highlighted difficulty to reconcile observational and theoretical internal structure constant values suggests there might be some bias in the interpretation of the apsidal motion in terms of the internal structure constant. Higher-order terms were shown to have a negligible contribution (see Section 3.1.3). Another scenario could arise from the presence of a third body orbiting the binary system. However, to date, there is no signature of a third body in the spectrum of HD 152219 (see review in Section 1.3.2 as well as Sections 2.3.1 and 2.3.3). The possibility that a ternary star would con-

tribute to the apsidal motion rate without being detected though is a priori conceivable (see e.g. Naoz et al. (2013) and Borkovits et al. (2015) for a review of the ensuing apsidal motion equations). At this stage, there is unfortunately no way to infirm or confirm the presence of a third body in the system. Yet, it is highly unlikely that a non-detected third body would contribute as much as 57% of the inner binary apsidal motion rate necessary to reconcile theoretical and observational k_2 values (see Section 3.4.3).

A third possibility could be a misalignment of the rotation axes of the stars with respect to the normal to the orbital plane. We here refer to the set of equations recalled in Section 3.1.4. We represent the quantities $C_{\mathrm{mis},j}$ (see Equation (3.28)) as a function of the angle α_j in Figure 3.38 for the specific case of $i = 89.58°$ (see Section 2.3.3.2). $C_{\mathrm{mis},j}$ takes its minimum and maximum values at $\alpha_j = 90°$ and 180°, respectively.

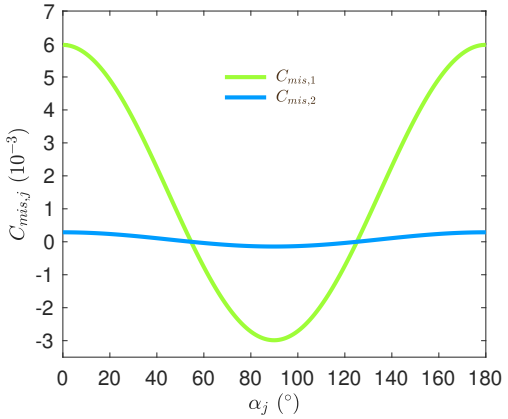

Figure 3.38. Behaviour of $C_{\mathrm{mis},1}$ and $C_{\mathrm{mis},2}$ as a function of α_1 and α_2, the angles between the primary and secondary stellar rotation axes, respectively, and the normal to the orbital plane. Figure adapted from Rosu et al. (2022a).

We computed the weighted-average internal structure constant $\bar{k}_{2,\mathrm{mis}}$ considering values of α_j ranging from 0 to 180°. Figure 3.39 shows the $\bar{k}_{2,\mathrm{mis}}$ value as a function of the two angles α_1 and α_2. The maximum value of $\bar{k}_{2,\mathrm{mis}}$ is 3.39×10^{-3} and is reached for $\alpha_1 = \alpha_2 = 90°$. As expected, the $\bar{k}_{2,\mathrm{mis}}$ value mostly changes with the primary stellar rotation axis inclination α_1 and is only slightly affected by a change in the secondary stellar rotation axis inclination α_2. This reflects the predominant contribution of the primary star to the total rate of apsidal motion, as already discussed in Section 3.4.1. For α_1 lower than about 40°, there is no significant impact on the $\bar{k}_{2,\mathrm{mis}}$ value.

In Section 3.4.2, the best-fit models we obtained for the primary star all had a $k_{2,1}$ value between ~ 2.4 and 2.5×10^{-3}. For these values to be compatible with the observational value, the primary stellar rotation axis should be inclined by an angle of at least $\sim 50°$ with respect to the normal to the orbital plane. Such a high misalignment angle would be surprising in a close binary system, especially since the two stars are about to reach pseudo-synchronisation.

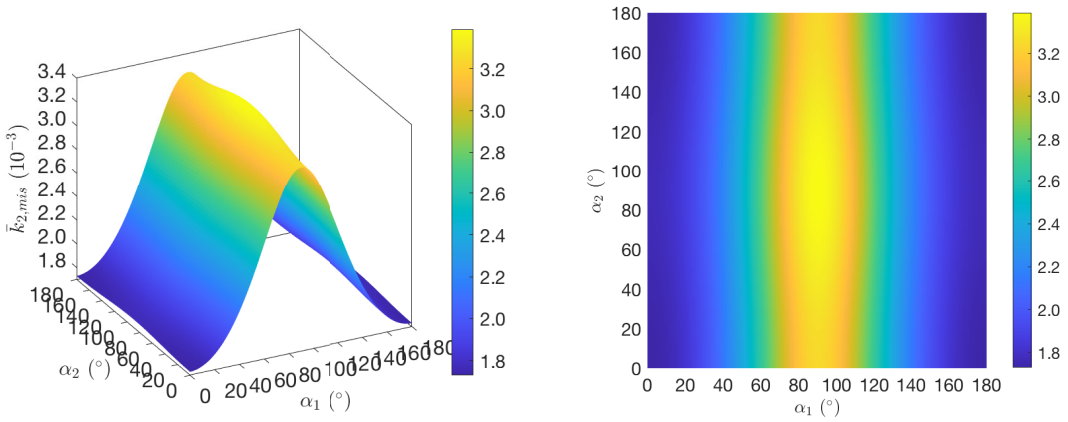

Figure 3.39. Behaviour of $\bar{k}_{2,\mathrm{mis}}$ as a function of α_1 and α_2, the angles between the primary and secondary stellar rotation axes, respectively, and the normal to the orbital plane. Figure adapted from Rosu et al. (2022a).

We may wonder whether the condition of sub-critical stellar rotation leads to a restriction on the values of α_1 and α_2, as discussed in Section 3.1.4.2. We used Equations (3.36) and (3.39) to enforce conditions on the equatorial rotational velocity for the primary and secondary stars: $v_{\mathrm{eq},1} \leq 583\,\mathrm{km\,s^{-1}}$ and $v_{\mathrm{eq},2} \leq 628\,\mathrm{km\,s^{-1}}$, respectively. Using the projected rotational velocities derived in Section 2.3.1.4, namely $v_{\mathrm{eq},1} \sin\beta_1 = 166\,\mathrm{km\,s^{-1}}$ and $v_{\mathrm{eq},2} \sin\beta_2 = 95\,\mathrm{km\,s^{-1}}$, we get the following constraints on the angles β_j: $\beta_1 \geq 16.5°$ and $\beta_2 \geq 8.7°$. In order to translate this condition on β_j into a condition on α_j, we need to assume a value for the azimuthal angle θ. As shown in Section 3.1.4, the largest impact of α_j on the apsidal motion rate occurs when θ equals 0° and 180°. For an azimuthal angle of 0°, we get the conditions that $\alpha_1 > 106.1°$ or $\alpha_1 < 73.0°$, and $\alpha_2 > 98.3°$ or $\alpha_2 < 80.9°$, whilst for an azimuthal angle of 180°, we get the conditions that $\alpha_1 > 107.0°$ or $\alpha_1 < 73.9°$, and $\alpha_2 > 99.1°$ or $\alpha_2 < 81.7°$. These conditions do not rule out the possibility to have inclination angles of $\sim 50°$ for the rotation axes of the stars.

As discussed in Section 2.3.4, the possibility of a misalignment between the primary stellar rotation axis and the axis of the binary system can in principle be tested via the Rossiter-McLaughlin effect. Indeed, we put a constraint on the value of α: $\alpha \leq 15°$ or $\alpha \geq 165°$. Moreover, given the proximity of the system's orbital inclination to 90°, the largest amplitude of the Rossiter-McLaughlin effect is expected for an alignment of the rotation and binary axes. In view of the amplitudes reported by Sana (2009), and keeping in mind the caveat about these amplitudes highlighted in Section 2.3.4, it seems thus unlikely that there exists a very large misalignment between the rotation and binary axes. Whilst this conclusion applies of course only to the primary star, we stress that it is actually the primary that has the largest rotational contribution to the rate of apsidal motion. Hence, a misalignment of the axes seems unlikely to be responsible for the discrepancy between the observational and theoretical values of $\dot{\omega}$.

3.4.7. HD 152219 in a nutshell

We built `Clés` stellar evolution models using the `min-Clés` routine to search for best-fit models of the two stars adopting the mass, radius, and effective temperature as constraints, sometimes complemented by k_2 for the primary star. A simultaneous analysis of the two stars gave no coherent results. We considered different prescriptions for the internal mixing occurring inside the stars. We notably performed several tests with different values of the overshooting parameter $\alpha_{\rm ov}$, the mass-loss rate scaling factor ξ, and the turbulent diffusion coefficient D_T. The primary star models were shown to have a smaller density contrast than suggested by the observations, that is to say, the theoretical internal structure constant was almost two times larger than the observational weighted-average $\bar{k}_2$ value. To simultaneously satisfy the three previously mentioned constraints together with the constraint that $k_{2,1} < \bar{k}_2$ in the models was impossible: The models were shown to have a strongly enhanced turbulent diffusion but both the effective temperature and k_2 value were overestimated. The best-fit models, that is to say, the models having the best compromise in terms of $M, R, T_{\rm eff}$, and $k_{2,1}$, all have an initial mass of $18.3 \pm 0.5\,M_\odot$ and an age of 9.5 ± 0.6 Myr. Regarding the secondary star, given that there is no strong constraint on $k_{2,2}$, we only enforced the stellar models to reproduce M, R, and $T_{\rm eff}$. The best-fit models obtained in this way all have an initial mass of $7.70 \pm 0.12\,M_\odot$, a $k_{2,2}$ value approximately equal to $4.7\,\bar{k}_2$, and an age estimate of 11.7 ± 0.6 Myr. Assuming these stellar models are representative of the secondary star, the $k_{2,2}$ value implies that $k_{2,1} = 0.00139$, thereby increasing even more the discrepancy with the stellar evolution models of the primary star. All things considered, the age estimated for the secondary star is incompatible with the age of the primary star. We also tested the impact of non-solar metallicity and helium abundance, and found that both an enhanced metallicity and depleted helium abundance go towards adjustments of the primary star that better reproduce $M, R, T_{\rm eff}$, and $k_{2,1}$. However, the corresponding models of the secondary star yield even higher ages, further increasing the inconsistency between primary and secondary ages.

Finally, we investigated the impact of a misalignment of the stellar rotation axis with respect to the normal to the orbital plane. Such a misalignment reduces the contribution of the rotational term to the Newtonian apsidal motion rate, thereby implying an increased value of $\bar{k}_2$ compared to the aligned configuration. In the present case, we found that a severe misalignment angle is required to get a $\bar{k}_2$ value high enough for the stellar models of the primary star to satisfy the constraint on $k_{2,1}$. Such a high misalignment is, however, ruled out by the observational constraint obtained via the analysis of the Rossiter-McLaughlin effect which sets an upper limit of 15° on the misalignment angle.

The difficulty to reconcile the k_2 value of the primary stellar models with the observational constraint on the $\bar{k}_2$ value as well as the internal inconsistency between the ages of the two stars are indications that some physics of stellar interior are still not completely understood. Obviously, all the tools used in our observational or theoretical analyses have their own limitations. Whilst we are quite confident in our determination of the masses of the stars as well as in the effective temperature of the primary star, we are less confident in the inferred values of the secondary effective temperature and the radii of both stars.

3.5. The high rate apsidal motion binary: CPD-41° 7742

The set of observationally determined properties of the binary CPD-41° 7742 is recalled in Table 3.5. Using our re-derived parameters of the binary (see Section 2.4), we inferred a value for $\dot{\omega}_{\rm GR}$ of $(0.41 \pm 0.01)^\circ\,{\rm yr}^{-1}$. As a consequence, the observational contribution of the Newtonian term $\dot{\omega}_{\rm N}$ amounts to $(14.97^{+0.42}_{-0.51})^\circ\,{\rm yr}^{-1}$. In the case of CPD-41° 7742, as in the case of HD 152219 (see Section 3.4), it is impossible to observationally constrain the individual values of the internal structure constants of both stars. Nevertheless, we computed the weighted-average apsidal motion constant $\bar{k}_2$ for the binary system using Equation (3.8) and got $\bar{k}_2 = 0.0064^{+0.0004}_{-0.0005}$. As the secondary star is smaller and less massive than the primary star, its k_2 value exceeds that of the primary. Therefore, we have $k_{2,1} < \bar{k}_2 < k_{2,2}$. Observationally, we have $\frac{c_1}{c_1+c_2} = 0.85$ and $\frac{c_2}{c_1+c_2} = 0.15$, meaning that $k_{2,1}$ has a much higher weight in the calculation of $\bar{k}_2$[7].

Table 3.5. Set of observationally determined properties of the binary system CPD-41° 7742 used for the `Clés` analysis, for which we adopted symmetric uncertainties.

Parameter	Value	
	Primary	Secondary
M ($M_\odot$)	17.8 ± 0.5	10.0 ± 0.3
R ($R_\odot$)	7.57 ± 0.09	4.29 ± 0.06
$T_{\rm eff}$ (K)	$31\,800 \pm 1000$	$24\,098 \pm 1000$
$\bar{k}_2$	0.0064 ± 0.0005	
$\dot{\omega}$ ($^\circ\,{\rm yr}^{-1}$)	15.38 ± 0.51	

We built stellar evolution models for the massive binary CPD-41° 7742 with the version of the `Clés` code that includes the computation of the internal structure constant. We search for best-fit models of the system using the `min-Clés` routine and solve for the apsidal motion constants and the theoretical rate of apsidal motion for the set of `Clés` models that best reproduce the observed stellar parameters. The aim of the present analysis is to see whether standard models reproducing the stellar physical properties are also capable of reproducing the apsidal motion rate inferred in Section 2.4.3.3. For all models built, we adopted the mass-loss rate scaling factor $\xi = 1$. All results of this section are presented in Rosu et al. (2022b).

3.5.1. Stellar structure and evolution models

In a first attempt to obtain stellar evolution models representative of both stars, we built two `Clés` models (Models $\rm I_P$ and $\rm I_S$) simultaneously, adopting the six corresponding constraints (M, R, and $T_{\rm eff}$ of both stars), and leaving the initial masses of the two stars and the age of the binary system as the only three free parameters. For both stars, we adopted

[7] We note, however, that this does not imply that the product $\frac{c_1}{c_1+c_2}k_{2,1}$ contributes 85% to $\bar{k}_2$.

an overshooting parameter $\alpha_{\rm ov} = 0.20$, and no turbulent diffusion. The parameters of the best-fit models are reported in Table 3.6. Except for the secondary effective temperature, all stellar parameters are well-reproduced within their error bars. The age of the binary system is estimated at 6.25 ± 0.30 Myr while the total (Newtonian + general relativistic) apsidal motion rate is estimated at $16.08^\circ\,{\rm yr}^{-1}$, slightly larger than the observational value (see Section 2.4.3.3). We then computed two models independently for each star (Models $\rm II_P$ and $\rm II_S$) adopting the same constraints and free parameters. The best-fit models in this case (see Table 3.6) have ages of 6.13 ± 0.37 and 7.47 ± 1.30 Myr, for the primary and secondary stars, respectively. The physical parameters of the two stars are better reproduced but the apsidal motion rate, of $15.98^\circ\,{\rm yr}^{-1}$ is still slightly larger than the observational value. We note that in principle, we should compute the apsidal motion rate of the system based on two stellar models having the same age. Nonetheless, the independent primary and secondary models have ages compatible within their error bars, and we could, therefore, enforce a value for $\dot{\omega}$ in this case.

Table 3.6. Parameters of some best-fit `Clés` models of CPD-41° 7742 discussed in Section 3.5.1.

Model	Age (Myr)	$M_{\rm init}$ ($M_\odot$)	M ($M_\odot$)	R ($R_\odot$)	$T_{\rm eff}$ (K)	$k_{2,\rm un.}$ (10^{-3})	k_2 (10^{-3})	$\dot{M}$ ($10^{-8} M_\odot\,{\rm yr}^{-1}$)	$\alpha_{\rm ov}$	D_T ($10^6\,{\rm cm^2\,s^{-1}}$)
Model $\rm I_P$	6.25	17.89	17.73	7.55	31 150	6.6573	6.2738	3.67	0.20	0
$\rm I_S$		10.11	10.11	4.26	25 292	9.7592	9.5318	4.10×10^{-2}	0.20	0
Model $\rm II_P$	6.13	18.07	17.91	7.57	31 300	6.7045	6.3196	3.88	0.20	0
Model $\rm II_S$	7.47	9.89	9.89	4.29	24 926	9.3022	9.0757	3.54×10^{-2}	0.20	0
Model $\rm III_P$ (1)	6.83	17.99	17.79	7.57	31 800	6.0474	5.6974	4.74	0.20	1.81
Model $\rm III_P$ (2)	6.81	17.99	17.79	7.57	31 800	6.0427	5.6930	4.73	0.25	1.41
Model $\rm III_P$ (3)	6.80	17.99	17.79	7.57	31 800	6.0389	5.6894	4.75	0.30	1.05
Model $\rm III_P$ (4)	6.79	17.99	17.79	7.57	31 800	6.0358	5.6865	4.74	0.35	0.74
Model $\rm III_P$ (5)	6.78	17.99	17.79	7.57	31 800	6.0338	5.6846	4.75	0.40	0.48
Model $\rm III_S$ (1)	6.99	9.96	9.95	4.27	25 045	9.4745	9.2482	3.69×10^{-2}	0.20	0.0
Model $\rm III_S$ (2)	7.22	9.95	9.94	4.28	25 060	9.4014	9.1759	3.74×10^{-2}	0.25	0.0
Model $\rm III_S$ (3)	7.50	9.92	9.92	4.28	25 054	9.3132	9.0888	3.74×10^{-2}	0.30	0.0
Model $\rm III_S$ (4)	7.72	9.92	9.92	4.29	25 075	9.2483	9.0246	3.80×10^{-2}	0.35	0.0
Model $\rm III_S$ (5)	7.88	9.92	9.91	4.29	25 104	9.2097	8.9869	3.87×10^{-2}	0.40	0.0

Notes. Columns 1 and 2 give the name of the model and its current age. Column 3 lists the initial mass of the corresponding evolutionary sequence. Columns 4, 5, and 6 give the current mass, radius, and effective temperature of the model. Columns 7 and 8 yield the k_2 respectively before and after applying the empirical correction for the effect of rotation of Claret (1999, Equation 3.51) of the model. Column 9 lists the mass-loss rate of the model. Columns 10 and 11 give the overshooting parameter and turbulent diffusion coefficient of the model. Models with subscript P (respectively S) correspond to the models of the primary (respectively secondary) star. Models I and II have D_T fixed to $0\,{\rm cm^2\,s^{-1}}$ while models III let it vary freely.

In a last attempt to reproduce the stellar properties and the apsidal motion rate of the system, we built a series of five independent models (Models III (1) to (5)) for the two stars adopting the same constraints as before, an overshooting parameter of 0.20, 0.25, 0.30, 0.35, and 0.40, respectively, and, as free parameters, the age, the initial mass, and the turbulent diffusion coefficient. The best-fit models are reported in Table 3.6. The models perfectly reproduce the stellar properties of the primary star thanks to the addition of turbulent diffusion. The best-fit turbulent diffusion coefficient decreases with increasing overshooting, indicating that both effects affect the k_2 parameter in a similar way (see the discussion in Section 3.3.2). We note that the turbulent diffusion of the secondary models converge

towards a value of $0\,\mathrm{cm^2\,s^{-1}}$. This behaviour was already observed for the secondary star of HD 152219 (see Section 3.4.3). The age estimates range from 6.78 to 6.83 Myr for the primary star and from 6.99 to 7.88 Myr for the secondary star. For each series of models ((1) to (5)), we computed the apsidal motion rate of the binary system and obtained values ranging between 14.79 and $14.89^\circ\,\mathrm{yr^{-1}}$. These values are compatible within the error bars with the observational value. We therefore conclude that to reproduce the apsidal motion rate of the binary system, and hence, the internal structure of the stars composing the system, turbulent diffusion needs to be included inside the models, at least for the most massive star of the system. These results confirm those obtained for the systems HD 152248 and HD 152219.

3.5.2. CPD-41° 7742 in a nutshell

We computed stellar evolution models for the two stars. The best-fit models of the stars, in terms of the masses, radii, and effective temperatures, predict a theoretical apsidal motion rate compatible within the error bars with the observed one provided that turbulent mixing is introduced in the primary stellar evolution models. This confirms the results obtained for the systems HD 152248 and HD 152219. The binary's age is estimated at 6.8 ± 1.4 Myr, and is compatible with the age of the NGC 6231 cluster. Initial masses of 18.0 ± 0.5 and $9.9 \pm 0.3\,M_\odot$ are derived for the primary and secondary stars, respectively.

3.6. The revisited binary: HD 152218

We briefly reconsider the binary HD 152218 in light of the newly available `min-Clés` routine that allows for a more efficient search for best-fit stellar evolution models. Compared to our former analysis (Rauw et al. 2016), turbulent diffusion is now included in `Clés`. The set of observationally determined properties of the binary is recalled in Table 3.7. Using the parameters of HD 152218 coming from Rauw et al. (2016), we determined a Newtonian and a general relativistic contributions to the apsidal motion rate of $(1.91^{+0.23}_{-0.24})^\circ\,\mathrm{yr}^{-1}$ and $(0.13 \pm 0.01)^\circ\,\mathrm{yr}^{-1}$, respectively. All results of this section are presented in Rosu et al. (2022b).

Table 3.7. Set of observationally determined properties of the binary system HD 152218 used for the `Clés` analysis, for which we adopted symmetric uncertainties.

Parameter	Value	
	Primary	Secondary
M ($M_\odot$)	19.8 ± 0.5	15.0 ± 1.1
R ($R_\odot$)	8.4 ± 1.1	7.8 ± 1.6
$T_{\rm eff}$ (K)	$33\,400 \pm 1000$	$29\,900 \pm 1000$
$\dot{\omega}$ ($^\circ\,\mathrm{yr}^{-1}$)	2.04 ± 0.24	

We built stellar evolution models with the `min-Clés` routine for HD 152218, adopting as constraints the masses, radii, and effective temperatures of the stars. We fixed $\xi = 1$, and left the age, initial masses, and turbulent diffusion as free parameters.

We first built two models (Models $\mathrm{I_P}$ and $\mathrm{I_S}$) simultaneously for the two stars. The parameters of the best fits are reported in Table 3.8. Except for the radius of the secondary star, all stellar parameters are well-reproduced within their error bars. The age of the binary system is estimated at 5.79 Myr, confirming the value of 5.8 ± 0.6 Myr obtained by Rauw et al. (2016). The apsidal motion rate is estimated at $1.60^\circ\,\mathrm{yr}^{-1}$. This value is slightly lower than the observational value.

To solve the discrepancies in the secondary radius and in the apsidal motion rate, we further built a series of five independent models (Models $\mathrm{II_P}$ (1) to (5) and $\mathrm{II_S}$ (1) to (5)) for the two stars adopting an overshooting parameter of 0.20, 0.25, 0.30, 0.35, and 0.40, respectively. The best-fit models are reported in Table 3.8. They reproduce well the stellar properties of both stars. As for HD 152248 and the primary stars of HD 152219 and CPD-41° 7742, we observe that the amount of turbulent diffusion necessary to fit the stellar properties decreases with the increasing overshooting parameter. The age estimates range from 6.71 to 6.76 Myr for the primary star and from 11.59 to 11.67 Myr for the secondary star. Given the important age difference between the primary and secondary models, we cannot compute a coherent apsidal motion rate for the binary system by simply summing the contributions of the two stars taken at different ages.

Table 3.8. Parameters of some best-fit `Clés` models of HD 152218 discussed in Section 3.6.

Model	Age (Myr)	$M_{\rm init}$ ($M_\odot$)	M ($M_\odot$)	R ($R_\odot$)	$T_{\rm eff}$ (K)	$k_{2,\rm un.}$ (10^{-3})	k_2 (10^{-3})	$\dot{M}$ ($10^{-8} M_\odot\,{\rm yr}^{-1}$)	$\alpha_{\rm ov}$	D_T ($10^6\,{\rm cm^2\,s^{-1}}$)
Model $\rm I_P$	5.79	20.02	19.72	8.12	32 696	6.0908	5.6951	7.81	0.20	1.0
$\rm I_S$		15.30	15.25	6.08	30 134	8.6278	8.2863	1.15	0.20	0.0
Model $\rm II_P$ (1)	6.76	20.23	19.80	8.40	33 400	4.9192	4.5680	11.5	0.20	2.07
Model $\rm II_P$ (2)	6.75	20.23	19.80	8.40	33 400	4.9106	4.5600	11.5	0.25	1.65
Model $\rm II_P$ (3)	6.73	20.23	19.80	8.40	33 400	4.9027	4.5527	11.5	0.30	1.27
Model $\rm II_P$ (4)	6.72	20.23	19.80	8.40	33 400	4.8957	4.5462	11.5	0.35	0.94
Model $\rm II_P$ (5)	6.71	20.23	19.80	8.40	33 400	4.8892	4.5402	11.5	0.40	0.65
Model $\rm II_S$ (1)	11.67	15.17	15.00	7.80	29 900	3.9358	3.6090	3.19	0.20	4.15
Model $\rm II_S$ (2)	11.65	15.17	15.00	7.80	29 900	3.9264	3.6004	3.19	0.25	3.75
Model $\rm II_S$ (3)	11.62	15.17	15.00	7.80	29 900	3.9179	3.5926	3.20	0.30	3.37
Model $\rm II_S$ (4)	11.60	15.17	15.00	7.80	29 900	3.9100	3.5853	3.19	0.35	3.01
Model $\rm II_S$ (5)	11.59	15.17	15.00	7.80	29 900	3.9028	3.5787	3.19	0.40	2.67
Model $\rm III_S$ (1)	9.92	15.11	15.00	7.12	29 900	5.2520	4.9169	2.13	0.20	2.51
Model $\rm III_S$ (2)	9.90	15.11	15.00	7.12	29 900	5.2450	4.9103	2.14	0.25	2.17
Model $\rm III_S$ (3)	9.88	15.11	15.00	7.12	29 900	5.2387	4.9044	2.14	0.30	1.84
Model $\rm III_S$ (4)	9.86	15.11	15.00	7.12	29 900	5.2331	4.8992	2.13	0.35	1.54
Model $\rm III_S$ (5)	9.85	15.11	15.00	7.12	29 900	5.2281	4.8945	2.14	0.40	1.26
Model $\rm IV_P$ (1)	4.98	20.69	20.41	7.98	33 071	6.9772	6.5606	7.90	0.20	0
Model $\rm IV_P$ (2)	5.09	20.66	20.37	8.01	33 090	6.8012	6.3895	8.12	0.25	0
Model $\rm IV_P$ (3)	5.20	20.63	20.33	8.04	33 110	6.6310	6.2241	8.34	0.30	0
Model $\rm IV_P$ (4)	5.31	20.60	20.29	8.08	33 130	6.4662	6.0641	8.56	0.35	0
Model $\rm IV_P$ (5)	5.42	20.57	20.26	8.11	33 151	6.3054	5.9082	8.79	0.40	0
Model $\rm IV_S$ (1)	7.39	15.53	15.45	6.87	29 554	6.8463	6.4640	1.52	0.20	0
Model $\rm IV_S$ (2)	7.61	15.52	15.43	6.92	29 566	6.6354	6.2556	1.59	0.25	0
Model $\rm IV_S$ (3)	7.84	15.50	15.42	6.98	29 580	6.4322	6.0550	1.65	0.30	0
Model $\rm IV_S$ (4)	8.06	15.49	15.40	7.03	29 594	6.2343	5.8599	1.72	0.35	0
Model $\rm IV_S$ (5)	8.29	15.47	15.37	7.09	29 608	6.0421	5.6706	1.80	0.40	0
Model $\rm V_S$ (1)	6.98	15.35	15.28	6.56	29 687	7.3970	7.0319	1.34	0.20	0
Model $\rm V_S$ (2)	7.20	15.33	15.26	6.60	29 700	7.1912	6.8282	1.39	0.25	0
Model $\rm V_S$ (3)	7.42	15.32	15.24	6.66	29 714	6.9904	6.6295	1.44	0.30	0
Model $\rm V_S$ (4)	7.65	15.30	15.22	6.70	29 728	6.7955	6.4370	1.50	0.35	0
Model $\rm V_S$ (5)	7.88	15.28	15.20	6.75	29 744	6.6039	6.2478	1.56	0.40	0

Notes. Columns 1 and 2 give the name of the model and its current age. Column 3 lists the initial mass of the corresponding evolutionary sequence. Columns 4, 5, and 6 give the current mass, radius, and effective temperature of the model. Columns 7 and 8 yield the k_2 respectively before and after applying the empirical correction for the effect of rotation of Claret (1999, Equation (3.51)) of the model. Column 9 lists the mass-loss rate of the model. Columns 10 and 11 give the overshooting parameter and turbulent diffusion coefficient of the model. Models with subscript P (respectively S) correspond to the models of the primary (respectively secondary) star. Models IV and V have D_T fixed to $0\,{\rm cm^2\,s^{-1}}$ while models I, II, and III allow it to vary freely.

As discussed in Rauw et al. (2016), the presence of only one eclipse in the light curves of HD 152218 leads to degeneracies in the determination of the stellar radii, the ratio of effective temperatures, and the inclination of the system. Rauw et al. (2016) derived a ratio of 1.18 ± 0.20 between the primary and secondary radii based on their ratio of bolometric luminosities and effective temperatures. Assuming that the radius of the primary star is well constrained, this relation translates into a secondary radius of $7.12\,R_\odot$. Thus, we built a series of five models for the secondary star assuming a constraint on the stellar radius of 7.12 rather than $7.80\,R_\odot$. These best-fit models (Models $\rm III_S$ (1) to (5)), which reproduce well the stellar properties, are reported in Table 3.8. Compared to Models $\rm II_S$, the age

estimate is lower and closer to that of the primary star models, and the ensuing apsidal motion rate ranges from $1.62^\circ\,\mathrm{yr}^{-1}$ to $1.63^\circ\,\mathrm{yr}^{-1}$.

We then built a `Clés` evolutionary sequence for the secondary star, starting with an initial mass of $15.17\,M_\odot$ and having $\alpha_{\rm ov} = 0.20$ and no turbulent diffusion. We stopped the sequence at the age of the best-fit models of the primary star (Models $\mathrm{II_P}$ (1)) and obtained a model of mass $15.11\,M_\odot$, radius $6.39\,R_\odot$, effective temperature 29 674 K, and $k_{2,2} = 7.68 \times 10^{-3}$. Combined with Model $\mathrm{II_P}$ (1) for the primary star, we obtained an apsidal motion rate of $1.60^\circ\,\mathrm{yr}^{-1}$. This value is slightly lower than the observational value but agrees with the previously obtained value.

Finally, in a last attempt to reproduce the apsidal motion rate of the system, we built models for the two stars assuming $D_T = 0\,\mathrm{cm}^2\,\mathrm{s}^{-1}$ (Models $\mathrm{IV_P}$ for the primary star, Models $\mathrm{IV_S}$ and $\mathrm{V_S}$ for the secondary star, when the constraint on the radius is 7.80 and $7.12\,R_\odot$, respectively). The stellar properties are still well reproduced within the error bars, and the apsidal motion rate (neglecting the age difference between the primary and secondary models) amounts to $1.81^\circ\,\mathrm{yr}^{-1}$ to $1.84^\circ\,\mathrm{yr}^{-1}$ and $1.72^\circ\,\mathrm{yr}^{-1}$ to $1.75^\circ\,\mathrm{yr}^{-1}$, respectively, when Models $\mathrm{IV_S}$ and $\mathrm{V_S}$ are considered. These values are compatible within the error bars with the observational value. Initial masses of 20.6 ± 1.5 and $15.5 \pm 1.1\,M_\odot$ are derived for the primary and secondary stars, respectively, and the binary's age is estimated at 5.2 ± 0.8 Myr as derived from the primary models. This age is in agreement with the age of the NGC 6231 cluster.

Chapter 4

A Door Opened to Future Prospects

"The most important thing is not to stop questioning. Curiosity has its own reason for existing."

(Albert Einstein)

The analysis of the apsidal motion in massive eccentric binary systems is a powerful tool to infer accurate stellar parameters on the observational side, and on the theoretical side, to constrain the internal mixing processes occurring inside the stars and the age of the binary systems. The present project investigated in details this specific topic in stellar astrophysics addressing key questions regarding massive stars (Section 4.1). As always in Science, at the end there is no end, and plethora of questions arose from this project (Section 4.2). How fantastic it will be to address those questions in the near future, and tons of other questions still open in other related astrophysics domains, as it will be another small stride on the long way towards the understanding of the Universe as a whole (Section 4.3).

Contents

4.1. A tiny little stone...

The purpose of this thesis project has been to study, from both the observational and theoretical points of view, the apsidal motion in short-period eccentric massive binaries. First, we better constrained the absolute parameters of the stars and of the binary orbits. Second, we built stellar evolution models reproducing the inferred properties to constrain the internal mixing processes occurring inside the stars as well as the stellar ages. We focused on four binaries belonging to the young open cluster NGC 6231, namely HD 152248, HD 152219, CPD-41° 7742, and HD 152218. Studying several binary systems belonging to the same cluster was deliberate as we could infer an age estimate for the cluster based on its massive binaries and confront it to the age estimates based on its less massive components.

We made use of the diversity of observational data – spectroscopy, radial velocities, and photometry – available for the binary systems under consideration. The spectroscopic observations allowed us to infer stellar properties such as the effective temperature and luminosity as well as the stellar wind properties such as the mass-loss rate. The large time span covered by the radial velocities, both our re-derived values based on the disentangling of the spectroscopic observations and those coming from the literature, allowed us to infer values for the longitude of periastron at a reference epoch, the orbital eccentricity, the orbital period and, most importantly in the present context, the rate of apsidal motion for each system. Moreover, the amplitudes of the radial velocity curves determined allowed us to infer values for the minimum masses of the stars. On the one hand, the photometric observations allowed us to constrain the orbital inclination and the Roche lobe filling factors of the two stars, and, sometimes also, the secondary effective temperature and the orbital eccentricity. From these values, we inferred values for the absolute masses and radii of the stars. On the other hand, the longitudes of periastron derived at the times of the photometric observations allowed us to at least make a consistency check of the apsidal motion rate derived from the radial velocities. In the case of HD 152248, we even went one step further as we combined the radial velocity and photometric data to determine the apsidal motion rate. In the case of CPD-41° 7742, the times of minima of the eclipses were used to infer an estimate for the apsidal motion rate of the system and thence to lift the severe degeneracy in best-fit solutions obtained from the adjustment of the radial velocity curves of this low-eccentricity system. In the case of HD 152248, we further used its twin property to observationally constrain the internal structure constants of the stars. Indeed, the apsidal motion rate is proportional to the internal structure constants of the stars, that are themselves a function of the mass distribution inside the stars or, in other words, the density contrast between the core and the external layers of the stars. In the cases of HD 152219 and CPD-41° 7742, we computed a weighted-average mean of the internal structure constants of the stars.

We built stellar evolution models using the `Clés` code for all binary systems. We made use of the `min-Clés` routine to search for best-fit models of the stars in terms of absolute parameters – mass, radius, and position in the Hertzsprung-Russell diagram – and apsidal motion rate. We included in the models mass-loss as well as internal mixing processes through both the overshooting and the turbulent diffusion. We showed that to reproduce the absolute parameters of the stars, more specifically both stars of HD 152248 and

HD 152219, and the primary stars of CPD-41° 7742 and HD 152218, a certain amount of turbulent diffusion was always necessary, whatever the value of the overshooting parameter. We further highlighted a correlation for the best-fit models between the overshooting parameter, the turbulent diffusion coefficient, and the mass-loss rate scaling factor. In the cases of HD 152248 and HD 152219, these best-fit models, however, predicted too high a value for the internal structure constants of the stars, that is to say, the models had too low a density contrast between the core and the external layers compared to what was expected from observations. This issue was (almost) solved by adding extra turbulent diffusion inside the models. Indeed, in the case of HD 152248, this enhanced mixing was sufficient and best-fit models in terms of mass, radius, position in the Hertzsprung-Russell diagram, and internal structure constant of the stars were obtained. In the case of HD 152219, we showed that this enhanced mixing was necessary to better reproduce the internal structure constant of the primary star, but at the cost that its effective temperature was not accurately reproduced anymore.

The origin of this enhanced turbulent diffusion is not completely understood. Indeed, in the case of HD 152248, we went one step further and built stellar evolution models for the stars with the `GENEC` code. The `GENEC` code includes both the effect of stellar rotation and binarity. Whilst the inclusion of binarity only slightly – but not significantly – modifies the age at which the star reaches a given state characterised by a given radius and internal structure constant, the inclusion of rotation has much more impact on the results. Indeed, rotation induces mixing inside the stars, and we reached the conclusion that the enhanced turbulent diffusion necessary in the `Clés` models might simply be due to the stellar rotation; however, this statement requires further investigations.

We conclude that the study of apsidal motion in massive eccentric binary systems is a powerful means to infer accurate stellar parameters on the observational side, and on the theoretical side, to constrain the internal mixing processes occurring inside the stars and the age of the binary systems.

4.2. ...and much more left...

The study of the apsidal motion in massive eccentric binaries is a long-term task, especially since it is rather difficult to render the procedure automatic as each binary system has its own characteristics, specificities, and proper set of observations. Notwithstanding, such analyses are worth the effort given the invaluable information they provide on massive stars. Therefore, increasing the number of systems analysed this way is of high interest. We already highlighted some promising binary systems we list here (non-exhaustive!): HD 165052, AR Cas, V436 Per, HD 163181, HD 193443, HD 206267 Aa, BD+60° 497, and HD 93205. We already started the analysis of the massive eccentric binary HD 165052 that undergoes apsidal motion at a high rate of about $12^\circ\ \mathrm{yr}^{-1}$ (Ferrero et al. 2013, Rosu et al. in preparation).

In the study of HD 152248, we suggested that the enhanced mixing introduced in the `Clés` models to reproduce the internal structure constants of the stars might be the signature of the stellar rotation (see Section 3.3.4). However, this assertion requires further

confirmation (or infirmation), especially since the comparison between `Clés` models with turbulent diffusion and `GENEC` models with rotation is not fully coherent. We here suggest to build grids of stellar evolution models including rotation such as the `GENEC` ones and confront these to models computed with the same code with turbulent diffusion but without any rotation. The procedure would be to compare models having the same mass, radius, position in the Hertzsprung-Russell diagram, and internal structure constant. For a given amount of rotational mixing, we would therefore highlight the amount of turbulent diffusion necessary to reproduce the aforementioned stellar properties. It would also be interesting to see wether other properties such as the surface abundances are affected the same way by the turbulent diffusion and the rotational mixing.

In line with that, confronting the results obtained with different stellar evolution codes in terms of internal mixing processes would be enriching. Indeed, each code has its own characteristics and assumptions, and the whole theoretical stellar astrophysics community would benefit from a broad comparison of stellar evolution models computed with different codes. Such a comparison would also allow us to confirm with more certainty the results obtained in the present work. In addition, it would be interesting to compare the results with models including other instabilities such as the magneto rotational instabilities (i.e. fluid instabilities that cause an accretion disk orbiting a massive central object to become turbulent) and/or the Taylor-Spruit dynamo.

Renzini (1987) pointed out that the mixing length theory treatment of overshooting is not likely to provide a reliable estimate of the actual size of stellar mixed core. Indeed, as the convective elements overshoot by a very small fraction of their size, treating them as point-like particles is unphysical, especially since the resolving power of the theory is of the order of one mixing length (Renzini 1987). Three-dimensional hydrodynamic simulations would suit best to this aim, but these are very CPU-time demanding (Cristini et al. 2019).

In our `Clés` models, we adopted a constant diffusion coefficient D_T throughout the star. It would be interesting to test different prescriptions, that is to say, to adopt different values of the exponent $n = 0$ in Equation (3.50). We performed a preliminary test for a few models: This is illustrated in Figure 4.1 where the ratio between the central density ρ_c and the mean density inside the star $<\rho>$ as well as the central hydrogen mass fraction X_c are plotted as a function of the stellar age for different models of initial mass of $19.0\,M_\odot$ having $\alpha_{\rm ov} = 0.20$ and different turbulent diffusion prescriptions. On the one hand, the curves with $D_T = 3.05 \times 10^6\,{\rm cm^2\,s^{-1}}$ and $n = 1$ or $n = 2$ and the curve with $D_T = 0\,{\rm cm^2\,s^{-1}}$ overlap perfectly because, starting from the stellar surface, the turbulent diffusion coefficient decreases so rapidly as a function of the density that it looks like there is no diffusion at all. On the other hand, adopting a value for n between 0 and 1 modifies the chemical composition profile in the partial mixing zone. This does not drastically affects the mass concentration but nevertheless allows us to replace the instantaneous mixing of the overshooting by a kind of diffusive overshooting with partial mixing.

Still regarding stellar evolution codes, another interesting avenue would be to account for the complete complex binary interactions when building the models. As specified in Section 3.2.2, the `GENEC` code only accounts for the mixing induced by tidal interactions,

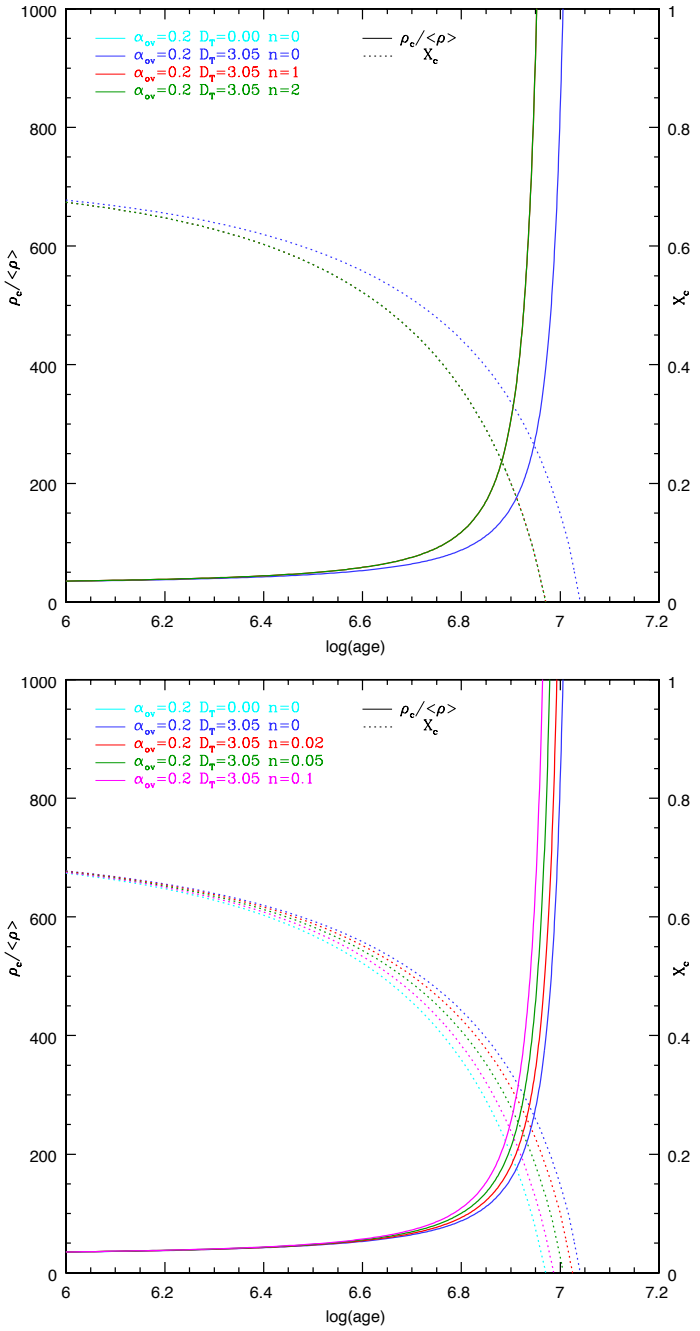

Figure 4.1. Evolution as a function of the stellar age of the ratio between the central density ρ_c and the mean density inside the star $<\rho>$ (solid lines) as well as the central hydrogen mass fraction X_c (dashed lines) for different models of initial mass of $19.0\,M_\odot$ having $\alpha_{\rm ov} = 0.20$ and different turbulent diffusion prescriptions.

but does not account for the temporal modulation of these effects due to the eccentricity. Hence, accounting for this modulation would certainly have an influence on the resulting models. In the `Clés` models, neither the rotational mixing nor the binary interactions are accounted for, and there is still some work to do in this avenue. Actually, a PhD student, Loïc Fellay, working in the ASTA team at the STAR Institute, is currently developing a code in `Clés` to compute fully three-dimensional static models of the internal structure of close massive binaries, taking into account the effects of the rotation and tidal forces. By coupling these structures to atmosphere models, taking into account the effects of radiative pressure on both components, models of binary light curves of unprecedented accuracy, providing a robust modelling of the gravity darkening and the orbital motions, will be provided. The modification of the gravitational potential due to the tidal deformations will be taken into account in a more rigorous way than through the Clairaut-Radau equation and the internal structure constant. These models will therefore allow us to predict a theoretical rate of apsidal motion closer to the reality. In the meantime, this code will also compute the adiabatic oscillations of the three-dimensional deformed models of close binaries. These models will help us to better understand the properties of the oscillation modes excited in close binary systems, recently discovered in the very young field of tidal asteroseismology (see e.g. Fuller et al. 2020; Handler et al. 2022).

Finally, a striking result appeared when we searched for best-fit `Clés` models in terms of mass, radius, position in the Hertzsrpung-Russell diagram, and internal structure constant. Indeed, in the Hertzsprung-Russell diagram, models having the same k_2 with all parameters identical except one (such as the initial mass or the turbulent diffusion coefficient) are lying on the same straight line. This is illustrated in Figure 4.2. These preliminary results suggest there might be empirical laws of the form

$$\begin{cases} \log_{10}(L/L_\odot) = C_1(D_T)\log_{10}(T_{\rm eff}) + C_2(D_T) & \forall M_{\rm init}, \\ \log_{10}(L/L_\odot) = D_1(M_{\rm init})\log_{10}(T_{\rm eff}) + D_2(M_{\rm init}) & \forall D_T, \end{cases} \tag{4.1}$$

where the C_j and D_j ($j = 1, 2$) are linear functions of the turbulent diffusion coefficient and the initial mass, respectively:

$$\begin{cases} C_j(D_T) = A_j D_T + B_j, \\ D_j(M_{\rm init}) = E_j M_{\rm init} + F_j, \end{cases} \tag{4.2}$$

where A_j, B_j, E_j, and F_j are real numbers having different values for different k_2 values. If we go one step further and build such empirical relations for a grid of k_2 values, we can find a linear relationship between the A_j, B_j, E_j, F_j, and k_2. We observe the same trend regarding the overshooting parameter. This result is interesting since k_2 is normally integrated throughout the star based on the density stratification, that is to say, the mass and radius of each stellar layer of infinitesimal thickness. These empirical relationships we found only depend upon global properties of the stars such as their effective temperature and luminosity. These results are preliminary and need further investigations to understand the physics behind these empirical relations. Especially, these results will need to be corroborated by other stellar evolutionary codes.

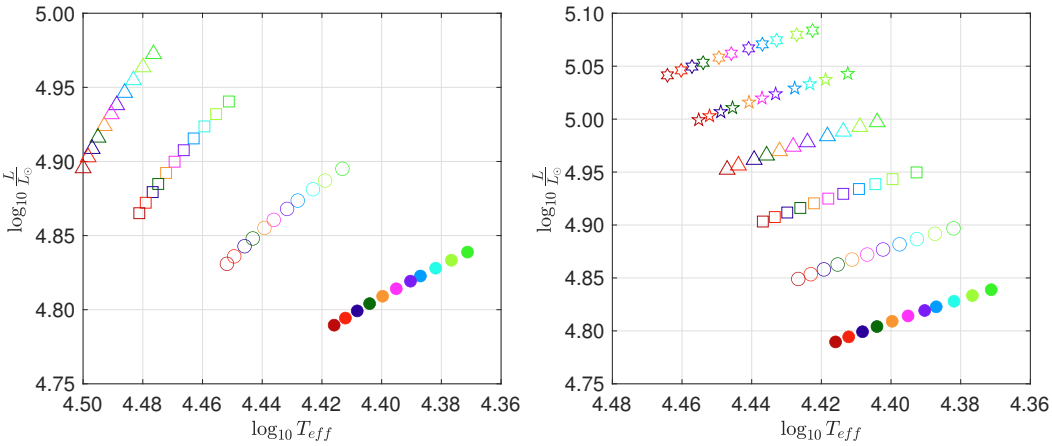

Figure 4.2. Hertzsprung-Russell diagrams. *Left panel:* Models of initial mass of $17.0\,M_\odot$. Models with $D_T = 0, 2 \times 10^6, 6 \times 10^6$, and $10 \times 10^6\,\mathrm{cm^2\,s^{-1}}$ are shown with filled symbols, open circles, open squares, and open triangles, respectively. The models have a k_2 ranging from 0.0010 to 0.0020 with a step of 0.0001 (from green to red). *Right panel:* Models having $D_T = 0\,\mathrm{cm^2\,s^{-1}}$. Models with initial mass $M_{\rm init} = 17, 18, 19, 20, 21$, and $22\,M_\odot$ are shown with filled symbols, open circles, open squares, open triangles, open five-branch stars, and open six-branch stars, respectively. The models have a k_2 ranging from 0.0010 to 0.0020 with a step of 0.0001 (from green to red).

4.3. ...towards the understanding of the Universe

The research carried out in the present thesis project, as well as all research projects carried out in stellar astrophysics and in astronomy in general by the whole scientific community, are just so many roads towards the comprehension of the processes occurring in stars and of the dynamics of clusters and galaxies. Thanks to the investment in research of each and every astronomer, we can better understand, day after day, the Universe in which we are born, we live, and finally die, just as the stars, clusters, and galaxies do, until, hopefully one day, our Universe will not have for us any secrets and mysteries anymore.

Appendix A

List of Publications

"Research is formalised curiosity. It is poking and prying with a purpose."

(Zora Neale Hurtson)

This Appendix summarises my list of publications related to this thesis project, in ascending chronological order in each section.

A.1. Articles in peer reviewed academic journals

1. **S. Rosu**, G. Rauw, K. E. Conroy, E. Gosset, J. Manfroid, & P. Royer, Apsidal motion in the massive binary HD 152248, A&A, 635, A145 (2020)

2. **S. Rosu**, A. Noels, M.-A. Dupret, G. Rauw, M. Farnir, & S. Ekström, Apsidal motion in the massive binary HD 152248 – Constraining the internal structure of the stars, A&A, 642, A221 (2020)

3. **S. Rosu**, What apsidal motion reveals about the interior of massive binary stars, Bulletin de la Société Royale des Sciences de Liège, 90, 1 (2021)

4. **S. Rosu**, G. Rauw, M. Farnir, M.-A. Dupret, & A. Noels, Apsidal motion in massive eccentric binaries in NGC 6231 – The case of HD 152219, A&A, 660, A120 (2022)

5. **S. Rosu**, Apsidal motion in massive eccentric binaries in NGC 6231, Belgian Journal of Physics, 1, 3 (April 2022)

6. **S. Rosu**, G. Rauw, Y. Nazé, E. Gosset, & C. Sterken, Apsidal motion in massive eccentric binaries: The case of CPD-41° 7742, and HD 152218 revisited, A&A, in press [arXiv:2205.11207]

7. **S. Rosu**, et al., Apsidal motion in the massive eccentric binary HD 165052, A&A, in preparation

A.2. Scientific congresses and symposia

Published communications with peer reviewing

1. **S. Rosu**, G. Rauw, E. Gosset, J. Manfroid, & P. Royer, Apsidal motion in the massive binary HD 152248, Contributions of the Astronomical Observatory Skalnaté Pleso, 50(2), 624-626 (2020)

2. **S. Rosu**, G. Rauw, M.-A. Dupret, A. Noels, & M. Farnir, Apsidal motion in NGC 6231: sounding the internal structure of massive binary stars, Proceedings IAU Symposium 361, submitted (2022)

3. **S. Rosu**, G. Rauw, Y. Nazé, E. Gosset, & C. Sterken, Apsidal Motion in Massive Binaries: CPD-41° 7742, an Extreme Case?, Proceedings IAU Symposium 361, submitted (2022)

Oral communications and posters

1. **S. Rosu**, G. Rauw, E. Gosset, J. Manfroid, & P. Royer, Apsidal Motion in The Massive Binary HD 152248, Poster session presented at the conference *Universe of Binaries, Binaries in the Universe*, Telc, Czech Republic (07–11 September 2019)

2. **S. Rosu**, Apsidal motion in NGC 6231: sounding the internal structure of massive binary stars, Oral communication at the *IAU Symposium 361: Massive Stars Near & Far*, Dublin, Ireland (07 May 2021)

3. **S. Rosu**, Apsidal motion in massive eccentric binaries in NGC 6231, Oral communication at the *General Scientific Meeting 2021 of the Belgian Physical Society*, Hasselt, Belgium (02 December 2021)

4. **S. Rosu**, G. Rauw, Y. Nazé, E. Gosset, & C. Sterken, Apsidal Motion in Massive Binaries: CPD-41° 7742, an Extreme Case?, Poster session presented at the *IAU Symposium 361: Massive Stars Near & Far*, Dublin, Ireland (08–13 May 2022)

A.3. Scientific conferences in Universities or research centres

S. Rosu, Apsidal Motion in Massive Eccentric Binary Stars in NGC 6231, Oral communication at the Stellar Group Meetings Geneva, Switzerland (18 November 2021)

Bibliography

Abbott, B. P., Abbott, R., Abbott, T. D., et al. 2016, Observation of Gravitational Waves from a Binary Black Hole Merger, Phys. Rev. Letters, **116**, 061102

Adelberger, E. G., García, A., Robertson, R. G. H., et al. 2011, Solar fusion cross sections. II. The pp chain and CNO cycles, Reviews of Modern Physics, **83**, 195

Albrecht, S., Reffert, S., Snellen, I., Quirrenbach, A., & Mitchell, D. S. 2007, The spin axes orbital alignment of both stars within the eclipsing binary system V1143 Cyg using the Rossiter-McLaughlin effect, A&A, **474**, 565

Andrae, R. 2010, Error estimation in astronomy: A guide, ArXiv e-prints [arXiv:1009.2755]

Andrae, R., Schulze-Hartung, T., & Melchior, P. 2010, Dos and don'ts of reduced chi-squared, ArXiv e-prints [arXiv:1012.3754]

Asplund, M., Grevesse, N., Sauval, A. J., & Scott, P. 2009, The Chemical Composition of the Sun, ARA&A, **47**, 481

Bailer-Jones, C. A. L., Rybizki, J., Fouesneau, M., Demleitner, G., & Andrae, R. 2021, Estimating Distances from Parallaxes. V. Geometric and Photogeometric Distances to 1.47 Billion Stars in Gaia Early Data Release 3, AJ, **161**, 147

Bailer-Jones, C. A. L., Rybizki, J., Fouesneau, M., Mantelet, G., & Andrae, R. 2018, Estimating Distance from Parallaxes. IV. Distances to 1.33 Billion Stars in Gaia Data Release 2, AJ, **156**, 58

Baroch, D., Giménez, A., Ribas, I., et al. 2021, Analysis of apsidal motion in eclipsing binaries using TESS data. I. A test of gravitational theories, A&A, **649**, 64

Bate, M. R., Bonnell, I. A., & Bromm, V. 2002, The formation of close binary systems by dynamical interactions and orbital decay, MNRAS, **336**, 705

Baume, G., Vázquez, R. A., & Feinstein, A. 1999, UBVI imaging photometry of NGC 6231, A&AS, **137**, 233

Borkovits, T., Forgács-Dajka, E., & Rappaport, S. A. 2019, Third-body perturbed apsidal motion in eclipsing binaries, in *Astro Fluid 2016*, eds. A. S. Brun, S. Mathis, C. Charbonnel, & B. Dubrulle, EAS Publications Series, **82**, 99

Borkovits, T., Forgács-Dajka, E., & Regály, Zs. 2005, The combined effect of the perturbations of a third star and the tidally forced apsidal motion on the O–C curve of eccentric binaries, in *Tidal Evolution and Oscillations in Binary Stars*, eds. A. Claret, A. Giménez, & J.-P. Zahn, ASP Conf. Ser., **333**, 128

Borkovits, T., Rappaport, S., Hajdu, T., & Sztakovics, J. 2015, Eclipse timing variation analyses of eccentric binaries with close tertiaries in the Kepler field, MNRAS, **448**, 946

Bouret, J.-C., Lanz, T., & Hillier, D. J. 2005, Lower mass loss rates in O-type stars: Spectral signatures of dense clumps in the wind of two Galactic O4 stars, A&A, **438**, 301

Bouzid, M. Y., Sterken, C., & Pribulla, T. 2005, Photometric study of the eclipsing binary V 1034 Sco, A&A, **437**, 769

Bozkurt, Z., & Değirmenci, Ö. L. 2007, Triple systems showing apsidal motion, MNRAS, **379**, 370

Bresolin, F., Crowther, P. A., & Puls, J. 2008, Massive Stars as Cosmic Engines, Proc. IAU Symposium, 250

Brott, I., de Mink, S. E., Cantiello, M., et al. 2011, Rotating massive main-sequence stars. I. Grids of evolutionary models and isochrones, A&A, **530**, A115

Brownlee, R. R., & Cox, A. N. 1953, Photoelectric Magnitudes and Colors in NGC 6231, ApJ, **118**, 165

Bulut, I., & Demircan, O. 2007, A New Catalogue of Eclipsing Binary Stars with Eccentric Orbits, MNRAS, **378**, 179

Cantiello, M., Lecoanet, D., Jermyn, A. S., & Grassitelli, L. 2021, On the Origin of Stochastic, Low-Frequency Photometric Variability in Massive Stars, ApJ, **915**, 112

Cassisi, S., Salaris, M., & Irwin, A. W. 2003, The Initial Helium Content of Galactic Globular Cluster Stars from the R-Parameter: Comparison with the Cosmic Microwave Background Constraint, ApJ, **588**, 862

Castelli, F., & Kurucz, R. L. 2004, Modelling of Stellar Atmospheres, IAU Symp., 210, eds. N. Piskunov, W. W. Weiss, & D. F. Gray, ASP, A20

Cazorla, C., Morel, T., Nazé, Y., Rauw, G., Semaan, T., Daflon, S., & Oey, M. S. 2017, Chemical abundances of fast-rotating massive stars - I. Description of the methods and individual results, A&A, **603**, A56

Claret, A. 1995, Stellar models for a wide range of initial chemical compositions until helium burning. I. From $X = 0.60$ to $X = 0.80$ for $Z = 0.02$, A&AS, **109**, 441

Claret, A. 1999, Studies on stellar rotation. I. The theoretical apsidal motion for evolved rotating stars, A&A, **350**, 56

Claret, A. 2000, A new non-linear limb-darkening law for LTE stellar atmosphere models. Calculations for -5.0 $\leq$ log[M/H] $\leq$ +1, 2000 K $\leq$ $T_{\rm eff}$ $\leq$ 50000 K at several surface gravities, A&A, **363**, 1081

Claret, A. 2004, New grids of stellar models including tidal-evolution constants up to carbon burning. I. From 0.8 to 125 $M_{\odot}$ at $Z = 0.02$, A&A, **424**, 919

Claret, A. 2007, Does convective core overshooting depend on stellar mass? Tests using double-lined eclipsing binaries, A&A, **475**, 1019

Claret, A. 2019, Updating the theoretical tidal evolution constants: Apsidal motion and the moment of inertia, A&A, **628**, A29

Claret, A., & Giménez, A. 1992, Evolutionary stellar models using Rogers & Iglesias opacities, with particular attention to internal structure constants, A&AS, **96**, 255

Claret, A., & Giménez, A. 1993, The apsidal motion test of the internal stellar structure: comparison between theory and observations, A&A, **277**, 487

Claret, A., & Giménez, A. 2010, The apsidal motion test of stellar structure and evolution: an update, A&A, **519**, A57

Claret, A., & Torres, G. 2016, The dependence of convective core overshooting on stellar mass, A&A, **592**, A15

Claret, A., & Torres, G. 2019, The Dependence of Convective Core Overshooting on Stellar Mass: Reality Check and Additional Evidence, ApJ, **876**, 134

Conti, P. S., & Alschuler, W. R. 1971, Spectroscopic studies of O-type stars. I. Classification and absolute magnitudes, ApJ, **170**, 325

Conti, P. S., & Ebbets D. 1977, Spectroscopic studies of O-type stars. VII. Rotational velocities $V \sin i$ and evidence for macroturbulent motions, ApJ, **213**, 438

Conti, P. S., Leep, E. M., & Lorre, J. J. 1977, Spectroscopic studies of O-type stars. VIII. Radial velocities and the K-term, ApJ, **214**, 759

Cox, J. P., & Giuli, R. T. 1968, Principles of stellar structure

Cristini, A., Hirschi, R., Meakin, C., Arnett, D., Georgy, C., & Walkington, I. 2019, Dependence of convective boundary mixing on boundary properties and turbulence strength, MNRAS, **484**, 4645

de Mink, S. E., Cantiello, M., Langer, N., et al. 2009, Rotational mixing in massive binaries – Detached short-period systems, A&A, **497**, 243

Donati, J.-F. 2003, ESPaDOnS: An Echelle SpectroPolarimetric Device for the Observation of Stars at CFHT, ASP Conference Series, **307**, 41

Duchêne, G., & Kraus, A. 2013, Stellar multiplicity, ARA&A, **51**, 269

Eggenberger, P., Meynet, G., Maeder, A., et al. 2008, The Geneva stellar evolution code, Ap&SS, **316**, 43

Ekström, S., Georgy, C., Eggenberger, P., et al. 2012, Grids of stellar models with rotation. I. Models from 0.8 to 120 $M_\odot$ at solar metallicity (Z=0.014), A&A, **537**, A146

Eversberg, T., Lepine, S., & Moffat, A. F. J. 1998, Outmoving Clumps in the Wind of the Hot O Supergiant zeta Puppis, ApJ, **494**, 799

Ferguson, J. W., Alexander, D. R., Allard, F., et al. 2005, Low-Temperature Opacities, ApJ, **623**, 585

Ferrero, G., Gamen, R., Benvenuto, O., & Fernández-Lajús, E. 2013, Apsidal motion in massive close binary systems – I. HD 165052, an extreme case?, MNRAS, **433**, 1300

Fitzpatrick, R. 2016, Introduction to Celestial Mechanics: `https://farside.ph.utexas.edu/teaching/celestial/Celestial/node140.html`

Foreman-Mackey, D. 2016, corner.py: Scatterplot matrices in Python, The Journal of Open Source Software, **1**, 24

Foreman-Mackey, D., Hogg, D. W., Lang, D., & Goodman, J. 2013, emcee: The MCMC Hammer, PASP, **125**, 306

Fuller, J., Kurtz, D. W., Handler, G., & Rappaport, S. A. 2020, Tidally trapped pulsations in binary stars, MNRAS, **498**, 5730

Gaia Collaboration, Brown, A. G. A, Vallenari, A., Prusti, T., et al. 2018, Gaia Data Release 2. Summary of the contents and survey properties, A&A, **616**, A1

Gaia Collaboration, Brown, A. G. A, Vallenari, A., Prusti, T., et al. 2021, Gaia Early Data Release 3. Acceleration of the Solar System from Gaia astrometry, A&A, **649**, A1

García, B., & Mermilliod, J.-C. 2001, High-mass binaries in the very young open cluster NGC 6231 – Implication for cluster and star formation, A&A, **368**, 122

Giménez, A. 2006, Equations for the analysis of the Rossiter-McLaughlin effect in extrasolar planetary transits, AJ, **650**, 408

Giménez, A., & Bastero, M. 1995, A Revision of the Ephemeris-Curve Equations for Eclipsing Binaries with Apsidal Motion, Ap&SS, **226**, 99

Giménez, A., & Garcia-Pelayo, J. M. 1983, A new method for the analysis of apsidal motions in eclipsing binaries, Ap&SS, **92**, 203

González, J. F., & Levato, H. 2006, Separation of composite spectra: the spectroscopic detection of an eclipsing binary star, A&A, **448**, 283

Gray, D. F. 2005, The Observation and Analysis of Stellar Photospheres, 3rd Edition, ISBN 0521851866, Cambridge University Press

Gray, D. F. 2008, The Observation and Analysis of Stellar Photospheres, 3rd edn. Cambridge: Cambridge University Press

Gray, R. O. 2009, A Digital Spectral Classification Atlas (`https://ned.ipac.caltech.edu/level5/Gray/frames.html`)

Handler, G., Jayaraman, R., Kurtz, D. W., Fuller, J., & Rappaport, S. A. 2022, Tidally Tilted Pulsators, Proceedings of the 40th meeting of the Polish Astronomical Society, [arXiv:2201.01722]

Hejlesen, P. M. 1987, Studies in stellar evolution. III - The internal structure constants, A&AS, **69**, 251

Hendry, P. D., & Mochnacki, S. W. 1992, The GDDSYN Light Curve Synthesis Method, ApJ, **388**, 603

Herrero, A., Kudritzki, R. P., Vilchez, J. M., et al. 1992, Intrinsic parameters of galactic luminous OB stars, A&A, **261**, 209

Hill, G., Crawford, D. L., & Barnes, J. V. 1974, Some new spectroscopic binary orbits in NGC 6231 and Sco OB1, AJ, **79**, 1271

Hillier, D. J. 1991, The effects of electron scattering and wind clumping for early emission line stars, A&A, **247**, 455

Hillier, D. J., & Miller, D. L. 1998, The Treatment of Non-LTE Line Blanketing in Spherically Expanding Outflows, ApJ, **496**, 407

Hinkle, K., Wallace, L., Valenti, J., & Harmer, D. 2000, Visible and Near Infrared Atlas of the Arcturus Spectrum 3727–9300 Å (San Francisco: ASP)

Hinton, S. R. 2016, ChainConsumer, The Journal of Open Source Software, **1**, 45

Hog, E., Fabricius, C., Makarov, V. V., et al. 2000, The Tycho-2 Catalogue of the 2.5 million brightest stars, A&A, **355**, L27

Hosokawa, Y. 1953, On the Rotation Effect of Velocity Curves in Eclipsing Binary Systems, PASJ, **5**, 88

Howarth, I. D., Siebert, K. W., Hussain, G. A. J., & Prinja, R. K. 1997, Cross-correlation characteristics of OB stars from *IUE* spectroscopy, MNRAS, **284**, 265

Humphreys, R. M., & McElroy, D. B. 1984, The initial mass function for massive stars in the galaxy and the magellanic clouds, AJ, **284**, 565

Iglesias, C. A., & Rogers, F. J. 1996, Updated Opal Opacities, AJ, **464**, 943

Jenkins, J. M., Caldwell, D. A., Chandrasekaran, H., et al. 2010, Overview of the Kepler Science Processing Pipeline, ApJ, **713**, L87

Jenkins, J. M., Twicken, J. D., McCauliff, S., et al. 2016, The TESS science processing operations center, Proceedings of the SPIE, **9913**, 99133E

Jones, D., Conroy, K. E., Horvat, M., et al. 2020, Physics of Eclipsing Binaries. IV. The Impact of Interstellar Extinction on the Light Curves of Eclipsing Binaries, ApJS, **247**, 63

Kaufer, A., Stahl, O., Tubbesing, S., et al. 1999, Commissioning FEROS, the New High-resolution Spectrograph at La Silla, The Messenger, **85**, 8

Kilian, J., Montenbruck, O., & Nissen, P. E. 1994, The galactic distribution of chemical elements as derived from B-stars in open clusters I. NGC 6231: stellar parameters and chemical abundances, A&A, **284**, 437

Kochanek, C. S., Shappee, B. J., Stanek, K. Z., Holoien, T. W.-S., Thompson, T. A., et al. 2017, The All-Sky Automated Survey for Supernovae (ASAS-SN) Light Curve Server v1.0, PASP, **129**, 104502

Kruckow, M. U., Tauris, T. M., Langer, N., et al. 2016, Common-envelope ejection in massive binary stars – Implications for the progenitors of GW150914 and GW151226, A&A, **596**, A58

Kuhn, M. A., Getman, K. V., Feigelson, E. D., et al. 2017a, The Structure of the Young Star Cluster NGC 6231. II. Structure, Formation, and Fate, AJ, **154**, 214

Kuhn, M. A., Medina, N., Getman, K. V., et al. 2017b, The Structure of the Young Star Cluster NGC 6231. I. Stellar Population, AJ, **154**, 87

Lanz, T., & Hubeny, I. 2003, A grid of Non-LTE line-blanketed model atmospheres of O-type stars, ApJS, **146**, 417

Lefever, K., Puls, J., Morel, T., Aerts, C., Decin, L., & Briquet, M. 2010, Spectroscopic determination of the fundamental parameters of 66 B-type stars in the field-of-view of the CoRoT satellite, A&A, **515**, A74

Levato, H., & Malaroda, S. 1980, Spectral types in the open cluster NGC 6231, PASP, **92**, 323

Levato, H., & Morrell, N. 1983, Rotation and binarity in NGC 6231, Astrophys. Lett., **23**, 183

Linder, N., Rauw, G., Martins, F., et al. 2008, High-resolution optical spectroscopy of Plaskett's star, A&A, **489**, 713

Liu, Z., Cui, W., Liu, C., Huang, Y., Zhao, G., & Zhang, B. 2019, A Catalog of OB Stars from LAMOST Spectroscopic Survey, Ap&SS, **241**, 32

Maeder, A. 1997, Stellar evolution with rotation. II. A new approach for shear mixing, A&A, **321**, 134

Maeder, A., & Zahn, J.-P. 1998, Stellar evolution with rotation. III. Meridional circulation with MU -gradients and non-stationarity, A&A, **334**, 1000

Mahy, L., Gosset, E., Sana, H., et al. 2012, Evidence for a physically bound third component in HD 150136, A&A, **540**, A97

Mahy, L., Rauw, G., Martins, F., et al. 2010, A new investigation of the binary HD 48099, ApJ, **708**, 1537

Mamajek, E. E., Prša, A., Torres, G., et al. 2015, IAU 2015 Resolution B3 on Recommended Nominal Conversion Constants for Selected Solar and Planetary Properties, ArXiv e-prints [arXiv:1510.07674]

Martinet, S., Meynet, G., Ekström, S., Simón-Díaz, S., Holgado, G., et al. 2021, Convective core sizes in rotating massive stars. I. Constraints from solar metallicity OB field stars, A&A, **648**, A126

Martins, F. 2011, UV, optical and near-IR diagnostics of massive stars, Bulletin de la Société Royale des Sciences de Liège, **80**, 29

Martins, F. 2018, Quantitative spectral classification of Galactic O stars, A&A, **616**, A135

Martins, F., Hervé, A., Bouret, J.-C., et al. 2015, The MiMeS survey of magnetism in massive stars: CNO surface abundances of Galactic O stars, A&A, **575**, A34

Martins, F., & Hillier, D. J. 2012, On the formation of C III 4647-50-51 and C III 5696 in O star atmospheres, A&A, **545**, A95

Martins, F., & Plez, B. 2006, *UBVJHK* synthetic photometry of Galactic O stars, A&A, **457**, 637

Martins, F., Schaerer, D., & Hillier, D. J. 2005, A new calibration of stellar parameters of Galactic O stars, A&A, **436**, 1049

Mas-Hesse, J. M., Giménez, A., Culhane, J. L., et al. 2003, OMC: An Optical Monitoring Camera for INTEGRAL. Instrument description and performance, A&A, **411**, L261

Mason, B. D., Gies, D. R., Hartkopf, W. I., et al. 1998, ICCD speckle observations of binary stars – XIX An astrometric/spectroscopic survey of O stars, AJ, **115**, 821

Mason, B. D., Hartkopf, W. I., Gies, D. R., Henry, T. J., & Helsel, J. W. 2009, The High Angular Resolution Multiplicity of Massive Stars, AJ, **137**, 3358

Mathys, G. 1988, The upper main sequence of OB associations – I Spectral types and lines of C and N of southern single-lined O stars, A&AS, **76**, 427

Mayer, P., Harmanec, P., Nesslinger, S., et al. 2008, Improved estimates of the physical properties of the O-star binary V1007 Sco = HD 152248 and notes on several other binaries in the NGC 6231 cluster, A&A, **481**, 183

Mayer, P., Lorenz, R., & Drechsel, H. 1992, Photometry of two bright early-type binaries: HD 101205 and HD 152248, Inf. Bull. Variable Stars, **3765**, 1

Mayor, M., Pepe, F., Queloz, D., et al. 2003, Setting new standards with HARPS, The Messenger, **114**, 20

Mazeh, T. 2008, Observational Evidence for Tidal Interaction in Close Binary Systems, EAS Publications Series, **29**, 1

Meynet, G., & Maeder, A. 1997, Stellar evolution with rotation. I. The computational method and the inhibiting effect of the μ-gradient, A&A, **321**, 465

Moreno, E., Koenigsberger, G., & Harrington, D. M. 2011, Eccentric binaries - Tidal flows and periastron events, A&A, **528**, A48

Moreno, E., Koenigsberger, G., & Toledano, O. 2005, Line profile variability from tidal interactions in binary systems, A&A, **437**, 641

Muijres, L. E., Vink, J. S., de Koter, A., Müller, P. E., & Langer, N. 2012, Predictions for mass-loss rates and terminal wind velocities of massive O-type stars, A&A, **537**, A37

Naoz, S., Farr, W. M., Lithwick, Y., Rasio, F. A., & Teyssandier, J. 2013, Secular dynamics in hierarchical three-body systems, MNRAS, **431**, 2155

Nesslinger, S., Drechsel, H., Lorenz, R., et al. 2006, Photometric Solution of the O-type Eclipsing Binary V1007 Sco, Ap&SS, **304**, 47

Ohta, Y., Taruya, A., & Suto, Y. 2005, The Rossiter-McLaughlin effect and analytic radial velocity curves for transiting extrasolar planetary systems, AJ, **622**, 1118

Otero, S. A., & Wils, P. 2005, New Elements for 80 Eclipsing Binaries VII., IBVS, **5644**, 1

Palate, M., & Rauw, G. 2012, Spectral modelling of circular massive binary systems. Towards an understanding of the Struve-Sahade effect?, A&A, **537**, A119

Palate, M., Rauw, G., Koenigsberger, G., & Moreno, E. 2013, Spectral modelling of massive binary systems, A&A, **552**, A39

Pasquini, L., Avila, G., Blecha, A., et al. 2002, Installation and commissioning of FLAMES, the VLT Multifibre Facility, The Messenger, **110**, 1

Paxton, B., Bildsten, L., Dotter, A., et al. 2011, Modules for Experiments in Stellar Astrophysics (MESA), ApJS, **192**, 3

Paxton, B., Cantiello, M., Arras, P., et al. 2013, Modules for Experiments in Stellar Astrophysics (MESA): Planets, oscillations, rotation, and massive stars, ApJS, **208**, 4

Paxton, B., Marchant, P., Schwab, J., et al. 2015, Modules for Experiments in Stellar Astrophysics (MESA): Binaries, pulsations, and explosions, ApJS, **220**, 15

Penny, L. R., Gies, D. R., & Bagnuolo, Jr., W. G. 1999, Tomographic separation of composite spectra. VI. The physical properties of the massive close binary HD 152248, ApJ, **518**, 450

Perry, C. L., Hill, G., Younger, P. F., & Barnes, J. V. 1990, A study of Scorpius and NGC 6231. I. New observational data, A&AS, **86**, 415

Pojmański, G., & Maciejewski, G. 2004, The All Sky Automated Survey. Catalog of Variable Stars. III. 12h-18h Quarter of the Southern Hemisphere, Acta Astron., **54**, 153

Press, W. H., Teukolsky, S. A., Vetterling, W. T., & Flannery, B. P. 1992, Numerical Recipes in Fortran, Cambridge University Press

Prinja, R. K., Barlow, M. J., & Howarth, I. D. 1990, Terminal Velocities for a Large Sample of O Stars, B Supergiants, and Wolf-Rayet Stars, ApJ, **361**, 607

Prša, A., Conroy, K. E., Horvat, M., et al. 2016a, Physics Of Eclipsing Binaries. II. Toward the Increased Model Fidelity, ApJS, **227**, 29

Prša, A., Harmanec, P., Torres, G., et al. 2016b, Nominal Values for Selected Solar and Planetary Quantities: IAU 2015 Resolution B3, AJ, **152**, 41

Prša, A., Zhang, M., & Wells, M. 2019, Finding the Needle in a Haystack: Detrending Photometric Timeseries Data of Strictly Periodic Astrophysical Objects, PASP, **131**, 068001

Raboud, D., & Mermilliod, J.-C. 1998, Evolution of mass segregation in open clusters: some observational evidences, A&A, **333**, 897

Raucq, F., Gosset, E., Rauw, G., et al. 2017, Observational signatures of past mass-exchange episodes in massive binaries: the case of LSS3074, A&A, **601**, A133

Raucq, F., Rauw, G., Gosset, E., et al. 2016, Observational signatures of past mass-exchange episodes in massive binaries: The case of HD 149404, A&A, **588**, A10

Rauw, G., & Nazé, Y. 2016, X-ray emission from interacting wind massive binaries: A review of 15 years of progress, AdSpR, **58**, 761

Rauw, G., Pigulski, A., Nazé, Y., et al. 2019, BRITE photometry of the massive post-RLOF system HD 149404, A&A, **621**, A15

Rauw, G., Rosu, S., Noels, A., et al. 2016, Apsidal motion in the massive binary HD 152218, A&A, **594**, A33

Reipurth, B. 2008, Handbook of Star Forming Regions, Vol. II: The Southern Sky (ASP Monograph Publications), **5**, 401

Renzini, A. 1987, Some embarrassments in current treatments of convective overshooting, A&A, **188**, 49

Repolust, T., Puls, J., & Herrero, A. 2004, Stellar and wind parameters of Galactic O-stars – The influence of line-blocking/blanketing, A&A, **415**, 349

Richer, J., Michaud, G., & Turcotte, S. 2000, The Evolution of AMFM Stars, Abundance Anomalies, and Turbulent Transport, ApJ, **529**, 338

Ricker, G. R., Winn, J. N., Vanderspek, R., et al. 2015, Transiting Exoplanet Survey Satellite (TESS), Journal of Astronomical Telescopes, Instruments, and Systems, **1**, 014003

Rosu, S. 2021, What apsidal motion reveals about the interior of massive binary stars, Bulletin de la Société Royale des Sciences de Liège, **90**, 1

Rosu, S., Noels, A., Dupret, M.-A., et al. 2020a, Apsidal motion in the massive binary HD 152248 – Constraining the internal structure of the stars, A&A, **642**, A221

Rosu, S., Rauw, G., Conroy, K. E., et al. 2020b, Apsidal motion in the massive binary HD 152248, A&A, **635**, A145

Rosu, S., Rauw, G., Farnir, M., Dupret, M.-A., & Noels, A. 2022a, Apsidal motion in massive eccentric binaries in NGC 6231 – The case of HD 152219, A&A, **660**, A120

Rosu, S., Rauw, G., Nazé, Y., Gosset, E., & Sterken, C. 2022b, Apsidal motion in massive eccentric binaries in NGC 6231 – The case of CPD-41° 7742, and HD 152218 revisited, A&A, in press [arXiv:2205.11207]

Royer, P., Vreux, J.-M., & Manfroid, J. 1998, A dedicated photometric system for the classification of Wolf-Rayet stars, A&AS, **130**, 407

Sana, H. 2009, The nature of the line profile variability in the spectrum of the massive binary HD 152219 (Research Note), A&A, **501**, 291

Sana, H., Antokhina, E., Royer, P., et al. 2005, The massive binary CPD-41° 7742. II. Optical light curve and X-ray observations, A&A, **441**, 213

Sana, H., de Mink, S. E., de Koter, A., et al. 2012, Binary Interaction dominates the Evolution of Massive Stars, Science, **337**, 444

Sana, H., Gosset, E., Nazé, Y., Rauw, G., & Linder, N. 2008a, The massive star binary fraction in young open clusters - I. NGC 6231 revisited, MNRAS, **386**, 447

Sana, H., Gosset, E., & Rauw, G. 2006, The OB binary HD 152219: a detached, double-lined, eclipsing system, MNRAS, **371**, 67

Sana, H., Hensberge, H., Rauw, G., & Gosset, E. 2003, The massive binary CPD-41° 7742 – I. High-resolution optical spectroscopy, A&A, **405**, 1063

Sana, H., Le Bouquin, J.-B., Lacour, S., et al. 2014, Southern Massive Stars at High Angular Resolution: Observational Campaign and Companion Detection, ApJS, **215**, 15

Sana, H., Nazé, Y., O'Donnell, B., Rauw, G., & Gosset, E. 2008b, The massive binary HD 152218 revisited: A new colliding wind system in NGC 6231, New Astron., **13**, 202

Sana, H., Rauw, G., & Gosset, E. 2001, HD 152248: Evidence for a colliding wind interaction, A&A, **370**, 121

Sana, H., Rauw, G., Sung, H., Gosset, E., & Vreux, J.-M. 2007, An *XMM-Newton* view of the young open cluster NGC 6231 – III. Optically faint X-ray sources, MNRAS, **377**, 945

Sana, H., Stevens, I. R., Gosset, E., Rauw, G., & Vreux, J.-M. 2004, A phase-resolved *XMM–Newton* campaign on the colliding-wind binary HD 152248, MNRAS, **350**, 809

Sanyal, D., Grassitelli, L., Langer, N., & Bestenlehner, J. M. 2015, Massive main-sequence stars evolving at the Eddington limit, A&A, **580**, A20

Schmitt, J. H. M. M., Schröder, K.-P., Rauw, G., et al. 2016, The α CrB binary system: A new radial velocity curve, apsidal motion, and the alignment of rotation and orbit axes, A&A, **586**, A104

Scuflaire, R., Théado, S., Montalbán, J., et al. 2008, CLES, Code Liégeois d'Evolution Stellaire, Ap&SS, **316**, 83

Shakura, N. I. 1985, On the Apsidal Motion in Binary Stars, Sov. Astron. Lett., **11**, 224

Simón-Díaz, S., Godart, M., Castro, N., et al. 2017, The IACOB project – III. New observational clues to understand macroturbulent broadening in massive O- and B-type stars, A&A, **597**, A22

Simón-Díaz, S., & Herrero, A. 2007, Fourier method of determining the rotational velocities in OB stars, A&A, **468**, 1063

Simón-Díaz, S., & Herrero, A. 2014, The IACOB project – I. Rotational velocities in northern Galactic O- and early B-type stars revisited. The impact of other sources of line-broadening, A&A, **562**, A135

Slettebak, A., Collins, G. W., Boyce, P. B., White, N. M., & Parkinson, T. D. 1975, A system of standard stars for rotational velocity determinations, ApJS, **29**, 137

Söderhjelm, S. 1982, Studies of the stellar three-body problem, A&A, **107**, 54

Song, H. F., Maeder, A., Meynet, G., et al. 2013, Close-binary evolution – I. Tidally induced shear mixing in rotating binaries, A&A, **556**, A100

Sota, A., Maíz Apellániz, J., Morrell, N. I., et al. 2014, The galactic O-star spectroscopic survey (GOSSS). II. Bright southern stars, ApJS, **211**, 10

Sota, A., Maíz Apellániz, J., Walborn, N. R., et al. 2011, The Galactic O-Star Spectroscopic Survey. I. Classification System and Bright Northern Stars in the Blue-violet at R ∼2500, ApJS, **193**, 24

Sterken, C. 1983, The ESO Messenger, **33**, 10

Sterken, C. 1994, in the Impact of Long-Term Monitoring on Variable-Star Research, NATO ARW, ed. C. Sterken, & M. de Groot, NATO ASI Series C, **436**, 1 (Kluwer AC. Publ.)

Sterne, T. E. 1939, Apsidal motion in binary stars, MNRAS, **99**, 451

Stickland, D. J., & Lloyd, C. 2001, Spectroscopic binary orbits from ultraviolet radial velocities. Paper 31: Stars with few *IUE* observations, The Observatory, **121**, 1

Stickland, D. J., Lloyd, C., & Penny, L. R. 1997, Spectroscopic binary orbits from ultraviolet radial velocities. Paper 25: HD 152218, The Observatory, **117**, 213

Stickland, D. J., Lloyd, C., Penny, L. R., Gies, D. R., & Bagnuolo, Jr., W. G. 1996, Spectroscopic binary orbits from ultraviolet radial velocities, The Observatory, **116**, 226

Struve, O. 1944, Radial velocities of twenty stars of early type in and near the galactic cluster NGC 6231, ApJ, **100**, 189

Sundqvist, J. O., Björklund, R., Puls, J., & Najarro, F. 2019, New predictions for radiation-driven, steady-state mass-loss and wind-momentum from hot, massive stars. I. Method and first results, A&A, **632**, A126

Sung, H., Bessell, M. S., & Lee, S.-W. 1998, *UBVRI* and Hα photometry of the young open cluster NGC 6231, AJ, **115**, 734

Sung, H., Sana, H., & Bessell, M. S. 2013, The Initial Mass Function and the Surface Density Profile of NGC 6231, AJ, **145**, 37

Tkachenko, A., Pavlovski, K., Johnston, C., Pedersen, M. G., Michielsen, M., et al. 2020, The mass discrepancy in intermediate- and high-mass eclipsing binaries: The need for higher convective core masses, A&A, **637**, A60

Tokovinin, A. A. 2000, On the origin of binaries with twin components, A&A, **360**, 997

Torres, G., Andersen, J., & Giménez, A. 2010, Accurate masses and radii of normal stars: Modern results and applications, A&ARv, **18**, 67

Vanbeveren, D., De Loore, C., & Van Rensbergen, W. 1998, Massive Stars, A&ARv, **9**, 63

van den Heuvel, E. P. J. 1976, Late Stages of Close Binary Systems, Proceedings of the Symposium "Structure and Evolution of Close Binary Systems", **73**, 35

Verschueren, W., & David, M. 1999, Random-error minimization during cross-correlation of early-type spectra, A&AS, **136**, 591

Vink, J. S., de Koter, A., & Lamers, H. J. G. L. M. 2001, Mass-loss predictions for O and B stars as a function of metallicity, A&A, **369**, 574

Voels, S. A., Bohannan, B., Abbott, D. C., & Hummer, D. G. 1989, Photospheres of Hot Stars. III. Luminosity Effects at Spectral Type O9.5, ApJ, **340**, 1073

Walborn, N. R., & Fitzpatrick, E. L. 1990, Contemporary optical spectral classification of the OB stars: a digital atlas, PASP, **102**, 379

Wellstein, S., Langer, N., & Braun, H. 2001, Formation of contact in massive close binaries, A&A, **369**, 939

Wichmann, R. 2002, `Nightfall` User Manual

Wichmann, R. 2011, Astrophysics Source Code Library [record ascl:1106.016]

Zacharias, N., Finch, C. T., Girard, T. M., et al. 2013, The Fourth US Naval Observatory CCD Astrograph Catalog (UCAC4) AJ, **145**, 44

Zahn, J.-P. 1992, Circulation and turbulence in rotating stars, A&A, **265**, 115

Zasche, P., & Wolf, M. 2019, Apsidal motion and absolute parameters of 21 early-type SMC eccentric eclipsing binaries, AJ, **157**, 87

"Whatever can be done will be done. By someone. Somewhere."
– Martin Rees

Sophie Rosu

Apsidal Motion in O-Star Binaries

Constraining the internal structure of the stars

Stars more massive than about ten solar masses play a key role in many processes in the Universe (winds, powerful supernova explosions, chemical enrichment of the Universe). More than 70% of them are bound by gravitational attraction to a companion star and, together, they orbit around each other on an elliptic orbit. The tidal interactions occurring between the two stars give rise to the slow precession of the orbit, called the apsidal motion. The rate of this motion is directly related to the internal structure constant of each star, which is a measure of the mass distribution between the core and the external layers of the star. Measuring the apsidal motion rate hence provides a diagnostic of the otherwise difficult to constrain internal structure of stars and offers a test of our understanding of stellar structure and evolution.